ABSTRACT

KHUWAILEH, BASSAM ABDULLAH AYED. Scalable Methods for Uncertainty Quantification, Data Assimilation and Target Accuracy Assessment for Multi-Physics Advanced Simulation of Light Water Reactors. (Under the direction of Dr. Paul. J. Turinsky).

High fidelity simulation of nuclear reactors entails large scale applications characterized with high dimensionality and tremendous complexity where various physics models are integrated in the form of coupled models (e.g. neutronic with thermal-hydraulic feedback). Each of the coupled modules represents a high fidelity formulation of the first principles governing the physics of interest. Therefore, new developments in high fidelity multi-physics simulation and the corresponding sensitivity/uncertainty quantification analysis are paramount to the development and competitiveness of reactors achieved through enhanced understanding of the design and safety margins. Accordingly, this dissertation introduces efficient and scalable algorithms for performing efficient Uncertainty Quantification (UQ), Data Assimilation (DA) and Target Accuracy Assessment (TAA) for large scale, multi-physics reactor design and safety problems.

This dissertation builds upon previous efforts for adaptive core simulation and reduced order modeling algorithms and extends these efforts towards coupled multi-physics models with feedback. The core idea is to recast the reactor physics analysis in terms of reduced order models. This can be achieved via identifying the important/influential degrees of freedom (DoF) via the subspace analysis, such that the required analysis can be recast by considering the important DoF only. In this dissertation, efficient algorithms for lower dimensional subspace construction have been developed for single physics and multi-physics applications with feedback. Then the reduced subspace is used to solve realistic, large scale forward (UQ) and inverse problems (DA and TAA).

Once the elite set of DoF is determined, the uncertainty/sensitivity/target accuracy assessment and data assimilation analysis can be performed accurately and efficiently for large scale, high dimensional multi-physics nuclear engineering applications. Hence, in this work a Karhunen-Loève (KL) based algorithm previously developed to quantify the uncertainty for single physics models is extended for large scale multi-physics coupled problems with feedback effect. Moreover, a non-linear surrogate based UQ approach is developed, used and compared to performance of the KL approach and brute force Monte Carlo (MC) approach.

On the other hand, an efficient Data Assimilation (DA) algorithm is developed to assess information about model's parameters: nuclear data cross-sections and thermal-hydraulics parameters. Two improvements are introduced in order to perform DA on the high dimensional problems. First, a goal-oriented surrogate model can be used to replace the original models in the depletion sequence (MPACT – COBRA-TF - ORIGEN). Second, approximating the complex and high dimensional solution space with a lower dimensional subspace makes the sampling process necessary for DA possible for high dimensional problems.

Moreover, safety analysis and design optimization depend on the accurate prediction of various reactor attributes. Predictions can be enhanced by reducing the uncertainty associated with the attributes of interest. Accordingly, an inverse problem can be defined and solved to assess the contributions from sources of uncertainty; and experimental effort can be subsequently directed to further improve the uncertainty associated with these sources. In this dissertation a subspace-based gradient-free and nonlinear algorithm for inverse uncertainty quantification namely the Target Accuracy Assessment (TAA) has been developed and tested.

The ideas proposed in this dissertation were first validated using lattice physics applications simulated using SCALE6.1 package (Pressurized Water Reactor (PWR) and

Boiling Water Reactor (BWR) lattice models). Ultimately, the algorithms proposed her were applied to perform UQ and DA for assembly level (CASL progression problem number 6) and core wide problems representing Watts Bar Nuclear 1 (WBN1) for cycle 1 of depletion (CASL Progression Problem Number 9) modeled via simulated using VERA-CS which consists of several multi-physics coupled models. The analysis and algorithms developed in this dissertation were encoded and implemented in a newly developed tool kit algorithms for Reduced Order Modeling based Uncertainty/Sensitivity Estimator (ROMUSE).

Scalable Methods for Uncertainty Quantification, Data Assimilation and Target Accuracy Assessment for Multi-Physics Advanced Simulation of Light Water Reactors

by
Bassam Khuwaileh

A dissertation submitted to the Graduate Faculty of
North Carolina State University
in partial fulfillment of the
requirements for the Degree of
Doctor of Philosophy

Nuclear Engineering

Raleigh, North Carolina

2015

APPROVED BY:

_____	_____
Dr. Paul J. Turinsky Committee Chair	Dr. Ralph C. Smith
_____	_____
Dr. Nam T. Dinh	Dr. Ugur Mertyurek

DEDICATION

In loving memory of my late grandfather *Ayed Khuwaileh* who filled my life with grace and wisdom. My greater sorrow is being and will forever be that I never had the chance to say a final good bye. Grandfather: you shall not be forgotten.

To the soul of Captain *Muath Al-Kasasbeh* who martyred defending our beloved Jordan. Captain: though we never met, and now never shall, your bravery and sacrifice will be forever engraved in our hearts.

Finally, to my father *Dr. Abdullah Khuwaileh*, mother *Entesar Al-Dawood* for their endless support and motivation. To my brother *Tarik Khuwaileh* who has been and will forever be my best friend. To my lovely sisters Rawan and Difaf and brothers Hamzah and Baker and everybody in my beloved Ramtha.

BIOGRAPHY

Bassam Abdullah Khuwaileh, born in Ramtha, Jordan on July 19th 1989 to Abdullah Khuwaileh (a university professor) and Entisar Al-Dawood (a school teacher). He received his elementary and secondary education in Ramtha, graduating from Ramtha High School in 2007 with honor.

Upon graduation from high school, Bassam joined the Nuclear Engineering department at Jordan University of Science and Technology in fall 2007. During his undergraduate studies Bassam developed interests and published research papers in the areas of reactor design, modeling and simulation. Besides Bassam has pursued interests in renewable energy sources. In 2012, Bassam graduated with a B. S. in Nuclear Engineering and was the top of his class, afterwards he joined the graduate program in the Nuclear Engineering department at North Carolina State University during which he was funded by the Consortium for Advanced Simulation of Light Water Reactors (CASL).

ACKNOWLEDGMENTS

My utmost and most sincere gratitude to my advisor, Prof. Paul J. Turinsky for the continuous support of my Ph.D study and related research, for his patience, motivation, and immense knowledge. His guidance helped me in all the time of research and writing of this dissertation.

Besides my advisor, my appreciation goes to my doctoral committee: Dr. Nam T. Dinh, Dr. Ugur Mertyurek and Dr. Ralph C. Smith for their insightful comments and encouragement. My sincere thanks also goes to Dr. Hany S. Abdel-Khalik, Dr.Youngsuk Bang, and Dr.Congjian Wang whom their help and collaborations was so precious. Also, I would like to thank Oak Ridge National laboratory and more specifically Dr. Goran Arbanas and Dr. Mark Williams who provided me an opportunity to join their team. Thanks for Texas Advanced Computing Center for offering the computer allocation required to perform a large part of this research without their precious support it would not be possible to conduct considerable part of this research. Also, I would like to thank the Consortium for Advanced Simulation of Light Water Reactors (CASL) and the U.S. Department of Energy for supporting this research.

I also would like to thank Mrs. Hermine Kabbendjian for everything she did for me and for the other students in CASL group. I thank my fellow lab-mates and friends (Jason Hite, Trip Dacus, Jun Fang, Shota Soga and Allison Lewis) for the stimulating discussions, for the sleepless nights we were working together before deadlines, and for all the fun we have had in the last three years. My heartfelt thanks to Dr. Moh'd Al-Nimr for his support throughout the past years. Above all, I am grateful to my parents, grandparents, and sibling for their unconditional love and support which uplifted my spirit throughout my life.

TABLE OF CONTENTS

LIST OF TABLES

LIST OF FIGURES

CHAPTER 1. INTRODUCTION

Enhancing the efficiency of existing nuclear power reactors and developing new reactor designs require rigorous modeling and simulation tools that allow engineers to further understand physical phenomena more thoroughly and precisely than ever before. However, developing such precise and robust Virtual Reactor tools (VR) requires the employment of accurate, yet computationally realistic, mathematical models.

Modeling nuclear reactors is a complex process due to the fact that the structure of reactors is highly heterogeneous. Fuel, gap, cladding, coolant, moderator, fuel grid, gaps, control rods, and other structural materials must be considered as separate mediums in the modeling process. Therefore, core wide calculations are performed in three steps with each dealing with a different scale of the reactor core. As shown in Figure 1, typically the core calculations can be divided into pin-cell (this step is bypassed in modern lattice physics codes), assembly and core-wide calculations. For pin-cell calculations, a fine group cross-section library is used to calculate intra-group quantities (e.g. neutron flux). The ultimate goal of the pin-cell calculations is to produce spatially dependent multi-group cross-section to be used in the next level of the calculations.

The next level of the calculations is the lattice physics calculations (assembly level calculations) which are performed using the multi-group cross-sections produced by the previous step. At this level the spatial meshing is finer than that used for pin-cell calculations. This is due to the fact that assemblies have many different mediums that accounts for the heterogeneity along with the azimuthal dependence that must be captured. The resultant of the lattice physics calculations is the production of the few-group cross-sections.

Finally, core-wide calculations use the assembly-averaged nuclear data cross-sections library, to determine the neutron flux distribution and power levels over the entire core (nodal power) [1]. All modeling steps use mathematical models that are integrated together to form the so called Virtual Reactor (VR). VR uses the available nuclear data cross-sections and other parameters obtained via experiments that are subjected to various sources of uncertainty; to simulate various reactor operation conditions (e.g. various fuel cycles, plant startup, power maneuvering, and core reload/fuel discharge), hence, in order to provide meaningful simulation results; these parameters (e.g. cross-sections) should be provided along with their associated uncertainties. Therefore, quantities predicted via the VR are subjected to uncertainties that might be significant in the process of reactor design and safety margins. This leads to the fact that uncertainty quantification and sensitivity analysis are vital and important to be available for any tool of high fidelity nuclear reactor simulation. Moreover, since model's parameters are considered a major source of uncertainty in the attributes of interest, efforts have been concentrated towards precisely determining these parameter. These efforts led to the application of inverse methods, adaptive core simulation and model calibration in nuclear reactor modeling and simulation using the experimental observables.

This dissertation builds upon previous efforts for adaptive core simulation developed by H. S. Abdel-Khalik, M. A. Jesse, and P. J. Turinsky [2, 3] and reduced order modeling algorithms developed by Y. Bang and H. S. Abdel-Khalik [4] for uncertainty quantification of single physics models towards coupled multi-physics models with feedback effect. In the following sub-sections, previous efforts will be reviewed and discussed, then new developments will be summarized as an introduction for chapters 2 through 6.

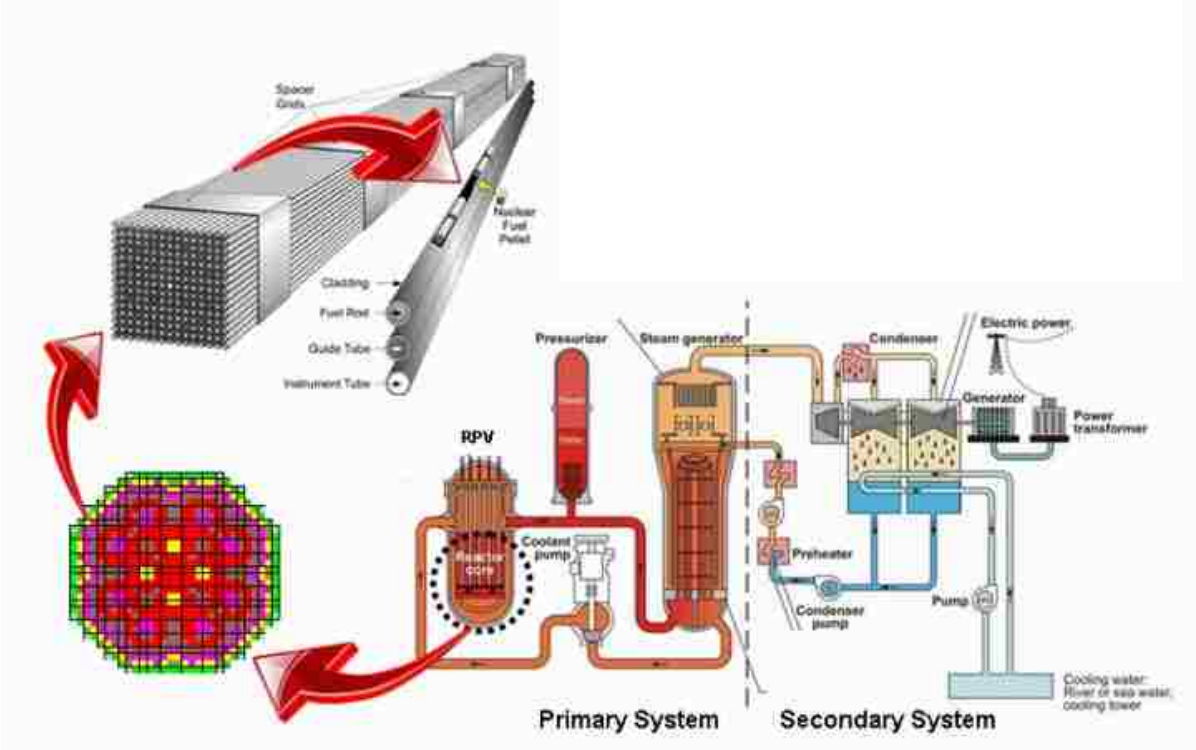

Figure 1. Nuclear Reactor (http://energy.gov/articles/modeling-and-simulation-nuclear-reactors-hub).

1.1 Motivation

Recently, there has been increasing demand in the nuclear industry, safety, and regulation communities for precise confidence bounds to be provided with high fidelity predictions. For example, the U. S. Nuclear Regulatory Commission requires conservatisms on the design to assure adequate safety margins. In order to achieve that, best-estimate high fidelity calculations accompanied by an uncertainty evaluation must be provided so that the conservative design assumptions are replaced by model based estimates of the margins. The largest effort in this direction might be represented by the Code Scaling, Applicability and Uncertainty (CSAU) which demonstrates the use of model-based analysis to quantify the uncertainties [5-8]. However, CSAU received a number of criticisms best summarized in Ref. [7]. A number of

questions reported in Ref. [7] summarized the most important concerns about CSAU. The most important comments which are concerns to this work are:

1- The generality of the CSAU formalism.
2- Too many uncertainty factors are ignored due to the high computational costs of encountering them.
3- Excessive use of engineering judgement.

Establishing a unified framework to estimate uncertainties, safety margins and parameter calibration is important and fundamental for the improvement of reactor modeling and simulation. Therefore, this dissertation develops a framework that can encounter large scale uncertainty quantification problems (core-wide uncertainty quantification). Moreover, the generality and the conditions of applicability of the proposed framework are discussed. This would provide a more realistic and physics-based measure of reactor safety and design calculations which help the practical implementation of risk informed regulations. Moreover, having simulation-based margins helps in accelerating the licensing process when using high fidelity computer codes in safety analysis. For example, design margins can be improved by reducing predictive uncertainty in key reactor attributes. However, the improvement of the uncertainties in such important attributes requires a robust experimental effort with potentially a huge investment in time and/or money. Nevertheless, with the availability of solid and efficient simulation tools the experimental effort can be directed in the most efficient and optimized manner so that the time-financial investment is minimized and the safety-competitiveness gain is maximized.

High fidelity nuclear reactor simulation involves solving equations describing various chemical phenomena, heat generation and heat transfer by convection and conduction, fluid

hydraulics, and radiation transport. However, these equations are typically nonlinear, entails properties that are functions of the solution state (e.g. burnup dependent isotopic number density in transport calculation is a function of the neutron flux distribution), and they are often strongly coupled to each other. Unfortunately, nuclear engineering design and safety analysis includes dozens of phenomena that need to be simulated via nonlinear tightly coupled large scale, multi-physics models operating at a diversity of time and spatial scales. Therefore, in order to perform high fidelity simulations, and hence improving the design and safety margins, scientist should tackle these problems providing the most efficient and timely reasonable techniques to account for these complications.

Current modeling and simulation tools solve these problems using the operator split methods, where the models are loosely coupled by decoupling phenomena and solving the resulting modified equations separately. If the coupled models are weakly dependent on each other, then each model can be simulated while fixing the other models (refer to Figure 2), followed by a solution of the second system given the result of the first model solution. On the other hand, if the coupled models are strongly dependent on each other and/or the coupled physics operate on disparate time scales then the former coupling technique usually converges very slowly if at all [9].

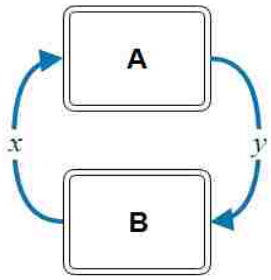

Figure 2. Two coupled multi-physics models.

A higher degree of coupling can be achieved via solving the models simultaneously employing a tightly coupled solution procedure by formulating a combined nonlinear algebraic system of equations which can be solved using a strongly convergent nonlinear solver such as the Jacobian–free Newton methods. Efforts in this direction can be exemplified by the Multi-physics Object Oriented Simulation Environment (MOOSE) tool developed by Idaho National Laboratory [9]. MOOSE provides the user with several coupling schemes.

Uncertainties in key reactor safety and design attributes originate from a variety of sources that must be identified, analyzed and improved. In order to efficiently reduce the uncertainties associated with key reactor attributes, the uncertainty sources must be identified along with their contributions to the overall uncertainty. This is possible through the combined activities of uncertainty quantification analysis, data assimilation and target accuracy assessment. Data assimilation (i.e. parameter calibration) links the wealth of precise integral experiments and modeling which result in accurate and more reliable calibrated parameters (e.g. gap conductivity and cross-sections). However, the application of the data assimilation process for nuclear engineering applications has a number of challenges such as the huge computational burden associated with the model's complexity and the scalability of the method for multi-physics problems. More details about the data assimilation methods and challenges associated with them will be introduced in later sections.

Target accuracy requirements can be defined based on the input from the safety, regulation and industrial bodies. Such target accuracies can be used along with the high fidelity and multi-physics simulation tools to assess the requirements on the uncertainty sources, hence, directing the subsequent experimental efforts in the most efficient and useful manner. After all, it is obvious that the Uncertainty Quantification (UQ) and Inverse Uncertainty Quantification

(IUQ) methods are at the heart of the development of reliable, safe and more competitive nuclear power plants.

The following sub-sections will briefly introduce the available theories and methodologies for UQ and IUQ, including data assimilation and target accuracy assessment). Moreover, problems and challenges related to the application of these methods will be highlighted and briefly discussed. Finally, Reduced Order Modeling (ROM) [10-12] will be introduced as a facilitator of the UQ and the IUQ analysis through a brief introduction on the usefulness of the ROM techniques to their current and potential applications in nuclear engineering modeling, simulation and uncertainty quantification.

1.2 Uncertainty Quantification

The ability to quantify the uncertainty in quantities predicted by computational models is important and paramount to various inference problems involved in nuclear engineering analysis. The UQ analysis quantifies the uncertainty in a certain response of interest (RoI) and identifies all plausible and important sources of uncertainty along with their contributions to the overall uncertainty.

Generally, computer codes are used to simulate various phenomena involved in the analysis of nuclear reactors. Using best estimate calculations that are combined with well estimated uncertainties provides more realistic evaluation of plant safety margins for licensing. In addition to that, there is nothing, in the uncertainty quantification methods and techniques that is limited to a specific reactor type or plant scenario (where conservatism varies for different reactor types, conditions and experts opinion). Once developed and agreed on, these methods and techniques can be applied to any reactor type (e.g. high temperature gas-cooled reactors or

liquid metal reactors) and any reactor condition (e.g. steady-state calculations, severe accident scenarios or operational transients…etc). Moreover, major sources of uncertainty can be determined and uncertainties reduced through robust and efficient experiments. This will lead to better response to emergencies due to the better understanding of the key phenomena.

Major sources of uncertainty might be classified as follow:

a- Modeling Uncertainties: originating from the assumptions and/or simplifications entailed in the model. For example in for nuclear physics calculations the various self-shielding approximations used in the multi-group cross sections generation introduce uncertainties into the self-shielded libraries.

b- Numerical Uncertainties: For example in deterministic methods the use of finite difference methods for spatial meshing introduce uncertainties and lack of full convergence of iterative methods.

c- Input Data Uncertainties: Frequently the major source of uncertainty in the key reactor attributes is due to uncertainties in evaluated nuclear data such as microscopic cross sections, fission spectra, neutron yield (nu-bar) and scattering distributions that are contained in ENDF/B. Data assimilation/adjustments have been used to improve the knowledge of this source of uncertainty so that they cause less uncertainty in the response or attribute of interest [13].

Models most times contain parameters that are obtained by fitting the model for experimental results. Since experiments contain uncertainty, even with a perfect conceptual model, the model will have uncertainty due to the associated parameters' uncertainties. In this work, the conceptual model will be assumed perfect, and parameters will refer to model parameters and input data. Various methods are available for uncertainty quantification. These

methods are either statistical or deterministic [14, 15]. Statistical methods (such as Monte Carlo simulations, adaptive sampling ... etc.) propagate the uncertainties in a stochastic manner, where the sources of uncertainties are sampled from previously assumed (Probability Density Functions) PDFs. Therefore, the uncertainties can be determined by statistically analyzing the samples of responses of interests (finding the low order moments of the collected data). The Monte Carlo (MC) sampling approach has been widely recognized as the most versatile approach to propagate the uncertainties due for many reasons: first, its computational cost depends on the number of samples rather than the dimensionality of the uncertainty sources space; second, it can be implemented in a non-intrusive manner; and third, no assumptions have to be made about the model order, e.g. linear vs. nonlinear. However, the stochastic nature of the MC sampling entails statistical uncertainties that would affect the results of the UQ analysis; moreover, the statistical approach does not provide information about the uncertainty contribution per uncertainty source.

On the other hand, deterministic methods usually require the accessibility to the sensitivity profile of the RoI with respect to the source of uncertainty; moreover, covariance libraries of the uncertainty sources must be provided. These two pieces of information are then combined linearly (e.g. sandwich rule) or non-linearly depending on the model of interest. However, the sensitivity profiles are usually hard to obtain especially for high dimensional problems. For example, nuclear engineering applications often involve models characterized with large input parameter dimensionality (e.g. nuclear data cross-sections) and/or high dimensional response space (e.g. 3-dimensional mesh-wise neutron angular flux distribution). Generally, there are two approaches to evaluate the sensitivities; the forward approach and the adjoint approach. The adjoint (variational) approach is preferred whenever the model is characterized with a high

dimensional input parameter space with few RoI. The adjoint approach entails the calculation of *m* adjoint profiles each corresponding to one of the responses (observables). Therefore, the computational cost of applying the adjoint approach depends on the number of responses. Nevertheless, if the dimensionality of the RoI-space is high and/or the adjoint model is not available, then the forward approach (brute force) might be used. Although the forward approach is always available to use, its computational cost depends on the number of inputs (dimensionality of input parameter space). Unfortunately, neutronics applications are characterized with a huge dimensionality in the input space (e.g. nuclear data cross-section) and in certain applications huge dimensionality in the response space (e.g. mesh wise neutron angular flux distribution).

1.3 Data Assimilation

Data Assimilation (DA) is the mathematical process by which the actual experimental measurements are incorporated in virtual models in order to improve their performance and simulation of the real physical phenomena. Data assimilation uses a variety of inverse methods to calibrate model's parameters which can be categorized as deterministic methods and statistical methods; a comprehensive representation of these methods is presented in Ref. [15]. The deterministic methods, such as the least squares methods solve the calibration problem as an optimization problem that seeks a parameter set that minimizes the residual between model's predictions and the experimental observables. Moreover, deterministic methods are computationally efficient and provides mathematical guarantee of the numerical convergence. Deterministic methods provide estimates of covariance matrix that characterize the parameters

set; however, much less details are provided about the posterior statistical distribution of the parameter set [15].

On the other hand, statistical methods are more attractive for applications where precise information are required about the statistical properties of the parameters of interest. These methods are categorized into Frequentist approaches and Bayesian approaches for model calibration and parameter estimation. Frequentist parameter estimation approaches relies on the assumption that the experimental observation is one possible outcome of infinite repetitions of the same experiment or phenomena. Moreover, the unknown parameters are treated as being fixed values; hence, no probabilities can be associated with them. However, true and false conclusions can be assigned with corresponding probabilities of each value (true and false). Bayesian parameter estimation approaches assume that the parameters are considered as random variables with associated probability density functions. Therefore, the result of the Bayesian approach is a posterior Probability Density Function (PDF).

Data assimilation has been used for parameter estimation and model calibration in nuclear engineering applications. Ref. [16-25] used various data assimilation techniques for neutronics and thermal hydraulics for key parameter estimation. More specifically, Ref. [21] used the subspace methods in the context of data assimilation for large scale problems. The method introduced therein regularizes the data assimilation problem via a lower dimensional subspace approximation obtained via a gradient-based approach. However, in this work the data assimilation problem will be efficiently solved utilizing other features of the subspace method. First a surrogate model will be used to replace the original complex model. Second, the problem will be regularized via a subspace obtained by a gradient-free approach.

In the remainder of this text, the data assimilation problem will be solved by the Bayesian approaches. Before introducing the details of the Bayesian approaches for parameter estimation and model calibration, the Bayesian interpretation of probability is reviewed here. Assume that the prior density $\pi_0(q)$ includes all the information about the model's parameter (q) prior to obtaining the experimental measurement or observation. This prior information might be coming from similar experiments or analytical approximations. From a Bayesian point of view the information coming from an observation (v) can be incorporated into the likelihood function as follow:

$$\pi(v \mid q) = \frac{\pi(q, v)}{\pi_0(q)}$$

where $\pi(q, v)$ is the joint probability of the random parameter and observation (v). So given a certain observation v_{obs}, the posterior density function of a certain state of the parameter (*q)* given an observation v_{obs} is :

$$\pi(q \mid v_{obs}) = \frac{\pi(q, v_{obs})}{\pi_0(v_{obs})}$$

where $\pi_0(v_{obs}) = \int_{\mathbb{R}^p} \pi(q, v_{obs})\, dq = \int_{\mathbb{R}^p} \pi(v_{obs} \mid q)\pi_0(q)\, dq$; hence, the posterior density function of *q* can be given as:

$$\pi(q \mid v_{obs}) = \frac{\pi(v_{obs} \mid q)\pi_0(q)}{\int_{\mathbb{R}^p} \pi(v_{obs} \mid q)\pi_0(q)\, dq} \tag{1}$$

Several algorithms implement the Bayesian approach for parameter estimation. Among these are the Markov Chain Monte Carlo (MCMC) Algorithms. Ref. [15] contains a comprehensive study and details about these algorithms. The main short coming of the MCMC

is that these algorithms generate samples from the posterior density function based on rejecting others, hence whenever the probability space is complex and high dimensional the MCMC methods fails to generate useful samples which results in the rejection of a large portion of the samples. In order to evaluate the likelihood of a sample; the model of interest must be run which means that rejecting many samples mean inefficiency in the computational cost of the method and slow convergence, if any.

Two Adaptive Metropolis-based algorithms can be used in order to perform parameter estimation and reduce the above difficulties. The first is the Delayed Rejection Adaptive Metropolis (DRAM) [27] and the DiffeRential Evolution Adaptive Metropolis (DREAM) [28]. In this work DRAM will be used to utilize available plant data (measurements and integral experiments) in order to estimate the key parameters and estimate the probability distribution that describes their effect on the overall uncertainty in certain key reactor attributes.

Ref.[20-26] are samples of the efforts to utilize the power of the data assimilation methodologies into nuclear reactor modeling and simulation. In these previous efforts, the mathematical framework of data assimilation was formulated and tested for calibrating modeling parameters for light water reactors and fast reactors [26].

Previous efforts [22-24] were made to apply a consistent method for further improving and understanding the nuclear data important for reactor modeling such as the inelastic discrete levels, evaporation temperatures for shielding applications and resolved resonance parameters of actinides (e.g. peak positions). These early studies indicated the validity of the method proposed therein but, on the other hand, they highlighted a number of challenges for large scale practical applications such as the way of getting the sensitivity coefficients and the need of reliable covariance information.

Moreover, in Ref. [25] a new approach was developed and implemented to link the integral experiments to basic nuclear parameters used for the generation of point cross-sections data files. By performing the data assimilation of few nuclear parameters (e.g. scattering radius, resonance parameters, optical model parameters, Statistical Hauser-Feshbach model parameters and Pre-equilibrium Exciton model parameters) allowed performing the data assimilation on a few parameters set while applying the results on all multi-group nuclear data cross-sections. On the other hand, and for large scale problems, Ref. [21] introduced the use of the subspace methods for the regularization of the data assimilation problem which results in reducing the computational cost of the problem and allows the analyst to encounter a relatively large number of parameters for the calibration study. More details about the former contributions will be given in the coming sections whenever convenient.

This dissertation introduces efficient techniques for the application of Metropolis algorithms in large scale nuclear engineering applications. The details of DRAM are outlined in chapter 5. The advancements introduced here can be summarized by first, replacing the complex models with goal-oriented surrogate models and obtaining necessary samples from a lower dimensional subspace instead of sampling from high dimensional complex spaces that characterize the problem. Details will be provided in chapter 5**.**

1.4 Inverse Uncertainty Quantification (Target Accuracy Assessment)

Nuclear reactor design and safety calculations require rigorous calculations of several important reactor attributes such as the multiplication factor, and reactor power and temperature distributions. Therefore, new developments in uncertainty reduction are paramount to improve the competitiveness of nuclear energy against other energy sources

making it an economic and safe energy alternative. Nuclear data are considered to be a major contributor to the uncertainties in the calculated reactor attributes. Therefore, it is natural to seek algorithms that identify the key nuclear data whose reduced uncertainties would have the highest impact on the uncertainties of reactor attributes of interest. Nuclear data experiments could then be established to reduce the uncertainty of the identified nuclear data. Given that the cost of experiments noticeably vary from one isotope-reaction-energy-specific cross-section to another, one must take into account both the cost of the experiment and the potential benefit of uncertainty reduction on the attributes of interest. This is possible via a constrained optimization problem that minimizes a cost function, representing the cost of the experiments, while being constrained by the reduced uncertainty sought for the attribute(s) of interest. This problem was tackled and appeared under the name nuclear data target accuracy assessment, initially developed by Uschev in 1970s [16]. We refer to this problem as the inverse sensitivity/uncertainty quantification (IUQ) problem or more specifically, target accuracy assessment. The IUQ problem has been applied for current and future reactors [19, 20]. These studies considered different integral quantities such as the multiplication factor, reactivity coefficients and various important reaction rates. Based on a target uncertainty for the attributes, as defined by design/economic consideration, these studies have shown that the current nuclear data evaluations need further improvements; see Ref. [19] for an example of a comprehensive study. Ideally, all parameters that might contribute significantly to the overall uncertainty of the attribute of interest must be included in the IUQ analysis, for example: nuclear fuel and structural material cross-sections, fission products yields, and any other potentially important source of uncertainty must be included. Hence the number of parameters might grow very large, which increases the computational cost of the IUQ analysis and weaken

the identifiabilty of the problem's solution. These challenges are usually addressed by the elimination of parameters that do not contribute significantly to the overall uncertainty [19]. The sensitivity of each response is calculated for a reference case composition, then, influential parameters are selected based on their contribution to the overall uncertainty. However, the sensitivity profile may not remain constant over a range of inputs around the reference case. Hence the contribution might change as the input parameters change. This means that eliminating parameters that do not significantly contribute to the uncertainty relies on the assumption that the uncertainty contribution of each source is constant. This assumption cannot be always asserted and/or guaranteed. Therefore, many sources of uncertainty must be involved in the IUQ analysis.

Previous sections discussed the necessity of high fidelity simulations, efficient uncertainty quantifications and design optimization for the development of advanced reactor designs. This section highlights on different techniques to perform uncertainty quantification and design optimization efficiently and the challenges involved in applying these techniques to reactor design and safety problems. Mainly, the huge dimensionality involved in the reactor design and safety problems forms the major challenge. Hence this work is devoted to develop efficient Reduced Order Modeling (ROM) based algorithms for the performance of the forward and inverse sensitivity/uncertainty quantification analysis for light water reactors (LWRs). The inverse uncertainty quantification analysis help to evaluate the impact of each neutron cross-section parameter uncertainty on the most important integral responses related to the core in general and nuclear fuel cycle and forward/inverse depletion calculations in specific.

1.5 Reduced Order Modeling

1.5.1 Overview

Forward and inverse statistical problems can be solved by either the Bayesian or frequentist approaches. However, either approach can be a computationally intensive endeavor, particularly when faced with large-scale complex models such as high fidelity nuclear reactor simulators (coupling neutronics with thermal-hydraulics). Therefore, subspace based reduced order modeling can offer several ways for reducing the computational cost of such problems:

1- Reducing the cost of the forward simulation: which implies replacing the original model with surrogate models or reduced-order models.

2- Reducing the effective dimensionality of the input parameter space. Hence dealing with a small number of DoF when solving the forward and/or inverse problems (UQ and IUQ)

3- Reducing the number of forward simulations required (i.e., more efficient sampling). For example in the Bayesian setting, these methods include adaptive and multi-stage Markov Chain Monte Carlo (MCMC) based algorithms.

Therefore, Reduced Order Modeling (ROM) can be one of the most important techniques that make the analysis of complex and computationally expensive models possible. Hence this dissertation introduces efficient ROM based algorithms that can be used for solving high dimensional single and multi-physics forward and inverse sensitivity/uncertainty quantification problems in nuclear engineering applications.

Reduced Order Modeling (ROM) achieves that by reducing the effective dimensionality of the variables associated with the various physics models, including physics input parameters, state functions, and responses of interest. The reduced dimensions are determined such that the resulting reduction errors (difference between the respective variable's variation in the original

space and those reconstructed from the reduced dimensions) meet pre-defined user tolerance limits with an overwhelmingly high probability [29, 30, 34]. Mathematically, the reduced dimensions are described by a subspace, whose basis dimension is in many cases considerably smaller than the dimension of the original space. Symbolically, this can be described as follows: let the *n* input parameters, e.g., cross-sections, be represented by a vector, $\bar{x} \in \mathbb{R}^n$; and similarly, the *m* components of the state, e.g., multi-group flux, with a vector $\bar{\phi} \in \mathbb{R}^m$, and the *p* responses, reaction rates for a number of nuclides that are tracked later by a depletion code, by $\bar{y} \in \mathbb{R}^p$. The reduced variables $\bar{x}_r$, $\bar{\phi}_r$, and $\bar{y}_r$ are, respectively, given by: $\bar{x}_r = \mathbf{U}_x^T \bar{x}$, $\bar{\phi}_r = \mathbf{U}_\phi^T \bar{\phi}$, and $\bar{y}_r = \mathbf{U}_y^T \bar{y}$, where the r_x columns of the matrix $\mathbf{U}_x \in \mathbb{R}^{n \times r_x}$ represent a basis for the active parameter subspace. Similarly, the r_ϕ columns of $\mathbf{U}_\phi \in \mathbb{R}^{n \times r_\phi}$, and the r_y columns of $\mathbf{U}_y \in \mathbb{R}^{n \times r_y}$ represent bases for the active subspaces for the state and responses, respectively. Considering the parameter space by way of an example, the r_x refers to the number of dominant or effective components in the parameter space. 'Dominant' or 'effective' implies that one can represent within a specified accuracy all possible parameter variations that are responsible for the response and state variations using only r_x degrees of freedom. The reduced degrees of freedom are used to reconstruct the parameters in the original space as follows:

$$\tilde{\bar{x}} = \mathbf{U}_x \mathbf{U}_x^T \bar{x} = \mathbf{U}_x \bar{x}_r ,$$

where now $\left\| \bar{x} - \tilde{\bar{x}} \right\| \le \varepsilon_x$ is denoted as the reduction error. It has been proven in earlier work that r_x may be selected to meet a user-defined upper-bound ε_x [30, 34].

The reduced dimensions are determined such that the resulting reduction errors (difference between the respective variable's variation in the original space and those reconstructed from

the reduced dimensions) meet pre-defined user tolerance limits with overwhelmingly high probability. Mathematically, the full dimensional space is approximated by a lower dimensional subspace (active subspace).

In order to calculate the basis of the active subspace, a plethora of techniques have been developed in different science and engineering fields [29-33]; for an overview of such techniques, the reader may consult Ref. [34] and the references therein. ROM approaches may be classified into two broad categories, parametric and nonparametric approaches. In parametric approaches, the model variations for the variable of interest are fitted to a response surface that is described by a pre-determined set of functions with unknown coefficients. These functions represent a basis for the active subspace, where the unknown coefficients are determined using an optimization search that minimizes the discrepancies between the variable's variations as calculated by the original model and those calculated by the assumed response surface [36 ,39]. Nonparametric approaches avoid the use of assumed set of functions; instead they use pattern recognition techniques to represent the dominant variations using a smaller number of degrees of freedom. Projection-based techniques belong to this category [40, 41]. Ref. [34] shows that the conventional linear algebra toolkit, including the singular value decomposition (SVD) algorithm and randomized Range Finding Algorithms (RFAs), can be used to identify an active subspace that approximates, with high probability, the dominant variations to a quantifiable accuracy for a general smooth nonlinear model [34]. If applied at the state level (i.e., flux in neutronics modeling), one can recast the model equations using their weak form to constrain the state variations to the identified active subspace. An example of such an approach is the Petrov-Galerkin rendition that is often employed for finite elements-based models [40]. Central to any nonparametric approach is the ability to determine

a basis for the active subspace. Many approaches have been developed to find such basis, e.g., the approximate balanced truncation methods [43], Krylov subspace methods [49] and the proper orthogonal decomposition (POD) [45 ,49]; Ref. [34] contains an excellent review of projection-based ROM techniques. The most common approach to constructing the subspace is the method of snapshots, where snapshots of the model are captured at successive points in time [32] or by perturbing the model's input parameters and capturing the corresponding state or response variations [34-40]. For sufficiently complex models, this approach may still be impractical, as the single execution of the model is considered to be computationally taxing, especially for models characterized by slow convergence rate. Hence, this work investigates the utilization of the non-converged iterates within the context of reduced order modeling in nuclear engineering applications.

For example, the Boltzmann equation is used to solve for the neutron flux inside the reactor core. This is a partial integro-differential equation in space, time, energy, and angle. To separate out the time dependence, the equation can be recast in the form of a generalized eigenvalue problem, where the eigenvalue is to be equal to one when the reactor is critical. For details on its construction, the reader is referred to Ref. [49]. The power iteration method is often used to calculate the fundamental eigenvalue (i.e., multiplication factor) and the corresponding fundamental eigenfunction (i.e., neutron flux distribution). However, the convergence rate of the power iteration is determined by the dominance ratio which is defined as the ratio of the second largest eigenvalue to the maximum eigenvalue. The power iteration converges very slowly for problems with relatively large dominance ratios, a situation that is common in problems of practical interest. For this reason, a number of acceleration methods have been developed and utilized; however, multiple iterations are still required to satisfy

stopping criteria. Therefore, whenever a snapshot based technique is used the application of ROM is hindered by the fact that the repeated execution of such models is computationally taxing.

1.5.2 Reduced Order Modeling Based Sensitivity Analysis, Uncertainty Quantification and Data Assimilation

Various efforts have demonstrated the use of dimensionality reduction in nuclear engineering applications, mostly, in sensitivity analysis, uncertainty quantification and data assimilation. For example the forward uncertainty propagation using the deterministic approach has a computational cost that is proportional to the dimension of the input space (uncertainty source space), hence a justified dimensionality reduction on this space would result in a more efficient forward uncertainty propagation. An early proposal of this technique is represented in Ref. [33-35]. Ref. [34] provided mathematical justification of the technique and applied it for uncertainty quantification in neutronics applications. Ref. [4, 34] perform a Karhunen-Loève (KL) expansion-based uncertainty quantification for single physics neutronics models. The principal KL expansion basis vectors are determined using a gradient-based version of the Range Finding Algorithm (RFA) to identify important Degrees of Freedom (DoF) in the form of subspace basis vectors. These DoF (basis vectors) are then used to propagate the uncertainty in the nuclear data cross-sections efficiently. Chapter 0 overviews the analysis and the algorithm provided in Ref. [34, 4]; moreover, the chapter introduces an extension of the proposed algorithm into multi-physics coupled models.

Bang and Abdel-Khalik utilized an intersection based algorithm to further reduce the number of DoF for serially coupled models (no feedback) to be reckoned with in subsequent

analysis (Figure 3) [50]. The intersection based algorithm depends on the down selection of the DoF that satisfy a set of constraints. These constraints are problem dependent. For example in the case of uncertainty quantification application, the two constraints are those DoF with high uncertainty components and high sensitivity components simultaneously. Hence, extracting the DoF that satisfy these two constraints will result in a smaller set of DoF yet without noticeable affecting the accuracy of the method. However, the proposed algorithm does not take into account coupled models with feedback effects (closed-loop coupling); moreover, the algorithm requires the availability of the sensitivity information which is either not available or computationally expensive to obtain. Therefore, chapter 3 introduces an improvement of the intersection-based algorithm by extending it to closed-loop coupled models via an iterative algorithm that takes into account the feedback effect. Moreover, a gradient-free algorithm is proposed in chapter 3 which enables the utilization of the intersection-based algorithm with models where the sensitivity information are not available.

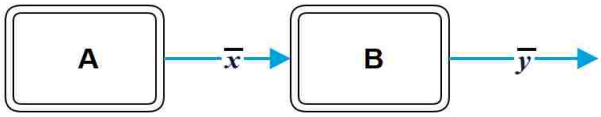

Figure 3. Two serially coupled models.

The low dimensional subspace approximation (active subspace) is used to simplify complex and computationally expensive analysis such as uncertainty quantification. In order to exemplify the process of subspace-based uncertainty quantification introduced in Ref. [4], consider the following model:

$$\bar{y} = f(\bar{x}).$$

If we assume that the sensitivity equations associated with the model is linear, the uncertainty in the input parameter vector ($\bar{x}$) can be propagated towards the RoI vector ($\bar{y}$) using the sandwich equation as follow:

$$\mathbf{C}_y = \mathbf{S}_{y/x}\mathbf{C}_x\mathbf{S}_{y/x}^T \tag{2}$$

where $\mathbf{C}_x$ is the covariance matrix of the input parameter ($\bar{x}$) and $\mathbf{S}_{y/x}$ represents the sensitivity profile of the RoI ($\bar{y}$) with respect to the input parameter ($\bar{x}$). However, taking into account that the covariance matrix $\mathbf{C}_x$ is symmetric then its singular value decomposition can be written as follow:

$$\mathbf{C}_x = \mathbf{U}_{\mathbf{C}_x}\boldsymbol{\Sigma}^2_{\mathbf{C}_x}\mathbf{U}^T_{\mathbf{C}_x}$$

where $\mathbf{U}_{\mathbf{C}_x}$ is the matrix of orthonormal basis of the space spanned by the columns of matrix $\mathbf{C}_x$ and $\boldsymbol{\Sigma}^2_{\mathbf{C}_x}$ is a diagonal matrix of the corresponding singular values. Hence, Eq.(42) can be rewritten as follow:

$$\begin{aligned}\mathbf{C}_y &= \mathbf{S}_{yx}\mathbf{U}_{\mathbf{C}_x}\boldsymbol{\Sigma}^2_{\mathbf{C}_x}\mathbf{U}^T_{\mathbf{C}_x}\mathbf{S}^T_{yx}\\ &= \mathbf{S}_{yx}\underbrace{\mathbf{U}_{\mathbf{C}_x}\boldsymbol{\Sigma}_{\mathbf{C}_x}}_{\mathbf{C}_x^{1/2}}\underbrace{\boldsymbol{\Sigma}_{\mathbf{C}_x}\mathbf{U}^T_{\mathbf{C}_x}}_{\mathbf{C}_x^{1/2,T}}\mathbf{S}^T_{yx}\\ &= \mathbf{S}_{yx}\mathbf{C}_x^{1/2}\mathbf{C}_x^{1/2,T}\mathbf{S}^T_{yx}\end{aligned}$$

Now if we assume that we have the basis of a lower dimensional subspace (**U**) that approximate the uncertainty space (i.e. the *x*-space) then Eq. (42) can be rewritten as follow:

$$\mathbf{C}_y = \mathbf{S}_{yx}\mathbf{C}_x^{1/2}\left(\mathbf{U}^{\|}\mathbf{U}^{\|,T} + \mathbf{U}^{\perp}\mathbf{U}^{\perp,T}\right)\mathbf{C}_x^{1/2,T}\mathbf{S}^T_{yx} \tag{3}$$

where $\left(\mathbf{U}^{\|}\mathbf{U}^{\|,T} + \mathbf{U}^{\perp}\mathbf{U}^{\perp,T}\right) = \mathbf{I}$ with $\mathbf{U}^{\|} \in \mathbb{R}^{n\times r}$ and $r \ll n$ if the components of *x* are highly correlated (e.g. the case with nuclear data cross-sections), where *m* is the full dimension of the

input parameter space (uncertainty source space) . The basis vectors represent the degrees of freedom (DoF) in the *x*-space that are characterized with high uncertainty and high sensitivity. From Eq. (3) the uncertainty in the attribute of interest can be segmented into two parts; the first part is coming from the active subspace and the minor (negligible) part is coming from the in-active (orthogonal subspace). If the active subspace is chosen correctly then the part coming from the orthogonal component will be negligibly small:

$$\mathbf{C}_y = \mathbf{S}_{yx}\mathbf{C}_x^{1/2}\mathbf{U}^{\|}\mathbf{U}^{\|,T}\mathbf{C}_x^{1/2,T}\mathbf{S}_{yx}^T + \mathbf{S}_{yx}\mathbf{C}_x^{1/2}\mathbf{U}^{\perp}\mathbf{U}^{\perp T}\mathbf{C}_x^{1/2,T}\mathbf{S}_{yx}^T$$

$$= \left(\mathbf{S}_{yx}\mathbf{C}_x^{1/2}\mathbf{U}^{\|}\right)\left(\mathbf{S}_{yx}\mathbf{C}_x^{1/2}\mathbf{U}^{\|}\right)^T + \left(\mathbf{S}_{yx}\mathbf{C}_x^{1/2}\mathbf{U}^{\perp}\right)\left(\mathbf{S}_{yx}\mathbf{C}_x^{1/2}\mathbf{U}^{\perp}\right)^T$$

From now on $\mathbf{U}$ will be used to denote $\mathbf{U}^{\|}$. If the lower dimensional subspace approximation is selected properly, then the uncertainty component associated with the orthogonal component will be negligibly small, and hence the uncertainty in the RoI (i.e. *y*) can be approximated as follow:

$$\mathbf{C}_y \simeq \left(\mathbf{S}_{yx}\mathbf{C}_x^{1/2}\mathbf{U}\right)\left(\mathbf{S}_{yx}\mathbf{C}_x^{1/2}\mathbf{U}\right)^T \tag{4}$$

This conclusion leads to the realization that the uncertainty can be evaluated via *r* models' executions instead of *m* executions. Each model execution would quantify the uncertainty in the RoI due to a certain basis vector (degree of freedom in the uncertainty sources space). Notice that the term $\left(\mathbf{S}_{yx}\mathbf{C}_x^{1/2}\mathbf{U}\right)$ can be written as:

$$\mathbf{S}_{yx}\mathbf{C}_x^{1/2}\mathbf{U} = \left[\mathbf{S}_{yx}\mathbf{C}_x^{1/2}\bar{u}^1 \,|\cdots|\, \mathbf{S}_{yx}\mathbf{C}_x^{1/2}\bar{u}^r\right], \tag{5}$$

where $\bar{u}^i$ is the i^{th} column of the matrix $\mathbf{U}$. On the other hand, the linearity assumption implies the following:

$$\mathbf{S}_{yx}\mathbf{C}_x^{1/2}\bar{u}_i = \bar{y}\left(x_0 + \mathbf{C}_x^{1/2}\bar{u}_i\right) - \bar{y}\left(\bar{x}_0\right) = \Delta\bar{y}^i,$$

Hence, the reduced uncertainty propagation Eq.(4) can be rewritten as:

$$\mathbf{C}_y \simeq \left[\Delta\bar{y}^1 \cdots \Delta\bar{y}^r\right]\left[\Delta\bar{y}^1 \cdots \Delta\bar{y}^r\right]^T = \mathbf{R}_y\mathbf{R}_y^T \tag{6}$$

Hence, this process can be viewed as a sort of Karhunen-Loève techniques with the neglected component (DoF) being selected based in their contribution to the uncertainty and sensitivity. In addition to that, **in multi-physics** coupled models, the important DoF must satisfy one more condition; taking into account the nature of multi-physics coupled model any selected DoF must have a **significantly possibility to appear in the interface space between the coupled models**. This down selection will be explained in more details in the following sub-section.

The error in this evaluation can be estimated as follow:

$$\begin{aligned} E_{C_y} &= \left\| \mathbf{C}_y - \left(\mathbf{S}_{yx}\mathbf{C}_x^{1/2}\mathbf{U}\right)\left(\mathbf{S}_{yx}\mathbf{C}_x^{1/2}\mathbf{U}\right)^T \right\| \\ &= \left\| \left(\mathbf{S}_{yx}\mathbf{C}_x^{1/2}\mathbf{U}^{\perp}\right)\left(\mathbf{S}_{yx}\mathbf{C}_x^{1/2}\mathbf{U}^{\perp}\right)^T \right\| \\ &= \left\| \mathbf{S}_{yx}\mathbf{C}_x^{1/2}\mathbf{U}^{\perp}\mathbf{U}^{\perp T}\mathbf{C}_x^{1/2,T}\mathbf{S}_{yx}^T \right\| \\ &= \left\| \mathbf{S}_{yx}\mathbf{C}_x^{1/2}\left(\mathbf{I} - \mathbf{U}\mathbf{U}^T\right)\mathbf{C}_x^{1/2,T}\mathbf{S}_{yx}^T \right\| \end{aligned}$$

The Range Finding algorithm (RFA) can be used to estimate an error upper bound in the L2-norm of the above error term [4, 30, 34]. This process has two major advantages: **first**, it does not require the accessibility to sensitivity profiles; **second,** it requires only *r* model's execution instead of *n*, where $r \ll n$.

Generally, Ref. [4, 34, 51] can be consulted for a comprehensive representation of the techniques proposed by Abdel-Khalik and Bang in their effort to facilitate the

sensitivity/uncertainty quantification analysis for high dimensional reactor physics applications.

Moreover, sensitivity analysis can be simplified significantly given the fact the computational cost of the sensitivity analysis depends directly on the dimensionality of the input and response spaces [51-52]. As mentioned before the computational cost of the adjoint approach depends directly on the response space dimensionality while the forward sensitivity approach depends on the dimensionality of the input space. Therefore, efforts have focused on how to capture lower dimensional subspace approximations to represent the input and response space using the RFA. These methods first appeared under the name Efficient Subspace Methods (ESM) developed in [2, 51]. This work, explored the potentialities of applying the subspace methods for sensitivity analysis, uncertainty quantification and data assimilation in nuclear engineering application. It showed the potentiality of ESM facilitating the uncertainty/sensitivity/data assimilation applications in nuclear engineering.

In addition to that, Ref.[21] employed the subspace based Reduced Order Modeling methods for the facilitation of the data assimilation problem. In our context data assimilation concerns the adjustment of macro and micro-level model's parameters (such as nuclear data cross-sections and fuel thermal conductivity), factoring in their priori uncertainty limits, in order to enhance the agreement between model predictions and measurements for key reactor attributes. Denoting that the experimentally measured attributes $\bar{y}_{\exp}$ and the calculated response $\bar{y}_{cal}$, then the data assimilation problem aims to minimize the disagreement between the measures and calculated values:

$$\min_{\Delta\bar{x}} \left\| \bar{y}_{\exp} - \left(\bar{y}_{cal} + \mathbf{S}^T \Delta\bar{x} \right) \right\|^2_{\mathbf{C}_y^{\exp}} + \alpha_x \left\| \Delta\bar{x} \right\|^2_{\mathbf{C}_x}$$

where $\Delta\bar{x}$ is the parameter adjustment vector, α_x is a regularization parameter, and $\mathbf{S}$ is the sensitivity coefficient matrix. Ref. [21] combines the sensitivity information and the parameter covariance information in order to determine the DoF which have large sensitivity and uncertainty components. Afterwards the data assimilation problem can be solved efficiently along these DoF via the regularization of the problem.

In this dissertation, we will imply a gradient free approach to determine the important DoF where these DoF are used to replace the original models with surrogates that have negligible computational cost to run. In the next sections various techniques for surrogate construction will be overviewed.

1.5.3 Reduced Order Modeling Based Goal-Oriented Surrogate Construction

Often, the analysis of models requires frequent running of the models of interest. However, these models are complex and associated with high computational cost. Therefore, the substitution of the original models with surrogates is an important and common practice in the analysis of complex models. As mentioned earlier, high fidelity models can be replaced by simpler surrogates that have negligible computational cost to run. Ref. [53] categorized surrogates into three groups [53]:

1- Data-fit models,

2- Reduced order models,

3- Hierarchical models.

Data-fit models are generated by the regression of simulation data (training set). Examples of data-fit models are the Taylor expansion based models, where the training set data are used to determine the coefficients of the suitable Taylor series expansion of the model of interest

over the interval of interest. Another example is the Gaussian processes surrogates [54]. These surrogates require modeling choices that specify the mean and covariance of the surrogate Gaussian process.

Reduced-order models are based upon projecting the model's equations into a certain reduced dimension subspace (active subspace). The basis of the active subspace is empirically determined via a training set of model's forward and/or adjoint runs.

Hierarchical surrogates are designed to span a range of applications; these models are derived from the high fidelity models in conjunction with ignoring certain high fidelity aspects. For example the computational cost of a model can be reduced by considering coarse discretization grids or loose convergence criteria. Therefore, hierarchical surrogates can be useful whenever the loss of accuracy is negligible with respect to the application of interest. Combining the first and second types of surrogate models in a goal-oriented view helps in overcoming the difficulties associated with the model complexity and high computational cost due to high parameter dimensionality.

Goal-oriented surrogate construction is introduced in Ref. [55] where reduced dimensionality analysis is used to determine the DoF that preserve application-specific features instead of preserving all model's features (i.e. goal-oriented DoF selection). These DoF are then used to construct the so called goal-oriented surrogate of the original complex model. Goal-oriented surrogate models have been used in nuclear engineering applications for uncertainty quantification purposes as represented in Ref. [4], where goal-oriented surrogate models are used to replace the neutronics model for purposes of uncertainty quantification. Ref. [4] finds the uncertainty-sensitivity specific DoF and then uses them in constructing a second order surrogate in the form:

$$\Delta y = \bar{\beta}_1^T \Delta \bar{x} + \left(\bar{\beta}_2^T \Delta \bar{x} \right)^2$$

If the surrogate is intended for uncertainty quantification purposes, then the variations in parameter $\bar{x}$ can be viewed as a random perturbation sampled from the distribution assumed by the covariance matrix $\mathbf{C}_x$:

$$\Delta \bar{x} = \mathbf{C}_x^{1/2} \bar{\xi}$$

where $\bar{\xi}$ being a random vector sampled from a normal distribution to generate a random sample of the input parameter. However, defining the columns of matrix $\mathbf{U}$ as the basis of the input parameter active subspace (DoF with high uncertainty-sensitivity component), then the perturbation vector $\bar{\xi}$ can be projected onto the basis of the active subspace which reduces the effective dimensionality of the models' input parameter space:

$$\Delta \bar{x} = \mathbf{C}_x^{1/2} \mathbf{U} \mathbf{U}^T \bar{\xi}$$

Therefore, an efficient goal-oriented surrogate can be constructed as follow:

$$\Delta y = \bar{\beta}_1^T \mathbf{C}_x^{1/2} \mathbf{U} \mathbf{U}^T \bar{\xi} + \left(\bar{\beta}_2^T \mathbf{C}_x^{1/2} \mathbf{U} \mathbf{U}^T \bar{\xi} \right)^2 = \bar{\beta}_{1,r}^T \bar{\alpha} + \left(\bar{\beta}_{2,r}^T \bar{\alpha} \right)^2 \tag{7}$$

Given that $\mathbf{U} \in \mathbb{R}^{nxr}$ and $\bar{\alpha} = \mathbf{U}^T \bar{\xi} \in \mathbb{R}^r$ then $\bar{\beta}_{1,r}^T = \bar{\beta}_1^T \mathbf{C}_x^{1/2} \mathbf{U} \in \mathbb{R}^r$ and $\bar{\beta}_{2,r}^T = \bar{\beta}_2^T \mathbf{C}_x^{1/2} \mathbf{U} \in \mathbb{R}^r$. Hence in order to determine the unknown elements of $\bar{\beta}_{1,r}$ and $\bar{\beta}_{2,r}$ the model needs to be run $2r$ times so that the coefficients are determined (refer to Figure 4 and Figure 5).

A similar goal-oriented surrogate model construction will be introduced the chapters 5 and 6 and used for data assimilation and target accuracy assessment, respectively.

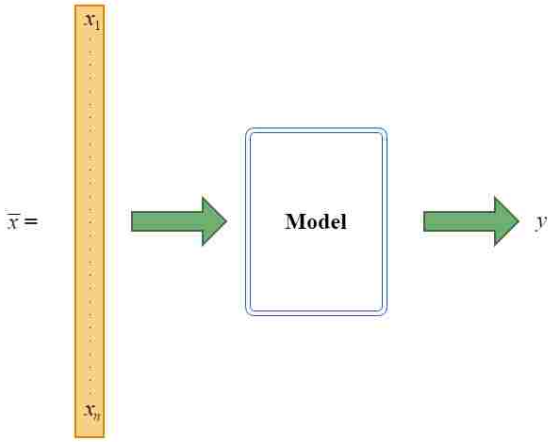

Figure 4. Original model: with high dimensional input space and high computational cost.

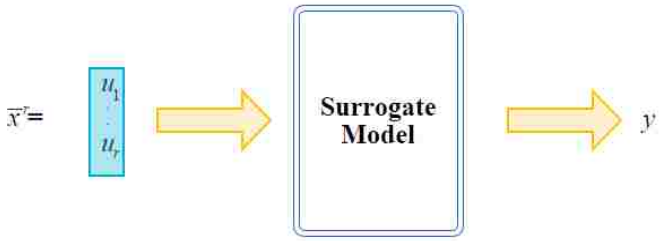

Figure 5. Goal oriented surrogate model: with few parameters and low computational cost.

1.6 SCALE

In this sub-section and the following one (1.7) the theory and implementation of reactor core simulation tools that will be used to validate the ideas proposed throughout this dissertation will be discussed. In this sub-section SCALE6.1 (*A Comprehensive Modeling and Simulation Suite for Nuclear Safety Analysis and Design*) [57] depletion sequence (TRITON) will be of concern while in the following sub-section VERA-CS (*Virtual Environment for Reactor Applications-Core Simulator*) [58, 59] will be discussed.

SCALE is a comprehensive modeling and simulation tool developed at Oak Ridge National Laboratory (ORNL) for nuclear design and safety analysis. SCALE provides a comprehensive, verified and validated, tool for criticality safety, reactor physics, radiation shielding, radioactive source term characterization, and sensitivity/uncertainty analysis which is constructed in a "plug-and-play" logic which allows the user to use a combination of the available 89 computational modules, including three deterministic and three Monte Carlo radiation transport solvers. SCALE depletion sequence (TRITON) is the specific sequence that will be used to test and validate the ideas introduced in this dissertation at the lattice physics level.

1.6.1 TRITON

TRITON sequence consists of several SCALE modules that supports transport, depletion, and sensitivity/uncertainty analysis [57]. TRITON calculates the problem-dependent cross-section with multi-group transport calculations for 1-, 2-, and 3- dimensional configurations. The 1-dimensional geometry transport calculations are performed using XSDRNPM while NEWT is used for 2-dimensional transport calculation (i.e. lattice physics). In addition, TRITON also includes Monte Carlo depletion modules, such as KENO V.a and KENO-VI. Coupled with the transport capabilities available through XSDRNPM, NEWT and KENO; along with ORIGEN depletion capabilities and SCALE multi-group cross-section processing calculations, collectively they provide a rigorous first-principles approach to predict the burnup of various isotopes in configurations that have a strong spatial dependence on the neutron flux. Moreover, source terms and decay heat, as well as few-group homogenized cross-sections used by nodal core calculations, can be determined.

Sensitivity analysis is available through the TSUNAMI-2D sequence in TRITON, which provides problem-dependent 2-dimensional forward and adjoint transport solutions via NEWT. The adjoint transport solution is then used to calculate the sensitivity coefficients, and the calculation of the uncertainty in *keff* and other relative responses due to cross-section provided covariance data. The module that is used to calculate the sensitivity of the response of interest with respect to the nuclear data is SAMS, which is capable of determining the sensitivity coefficients as a function of nuclide, reaction type, material region, and energy group. Once the sensitivity data are obtained the uncertainty can be estimated via the sandwich equation (refer to Eq.(2)). The implicit effects of the cross-section are treated at the sensitivity coefficient level rather than at the covariance matrix level, were the sensitivity coefficients have the following components:

$$\left(S_{R,\Sigma^i_{x,g}}\right)_{\text{complete}} = \left(S_{R,\Sigma^i_{x,g}}\right)_{\text{explicit}} + \left(S_{R,\Sigma^i_{x,g}}\right)_{\text{implicit}}$$

where R is the response of interest, g is the energy group, i is a nuclide of interest and x is the reaction type of interest. In a more detailed view of the equation above, the implicit term accounts for the indirect effect of perturbing a certain cross-section on the response:

$$\left(S_{R,\Sigma^i_{x,g}}\right)_{\text{complete}} = \left(\frac{\Sigma^i_{x,g}}{R}\frac{\partial R}{\partial \Sigma^i_{x,g}}\right) + \left(\sum_j \sum_h \frac{\Sigma^j_{y,h}}{R}\frac{\partial R}{\partial \Sigma^j_{y,h}} \times \frac{\Sigma^i_{x,g}}{\Sigma^j_{y,h}}\frac{\partial \Sigma^j_{y,h}}{\partial \Sigma^i_{x,g}}\right)$$

In this dissertation, the lattice physics based depletion sequence (*T-DEPL*) will be used to deplete the reactor core (or assembly) models. While TSUNAMI-2D will be used to generate the sensitivity information required throughout this work. *T-DEPL* is the 2-dimensional TRITON sequence which uses NEWT for the transport calculations, and also provides the capability to generate lattice-physics data for nodal core calculations. The *T-DEPL* sequence

consists of three main modules: NEWT, COUPLE and ORIGEN. NEWT generates the transport flux distribution which is then used to compute the region-averaged, multi-group cross-sections along with the multi-group flux for each of the depleted materials. COUPLE generates the 1-group cross-section for each of the depletion materials. Finally, ORIGEN depletes each of the isotopes based on the normalized material flux (or power) using the 1-group cross-sections computed by COUPLE. In the following subsections, more details are given about the main modules in *T-DEPL* sequence [57].

T-DEPL uses a predictor-corrector approach where the cross-section processing and transport calculations use isotopic concentrations at the midpoint of depletion sub-intervals (assuming the reaction rates are constant and equal to their values at the beginning of the subinterval). After that cross-sections and neutron flux distributions are calculated at this midpoint and used to deplete the fuel over the full subinterval. Depletion calculations are then extended to the midpoint of the next sub-interval, followed by cross-section processing and transport calculations at the new midpoint. This process goes on for all depletion sub-intervals. The following two sub-sections (1.6.2, 1.6.3) will highlight the two major components of the depletion sequence (*T-DEPL*).

1.6.2 NEWT

NEWT solves the time-independent form of the linear Boltzmann equation (transport equation):

$$\hat{\Omega} \bullet \vec{\nabla} \psi \left(\bar{r}, \hat{\Omega}, E \right) + \Sigma_t \left(\bar{r}, E \right) \psi \left(\bar{r}, \hat{\Omega}, E \right) = Q \left(\bar{r}, \hat{\Omega}, E \right) \tag{8}$$

where $\psi \left(\bar{r}, \hat{\Omega}, E \right)$ is the neutron angular flux at position $\bar{r}$ per unit volume, in direction $\hat{\Omega}$ per unit solid angle and at energy E per unit energy.

$\Sigma_t(\bar{r},E)$ is the macroscopic total cross-section at position $\bar{r}$ and energy E.

$Q(\bar{r},\hat{\Omega},E)$ is the neutron source term at position $\bar{r}$ per unit volume, in direction $\hat{\Omega}$ per unit solid angle and at energy E per unit energy. This source includes the fission source, scattering source and any external neutron source.

NEWT solves Eq.(8) via the multi-group discrete-ordinates method using the Method Of Characteristics (MOC) in which the transport equation is solved analytically along characteristic directions within a computational cell [57]. The MOC represents the spatial variables along the characteristic directions (rays); these rays substitute the conventional finite difference representation with these characteristic variations that incorporate both the position information ($\bar{r}$) and the directional information ($\hat{\Omega}$). These characteristics are represented by the s-axis as follow:

$$\hat{\Omega}\bullet\vec{\nabla}\psi(\bar{r},\hat{\Omega},E)=\frac{d\psi(s,E)}{ds}.$$

Therefore, Eq. (8) can be re-written in terms of the s-axis as follow:

$$\frac{d\psi(s,E)}{ds}+\Sigma_t(s,E)\psi(s,E)=Q(s,E) \tag{9}$$

Eq. (9) has the following solution [61]:

$$\psi(s,E)=\psi_0(E)e^{-\Sigma_t(E).s}+e^{-\Sigma_t(E).s}\int_0^s Q(s',E)e^{\Sigma_t(s',E).s'}ds'$$

In this case *s* represent the distance along a specific characteristics direction ($\hat{\Omega}$) and $\psi_0(E)$ is an energy dependent known angular flux at *s*=0 which can be obtained from the boundary conditions. For more information on the MOC Ref. [61 - 62] can be consulted.

NEWT uses this angular flux distribution via numerical integration to obtain the neutron scalar flux distribution:

$$\phi(\bar{r},E)=\int_{4\pi}\psi\left(\bar{r},\hat{\Omega},E\right)d\hat{\Omega}$$

1.6.3 ORIGEN

The ORIGEN-ARP sequence completes the point-depletion calculations using problem-dependent cross sections. The problem-dependent cross-section libraries are generated using the ARP (**A**utomatic **R**apid **P**rocessing) module employing an interpolation algorithm that operates on pre-generated libraries created for a range of fuel properties and operating conditions [63].

In determining the time dependence of nuclide concentrations in the nuclear reactor core, ORIGEN solves the ordinary differential equation representing the rates of appearance and disappearance of each isotope. Generally, isotopes in the reactor core appears due to various mechanisms: radioactive decay of other isotopes, fission of heavy elements into lighter elements, and neutron capture. The disappearance mechanisms are: radioactive decay of the isotope itself, fission and the capture of neutrons transforming the isotope into another. The time rate of change of the concentration for a particular nuclide (N_i) is determined solving the following coupled ordinary differential equations::

$$\frac{dN_i}{dt}=\sum_{j=1}^{m}l_{ij}\lambda_j N_j+\bar{\phi}\sum_{k=1}^{m}f_{ik}\sigma_k N_k-\left(\lambda_i+\bar{\phi}\sigma_i\right)N_i \quad \text{for } i=1,2,\cdots \tag{10}$$

where

N_i: Atom density of the i^{th} isotope.

$\bar{\phi}$: Space-energy-averaged neutron flux.

λ_i : Decay constant of the i^{th} isotope.

l_{ij} : Branching ratio from the j^{th} isotope.

f_{ik} : Branching ratio for neutron absorption by the k^{th} isotope which lead to the formation the i^{th} isotope.

σ_i : Flux-averaged neutron absorption cross-section the i^{th} isotope.

1.7 VERA-CS

VERA-CS (*Virtual Environment for Reactor Applications-Core Simulator*) is a steady state Light Water Reactors (LWRs) core simulator applicable for predicting over a range of operating conditions including various fuel cycles, plant startup, power maneuvering, and core reload/fuel discharge. VERA-CS can be, relatively, considered a high-fidelity core simulator which provides the capability to perform 3-dimensional geometry simulations along with considering coupling effects (e.g. thermal-hydraulics feedback) [64]. VERA-CS has various computational models that might be combined to perform the analysis of interest. In this dissertation, a specific VERA-CS depletion sequence will be used. Figure 6 shows the models involved in this depletion sequence, where MPACT is a transport solver that determines the neutron flux distribution and the pin power distribution necessary for COBRA-TF, which is a thermal-hydraulics solver which determines the fuel and coolant temperature distributions along with thee coolant density distribution which are given as feedback to the transport solver. Neutronics and thermal-hydraulics models are iterated using operator splitting approach until a certain stopping criteria are satisfied. After that ORIGEN (refer to section 1.6.3) performs

the fuel depletion calculations, hence updating the material composition of the fuel to be used in the next time step. Interface parameters transfer is handled by the Data Transfer Kit (DTK). More details about each of these components is given in the coming sub-sections (1.7.1, 1.7.2) while more details about the interface parameters will be provided in the coming chapters.

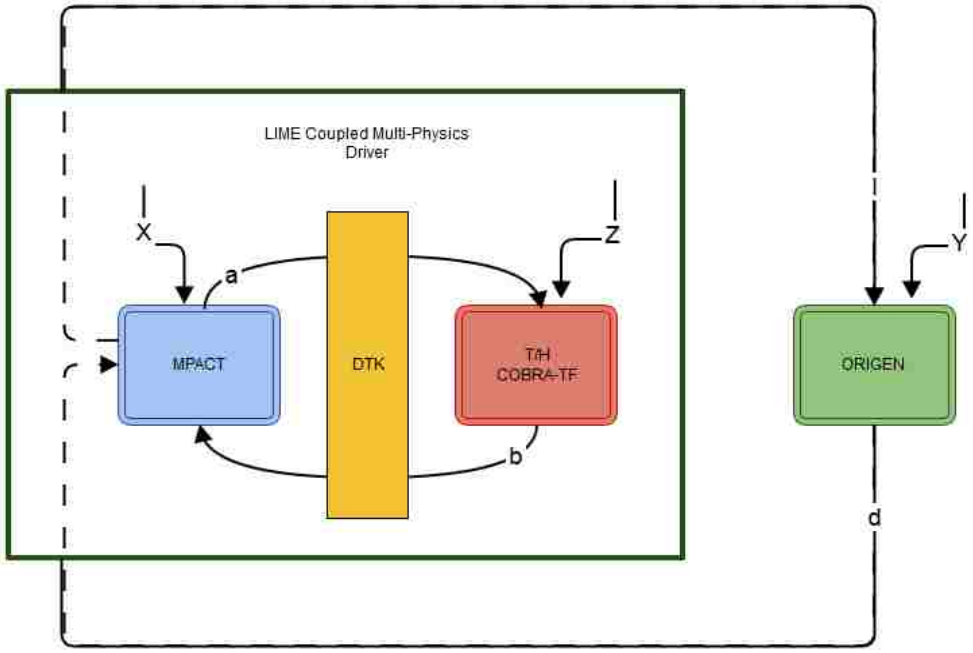

Figure 6. Depletion with thermal-hydraulics feedback using VERA-CS (Predictor-corrector method).

1.7.1 MPACT

MPACT is a core-wide transport solver (**M**ichigan **P**arallel **A**nalysis based on **C**haracteristic **T**racing). MPACT solves an integral form of the linear Boltzmann equation across for heterogeneous material region, which enables the simulator to generate sub-pin level power distributions that are necessary for detailed thermal-hydraulic updates. The Boltzmann equation is solved via the method of characteristics (MOC) [64-65] with discrete ray tracing within each fuel pin. MPACT can provide two solution types:

1- A 3-D MOC solution: where the 3 dimensional Boltzmann equation is solved. However, for high fidelity core wide calculations this solution is computationally expensive and might require the allocation of huge memory and computer capabilities. Hence the second solution type is provided.

2- A “2D-1D" solution: in which MOC solutions are performed by dividing the problem into radial planes (2D solution) and the axial solution is performed using a lower-order one-dimensional (1D) diffusion or SP3 approximation (1D solution).

For simplicity, the 3-dimensional mono-energetic Boltzmann equation with isotropic scattering in a homogeneous medium is going to be used to highlight the difference between the 3D and 2D-1D methods in MPACT:

$$\bar{\Omega} \bullet \vec{\nabla}\varphi\left(\bar{r},\bar{\Omega}\right)+\Sigma_t\varphi\left(\bar{r},\bar{\Omega}\right)=\frac{\Sigma_s}{4\pi}\int_{4\pi}\varphi\left(\bar{r},\bar{\Omega}'\right)d\Omega'+\lambda\frac{\nu\Sigma_f}{4\pi}\int_{4\pi}\varphi\left(\bar{r},\bar{\Omega}'\right)d\Omega', \qquad (11)$$

In Eq.(11) :

$\bar{r}=\left(x,y,z\right)$ is the position vector which indicates the radial, axial spatial index:

$$\bar{r}=\begin{cases}\left(x,y\right)\in R\\ 0\le z\le Z\end{cases}$$

while $\bar{\Omega}=\left(\Omega_x,\Omega_y,\Omega_z\right)$ is the direction -of-flight variable. Figure 7 shows an example of a cylindrical homogenous system volume. The geometry consists of a radial slice (***R***) and an axial elevation (***z***). Figure 8 resembles a control volume in the rectangular geometry.

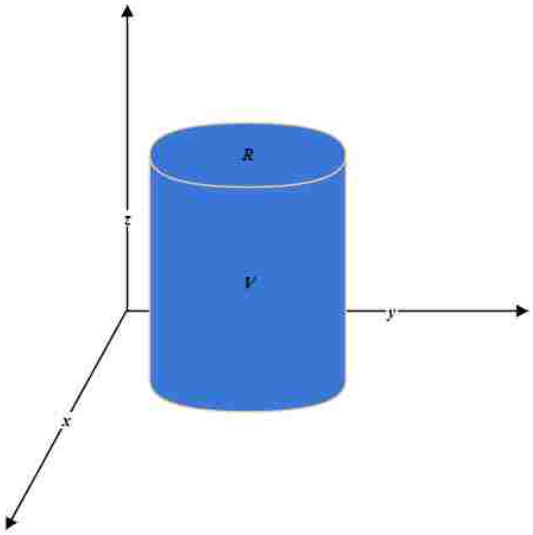

Figure 7. 3-dimensional cylindrical geometry (system volume V).

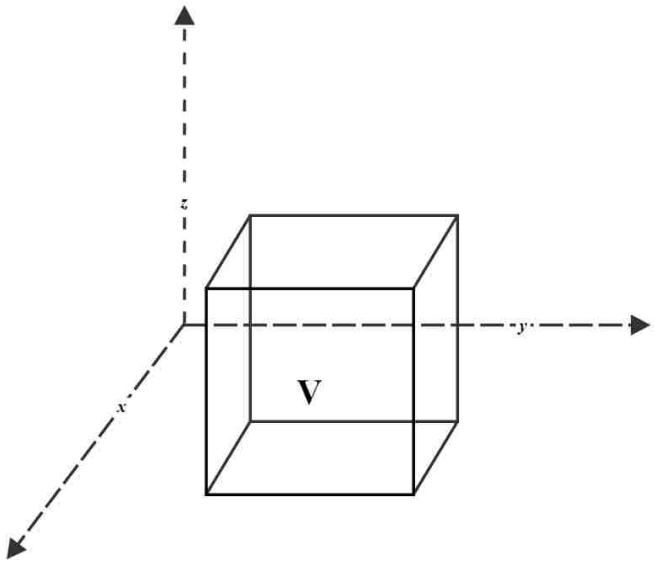

Figure 8. 3-dimensional rectangular geometry (system volume V).

The 2D-1D method does not solve Eq.(11); instead, it solves a combination of 2D version along with 1D version which makes the process more computationally efficient. The 2D version resembles the radial slice solution assuming an isotropic axial leakage term:

$$\Omega_x \frac{\partial \varphi}{\partial x}\left(\bar{r},\bar{\Omega}\right)+\Omega_y \frac{\partial \varphi}{\partial y}\left(\bar{r},\bar{\Omega}\right)+\Sigma_t \varphi\left(\bar{r},\bar{\Omega}\right)=\frac{\Sigma_s}{4\pi}\int_{4\pi}\varphi\left(\bar{r},\bar{\Omega}'\right)d\Omega'+\lambda\frac{\nu\Sigma_f}{4\pi}\int_{4\pi}\varphi\left(\bar{r},\bar{\Omega}'\right)d\Omega'-\frac{1}{4\pi}\frac{\partial J_z}{\partial z},$$

The axial current term can be approximated as follows, with appropriate boundary conditions:

$$J_z\left(x\right)\approx\int_{4\pi}\Omega_z\varphi\left(\bar{r},\bar{\Omega}\right)d\bar{\Omega}$$

On the other hand, the 1D axial transport version which resembles the axial distribution can be formulated as follows:

$$\Omega_z \frac{\partial \varphi}{\partial z}\left(\bar{r},\bar{\Omega}\right)+\Sigma_t \varphi\left(\bar{r},\bar{\Omega}\right)=\frac{\Sigma_s}{4\pi}\int_{4\pi}\varphi\left(\bar{r},\bar{\Omega}'\right)d\Omega'+\lambda\frac{\nu\Sigma_f}{4\pi}\int_{4\pi}\varphi\left(\bar{r},\bar{\Omega}'\right)d\Omega'-\frac{1}{4\pi}\left(\frac{\partial J_x}{\partial x}+\frac{\partial J_y}{\partial y}\right), \quad (12)$$

In MPACT, the axial transport equation (Eq.(12)) is not solved directly; instead the SP1, SP3 approximations is solved. The SP1 approximation to Eq.(12) is given by the 1D axial diffusion equation. Solving the SP1 and SP3 approximation is much simpler than solving Eq.(12). The above analysis highlights the difference between the 3D and 2D-1D approximate methods. For more details about the solution methodology and various options available in MPACT, the reader is referred to Ref. [65].

1.7.2 COBRA-TF

COBRA-TF (**CO**olant-**B**oiling in **R**od **A**rrays-**T**wo **F**luids) is a thermal-hydraulics simulator that was originally developed by the Pacific Northwest Laboratory (PNL) and is currently a part of VERA-CS. COBRA-TF is designed to perform a two fluid, three-fields approach (i.e. continuous vapor, continuous fluid and fluid droplets dispersed in vapor) for

Light Water Reactors (LWRs). This sub-section briefly summarizes the two-fluid model used in COBRA-TF [67].

COBRA-TF, models each of these fields using separate equilibrium equations; however, liquid and droplet fields are assumed to be in equilibrium with each other, hence, they share the same energy equations. In general these equations are formulated via Cartesian coordinates or a sub-channel method. The conservative equations are solved simultaneously using the Semi-Implicit Method for Pressure-Linked Equations (SIMPLE) [69].

Eq.(13) presents the phasic mass conservation equation. The equation is written for the k^{th} field, where the left hand side represents the time rate of change of the mass and the advection of the field mass into or out of the differential volume. The first term of the right hand side (i.e. L_k) is the mass transfer out /into of phase *k*. Finally, M_e^T represents the mass transfer in the mesh cell due to turbulent mixing and void drift. Note that COBRA-TF uses a simple turbulent diffusion-based model to calculate the axial turbulent transfer across the sub-channel gaps (when using the sub-channel method). $\bar{V}_k$ is the velocity field and ρ_k is the density, while α_k is the void fraction for the k^{th} phase. For more information about the diffusion approximation and void drift models, the reader is referred to Ref.[67].

$$\frac{\partial}{\partial t}\left(\alpha_k \rho_k\right) + \nabla.\left(\alpha_k \rho_k \bar{V}_k\right) = L_k + M_e^T \tag{13}$$

The inter-phase mass transfer term accounts for evaporation /condensation and entrainment/de-entrainment. Hence the *L* term can be expanded into three components:

$$L_v = \Gamma'''$$
$$L_l = -\left(1-\eta\right)\Gamma''' - S'''$$
$$L_e = -\eta\Gamma''' + S'''$$

The vapor field is denoted by *v* while the liquid film and entrained droplet fields are denoted by *l* and *e*, respectively. In the above three equations, Γ''' is the volumetric mass transfer due to phase change, and S''' denotes the continuous liquid to entrained droplet volumetric mass transfer. The η term is the fraction of phase change (entrained droplets → vapor). Note that this term will be defined based on the explicit process of interest:

$$\eta_{evap} = \min \begin{cases} 1 - \dfrac{Q'''_{wl}}{\Gamma''' H_{fg}} \\ \dfrac{\alpha_e}{1-\alpha_v} \end{cases}$$

$$\eta_{cond} = \frac{\alpha_e}{1-\alpha_v}$$

η_{evap} is the evaporation term and η_{cond} is the condensation term. Q'''_{wl} is the volumetric heat transfer from the wall to the liquid phase and H_{fg} is the heat of vaporization.

On the other hand, Eq.(14) represents the phasic momentum conservation equation. The left hand side denotes the time rate of change of the momentum and the advection term (note that Eq.(14) resembles the Cartesian coordinate's case). u_k, v_k, w_k are the Cartesian directional components of the velocity field (note that in Cartesian coordinates the momentum conservation equation will consist of three separate equations for the momentum transfer in each direction). The pressure force ($\alpha_k \bar{\nabla} P$), turbulent and viscous shear stress ($\bar{\nabla}.\left(\alpha_k \left(\tau_k^{ij} + T_k^{ij}\right)\right)$), gravitational force ($\alpha_k \rho_k \bar{g}$), and momentum loss/gain due to phase change, drag force and momentum transfer ($\bar{M}_k^L + \bar{M}_k^d + \bar{M}_k^T$) are represented by the right hand side.

$$\frac{\partial}{\partial t}\left(\alpha_k \rho_k \bar{V}_k\right)+\frac{\partial}{\partial x}\left(\alpha_k \rho_k u_k \bar{V}_k\right)+\frac{\partial}{\partial y}\left(\alpha_k \rho_k v_k \bar{V}_k\right)+\frac{\partial}{\partial z}\left(\alpha_k \rho_k w_k \bar{V}_k\right)$$
$$=\alpha_k \rho_k \bar{g}-\alpha_k \nabla P+\nabla.\left(\alpha_k\left(\tau_k^{ij}+T_k^{ij}\right)\right)+\bar{M}_k^L+\bar{M}_k^d+\bar{M}_k^T \tag{14}$$

The viscous shear stress term can be expanded into fluid-fluid shear and wall-fluid shear:

$$\vec{\nabla}\left(\alpha_e \tau_e^{ij}\right)=\bar{\tau}_{we}'''$$
$$\vec{\nabla}\left(\alpha_v \tau_v^{ij}\right)=\bar{\tau}_{wv}'''+\vec{\nabla}\left(\alpha_v \sigma_v^{ij}\right)$$
$$\vec{\nabla}\left(\alpha_l \tau_l^{ij}\right)=\bar{\tau}_{wl}'''+\vec{\nabla}\left(\alpha_l \sigma_l^{ij}\right)$$

$\bar{\tau}_{we}''', \bar{\tau}_{wv}''', \bar{\tau}_{wl}'''$ are the volumetric wall drag of the entrained, vapor and liquid phases (note that COBRA-TF does not model the liquid-liquid viscous shear stresses). The $\bar{M}_k^L$ term is the momentum gain/loss term due to phase change, with this term can be expanded in terms of the three possible phase changes as follow:

$$\bar{M}_v^L=\Gamma'''\bar{V}$$
$$\bar{M}_l^L=-\Gamma'''(1-\eta)\bar{V}-S'''\bar{V}$$
$$M_e^L=-\Gamma'''\eta\bar{V}+S'''\bar{V}$$

Moreover, $\bar{M}_k^d$ is the interfacial drag term which can be, also, expanded into three terms, and $\bar{M}_k^T$ is the axial momentum resulting from the turbulent mixing.

Finally, the energy conservation equation is represented by Eq.(15), in which the left hand side denotes the energy time rate of change and change in energy due to the advection into and out of the differential volume. The right hand side represents the phase conduction and turbulent heat flux ($-\nabla.\left[\alpha\left(\bar{Q}_k+q_k^T\right)\right]$), energy transfer due to phase change ($\Gamma_k h_k^i$), volumetric heat transfer through the wall (q_{wk}''') and finally, the pressure work term ($\alpha_k \frac{\partial P}{\partial t}$).

$$\frac{\partial}{\partial t}\left(\alpha_k \rho_k h_k\right)+\nabla.\left(\alpha_k \rho_k h_k \bar{V}_k\right)=-\nabla.\left[\alpha\left(\bar{Q}_k+q_k^T\right)\right]+\Gamma_k h_k^i+q_{wk}'''+\alpha_k \frac{\partial P}{\partial t} \tag{15}$$

COBRA-TF solves the conservation equations (Eqs.(13), (14), (15)) after applying various assumptions such as:

1- No modeling for the heat conduction in the fluids ($\bar{Q}_k = 0$).

2- Energy exchange happens only in the lateral and orthogonal directions.

3- Liquid-liquid viscous shear stresses are not modeled.

4- A simple turbulent diffusion model is used to estimate the turbulent transfer of axial momentum across sub-channel gaps.

For more information about the assumptions in COBRA-TF and the numerical methods used to obtain the solution, the reader is referred to Ref. [67].

CHAPTER 2. EFFICIENT SUBSPACE APPROXIMATION FOR SINGLE PHYSICS MODELS

Note: *The work presented in this section was developed in collaboration with C. Wang, Y. Bang and H. S. Abdel-Khalik.*

Given the complexity of modern predictive modeling and simulation tools, new developments in reduced order modeling are continuously being pursued by computational scientists as an effective means to render practical the repeated evaluations of the associated physics models. Reduced Order Modeling (ROM) achieves that by reducing the effective dimensionality of the variables associated with the various physics models, including physics input parameters, state functions, and responses of interest. The reduced dimensions are determined such that the resulting reduction errors (difference between the respective variable's variation in the original space and those reconstructed from the reduced dimensions) meet pre-defined error tolerance limits with an overwhelmingly high probability [29, 30]. Mathematically, the reduced dimensions are described by an active subspace, whose dimension is considerably smaller than the dimension of the original full space. To construct the active subspace, most ROM algorithms require the repeated execution of the forward model, a process that could be computationally taxing especially for complex systems, such as nuclear reactor calculations. This chapter introduces a new approach to reduce the computational cost required to construct the active subspace.

This work proposes a modification to the algorithm developed previously in [34]; that is instead of collecting the snapshots based on the converged solution, the non-converged iterates of the solution (non-converged snapshots), obtained by randomly perturbing the input parameters after each iteration, are collected and used to construct a lower dimensional

subspace. We propose to use this subspace in lieu of the one constructed with the converged snapshots as done in earlier work. Note that in the proposed algorithm, the snapshots will not represent the converged solution for the given parameter perturbations. However, the premise is that the variability of the non-converged snapshots can be used to capture the subspace constructed from the converged solutions. As will be shown later, it is possible to prove that the proposed algorithm yields a subspace that is inclusive of the subspace generated using the converged snapshots.

The basis constructed from the non-converged iterates is validated by comparing its performance with that constructed using the converged snapshots. The application used here is based on a recently developed version of generalized perturbation theory, called exact-to-precision generalized perturbation theory (EPGPT) [56]. The EPGPT utilizes the constructed reduced basis to efficiently compute the high order variations of given responses with respect to the input parameters perturbations, such as cross-sections perturbations, temperature variations and control rod insertions. In this chapter, the reduced basis obtained by the converged and the non-converged snapshots are combined separately with EPGPT to calculate the variations of the multiplication factor and neutron flux distribution for a range of nuclear cross-section variations. The following sections discuss the main idea, details of implementation, applications, and numerical tests conducted with SCALE6.1 package [57].

This algorithm emulates the so-called Range Finding Algorithms (RFAs) from linear algebra. An RFA attempts to answer the following question: Given a large number of vectors stacked as columns in a matrix **A**, can one find a matrix **U** with a smaller number of columns whose range contains all the original vectors in **A** to a user-defined tolerance? An RFA generates a number of snapshots, each representing a random linear combination of the

columns of the matrix **A**, and subsequently employs a rank revealing decomposition to determine the matrix **U** and its rank *r*, i.e., the minimum number of columns to whose range all the original vectors belong within a user-defined error tolerance. The number of snapshots needed is equal to the rank *r*, or slightly larger, depending on the type of RFA algorithm employed [41]. More importantly, the algorithm does not specify how the snapshots should be generated; it only requires that they are generated in a manner that ensures with high probability their linear independence. This means that if one has another matrix **B** whose range is believed (say based on physics argument) to be equal to the range of **A**, one can use random linear combinations of the columns of **B** to determine the range of **A**. We take this observation a step further by noting that if **B** is selected such that the range of **B** is inclusive of the range of **A**, the identified active subspace for **B** will be inclusive of **A**'s active subspace. This observation can be assessed by calculating the angle between the two subspaces (described later). This represents the core idea of the proposed algorithm. In our context, the matrix **A** (to be denoted later as $\mathbf{\Phi}_C$) aggregates snapshots of the converged flux solution, whose computational cost of generating depends not only on the rank of the active subspace but also on the model complexity which translates into the cost required to obtain a converged solution for each snapshot.

2.1 Algorithm

Consider the following iterative representation of an eigenvalue problem:

$$\mathbf{L}\bar{\phi}^{(j)} = \frac{1}{k^{(j-1)}}\mathbf{F}\bar{\phi}^{(j-1)} \tag{16}$$

where $\mathbf{L}$ and $\mathbf{F}$ are the neutron loss and production operators, respectively. This equation is often solved using power iterations with some form of acceleration; where the index j denotes the iteration index. A lower dimensional subspace in the state space, i.e., the flux ($\bar{\phi}$), can be constructed using the range finding algorithm (RFA) [34] by solving Eq. (16) a number of times, wherein model input parameters are randomly perturbed in each run and the flux variation from the reference-unperturbed case is recorded. The process is repeated until the accumulated snapshots span a subspace that represents the flux variations within certain user-defined error tolerance [41, 34] (i.e. an active subspace). The dimension of this active subspace is found to be considerably smaller than the dimension of the original space. Symbolically, this can be described as follows: let the *n* components of the state, e.g., multi-group flux, be represented with a vector $\bar{\phi} \in \mathbb{R}^n$. The reduced variables $\bar{\phi}_r$ are represented by a vector given by:

$$\bar{\phi}_r = \mathbf{U}^T\bar{\phi}$$

where the *r* columns of the orthonormal matrix $\mathbf{U} \in \mathbb{R}^{n\times r}$ represent a basis for the active subspace. The premise here is that all dominant flux variations can be represented as linear combinations of the basis vectors of the active subspace, i.e., the columns of $\mathbf{U}$. The reduced variables can be subsequently used to reconstruct the flux in its original full dimensional space as follows:

$$\tilde{\bar{\phi}} = \mathbf{U}\mathbf{U}^T\bar{\phi} = \mathbf{U}\bar{\phi}_r ,$$

where $\left\|\bar{\phi} - \tilde{\bar{\phi}}\right\|_2$ is denoted as the reduction error measured using an L_2 norm. To be effective, one needs to find an *r* value that renders this error considerably small. Earlier work has proven that *r* may be selected to meet a user-defined upper bound ε_{upper} [30]. The basis of the active subspace for the state variable $\bar{\phi}$ in Eq. (16) may be constructed using the following algorithm:

1. Generate *m* random perturbed realizations of the input parameters represented by the matrices $\{\mathbf{L}_i\}_{i=1}^m$ and $\{\mathbf{F}_i\}_{i=1}^m$, where:

$$\mathbf{F}_i = \mathbf{F} + \delta\mathbf{F}_i \text{ and } \mathbf{L}_i = \mathbf{L} + \delta\mathbf{L}_i$$

2. For every parameter perturbation, solve Eq.(16), record the converged solution $\bar{\phi}_i \in \mathbb{R}^n$, and aggregate in a matrix $\mathbf{\Phi}_\mathrm{C}$.

3. Calculate the singular value decomposition (SVD) of the *m* snapshots of the flux variation from the reference value:

$$\left[\Delta\bar{\phi}_1 \cdots \Delta\bar{\phi}_i \cdots \Delta\bar{\phi}_m\right] = \mathbf{\Phi}_\mathrm{C} = \mathbf{U}_\mathrm{C}\mathbf{S}_\mathrm{C}\mathbf{V}_\mathrm{C}^T .$$

   $\mathbf{U}_\mathrm{C}$ is a unitary matrix with orthonormal columns which can be regarded as basis vectors of the column space of $\mathbf{\Phi}_\mathrm{C}$.

4. Generate *p* extra snapshots of the solution variation $\Delta\hat{\bar{\phi}}_j$, as done in steps 1 and 2 (this step is done once to bound the reduction error). If the inequality below is not satisfied, then the dimension of the active subspace is too small to satisfy the user-defined error bound, and one must go back to step 1 and add more snapshots, i.e., increase *m* [29]:

$$10\sqrt{\frac{2}{\pi}}\max_{j=1,\ldots p}\left\|\left(\mathbf{I}-\mathbf{U}_{\mathrm{C}}\mathbf{U}_{\mathrm{C}}^{T}\right)\Delta\bar{\hat{\phi}}_{j}\right\|_{2}=\varepsilon_{upper}$$

The orthonormal basis matrix $\mathbf{U}_C$ can be obtained using any rank revealing decomposition.

5. If the inequality is satisfied, set $r_{\mathrm{C}}=m$; the determined active subspace is expected to satisfy the user-defined error bound with probability $1-10^{-p}$.

This algorithm emulates the Range Finding Algorithm (RFA) from linear algebra. Symbolically, this may be described as follows: the computational cost $c_{\text{Converged}}$ of constructing the active subspace using the conventional algorithm described above is a function of both the rank of the active subspace (step 4) and the complexity of the model (step 2) since a converged solution is sought:

$$c_{\text{Converged}}=f(r,\xi)$$

where ξ is a variable characterizing the effect of the model's complexity on the number of iterations, s required for convergence.

The matrix **B** however (to be denoted later as $\mathbf{\Phi}_{\mathrm{N}}$) aggregates random vectors which belong to a subspace that is inclusive of the range of **A** (this property will be proved later). The advantage here is that the cost $c_{\text{Non-converged}}$ of obtaining the columns of **B** is less dependent on the model complexity since convergence is not pursued, and is therefore a function of the rank only:

$$c_{\text{Non-converged}}=f(r)$$

To implement the proposed algorithm, step 2 of the above algorithm is modified such that the non-converged solution snapshots are collected in lieu of the converged snapshots, which

might be computationally taxing. To differentiate between these two subspaces in the remainder of this chapter, we employ **C**-subspace to denote the converged subspace generated using converged snapshots, while the **N**-subspace implies the use of the non-converged iterates to construct the active subspace (i.e. constructing a non-converged subspace).

Consider the computational cost associated with each iteration to be fixed and given by c (i.e. model's complexity). For a single model run requiring s iterations to converge, the computational cost is:

$$c_{\text{model-C}} = s \times c \tag{17}$$

Assuming that for a certain error tolerance the dimension of the subspace sought is r_{C}, the total cost required to construct the **C**-subspace is:

$$c_{\text{Converged}} = r_{\text{C}} \times c_{\text{model-C}} \tag{18}$$

The proposed algorithm randomly perturbs the input parameters following a fixed number of iterations *I* that are much less than the total number of iterations needed for convergence[1], (i.e., $I \ll s$, where I can be a single iteration), and records the non-converged iterates as snapshots. This process is repeated in a similar fashion to the algorithm above until the user-defined error bound is satisfied. Assuming the dimension of the **N**-subspace determined in this manner is given by r_{N}, the total cost required would be given by:

$$c_{\text{Non-converged}} = r_{\text{N}} \times c_{\text{model-N}}, \tag{19}$$

where $c_{\text{model-N}} = I \times c$. If the following inequality holds:

$$I \times r_{\text{N}} < s \times r_{\text{C}}, \tag{20}$$

[1] Needed to satisfy stopping criteria

then the computational cost required to construct the active subspace would be reduced by a factor of $1-(I\times r_{\mathrm{N}})/(s\times r_{\mathrm{C}})$. It is expected that r_{N} will be larger than r_{C}, as will be shown later. The closer r_{N} is to r_{C}, the higher the computational savings. The saving is unknown a priori and is expected to be model-dependent; therefore, one must determine it numerically for the given model. Also note that for models with low *s* (i.e., models that require few iterations to converge), the expected computational savings will be diminished, implying that the proposed algorithm will be of value to models with slow convergence which is the main motivation for this work.

Figure 9 compares the differences between the conventional and proposed algorithms for active subspace construction. In Figure 9a, each cascade of squares represents one model execution, with each square representing a single power iteration. In Figure 9b, the parameters are perturbed after each iteration (i.e. $I=1$) to construct the **N**-subspace. Note that in the proposed algorithm the non-converged flux iterate is used to initialize the flux for the following iteration.

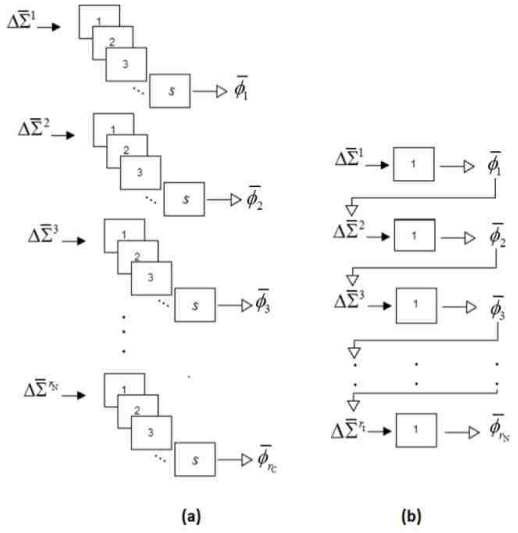

Figure 9. Algorithm schematic for: (a). **C**-Subspace (b). **N**-subspace.

Define two matrices $\mathbf{\Phi}_{\mathrm{C}}$ and $\mathbf{\Phi}_{\mathrm{N}}$ whose columns represent the **flux variations** from the conventional and proposed algorithm, respectively. All variations are calculated relative to a given reference converged solution $\bar{\phi}_0$. Matrix $\mathbf{\Phi}_{\mathrm{C}}$ can be used to construct a basis for the **C**-subspace by performing the SVD of the form: $\mathbf{\Phi}_{\mathrm{C}} = \mathbf{U}_{\mathrm{C}}\mathbf{S}_{\mathrm{C}}\mathbf{V}_{\mathrm{C}}^{T}$. Generally, the error in flux variation $\Delta\bar{\phi}^{\perp}$ associated with subspace representation using the basis $\mathbf{U}$ is given by:

$$\Delta\bar{\phi}_i^{\perp} = \left(\mathbf{I} - \mathbf{U}\mathbf{U}^T\right)\Delta\bar{\phi}_i . \tag{21}$$

where

$$\Delta\bar{\phi}_i = \bar{\phi}_i - \bar{\phi}_0 . \tag{22}$$

Earlier work showed that one can increase the dimension of the **C**-subspace until this error is bounded by a user-defined limit. See Ref. [34] for more details. The **N**-subspace is constructed by the SVD of the matrix $\mathbf{\Phi}_{\mathrm{N}}$; $\mathbf{\Phi}_{\mathrm{N}} = \mathbf{U}_{\mathrm{N}}\mathbf{S}_{\mathrm{N}}\mathbf{V}_{\mathrm{N}}^{T}$, where the columns of matrix $\mathbf{U}_{\mathrm{N}}$ form a basis for the matrix $\mathbf{\Phi}_{\mathrm{N}}$ and its rank is determined in a similar manner to the **C**-subspace using the RFA. Our goal is to show that the range of $\mathbf{U}_{\mathrm{N}}$ is a superset of the range of $\mathbf{U}_{\mathrm{C}}$ for linear eigenvalue problem, i.e.,

$$R\left(\mathbf{U}_{\mathrm{C}}\right) \subseteq R\left(\mathbf{U}_{\mathrm{N}}\right) \tag{23}$$

Before proving this, the detailed steps of the proposed algorithm are given below:

1. Generate *m* random perturbed realizations of the input parameters represented by the matrices $\left\{\mathbf{L}_i\right\}_{i=1}^{m}$ and $\left\{\mathbf{F}_i\right\}_{i=1}^{m}$, where:

$$\mathbf{F}_i = \mathbf{F} + \delta\mathbf{F}_i \text{ and } \mathbf{L}_i = \mathbf{L} + \delta\mathbf{L}_i$$

2. For every parameter perturbation, solve Eq.(16) using a fixed number of iterations I (where $I \ll s$, s being the number of iterations required for convergence), and aggregate the iterates in a matrix $\mathbf{\Phi}_I$, with the I^{th} iterate ($\bar{\phi}^{(I)}$) given by:

$$\bar{\phi}^{(I)} = \left(\frac{1}{k^{I-1}} \mathbf{L}^{-1}\mathbf{F} \cdots \left(\frac{1}{k^2} \mathbf{L}^{-1}\mathbf{F} \left(\overbrace{\frac{1}{k^1} \mathbf{L}^{-1}\mathbf{F} \left(\overbrace{\frac{1}{k^0} \mathbf{L}^{-1}\mathbf{F}\bar{\phi}_0}^{\bar{\phi}^{(1)}} \right)}^{\bar{\phi}^{(2)}} \right) \right) \right)$$

3. Calculate the singular value decomposition (SVD) of the *m* snapshots of the flux variation from the reference value:

$$\left[\Delta\bar{\phi}_1^{(I)} \cdots \Delta\bar{\phi}_i^{(I)} \cdots \Delta\bar{\phi}_m^{(I)} \right] = \mathbf{\Phi}_{\mathrm{N}} = \mathbf{U}_{\mathrm{N}}\mathbf{S}_{\mathrm{N}}\mathbf{V}_{\mathrm{N}}^T .$$

$\mathbf{U}_{\mathrm{N}}$ is a unitary matrix with orthonormal columns which can be regarded as basis vectors of the column space of matrix $\mathbf{\Phi}_{\mathrm{N}}$.

4. Generate *p* extra snapshots of the solution $\Delta\bar{\hat{\phi}}_j^{(I)}$, as done in steps 1 and 2 (this is done once). If the inequality below is not satisfied, then the dimension of the active subspace is too small to satisfy the user-defined error bound, consequently, go back to step 1 to add more realizations, i.e., increase m [29]:

$$\varepsilon_{tol} > 10\sqrt{\frac{2}{\pi}} \max_{j=1,\ldots p} \left\| \left(\mathbf{I} - \mathbf{U}_{\mathrm{N}}\mathbf{U}_{\mathrm{N}}^T \right) \Delta\bar{\hat{\phi}}_j^{(I)} \right\|_2 = \varepsilon_{upper}$$

$\mathbf{U}_{\mathrm{N}}$ is the orthonormal basis matrix which can be obtained using any rank revealing decomposition. ε_{tol} is the user-defined error tolerance.

5. If the inequality is satisfied, set $r_{\mathrm{N}} = m$; the determined active subspace is expected to satisfy the user-defined error bound with probability $1-10^{-p}$.

   Notice that the tightly converged iterative solution of Eq.(16) can be represented as:

$$\bar{\phi}^{(s)} = \left(\frac{1}{k^{s-1}} \mathbf{L}^{-1}\mathbf{F} \cdots \left(\frac{1}{k^{2}} \mathbf{L}^{-1}\mathbf{F} \left(\overbrace{\left(\frac{1}{k^{1}} \mathbf{L}^{-1}\mathbf{F} \left(\overbrace{\left(\frac{1}{k^{0}} \mathbf{L}^{-1}\mathbf{F}\bar{\phi}_0 \right)}^{\bar{\phi}^{(1)}} \right) \right)}^{\bar{\phi}^{(2)}} \right) \right) \right),$$

where $\bar{\phi}_0$ is the initial guess, $\bar{\phi}^{(1)}$ is the solution after one iteration and $\bar{\phi}^{(s)}$ is the tightly converged solution snapshot. Also, notice that:

$$\bar{\phi}^{(1)} \in R\left(\mathbf{L}^{-1}\mathbf{F}\right) = \gamma_1,$$

$$\bar{\phi}^{(s)} \in R\left(\mathbf{L}^{-1}\mathbf{F} \cdots \left(\mathbf{L}^{-1}\mathbf{F} \cdots \left(\mathbf{L}^{-1}\mathbf{F} \left(\mathbf{L}^{-1}\mathbf{F} \left(\mathbf{L}^{-1}\mathbf{F} \right)_1 \right)_2 \right)_3 \cdots \right)_I \cdots \right)_s = \gamma_s,$$

where $R(\mathbf{L}^{-1}\mathbf{F})$ is the range of matrix $\mathbf{L}^{-1}\mathbf{F}$ obtained after one iteration. This is denoted by γ_1 while γ_s denotes the range of the matrix obtained after *s* iterations (or *s* multiplications of $\mathbf{L}^{-1}\mathbf{F}$). The range of an arbitrary matrix (**A**) (sometimes called the matrix's column space Col(**A**)) is the set of all possible linear combinations of its columns. From linear algebra, the range of a matrix either shrinks or stays the same after successive multiplications [60]. This assertion is proven as follow:

For $\bar{b} \in R(\mathbf{AB}) \Rightarrow \exists\, \bar{x}$ such that $\bar{b} = \mathbf{AB}\bar{x} = \mathbf{A}(\mathbf{B}\bar{x})$, therefore, $\bar{b} \in \mathrm{R}(\mathbf{A})$. Hence:

$$R(\mathbf{AB}) \subseteq R(\mathbf{A}). \tag{24}$$

For $I < s$ the argument above leads to the following conclusion:

$$\gamma_s \subseteq \gamma_I \subseteq \gamma_1 .$$

Therefore, if we assume that the RFA can capture the subspaces that represent γ_s and γ_I accurately, then the non-converged iterates will formulate a subspace that is inclusive of the subspace that contains the converged solutions. Consequently, one may express this observation as follows:

$$\mathbf{C}\text{-subspace} \subseteq \mathbf{N}\text{-subspace} . \tag{25}$$

A more intuitive viewpoint is given by considering the convergence of the power iteration. It is known that the higher overtones of the flux equate to the eigenvectors and die off each power iteration as the higher overtones' eigenvalues to the fundamental eigenvalue ratios. This implies the converged flux solution will be contaminated with higher overtones if the power iteration is terminated prematurely. This in turn implies a larger subspace that includes the converged subspace.

The proposed algorithm employs the RFA to determine the **C**-subspace and the **N**-subspace. However, RFA approximates these subspaces within user-defined accuracy. So the **C**-subspace and **N**-subspace obtained by the RFA satisfies the statement of Eq.(25) upon the condition that they represent the ranges γ_s and γ_I, respectively, with relatively high accuracy. One way to test the statement of Eq.(25) is to measure the angle between the two subspaces. If the **N**-subspace is perfectly inclusive of the **C**-subspace then the angle between the two subspaces must be zero. A measure of the sine of the dominant angle between the two subspaces has been developed elsewhere [70], and is calculated by the following equation:

$$\sin(\vartheta) = \left\| \mathbf{U}_{\mathrm{N}} \mathbf{U}_{\mathrm{N}}^{T} - \mathbf{U}_{\mathrm{C}} \mathbf{U}_{\mathrm{C}}^{T} \right\|_2 \tag{26}$$

where ϑ is the dominant angle between the two subspaces of interest which are spanned by the columns of the two matrices $\mathbf{U}_{\mathrm{N}}$ and $\mathbf{U}_{\mathrm{C}}$.

The premise of this chapter is to produce an Efficient version of the Range Finding Algorithm (ERFA). So for a general model (i.e. $\bar{y} = f(\bar{x})$), the following steps summarize the use of the ERFA to construct a lower dimensional subspace (active subspace) for the response i.e. $\bar{y}$. (**ERFA**):

1. Generate *k* random perturbed realizations of the input parameters of the model of interest:

$$\mathbf{X} = \left[\bar{x}^{(1)} \cdots \bar{x}^{(k)} \right],$$

2. For every parameter perturbation, execute the model of interest using a fixed number of iterations I (where $I \ll s$, s being the number of iterations required for tight convergence), the variations from the references response value are aggregated in the matrix **Y**:

$$\mathbf{Y} = \left[\Delta\bar{y}_1 \cdots \Delta\bar{y}_k \right]$$

3. Calculate the singular value decomposition (SVD) of the aggregated response snapshots:

$$\mathbf{Y} = \mathbf{U}\mathbf{S}\mathbf{V}^T.$$

$\mathbf{U} \in \mathbb{R}^{nxk}$ is a unitary matrix with orthonormal columns which can be regarded as basis vectors of the column space of matrix $\mathbf{Y}$.

4. Generate *p* extra snapshots of the response $\mathbf{Y}$, as done in steps 1 and 2 (this is done once). If the inequality below is not satisfied, then the dimension of the active subspace is too small to satisfy the user-defined error bound, consequently, go back to step 1 to add more realizations, i.e., increase *k* [29]:

$$\varepsilon_{tol} > 10\sqrt{\frac{2}{\pi}} \max_{j=1,\ldots p} \left\| \left(\mathbf{I} - \mathbf{U}\mathbf{U}^T \right) \Delta \bar{\hat{y}}_j \right\|_2 = \varepsilon_{upper} \tag{27}$$

$\mathbf{U}$ is the orthonormal basis matrix which can be obtained using any rank revealing decomposition.

5. If the inequality is satisfied, set $r = k$; the determined active subspace is expected to satisfy the user-defined error bound with probability $1 - 10^{-p}$.

The flow chart below (Figure 10) summarizes the 5 steps listed above. Note that the main difference between the ERFA and the RFA is that the ERFA utilizes low fidelity snapshots to find a subspace that is spanned by the variations of the high fidelity snapshot

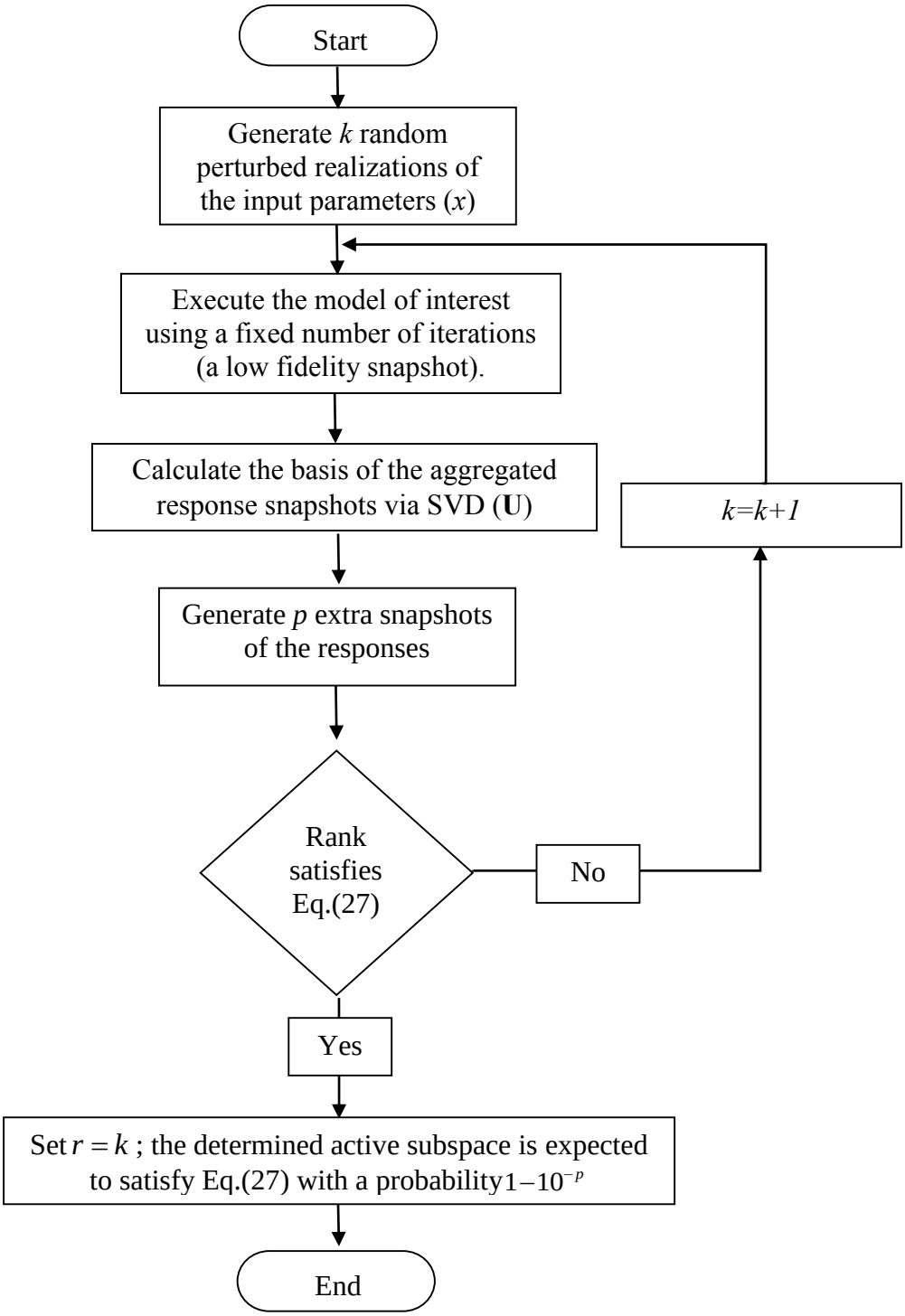

Figure 10. ERFA flow char.

2.2 Numerical Test: Lattice Physics

Our goal in this section is to demonstrate that reduction errors of both **N**- and **C**-subspaces can be upper-bounded. Next, we demonstrate the computational savings resulting from the use of the **N**-subspace for two cases with different dominance ratios, representing both a PWR and a BWR lattice model. Next, we verify the assertion that the **N**-subspace is inclusive of the **C**-subspace. Finally, we employ both the **C**- and **N**-subspace to calculate flux and eigenvalue variations for a range of conditions using a recently developed method, referred to as exact-to-precision generalized perturbation theory. Modifications were implemented into the SCALE6.1's NEWT code [57] in order to automate the process of building the active subspace via the proposed algorithm (**Refer to Section 1.6.2).**

Two different eigenvalue problems are used for demonstration. One is characterized by a relatively high dominance ratio (BWR lattice) while the other is characterize by a lower dominance ratio (PWR quarter lattice). The response of interest is the 44 energy group angular flux. For the quarter PWR fuel lattice, the numerical solution employs 790 spatial cells, each with 24 angular directions. The resulting angular flux has 834,240 components (i.e., belong to a space $\mathbb{R}^{834,240}$) over space, energy, and angles. For the BWR fuel lattice, the numerical solution has 1284 spatial cells, each with 24 angular directions. Similarly, the response of interest is the 44 energy group angular flux, which is characterized by a vector of 1,355,904 components, i.e., belongs to $\mathbb{R}^{1,355,904}$. The fission (Σ_f), elastic scattering (Σ_s), fission spectrum (χ) and average total (prompt plus delayed) number of neutrons released per fission event ($\bar{\nu}$) cross sections are perturbed ($\pm 30\%$) to obtain the active subspace. The nuclide

considered in this study are: $^{234}_{92}\mathrm{U}$, $^{235}_{92}\mathrm{U}$, $^{236}_{92}\mathrm{U}$, $^{238}_{92}\mathrm{U}$, $^{1}_{1}\mathrm{H}$, $^{16}_{8}\mathrm{O}$, and the naturally occurring isotopes of B, Zr, Fe, Sn, Na**,** Al, Si, K and N**.** Figure 11 depicts the two lattices.

The angular flux active subspace is constructed using both the converged snapshots (**C**-subspace) and the non-converged flux snapshots (**N**-subspace). The two subspaces are then compared in terms of their associated computational cost and the rank required to achieve a certain error upper-bound associated with the subspace representation using the basis matrix $\mathbf{U}$. This upper bound[2] is given by Eq. (28) with a probability of $1-10^{-p}$ [29] (we select $p=10$):

$$\varepsilon_{upper} = 10\sqrt{\frac{2}{\pi}} \max_{j=1,\ldots p} \left\| \left(\mathbf{I}-\mathbf{U}\mathbf{U}^{T}\right)\Delta\bar{\hat{\phi}}_{j} \right\|_{2} \tag{28}$$

Figure 12 and Figure 13 apply Eq. (28) using both the basis matrices $\mathbf{U}_{\mathrm{C}}$ and $\mathbf{U}_{\mathrm{N}}$ obtained by both the PWR and BWR lattices, respectively. Figure 12 plots the error upper bound (ε_{upper}) versus the ranks of the matrices $\mathbf{U}_{\mathrm{C}}$ and $\mathbf{U}_{\mathrm{N}}$ for the PWR fuel lattice. As predicted by Eq. (25), the **N**-subspace is bigger in size than the **C**-subspace. For example, for a user-defined error upper bound of 10^{-2}, the corresponding ranks of the **N**-subspace and the **C**-subspace are 100 and 78, respectively. Although the **N**-subspace is bigger than the **C**-subspace, the **N**-subspace is considerably less computationally expansive to construct as demonstrated by equations (17) through (19). This is mainly due to the fact that the **N**-subspace is constructed using non-converged snapshots of the model's solution.

[2] It is important to note that Eq.(28) employs the Euclidean norm which sums up the squared errors for all the flux components. Given the enormous dimension of the flux vector, the individual component errors are typically much smaller than the upper bound.

Figure 13 compares the **N**-subspace and the **C**-subspace in a relatively high dominance ratio system (i.e. BWR fuel lattice). Since the convergence of this system is slower than that of the PWR system, the **N**-subspace is expected to be larger when compared to the **C**-subspace. Table I summarizes the numerical results for both the PWR and BWR systems. The BWR system requires an average of 279 outer iterations for its eigenvalue (multiplication factor) to converge to within 10^{-8}, while the PWR requires only an average of 55 iterations for the same convergence criterion. Taking into consideration the total computational burden involved in each basis construction algorithm, Table 1 indicates the computational cost to construct the **N**-subspace to be about 43 times less than that of the **C**-subspace for the PWR system. However, given the low convergence rate in the case of the BWR systems, the computational cost to construct the **N**-subspace is 166 times less than that of the **C**-subspace. This demonstrates the power of the algorithm when the cost of the converged solution is relatively high.

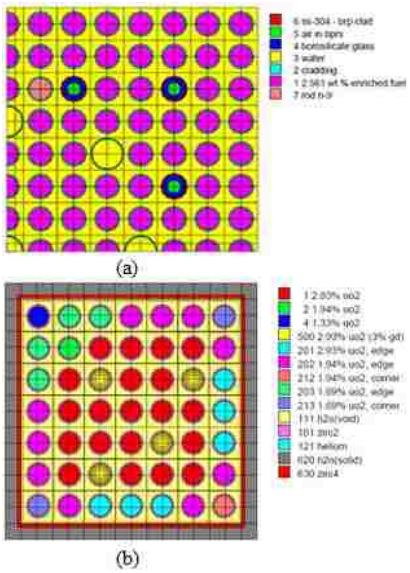

Figure 11. (a) PWR quarter fuel lattice. (b) BWR fuel lattice.

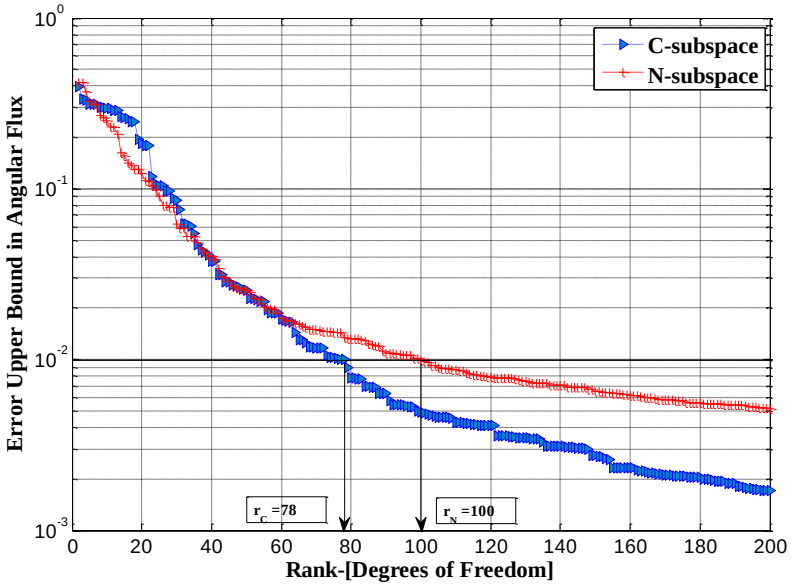

Figure 12. Error in the flux as obtained from the **N**-subspace vs. the **C**-subspace (PWR).

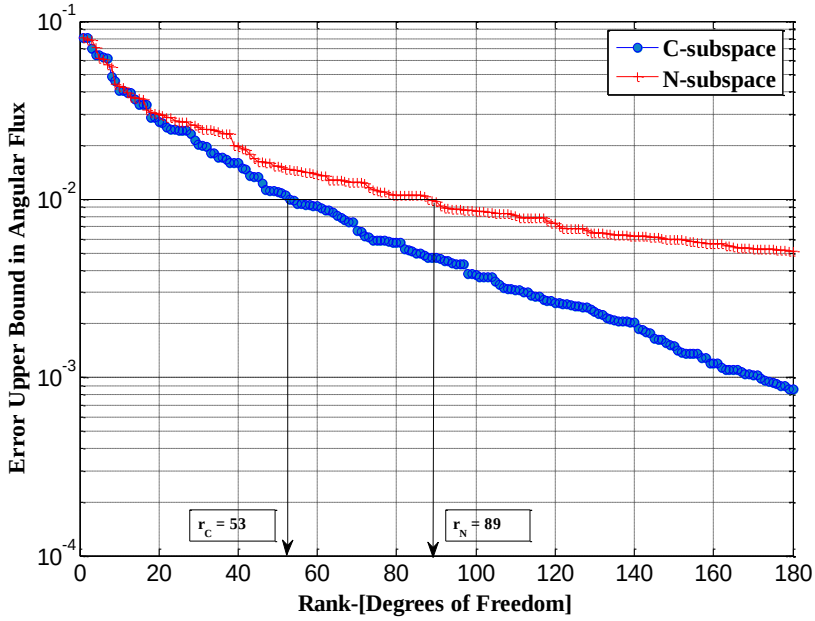

Figure 13. Error in the flux as obtained from the **N**-subspace vs. the **C**-subspace (BWR).

Table 1. Computational costs required for constructing the **N**-subspace and **C**-subspace.

Subspace	PWR		BWR	
	Rank	Computational Cost	Rank	Computational Cost
C-subspace	$r_C = 78$	$c_{\text{Converged}} = 55\text{x}\,c\text{x}78$	$r_C = 53$	$c_{\text{Converged}} = 279\text{x}\,c\text{x}53$
N-subspace	$r_N = 100$	$c_{\text{Non-converged}} = 1\text{x}\,c\text{x}100$	$r_N = 89$	$c_{\text{Non-converged}} = 1\text{x}\,c\text{x}89$

Next we verify the assertion made by Eq.(25) that is the **N**-subspace is inclusive of the **C**-subspace. This can be achieved by calculating the dominant angle between the two subspaces using Eq.(26). When the **N**-subspace and the **C**-subspaces are properly approximated, the angle between the two subspaces should be zero, since the former is inclusive of the latter. Figure 14 shows the dominant angle (in radians) between the two subspaces for the PWR fuel lattice calculated as a function of the rank. As would be expected, increasing the rank improves the approximation of the respective subspaces resulting in a gradual decline of the dominant angle. The implication of this graph is that if one chooses a rank that is too small, the **N**-subspace would not adequately represent the **C**-subspace and therefore the associated reduction errors would be noticeably higher than those calculated using the **C**-subspace. As the rank is increased however and the angle between the two subspaces diminishes, the reduction errors associated with both subspaces are expected to become more comparable to each other. This provides a good utility for the dominant angle as a metric that determines the proper size of the **N**-subspace.

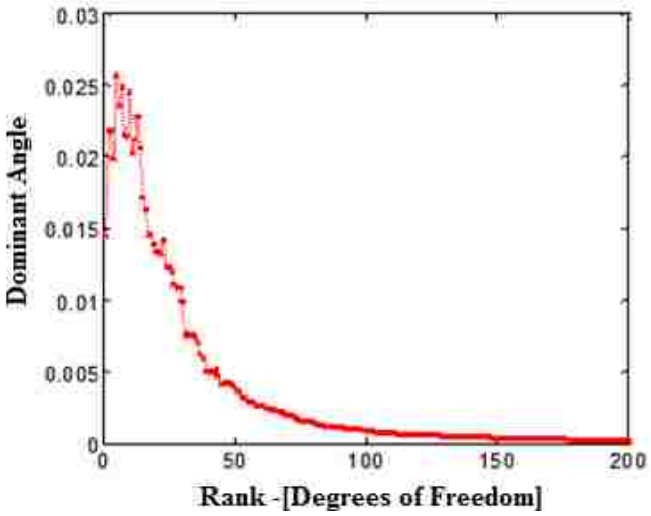

Figure 14. The dominant angle reduction as the rank increases (PWR).

Finally, we investigate the use of the proposed algorithm to render reduction for applications that require repeated execution of the model. For example, in lattice physics calculations, the few-group cross-sections are functionalized in terms of various thermal-hydraulic and reactivity control core conditions, so repeated solving of the Boltzmann equation is required as iterations with the thermal-hydraulic equations solver and critically search routine are completed. For demonstration, we employ a recent method, referred to as exact-to-precision generalized perturbation theory (E_PGPT) [56]. The E_pGPT calculates high order sensitivities using the active subspace, which are then used to constructs a surrogate that replaces the solution of the Boltzmann equation. A prerequisite for E_PGPT is the calculation of an active subspace for the flux. The quality of the active subspace as measured in terms of its associated reduction error in the sense of Eq. (27), determines the quality of the surrogate predictions. We employ both the **C**- and **N**-subspace in conjunction with E_PGPT to calculate flux and eigenvalue variations for a range of conditions.

In general, one can estimate the variations in a response *R* that is a function of the neutron flux via the GPT analysis with the linearity assumption:

$$R = f(\bar{\phi})$$

If other physics-based restrictions are available then they can be represented as constraints on the flux solution:

$$g(\bar{\phi}) = l$$

The GPT variational analysis uses a Lagrangian (auxiliary function) to represent the variation in the response given a set of constraints. In the current analysis, and for the eigenvalue problem:

$$F = R - l^* \left(g(\bar{\phi}) - l \right) - \vec{\beta}^{*T} \left(\mathbf{L} - \lambda \mathbf{F} \right) \bar{\phi} \tag{29}$$

where l^* and $\vec{\beta}^*$ are the Lagrange multipliers associated with the eigenvalue problem. Eq.(29) suggests that the Lagrange function (F) represents the response (R) whenever the exact solutions ($\bar{\phi}$ and λ) are employed; therefore, for any parameter perturbation the variation in the converged value of the Lagrangian function is equal to that of the response of interest (i.e. $\delta F = \delta R$).

EPGPT is a hybrid methodology combining the generalized perturbation theory (GPT) and the RFA to reduce the computational cost required to calculate the exact response variations in support of nuclear reactor calculations, when both the numbers of responses and parameters are very large. The method is predicated on the assumption that the flux variations can be approximated by a small active subspace whose rank is much smaller than the dimension of the full flux space (i.e. $r \ll n$). Given that the dimension of the reduced flux $\Delta\bar{\phi}_r = \mathbf{U}^T \Delta\bar{\phi} \in \mathbb{R}^r$

is much smaller than the original dimension of the flux $\Delta\bar{\phi} \in \mathbb{R}^n$, one can recast GPT in terms of a set of *r* pseudo responses, i.e. $R_{pseudo,i} = \left\langle \bar{q}_i, \bar{\phi} \right\rangle$, for $i = 1, \cdots, r$ and q_i is the i^{th} column of matrix $\mathbf{U}$, such that the reduced variable $\Delta\phi_r$ can be estimated as follow:

$$\Delta\bar{\phi}_r = -\left(\mathbf{I}_{r\times r} + \mathbf{T}\right)^{-1} \bar{\varpi}, \mathbf{T} \in \mathbb{R}^{r\times r}, \bar{\varpi} \in \mathbb{R}^r \tag{30}$$

with

$$\bar{\varpi} = \left[\left\langle \Gamma_1^*, \Delta\mathbf{P}\bar{\phi}_0 \right\rangle \quad \cdots \quad \left\langle \Gamma_r^*, \Delta\mathbf{P}\bar{\phi}_0 \right\rangle \right]^T$$

$$\mathbf{T} = \begin{bmatrix} \left\langle \Gamma_1^*, \Delta\mathbf{P}\bar{q}_1 \right\rangle & \cdots & \left\langle \Gamma_1^*, \Delta\mathbf{P}\bar{q}_j \right\rangle & \cdots & \left\langle \Gamma_1^*, \Delta\mathbf{P}\bar{q}_r \right\rangle \\ \vdots & \ddots & \vdots & \iddots & \vdots \\ \left\langle \Gamma_i^*, \Delta\mathbf{P}\bar{q}_1 \right\rangle & \cdots & \left\langle \Gamma_i^*, \Delta\mathbf{P}\bar{q}_j \right\rangle & \cdots & \left\langle \Gamma_i^*, \Delta\mathbf{P}\bar{q}_r \right\rangle \\ \vdots & \iddots & \vdots & \ddots & \vdots \\ \left\langle \Gamma_r^*, \Delta\mathbf{P}\bar{q}_1 \right\rangle & \cdots & \left\langle \Gamma_r^*, \Delta\mathbf{P}\bar{q}_j \right\rangle & \cdots & \left\langle \Gamma_r^*, \Delta\mathbf{P}\bar{q}_r \right\rangle \end{bmatrix} \in \mathbb{R}^{r\times r}$$

where $\mathbf{I}_{r\times r}$ is *r* by *r* identity matrix, and $\Delta\mathbf{P} = \left(\Delta\mathbf{L} - \lambda\Delta\mathbf{F} - \Delta\lambda\mathbf{F} - \Delta\lambda\Delta\mathbf{F}\right)$ is the perturbed neutron transport operator with $\lambda = 1/k$. The Γ_i^* is the pre-computed solution of the GPT equation for the pseudo response $R_{pseudo,i}$. In addition, $\left\{\Gamma_i^*\right\}_{i=1}^r$ need to be computed only once for the given active subspace. The variation $\Delta\lambda$ can be accurately approximated using an iterative approach proposed in Ref. [56] with very low computational cost. Therefore, EPGPT can directly employ the basis vectors from **C**-subspace and **N**-subspace to efficiently calculate the responses variations:

$$\Delta\bar{\phi} = \mathbf{U}\Delta\bar{\phi}_r = -\mathbf{U}\left(\mathbf{I}_{r\times r} + \mathbf{T}\right)^{-1} \varpi \tag{31}$$

We use the same PWR fuel lattice model described before to examine the **N**- and **C**-subspaces via EPGPT. The eigenvalue in Eq.(16) is calculated and compared in Figure 15. The

exact eigenvalue and flux are calculated by executing the PWR lattice model one more time with the perturbed parameters (e.g. control rod insertion). The multiplication factor discrepancy (Δk) reported in Figure 15 is defined as follow:

$$\Delta k = k_{\text{model}} - k_{surrogate}$$

where this error is calculated for different subspace sizes, where each subspace size would result in different $k_{surrogate}$. As can be observed in Figure 15, both subspaces can predict the eigenvalue accurately, i.e. the discrepancy is less than 100 pcm, when the dimension of active subspace is bigger than 60. The estimation accuracy is examined using 20 different test samples illustrated in Figure 16 and Figure 17, showing a maximum error of approximately 100 pcm which is representative of the modeling errors of transport calculations. The test samples are created using different reference fuel compositions. Figure 18 and Figure 19 show similar results for the neutron flux. It is noted that the highest errors appear in the thermal range below 0.01 eV where the importance of neutrons is very low. This is to be expected as the active subspace identifies the dominant flux variations, implying that higher errors are to be expected in energy ranges where the neutron importance is low.

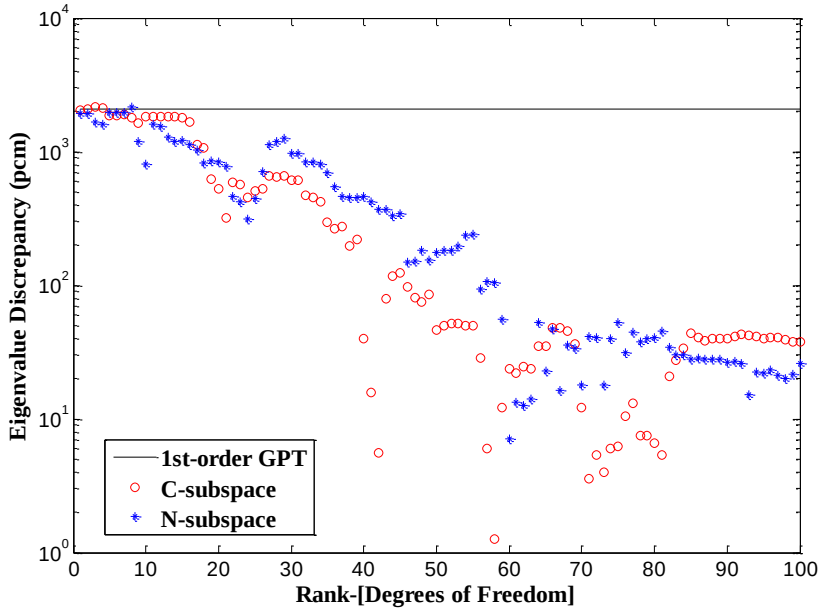

Figure 15. Eigenvalue errors for the **N**- and. the **C**-subspace.

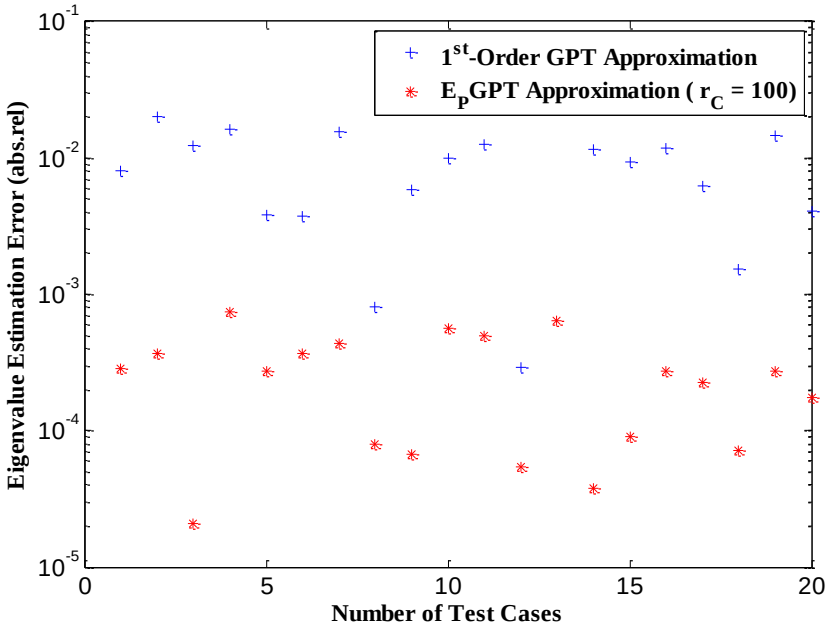

Figure 16. The eigenvalue errors for the **C**-subspace (1st order vs. 2nd order).

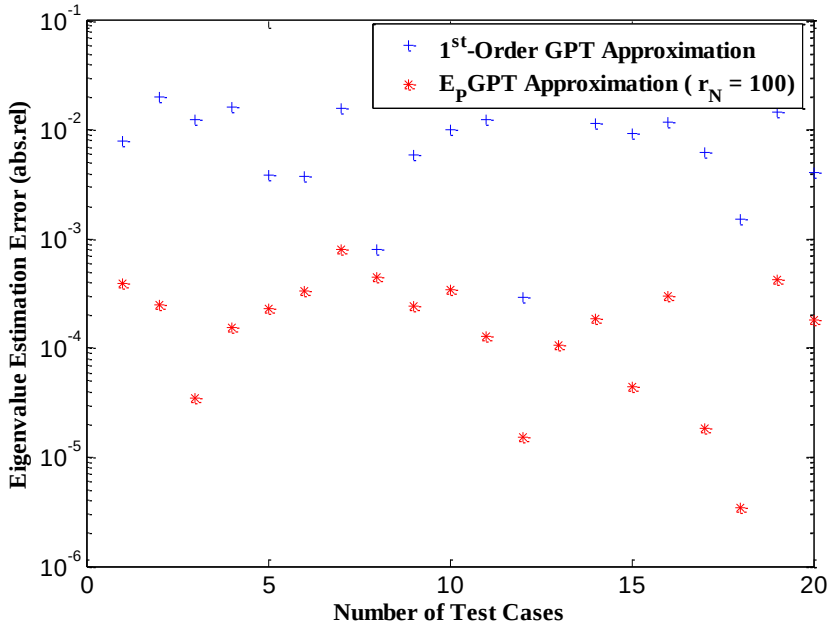

Figure 17. The eigenvalue errors for the **N**-subspace (1st order vs. 2nd order).

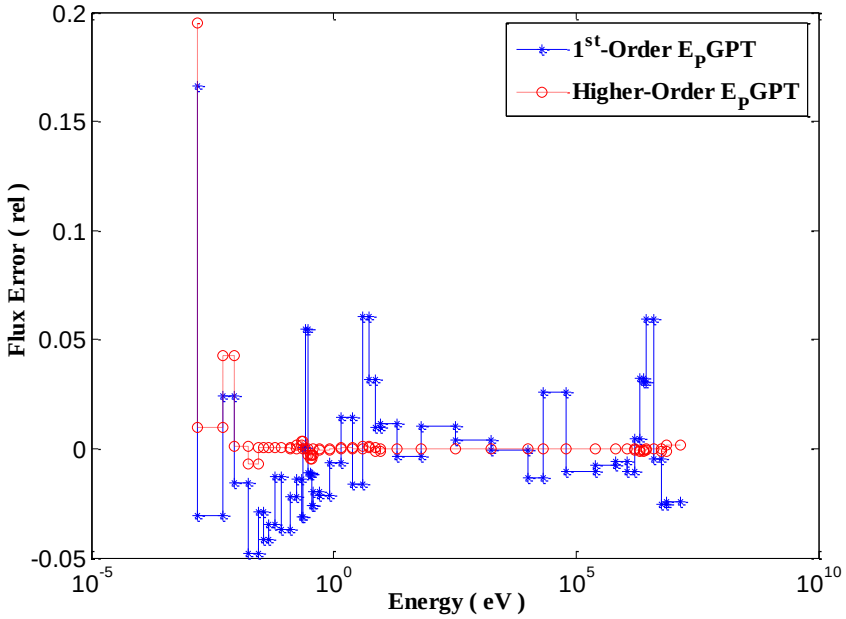

Figure 18. The flux errors for the EPGPT's **C**-subspace (1st order vs. 2nd order).

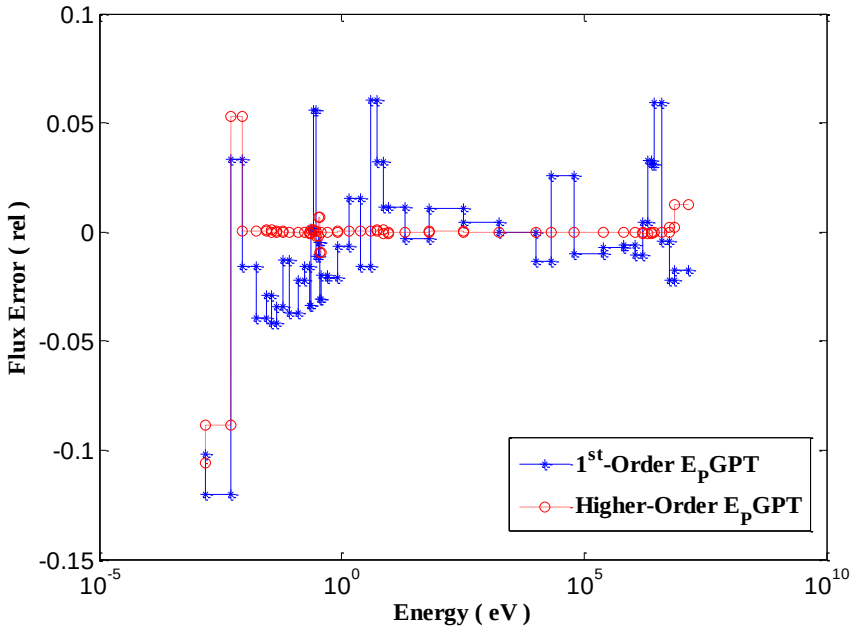

Figure 19. The flux errors for the EPGPT's **N**-subspace (1st order vs. 2nd order).

2.3 Numerical Test: 3-Dimensional Assembly Model Calculations

In this section, a 3-dimensional depletion problem with thermal-hydraulics feedback is used to exemplify the application of the **ERFA** on coupled problems where key reactor attributes are passed from one model to another in the sequence of models that simulate reactor operating conditions (e.g. reactor fuel depletion). This example will help to explore the possibility of obtaining the active subspace based on low fidelity snapshots of 3-dimensional coupled simulation problems.

CASL progression problem 6 is used as an illustrative example of a single assembly model neutronic solution (MPACT) coupled with thermal-hydraulics feedback (COBRA-TF), where the material composition is updated over certain time steps via the solution of a generalized form of the Bateman equations (ORIGEN). This sequence of models is coupled under the

umbrella of the Virtual Environment for Reactor Applications-Core Simulator (VERA-CS) described more thoroughly in section 1.7 [58, 59, 65, 67] (for more information about VERA-CS, MPACT and COBRA-TF refer to section 1.7).

CASL progression problem 6 is a single PWR 17x17 assembly (Westinghouse fuel design) with uniform fuel enrichment resembling fuel used in Watts Bar Unit 1 Cycle 1 at Hot Full Power (HFP). The example used here uses a boron concentration of 1300 ppm and 100% power level with no axial blankets or different enrichment regions. Overall, the total number of fuel rods is 264 fuel rods, with 24 guide tubes and a single instrument tube at the center. (NOTE: There are no control rods or removable burnable absorber rods in this problem) [68]. For more information about the problem's parameters, refer to Table 2.

In this numerical example the response of interest would be the pin power distribution (calculated by MPACT). In order to provide the pin powers MPACT calculates the sub-pin level power distributions using the method of characteristics (MOC) in a 3-dimensional (3D) or a 2 Dimensional/1 Dimensional (2D/1D) fashion as previously described. For results reported here, the 2D/1D method is used with the axial component treated employing SP1.

Table 2. CASL Problem 6 Specifications [68].

Parameter Name	Value
Fuel Pellet Radius	0.4096 cm
Fuel Cladding Inner Radius	0.4180 cm
Fuel Clad Outer Radius	0.4750 cm
Guide Tube Inner Radius	0.5610 cm
Guide Tube Outer Radius	0.6020 cm
Instrument Tube Inner Radius	0.5590 cm
Instrument Tube Outer Radius	0.6050 cm
Outside Rod Height	385.10 cm
Fuel Stack Height (active fuel)	385.76 cm
Plenum Height	16 cm
End Plug Heights (x2)	1.67 cm
Fuel	UO_2
Clad / Caps / Guide Tube Material	Zircaloy-4

The pin powers are calculated at each axial level, hence, 17x17 elements, along with 49 fuel axial levels out of 58 total axial levels, which produces a large number of pin power responses (i.e. 17x17x49 = 14161). The basis of the active space of the pin powers will be calculated via the RFA and then compared to the basis calculated via the ERFA. The comparison is made by comparing the error values calculated by Eq.(32) , where $\mathbf{U}$ is the basis of the pin power distribution vector and $\vec{P}_j$ is a high fidelity snapshot of the pin power

distribution. By projecting the high fidelity snapshots on the space of interest, the orthogonal component (i.e. the component of the high fidelity snapshots that cannot be expressed as a combination of the basis of interest) reflects how well is the subspace represents the different variations of the quantity of interest (e.g. $\vec{P}_j$). Mathematically, the following inequality should be satisfied [29-30]:

$$\varepsilon_{tol} > 10\sqrt{\frac{2}{\pi}} \max_{j=1,\dots p} \left\| \left(\mathbf{I} - \mathbf{U}\mathbf{U}^T \right) \Delta\vec{P}_j \right\|_2 = \varepsilon_{upper} \tag{32}$$

In the above equation: $\Delta\vec{P}_j = \vec{P}_j - \vec{P}_0$, where $\vec{P}_0$ is the reference pin power distribution. The basis will be calculated via a set of high fidelity snapshots obtained by "2D-1D" MPACT runs coupled with COBRA-TF and ORIGEN (i.e. The subspace for tight stopping criteria solutions will be represented by the basis $\mathbf{U}_C$: **C**-subspace) and the subspace for the loose stopping criteria solutions will be represented by the basis $\mathbf{U}_N$: **N**-subspace). Table 3 indicates the stopping criteria employed.

In order to test the performance of the ERFA for time dependent problems two sub-tests will be used. The first sub-test suggests the use of the time dependent snapshots using loose stopping criteria to build the **N**-subspace (computational savings come from the fact that loose stopping criteria require less computational time). This test means that the depletion problem will be solved at all points in the fuel irradiation period; however, the **N**-Subspace basis is calculated using a set of loosely converged pin powers (at each time-step). The second sub-test uses tightly converged (high fidelity) time-independent snapshots to build a subspace without considering fuel depletion (computational savings come from the fact that solving the problem for one time point requires less computational resources than solving the problem at every time point on the interval of interest). This means that the variations in the pin powers distribution

for the time-independent problem (fresh fuel assembly) will be used to build the basis of the **N**-subspace.

Table 3. Stopping criteria for VERA-CS analysis of 3D assembly.

Response	Loose Convergence Criteria	Tight Convergence Criteria
Eigenvalue	100 (pcm)	5 (pcm)
Temperature	10 (C^o)	1 (C^o)
Boron Concentration	1 ppm	0.1 ppm

Figure 20 shows a comparison of the error upper bound associated with each basis. In this case the pin power distribution variations at 30 GWd/MTU are approximated by the snapshots obtained via converged power distribution at 30 GWd/MTU (C-subspace), non-converged distribution at 30 GWd/MTU (N-subspace: time-dependent) and converged snapshots at 0.0 GWd/MTU (N-subspace: time-independent). The figure shows that (N-subspace: time-dependent) power snapshots can be used to capture the variations (important DoFs) of the power distribution at 30 GWd/MTU in a superior manner to the (N-subspace: time-independent). Hence, the non-converged snapshots can be used to construct the basis of an active-subspace of the variations of the power distribution. At rank 50 the error upper bound in the 2-norm is around 1 W/cm. Note that the pin power distribution at the reference composition has a maximum of 274.1 W/cm and a minimum of 33.7 W/cm. For the worst case scenario the error in the L2 norm will be concentrated in the smallest pin power component (i.e. 33.7 W/cm), implying a corresponding relative error of below 3%. However, usually this error is distributed more evenly among all the components.

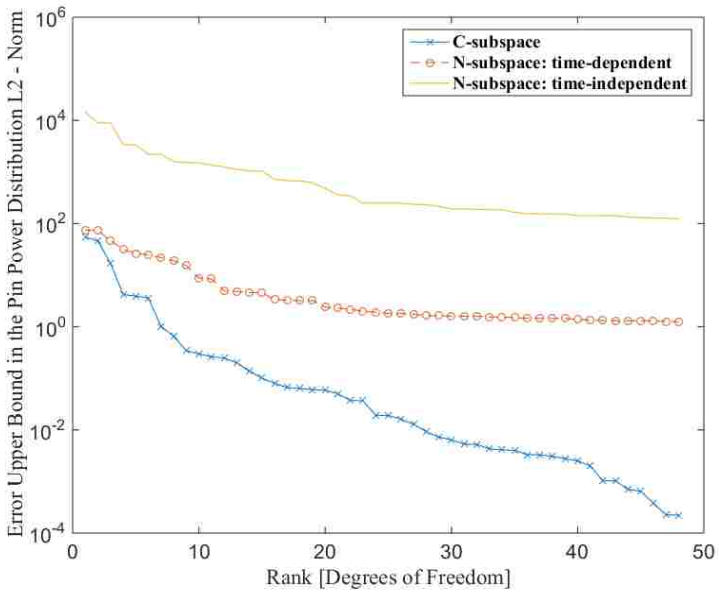

Figure 20. Error in the *L2* norm of the 3-D pin power distribution (the **N**-subspace vs. the **C**-subspace). Refer to Eq.(32).

CHAPTER 3. EFFICIENT SUBSPACE APPROXIMATION FOR MULTI-PHYSICS COUPLED MODELS WITH FEEDBACK

Note: The work presented in this section was developed in collaboration with J. Hite, H. S. Abdel-Khalik and Y. S. Bang (Ref. [71]).

Recently, the requirement of high fidelity models that are accompanied with uncertainty capabilities has contributed to increasing the complexity of reactor modeling and simulation tools; therefore, new developments in reduced order modeling are continuously being pursued by computational scientists as an effective means to render practical the repeated evaluations of the associated physics models. In the context of this dissertation, reduced order modeling is capable of reducing the effective dimensionality at the parameter, state and response levels, which reduces the number of degrees of freedom to deal with whenever performing certain types of analysis (e.g. uncertainty quantification, forward and adjoint sensitivity analysis). Moreover, reduced order modeling can utilize such reduction in replacing the original models with surrogates that are accurate in representing the original model to within a certain user-defined error tolerance. This chapter will focus on performing gradient-based and gradient free reduced order modeling for coupled multi-physics models.

Reference [34] develops a gradient based reduction approach while the previous section introduced a gradient-free reduction approach [72]. Gradient-based reduction randomly samples the derivatives of the responses with respect to input parameters and subsequently determines the dominant directions (Degrees of Freedom - DoFs) in the parameter space via a linear algebraic algorithm called the Range Finding Algorithm (RFA) which represents the randomization, collection of gradient samples and the subsequent filtering of dominant directions.. The space spanned by those dominant directions is collectively referred to as the

"*parameters active subspace*". The derivatives are evaluated using an adjoint sensitivity analysis procedure, which is mostly suitable for neutron transport calculations (more generally calculations involving linear operators) where the number of parameters is high (i.e. nuclear data cross-sections) with few responses of interest (e.g. multiplication factor and pin powers); therefore, the adjoint approach is computationally efficient for neutronics calculations. As discussed in chapter 2, the second type of reduction, i.e., gradient-free reduction, employs RFA to reduce the dimensionality of the state or response spaces via multiple randomized executions of the forward model using high fidelity snapshots (RFA) or low fidelity snapshots (ERFA). In chapter 2, both of these types of reductions were applied to single physics models. In this chapter, we integrate these two types of reduction algorithms to allow reduction of multi-physics models. The idea is to perform three RFA-type reductions at each physics-to-physics interface, one based on the upstream physics (gradient-free reduction algorithm), another for the downstream physics (gradient-based reduction), and a third for the interaction thereof (i.e. finding the important DoFs for both the upstream and downstream physics). Moreover, a mathematical proof will be presented to show the convergence of the proposed algorithm (with increasing DoFs). In the following sections, our proposed algorithm will be referred to as Multi-Physics Range Finding Algorithm (MPRFA).

Without the loss of generality, this chapter will consider a two loosely-coupled models case (A and B) where the output of model A serves as input for model B and the output of model B serves as input for model A (see Figure 21)**.** However, conclusions made in this chapter can be extended to any number of coupled multi-physics models.

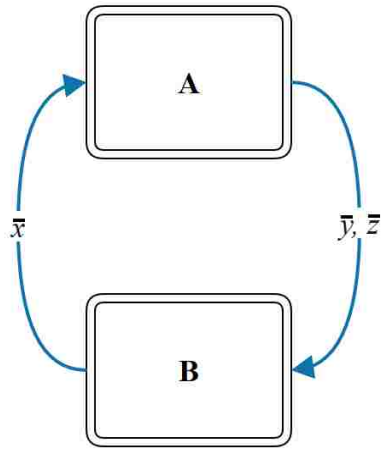

Figure 21. A schematic of coupled models.

Models A and B might represent any two coupled physics models. For example, model A may depend on the output of model B, e.g. model A transport operator cross-section dependencies on the thermal-hydraulics (Model B) operator prediction of fluid and fuel temperatures. However, this sections assumes that these models represent a set of coupled source problems of the following form:

$$\mathbf{A}\bar{x}^i = \bar{y}^i \text{ and } \mathbf{B}\bar{y}^i = \bar{x}^{i+1}$$

where **A** and **B** are matrices that represent the effect of the corresponding models. This entails the assumption that the effect of these modules can be approximated by the linear operators **A** and **B**. To make this linearity assumption more plausible, note that $\bar{x}$ and $\bar{y}$ can be considered perturbations from some reference state. Moreover, the assumption that both operators **A** and **B** are rank deficient implies that the associated system of equation has infinitely many solutions, hence in order to determine a unique solution, a constraint is required such as normalization.

Since each operator (**A** and **B**) is rank deficient then the coupled system is rank deficient. In order to prove this; one can consider the effect of the coupling process as a successive application of the operators (**A** and **B**) as follow:

$$\bar{y}^i = \mathbf{A}\bar{x}^i$$

$$\bar{x}^{i+1} = \mathbf{B}\bar{y}^i = \mathbf{BA}\bar{x}^i$$

$$\bar{y}^{i+1} = \mathbf{A}\bar{x}^{i+1} = \mathbf{AB}\bar{y}^i$$

These last two equations indicate that the operators **BA-I** and **AB-I** must be singular for there to be a nontrivial solution. **BA** is a combined operator equivalent to one coupling step. Eq. (23) and the proof therein shows that:

$$rank(\mathbf{B}) \geq rank(\mathbf{BA})$$

which means that if one of the coupled models is rank deficient (i.e. singular operator) then the coupled system is rank deficient (i.e. singular combined operator) which guarantees the availability of non-trivial solution.

3.1 Gradient-Based Multi-Physics Range Finding Algorithm

In section 1.5 the idea of minimizing the size of the subspace was discussed. Previous efforts demonstrated the use of the intersection subspace for serially coupled models [50]. However, in the case of closed-loop coupled models (Figure 21), the interface parameters (x and y) are updated at each coupling step making the parameters functions of each other:

$$y = f(x) \text{ and } x = g(y)$$

Therefore, the intersection subspace technique presented in Ref. [50] does not take this closed-loop coupling into account. Hence, in this section an iterative intersection subspace-

based algorithm is introduced to take into account the coupled nature of the models which better represents the actual multi-physics coupling required in nuclear reactor physics modeling and simulation. The algorithm may be broken up into three stages as follows (**GB-MPRFA**):

Stage 1: Gradient-free Reduction of Upstream Model's Outputs.

1. Create *k* random realizations of the model A's inputs, aggregated in a matrix:

$$\mathbf{X} = [\bar{x}^{(1)} \cdots \bar{x}^{(k)}]$$

where $x^{(i)}$ represents the i^{th} random sample of model A inputs, and execute model **A** *k* times.

2. Collect the corresponding outputs in a matrix $\mathbf{Y} = [\bar{y}^{(1)} \cdots \bar{y}^{(k)}]$.

3. Given a user-defined error tolerance for *y*, defined by ε_y, employ ERFA to determine the necessary size of the active subspace, defined by $r_{\mathbf{A},y}$ which upper-bounds the error such that: $\left\| \bar{y} - \tilde{\bar{y}} \right\|_2 \le \varepsilon_y$, where $\tilde{\bar{y}}$ is the output constrained to the active subspace.

4. Determine an orthonormal basis for the active subspace using the SVD decomposition:

$$\mathbf{Y} = \mathbf{U}_{\mathbf{A},y} \mathbf{S}_{\mathbf{A},y} \mathbf{V}_{\mathbf{A},y}^T$$

5. If the subspace is intended to be used for UQ analysis, then use the singular value decomposition of the *y* covariance matrix to find the DoF with highest component of the uncertainty in the *y*-space:

$$\mathbf{C}_y = \mathbf{U}_{\mathbf{C}_y} \mathbf{S}_{\mathbf{C}_y} \mathbf{U}_{\mathbf{C}_y}^T \tag{33}$$

where $\mathbf{U}_{\mathbf{C}_y} \in \mathbb{R}^{r_{\mathbf{C}_y}}$, $r_{\mathbf{C}_y}$ is the rank of the subspace or the proper number of DoF that carry most of the uncertainty components as determined by the RFA.

Stage 2. Gradient-Based Reduction of Downstream Model's Inputs.

6. To limit the number of model B adjoint calculations, define a pseudo response for model B, defined as a random linear combination of its outputs:

$$x_{pseudo} = \sum_i w_i x_i ,$$

where $\{w_i\}$ are randomly generated.

7. Employ the adjoint of model B to calculate the derivatives of the pseudo response with respect to model B's inputs. Repeat this process $r_{\mathbf{B},y}$ (the current estimate of the size of the active subspace of $\bar{x}$, can be initially any value *k*) times and aggregate the derivatives in a matrix:

$$\mathbf{D} = [\frac{\partial x_{pseudo}^{(1)}}{\partial \bar{y}}, \frac{\partial x_{pseudo}^{(2)}}{\partial \bar{y}}, \cdots, \frac{\partial x_{pseudo}^{(r_{B,i})}}{\partial \bar{y}}]$$

Stage 3. Intersection Subspace-based Reduction at the Model-to-Model Interface.

8. Calculate the intersection between $\mathbf{U}_{\mathbf{A},\mathbf{y}}$ and ($\mathbf{U}_{\mathbf{C}_y}$ if available) **D** subspaces by forming:

$$\mathbf{N} = \mathbf{U}_{\mathbf{A},y}\mathbf{U}^T{}_{\mathbf{A},y}\mathbf{D} \quad \text{or} \quad \mathbf{N} = \mathbf{U}_{\mathbf{C}_y}\mathbf{U}_{\mathbf{C}_y}^T\left(\mathbf{U}_{\mathbf{A},y}\mathbf{U}^T{}_{\mathbf{A},y}\mathbf{D}\right) \qquad (34)$$

9. Construct an orthonormal basis by performing SVD decomposition:

$$\mathbf{N} = \mathbf{U}\mathbf{S}\mathbf{V}^T ,$$

where the **U** matrix represents a basis for the intersection subspace at the first interface between the models in the direction A → B (i.e. *y*-space). And repeat steps 1 through 9 for the interface B → A (i.e. *x*- space).

For *M* coupled models, similar steps must be performed at each model to model interface. The more interfaces we have, the more physical constraints are applied on the reduced space.

The flow chart below (Figure 22) summarizes the steps listed above:

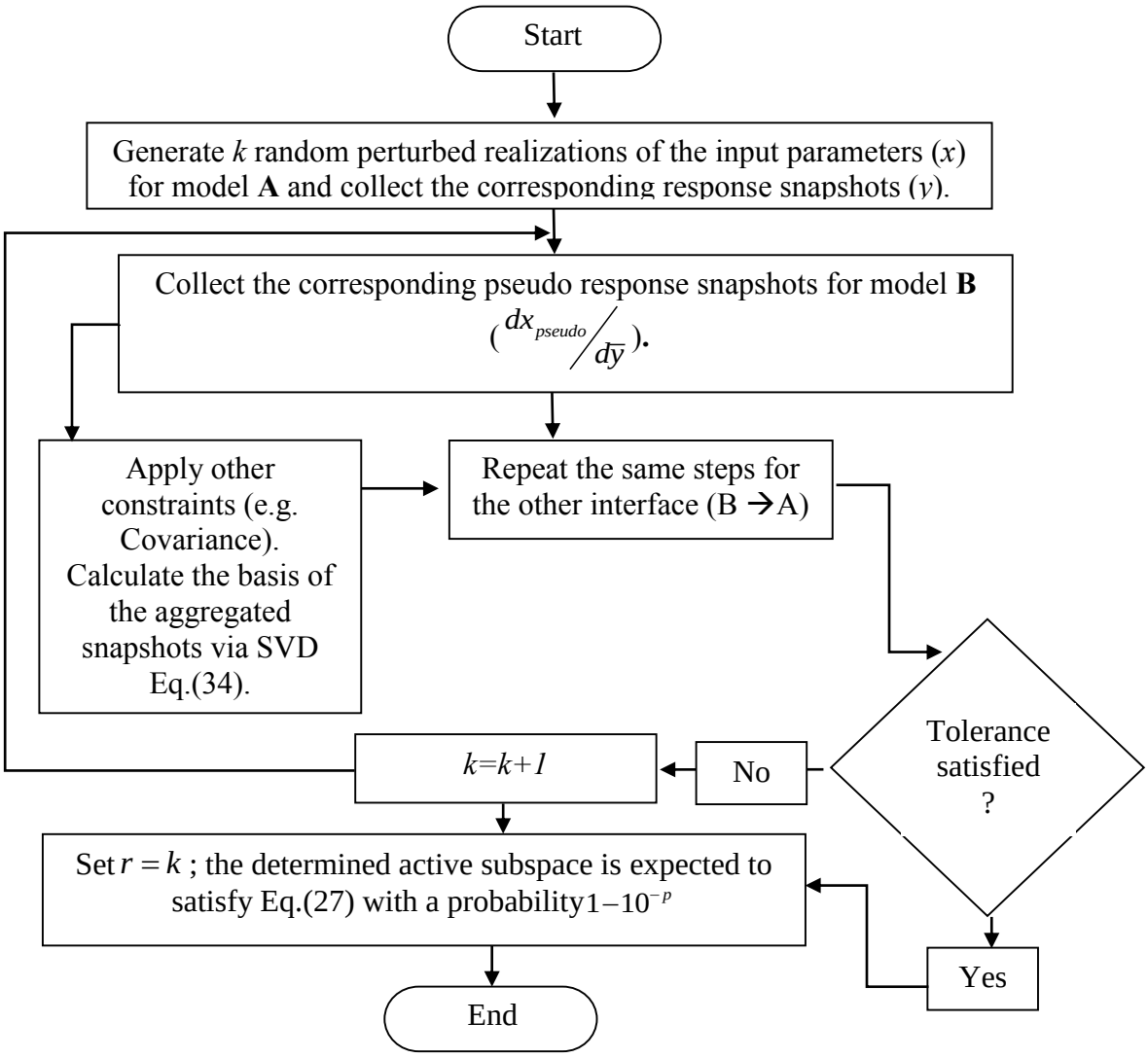

Figure 22 . GB-MPRFA flow diagram.

In order to prove the convergence of the algorithm presented above, assume that models A and B are loosely coupled. Assume that the model A can be linearized as follow:

$$\bar{y} = \mathbf{A}\bar{x} ,$$

while model B can also be linearized as follow:

$$\bar{x} = \mathbf{B}\bar{y}$$

Coupling the two models can be viewed as a linear process applied over and over on the vector $\bar{x}$:

$$\bar{y}^i = \mathbf{A}\bar{x}^i$$

$$\bar{x}^{i+1} = \mathbf{B}\bar{y}^i = \mathbf{BA}\bar{x}^i$$

$$\bar{y}^{i+1} = \mathbf{A}\bar{x}^{i+1} = \mathbf{ABA}x^i$$

The vector $\bar{y}^i$ is in the range of matrix **A** while $\bar{y}^{i+1}$ is in the range of matrix **ABA**:

$$\bar{y}^i \in R^{\bar{y}^i} = R(\mathbf{A})$$

$$\bar{y}^{i+1} \in R^{\bar{y}^{i+1}} = R(\mathbf{ABA})$$

For $\bar{b} \in R(\mathbf{AB}) \Rightarrow \exists\, \bar{x}$ such that $\bar{b} = \mathbf{AB}\bar{x} = \mathbf{A}(\mathbf{B}\bar{x})$, therefore, $\bar{b} \in \mathrm{R}(\mathbf{A})$. Hence:

$$R(\mathbf{AB}) \subseteq R(\mathbf{A})$$

hence;

$$R(\mathbf{ABA}) \subseteq R(\mathbf{A})$$

$$r_{\bar{y}}^{i+1} \leq r_{\bar{y}}^{i}$$

Hence, over the coupling process the rank of the interface spaces will either shrink or remain the same, therefore, for linear problems it is safe to say that the MPRFA converges.

One more point in the MPRFA that needs elaboration is stage number 2; that is to explain why does the sampling of a pseudo response capable of capturing the important DoFs with respect of each of the real-physical responses?

Consider the following example (Figure 23). Before determining the important DoFs in the $\bar{x}$-space with respect to the responses ($\bar{y}$), the MPRFA defines a pseudo response that is a random combination of all responses (components of the vector $\bar{y}$):

$$y_{pseudo} = \sum_{j}^{m} w_j y_j \tag{35}$$

where w_j are randomly generated factors. y_j is the j^{th} element of the response vector $\bar{y}$ and m is the dimension of the response vector $\bar{y}$. The goal is to calculate the sensitivity profile for the pseudo response:

$$\frac{\partial y_{pseudo}}{\partial \bar{x}}.$$

Considering Eq.(35), the derivative of the pseudo response can be expanded as follow:

$$\left(\frac{\partial y_{pseudo}}{\partial \bar{x}}\right)^i = w_1^i \frac{\partial y_1}{\partial \bar{x}} + \cdots + w_m^i \frac{\partial y_m}{\partial \bar{x}},$$

which can be written in a matrix – vector product form:

$$\left(\frac{\partial y_{pseudo}}{\partial \bar{x}}\right)^i = \left[\frac{\partial y_1}{\partial \bar{x}} | \cdots | \frac{\partial y_m}{\partial \bar{x}}\right] \bar{w}^i \quad \rightarrow \quad \bar{s}_{pseudo}^i = \mathbf{S}\bar{w}^i,$$

where $\bar{w}^i$ is a vector with the i^{th} samples of the factors. So if the pseudo response derivative is sampled at different points (to account for non-linearity effects) in the input parameter space ($\bar{x}$) then the resultant is a matrix of random samples of the pseudo response derivatives:

$$\left[\bar{s}_{pseudo}^1 | \cdots | \bar{s}_{pseudo}^i\right] = \mathbf{S}_{pseudo}$$

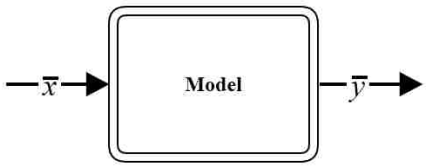

Figure 23. Illustration example.

So this process is a range finding process where the range of matrix $\mathbf{S}$ is approximated via the range of matrix $\mathbf{S}_{pseudo}$, that is the Range Finding Algorithm (RFA) approximates $R(\mathbf{S})$ using $R(\mathbf{S}_{pseudo})$. In other words if *i* is large enough, then y_{pseudo} samples have enough information about the original responses vector $\bar{y} = [y_1, \cdots, y_m]^T$ so that its features can be retrieved. Also, note that due to local linearity of each point in the input space, one can use only one sample of $\bar{s}^i_{pseudo}$ (i.e. sample of $\bar{w}^i$) per sampling point in the parameter space. Therefore, the range of $\mathbf{S}_{pseudo}$ (i.e. $R(\mathbf{S}_{pseudo})$) would represents the range of the variations of $\mathbf{S}$ (i.e. $R(\mathbf{S})$).

Ref. [73] represents an algorithm that can be used as an extension for the GB-MPRFA. The reference introduces a basis filtering algorithm that can filter the subspace basis from any DoFs that are unnecessary with respect to the application of interest.

3.1.1 Case Study: CASL Progression Problem 2 – lattice.

In this numerical test a quasi-static lattice physics depletion problem based on CASL progression problem number 2 is used to demonstrate the application of the proposed MPRFA. The model is composed of two physics models, a neutron transport calculations model to estimate the neutron flux distribution, and a depletion model to estimate the concentration and contents of various isotopes with time. The calculation of the reaction rates required for depletion calculations and the isotopic-dependent resonance treatment are assumed to be part of the depletion model; thus rendering the two interfaces to be the neutron flux and the macroscopic cross-sections. Many other choices for the interfaces variables could be

envisioned. We focus here on a single choice in support of this initial study. The neutron transport calculations are performed by the NEWT module which is a part of SCALE 6.1. The depletion calculations are performed using multiple modules, including BONAMI, NITAWL, MALOCS, WAX, COUPLE, ORIGEN, and OPUS [57]. Figure 24 illustrates the coupling between the two physics models. The following nuclei are considered in the depletion calculations: ${}^{234}_{92}\mathrm{U}$, ${}^{235}_{92}\mathrm{U}$, ${}^{236}_{92}\mathrm{U}$, ${}^{238}_{92}\mathrm{U}$, ${}^{237}_{93}\mathrm{Np}$, ${}^{238}_{94}\mathrm{Pu}$, ${}^{239}_{94}\mathrm{Pu}$, ${}^{240}_{94}\mathrm{Pu}$, ${}^{241}_{94}\mathrm{Pu}$ ${}^{242}_{94}\mathrm{Pu}$, ${}^{242}_{96}\mathrm{Cm}$, ${}^{241}_{95}\mathrm{Am}$, ${}^{242}_{95}\mathrm{Am}$, ${}^{243}_{95}\mathrm{Am}$, ${}^{16}_{8}\mathrm{O}$, ${}^{1}_{1}\mathrm{H}$, ${}^{16}_{8}\mathrm{O}$, and naturally occurring isotopes of Zr.

For the current example, the following cross sections were perturbed: fission spectrum (χ), fission (Σ_f), elastic scattering (Σ_s), and average total (prompt plus delayed) number of neutrons released per fission event ($\bar{\nu}$). A quarter PWR lattice is considered (see Figure 25) which includes 64 fuel pins. The dimension of the cross sections subspace is 239,360 (i.e. $\bar{\Sigma} \in \mathbb{R}^{239,360}$). The scalar flux lives in a space of dimensions 100,056 (i.e. $\bar{\phi} \in \mathbb{R}^{100,056}$).

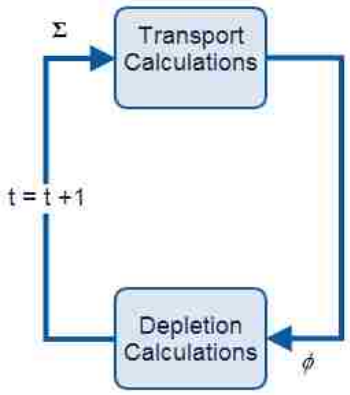

Figure 24. Transport model (Physics A) coupled with depletion model (Physics B).

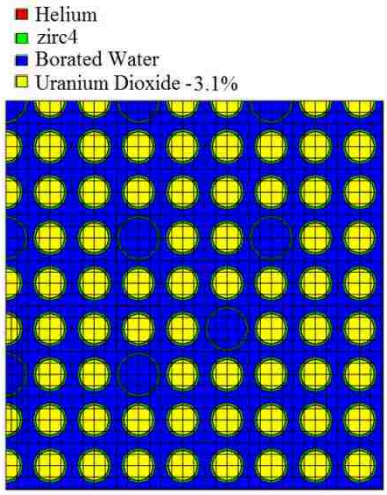

Figure 25. CASL Progression Problem number 2 – lattice.

In order to compare the MPRFA to the performance of the RFA (study each model separately without considering the coupling) the following two aspects will be highlighted. First, the size of the intersection subspace associated with the coupled physics model will be compared to the size of the subspace associated with a single physics model. Second, the intersection subspace will be used to calculate model responses for general cross-section perturbations. If the intersection subspace is not captured correctly, i.e., it is missing directions that are important to the coupled physics model, one would expect the response variations calculated using the reduced model to be in gross error (exceeding the user-defined error tolerance) when compared to the variations calculated using the exact model.

To investigate the first property, we employ the standard ERFA (refer to chapter 2) algorithm to calculate the size of the active subspaces for the flux and cross-sections as calculated independently by the two models, and compare their respective size against the intersection subspace calculated by the MPRFA algorithm, as shown in Figure 26 and Figure 27. Single-physics space is calculated using the ERFA (refer to chapter 2) while the multi-physics subspace is constructed using the GB-MPRFA proposed in this section. Results

suggest that greater reduction for the respective spaces can be achieved when codes are coupled. This is an attractive quality as it implies the computational cost per physics model can be significantly reduced when models are coupled, which represent the real scenario under which the models are utilized.

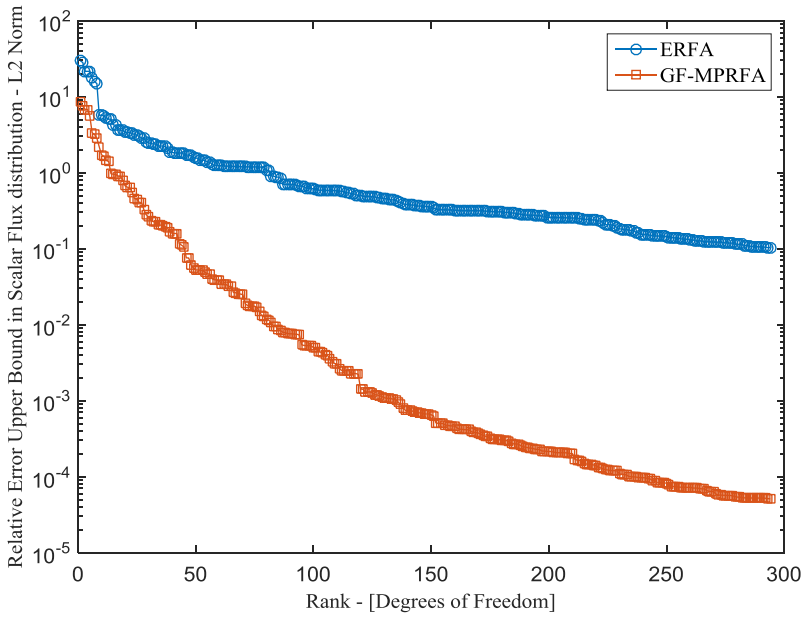

Figure 26. Single-Physics vs. Multi-Physics Active Subspace ($\bar{\phi}$).

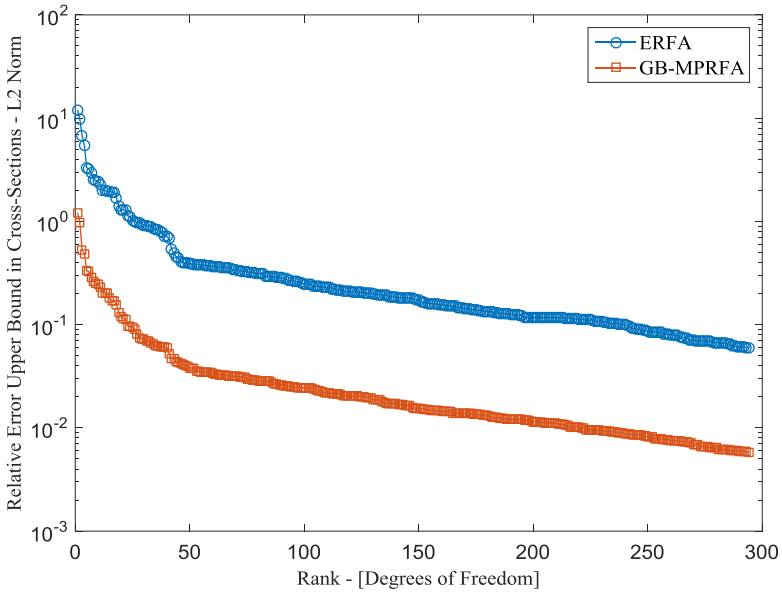

Figure 27. Cross section subspace as obtained from the single physics examination compared to the one obtained from the multi-physics examination ($\overline{\Sigma}$).

Regarding the adequacy of the intersection subspace, we compare the response variations as constrained to the single-physics-determined subspace (ERFA) and the MPRFA-determined subspace. Recall that the proposed approach assumes that variations that are deemed dominant by a single physics, but not by the other physics, will be dropped out during the iterative search for the solution because their effect is not significant from the coupling point of view. To test this assertion, we compare overall model variations for the neutron flux distribution (a function of energy and space) and eigenvalue (multiplication factor) for a given cross-section perturbation. The exact variation for both the flux and eigenvalue can be calculated by simply executing the forward model until convergence. Next, we project the cross-section perturbation along two subspaces (the subspace from the ERFA and the MPRFA subspace) and repeat the execution till tightly converged. The first subspace is determined by a single physics, expected to be bigger than the second subspace determined by the MPRFA algorithm. The

corresponding variations in the eigenvalue and the flux are compared with the exact variations. The initial cross-section are projected according to:

$$\bar{\Sigma}^{\|} = \mathbf{U}\mathbf{U}^{\mathbf{T}}\bar{\Sigma} \tag{36}$$

where $\mathbf{U}$ is the orthonormal matrix associated with the respective subspaces as calculated by the three stages of the GB-MPRFA algorithm.

Table 4 compares the change in the multiplication factor calculated using both approaches. First, k_{eff} for the original model is calculated (denoted as the full space model). Then, the subspace for the depletion cycle is calculated using both the standard **ERFA** and also using the proposed **GB-MPRFA**. Finally, we calculate the relative deviation from the reference solution for each method and compare. The overall effect of applying the **GB-MPRFA** is to render a greater reduction at the interfaces than can be done using the **ERFA**. Thus, when using the **ERFA** the Δk_{eff} are larger than those calculated using the **GB-MPRFA** (even if the **ERFA** is using r = 1000), implying that the values calculated using the **GB-MPRFA** is superior to the **ERFA**.

Table 4. Error in k_{eff} due to cross-section approximation using Eq.(36)

Depletion step GWD/MTU	Reference (Full Space)	Reduced Space (**GB-MPRFA**) r=100	Reduced space (**ERFA**) r=1000
-	k_{eff}	Δk_{eff} [pcm]	Δk_{eff} [pcm]
0	1.17320403	-37.31	-47.815
10.880	1.09931821	-97.234	-118.174
20.680	1.02163022	-71.299	-72.820
26.390	0.95841733	-41.231	-29.15

3.2 Gradient-Free Multi-Physics Range Finding Algorithm

Since many computational models are not equipped with sensitivity calculation capability, a Gradient-Free MPRFA (**GF-MPRFA**) will be introduced here to compensate for the gradient based step introduced in the MPRFA algorithm. The second stage in the MPRFA performs a gradient-based reduction of downstream model's inputs. This reduction is based on recognizing the DoF in the spaces of interest (e.g. *y*-space in Figure 21) that are important to the responses of the downstream physics which is obtained by sampling the derivative of a pseudo response of the downstream physics (e.g. model **B** in Figure 21); however, one can identify these degrees of freedom using a gradient-free approach. The logic is based on the linearity assumption, where the effect of model **B** can be approximated as follow:

$$\bar{x} = \mathbf{B}\bar{y}$$

If so, then the range finding algorithm (RFA) can be used to calculate the basis of the column and row spaces of matrix **B** as follow:

1. Sample the model's input ($\bar{y}$) – *k* samples;
2. Collect the corresponding response snapshots ($\mathbf{X}_{\text{model}} = \left[\bar{x}^1 \cdots \bar{x}^k \right]$);
3. Compute the SVD of the snapshots matrix ($\mathbf{X}_{\text{model}}^{nxk} = \mathbf{U}_x^{nxn}\mathbf{S}_x^{nxm}\mathbf{V}_x^{T,kxk}$) where the columns of matrix **U** form the orthonormal basis of the column space of matrix **B**. If this basis is calculated accurately using the RFA, then any snapshot in the *x*-space can be represented as follow:

$$\bar{x}^{n\text{x}1} = \mathbf{U}_x^{nxr_x}\bar{\alpha}_x^{n\text{x}1} \ . \tag{37}$$

So one can create extra snapshots of model's B response (i.e. $\bar{x}$) **<u>without the need to run</u>** model B.

4. Random snapshots of the reduced parameter $\bar{\alpha}_x^{nx1}$, which are used to create extra snapshots ($\mathbf{X}_{extra}$), can be sampled from a PDF determined by the previous step. Extra $(m-r_x)$ snapshots are required to complete the space:

$$\mathbf{X}_{extra} = \mathbf{U}_x^{nxr_x} \boldsymbol{\alpha}^{r_x x (m-r_x)} \tag{38}$$

where $\boldsymbol{\alpha}$ is the matrix of the reduced parameter snapshots. Now aggregating the two snapshot matrices one can have a full snapshots matrix that can be used to reveal the row space of matrix B without the need to access sensitivity information:

$$\mathbf{X} = \left[\mathbf{X}_{\text{model}}^{nxr_x} \mid \mathbf{X}_{\text{extra}}^{nx(m-r_x)} \right] = \mathbf{U}_x^{nxn} \mathbf{S}_x^{nxm} \mathbf{V}_x^{T,mxm} \quad . \tag{39}$$

The columns of matrix $\mathbf{V}_x$ form the orthonormal basis of the row space of matrix **B.** Matrix $\mathbf{U}_x$ is the orthonormal basis of the column space which is used later in the reduction of the other interface (*x*-space in Figure 21).

In general, if the linearity assumption is not accurate then matrix **B** must be sampled so that its variations are captured. In this case the computational cost of capturing the gradient-based subspace is proportional to $r_y.r_x$. Hence this method introduces computational savings whenever $r_y.r_x \ll \min\{n,m\}$ or whenever the sensitivity capability is not available (e.g. the adjoint model is not available) and $r_y.r_x \ll \min\{n\}$. However, if the linearity assumption is sufficient, then the methodology presented above is sufficient to substitute the gradient based step in the GB-MPRFA with a gradient free step. The following is a summary of a gradient free MPRFA (**GF-MPRFA**): Refer to Figure 28.

Stage 1: Gradient-free Reduction of Upstream Model's Outputs.

1. Create *k* random realizations of the model A's inputs, aggregated in a matrix:

$$\mathbf{X} = [\bar{x}^{(1)} \cdots \bar{x}^{(k)}]$$

where $x^{(i)}$ represents the i^{th} random sample of model A inputs, and execute model **A** *k* times.

2. Collect the corresponding outputs in a matrix $\mathbf{Y} = [\bar{y}^{(1)} \cdots \bar{y}^{(k)}]$.

3. Given a user-defined error tolerance for *y*, defined by ε_y, employ ERFA to determine the necessary size of the active subspace, defined by $r_{\mathbf{A},y}$ which upper-bounds the error such that: $\left\| \bar{y} - \bar{\tilde{y}} \right\|_2 \leq \varepsilon_y$, where $\bar{\tilde{y}}$ is the output constrained to the active subspace.

4. Determine an orthonormal basis for the active subspace using the SVD decomposition:

$$\mathbf{Y} = \mathbf{U}_{\mathbf{A},y} \mathbf{S}_{\mathbf{A},y} \mathbf{V}_{\mathbf{A},y}^T$$

5. If the subspace is intended to be used for UQ analysis, then use the singular value decomposition to find the DoF with highest component of the uncertainty in the *y*-space:

$$\mathbf{C}_y = \mathbf{U}_{\mathbf{C}_y} \mathbf{S}_{\mathbf{C}_y} \mathbf{U}_{\mathbf{C}_y}^T \tag{40}$$

where $\mathbf{U}_y \in \mathbb{R}^{r_{\mathbf{C}_y}}$, $r_{\mathbf{C}_y}$ is the rank of the subspace or the proper number of DoF that carry most of the uncertainty components as determined by the RFA.

Stage 2. Gradient-Free Reduction of Downstream Model's Inputs.

6. Create *k* random realizations of the model B's inputs, aggregated in a matrix:

$$\mathbf{Y} = [\bar{y}^{(1)} \cdots \bar{y}^{(k)}]$$

where $y^{(i)}$ represents the i^{th} random sample of model B inputs, and execute model B *k* times.

7. Collect the corresponding outputs in a matrix. $\mathbf{X}_{\text{model}} = [\bar{x}^{(1)} \cdots \bar{x}^{(k)}]$

8. Determine an orthonormal basis for the active subspace using the SVD decomposition:

$$\mathbf{X}_{\text{model}} = \mathbf{U}_{\mathbf{B},x}\mathbf{S}_{\mathbf{B},x}\mathbf{V}_{\mathbf{B},x}^{T}$$

9. Create extra snapshots using Eq. (38) and aggregate them with $\mathbf{X}_{\text{model}}$. Eq. (39) can be used to calculate the orthonormal basis of the row space of the matrix operator **B** denoted $\mathbf{V}_{\mathbf{B},x}$. If the linearity assumption is sufficient, then these columns represent a subspace that is equivalent to the one calculated by stage 2 in the **GB-MPRFA**.

Stage 3. Intersection Subspace-based Reduction at the Model-to-Model Interface.

10. Calculate the intersection between the subspaces represented by the basis $\mathbf{U}_{\mathbf{A},\mathbf{y}}$ and ($\mathbf{U}_{\mathbf{C}_y}$ if available) $\mathbf{V}_x$ subspaces by forming:

$$\mathbf{N} = \mathbf{U}_{\mathbf{A},y} \cap \mathbf{U}_{\mathbf{C}_y} \cap \mathbf{V}_x$$

11. Construct an orthonormal basis by perform SVD decomposition:

$$\mathbf{N} = \mathbf{U}\mathbf{S}\mathbf{V}^{T},$$

where the **U** matrix represents a basis for the intersection subspace at the first interface between the models in the direction A → B**.** And repeat steps 1 through 11 for the interface B → A (i.e. *x*- space).

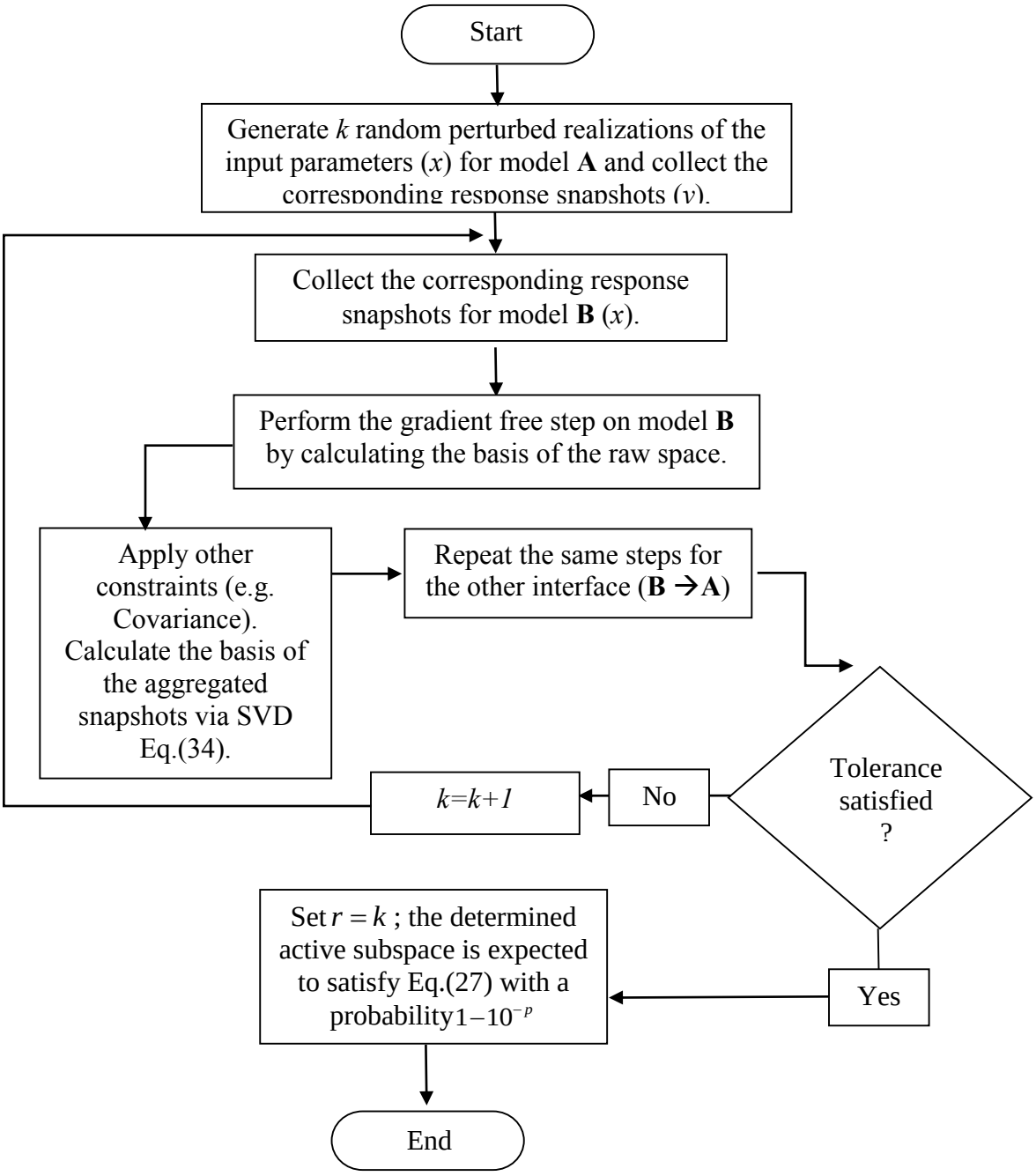

Figure 28.GF-MPRFA flow diagram.

3.2.1 Case Study: Gradient-Free vs. Gradient-Based.

A simple numerical test is used to demonstrate the **GF-MPRFA** algorithm application. CASL VERA progression problem number 1a is used in a fuel depletion calculation application to demonstrate a multi-physics coupled models application [74]. The problem represents a single two dimensional PWR pin cell eigenvalue problem (Figure 29). The problem's fuel represents the Westinghouse-type fuel. The fuel consists of uranium dioxide with helium gap, Zircaloy-4 cladding and water with soluble boron as moderator. The depletion problem is simulated using the TRITON sequence in SCALE6.1 package [57]. TRITON is the depletion sequence provided with SCALE6.1; the sequence's ultimate goal is to solve Eq.(10) to determine the time dependent isotopic content of reactor fuel. The sequence consists of two major solution steps, a transport solver (NEWT) and a set of modules to solve Eq.(10). In this numerical test the two major solution steps will be considered as two different coupled multi-physics models where the space of cross-sectional variation over the time steps is investigated via the two algorithms (GB-MPRFA and GF-MPRFA) separately. Figure 24 illustrates the coupled models with the interface parameters. In this numerical test, the nuclear data cross-sections ($\bar{\Sigma} \in \mathbb{R}^{21824}$) space is constructed using both the GB-MPRFA and the GF-MPRFA. A comparison between the two spaces is depicted via the error criteria defined by the following term:

$$\varepsilon_{upper} = 10\sqrt{\frac{2}{\pi}} \max_{j=1,\dots p} \left\| \left(\mathbf{I} - \mathbf{U}\mathbf{U}^T \right) \bar{\Sigma}^{(j)} \right\|_2 . \tag{41}$$

Figure 30 plots the error upper bound criteria (ε_{upper}). One can notice that both bases can approximate the variations of $\bar{\Sigma}$ equivalently, hence, the GF-MPRFA can replace the GB-MPRFA whenever the gradient capability is not available.

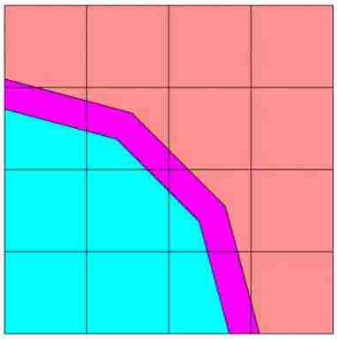

Figure 29. CASL VERA problem number 1 simulated using SCALE6.1.

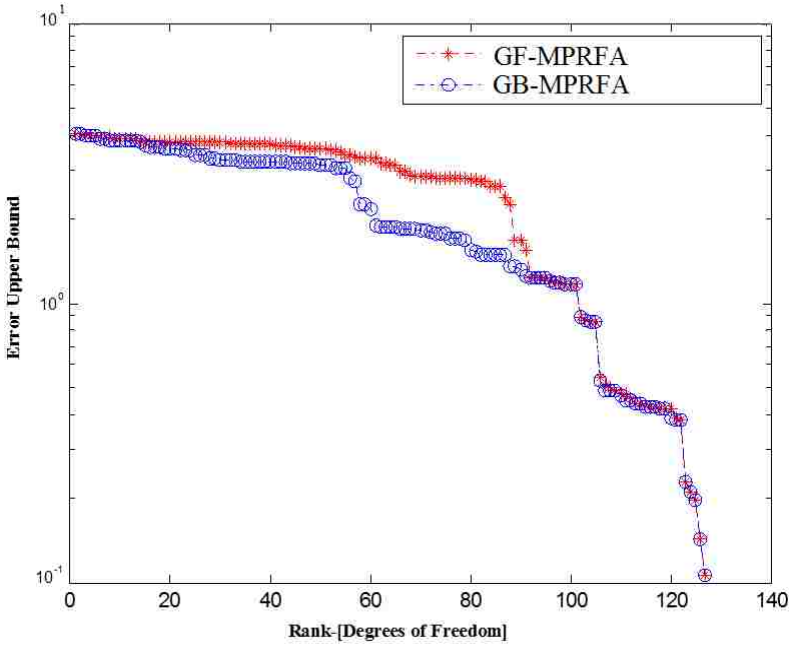

Figure 30. GB-MPRFA vs. GF-MPRFA

3.3 Case Study: 3-D Depletion Problem with Thermal-Hydraulics Feedback.

In this section the MPRFA will be used to apply dimensionality reduction on an example of a multi-physics coupled problem in three dimensional coordinates. The problem of interest is described in section 2.3, however, in this section the goal is different. While section 2.3

performed reduction at the response level (pin power distribution level), this section will seek reduction at the input parameter level (nuclear data cross-sections). The depletion problem has many parameters that can be considered as an input (e.g. nuclear data cross-sections, fission yields, thermal-hydraulics parameters … etc), however, since this dissertation is partially concerned about the uncertainty quantification for large scale problems, it is obvious that the nuclear data cross-sections and their dimensionality are a major challenge to be confronted by this dissertation. Hence, this section will utilize the GF-MPRFA to reduce the dimensionality of the nuclear data cross-sections space.

As described in section 2.3, VERA-CS is used to perform the fuel depletion with thermal –hydraulics feedback. The reader is referred to section 1.7 for more details on VERA-CS and its components.

Since VERA-CS does not have any adjoint based sensitivity analysis capability, our attention will be towards the Gradient-Free MPRFA (GF-MPRFA). Three responses of interest will be considered (multiplication factor, maximum pin power and maximum pin temperature) while the important DoFs of the nuclear cross-sections will be determined accordingly.

The **GF-MPRFA** requires two pieces of information: a covariance library for the measured nuclear data cross-sections ($\mathbf{C}_y$ in the **GF-MPRFA**) and snapshots of the interface parameters (i.e. neutron flux distribution, pin powers, pin temperatures, time-dependent isotopic number densities) which represent *x* and *y* **interfaces** in the **GF-MPRFA** (refer to section 3.2).

Running VERA-CS for depletion problems is computationally expansive (assembly and core wide levels), therefore, Figure 31 compares the performance of the GF-MPRFA along with that of the ERFA in terms of the relative error upper bound in retrieving the cross-section variation vectors:

$$\varepsilon_{upper} = 10\sqrt{\frac{2}{\pi}}\max_{j=1,\dots p}\left\|\frac{\Delta\bar{\Sigma}^{(j)}}{\bar{\Sigma}^{(ref)}}\right\|_2, \qquad \Delta\bar{\Sigma}^{(j)} = \left(\mathbf{I}-\mathbf{U}\mathbf{U}^T\right)\bar{\Sigma}^{(j)}.$$

Obviously, the **ERFA** offers a poor alternative to **GF-MPRFA**. For example at a rank (number of DoFs) of 30 the **ERFA** approximates the variations of the cross-section (over the fuel depletion process) with a relative error upper bound of 95.6% (a very bad approximation) while the **GF-MPRFA** does the approximation with a relative error upper bound of 0.038%. Depending on the subsequent application, one might choose the proper algorithm (i.e. **ERFA** vs. **GF-MPRFA**). In chapter 4 the GF-MPRFA will be used to perform efficient uncertainty quantification and surrogate construction.

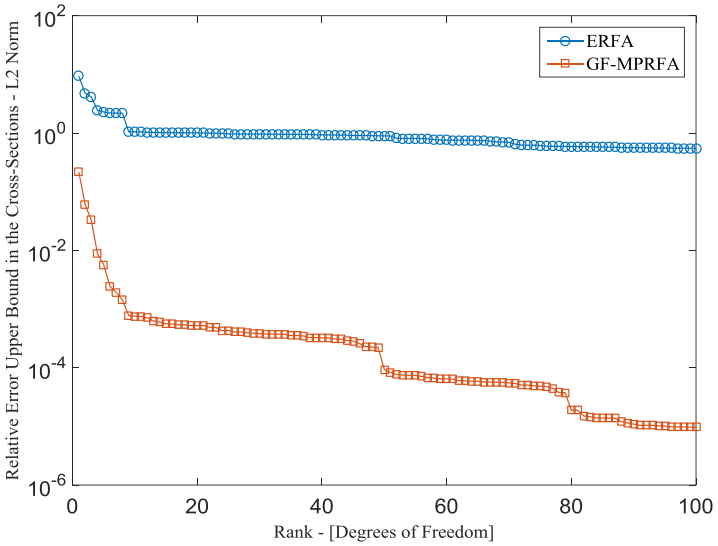

Figure 31. GF-MPRFA vs. ERFA.

CHAPTER 4. EFFICIENT MULTI-PHYSICS UNCERTAINTY QUANTIFICATION

In order to achieve high fidelity simulation, engineers have to precisely parameterize mathematical models in terms of all available parameters. For example, nuclear data cross-section libraries must be evaluated on finer energy intervals, wider range of isotopes and at different temperature values. However, this increases the dimensionality of the problem; therefore, the deterministic uncertainty quantification process become more computationally expensive. On the other hand, the increased complexity of the high fidelity nuclear reactor simulators results in computationally expensive models which hinders the application of Monte Carlo uncertainty quantification approaches.

In establishing the nuclear data-specific uncertainty libraries one can distinguish four different classes of fuel related isotopes [19]:

1. Major isotopes (i.e., ^{235}U, ^{238}U, and ^{239}Pu),
2. Other isotopes of Uranium and Plutonium,
3. Minor actinides up to ^{245}Cm (i.e., ^{237}Np, ^{241}Am, ^{242}Am, ^{243}Am, ^{242}Cm, ^{244}Cm and ^{245}Cm),
4. Higher mass minor actinides.
5. Fission Products, control and structural materials.

Except for the 4th group, the uncertainties in the other groups have been studied and reported in various libraries [13, 75, 76]. The fundamental issue when using a linear response model or building a surrogate model to reduce computer resources requirements comes from the high dimensionality of the input parameter space or more specifically, the uncertainty source space. In order to circumvent this issue, Reduced Order Modeling (ROM) techniques can be employed to reduce the required execution time [77, 4]. In order to perform

dimensionality reduction, a physics based approach can be utilized to identify the important dimensions (degrees of freedom) in the form of the basis of a lower dimensional subspace approximation (active subspace). An important uncertainty source is the one that has both high sensitivity and large uncertainty.

One final issue needs to be addressed: how can one get a physics-based active subspace efficiently? This question was not specifically addressed in previous efforts [4-77]. However, previous sections addressed this question for single physics problems and for multi-physics loosely coupled problems. Moreover, once the active subspace is generated, it can be used for many applications and problems that are within the range of its validity.

In this chapter, two approaches for multi-physics uncertainty propagation will be introduced, discussed and tested on both lattice physics and 3-dimensional reactor physics problems. The first approach is a linear approach that utilizes the obtained subspace along with a Karhunen-Loève (KL) expansion-based approach to quantify the uncertainty in attributes calculated by multi-physics coupled models. The second approach is a surrogate model based approach that replaces the original complex model with a simple surrogate form (e.g. polynomial, Gaussian process surrogate) and then quantifies the uncertainty via a Monte Carlo approach. The dimensionality reduction will be used to reduce the computational burden of evaluating the uncertainties whenever the uncertainty source space is high dimensional or there is no access to the sensitivity information and the model is characterized by high computational cost. Ref. [77] and Ref. [4] proposed the use of reduced dimensionality for efficient performance of uncertainty quantification; however, the work was limited to single physics applications while the current work extends the method to multi-physics coupled models.

Moreover the current work proposes a metric to measure the contribution of each source of uncertainty in the overall uncertainty in the RoI.

4.1 Efficient Uncertainty Quantification for Single Physics

Before getting into the multi-physics uncertainty quantification algorithm, it is useful to re-introduce the work presented in Ref. [4]. To start, consider the following model:

$$\bar{y} = f\left(\bar{x}\right),$$

If we assume that the model is linear, the uncertainty in the input parameter vector ($\bar{x}$) can be propagated towards the RoI vector ($\bar{y}$) using the sandwich equation as follow:

$$\mathbf{C}_y = \mathbf{S}_{yx}\mathbf{C}_x\mathbf{S}_{yx}^T \tag{42}$$

where $\mathbf{C}_x$ is the covariance matrix of the input parameter ($\bar{x}$) and $\mathbf{S}_{yx}$ represents the sensitivity profile of the RoI ($\bar{y}$) with respect to the input parameter ($\bar{x}$). However, taking into account that the covariance matrix $\mathbf{C}_x$ is symmetric then its singular value decomposition can be written as follow:

$$\mathbf{C}_x = \mathbf{U}_{\mathbf{C}_x}\boldsymbol{\Sigma}^2_{\mathbf{C}_x}\mathbf{U}^T_{\mathbf{C}_x}$$

where $\mathbf{U}_{\mathbf{C}_x}$ is the matrix of orthonormal basis of the space spanned by the columns of matrix $\mathbf{C}_x$ and $\boldsymbol{\Sigma}^2_{\mathbf{C}_x}$ is a diagonal matrix of the corresponding singular values denoting the variances. Hence, Eq.(42) can be rewritten as follow:

$$\mathbf{C}_y = \mathbf{S}_{yx}\mathbf{U}_{\mathbf{C}_x}\boldsymbol{\Sigma}^2_{\mathbf{C}_x}\mathbf{U}^T_{\mathbf{C}_x}\mathbf{S}^T_{yx}$$

$$= \mathbf{S}_{yx}\underbrace{\mathbf{U}_{\mathbf{C}_x}\boldsymbol{\Sigma}_{\mathbf{C}_x}}_{\mathbf{C}_x^{1/2}}\underbrace{\boldsymbol{\Sigma}_{\mathbf{C}_x}\mathbf{U}^T_{\mathbf{C}_x}}_{\mathbf{C}_x^{1/2,T}}\mathbf{S}^T_{yx}$$

$$= \mathbf{S}_{yx}\mathbf{C}_x^{1/2}\mathbf{C}_x^{1/2,T}\mathbf{S}_{yx}^T$$

Now if we assume that we have the basis of a lower dimensional subspace (**U**) that approximates the uncertainty space (i.e. the *x*-space), then Eq. (42) can be rewritten as follows:

$$\mathbf{C}_y = \mathbf{S}_{yx}\mathbf{C}_x^{1/2}\left(\mathbf{U}^{\|}\mathbf{U}^{\|,T} + \mathbf{U}^{\perp}\mathbf{U}^{\perp,T}\right)\mathbf{C}_x^{1/2,T}\mathbf{S}_{yx}^T \tag{43}$$

where $\left(\mathbf{U}^{\|}\mathbf{U}^{\|,T} + \mathbf{U}^{\perp}\mathbf{U}^{\perp,T}\right) = \mathbf{I}$ with $\mathbf{U}^{\|} \in \mathbb{R}^{n\times r}$ and $r \ll n$ if the components of *x* are highly correlated (e.g. the case with nuclear data cross-sections), where *n* is the full dimension of the input parameter space (uncertainty source space). The basis vectors represent the degrees of freedom (DoF) in the *x*-space that are characterized with high uncertainty and high sensitivity. From Eq. (43) the uncertainty in the attribute of interest can be segmented into two parts; the first part is coming from the active subspace and the minor (negligible) part is coming from the in-active (orthogonal subspace). If the active subspace is chosen correctly then the part coming from the orthogonal component will be negligibly small:

$$\mathbf{C}_y = \mathbf{S}_{yx}\mathbf{C}_x^{1/2}\mathbf{U}^{\|}\mathbf{U}^{\|,T}\mathbf{C}_x^{1/2,T}\mathbf{S}_{yx}^T + \mathbf{S}_{yx}\mathbf{C}_x^{1/2}\mathbf{U}^{\perp}\mathbf{U}^{\perp T}\mathbf{C}_x^{1/2,T}\mathbf{S}_{yx}^T$$

$$= \left(\mathbf{S}_{yx}\mathbf{C}_x^{1/2}\mathbf{U}^{\|}\right)\left(\mathbf{S}_{yx}\mathbf{C}_x^{1/2}\mathbf{U}^{\|}\right)^T + \left(\mathbf{S}_{yx}\mathbf{C}_x^{1/2}\mathbf{U}^{\perp}\right)\left(\mathbf{S}_{yx}\mathbf{C}_x^{1/2}\mathbf{U}^{\perp}\right)^T$$

From now on **U** will be used to denote $\mathbf{U}^{\|}$. If the lower dimensional subspace approximation is selected properly, then the uncertainty component associated with the orthogonal component will be negligibly small, and hence the uncertainty in the RoI (i.e. *y*) can be approximated as follow:

$$\mathbf{C}_y \simeq \left(\mathbf{S}_{yx}\mathbf{C}_x^{1/2}\mathbf{U}\right)\left(\mathbf{S}_{yx}\mathbf{C}_x^{1/2}\mathbf{U}\right)^T \tag{44}$$

This conclusion leads to the realization that the uncertainty can be evaluated via *r* models executions instead of *n* executions. Each model execution would quantify the uncertainty in

the RoI due to a certain basis vector (degree of freedom in the uncertainty sources space). Notice that the term $\left(\mathbf{S}_{yx}\mathbf{C}_x^{1/2}\mathbf{U}\right)$ can be written as:

$$\mathbf{S}_{yx}\mathbf{C}_x^{1/2}\mathbf{U}=\left[\mathbf{S}_{yx}\mathbf{C}_x^{1/2}\bar{u}^1\,|\cdots|\,\mathbf{S}_{yx}\mathbf{C}_x^{1/2}\bar{u}^r\right], \tag{45}$$

where $\bar{u}^i$ is the i^{th} column of the matrix **U**. On the other hand, the linearity assumption imposes the following:

$$\mathbf{S}_{yx}\mathbf{C}_x^{1/2}\bar{u}_i=\bar{y}\left(\bar{x}_0+\mathbf{C}_x^{1/2}\bar{u}_i\right)-\bar{y}\left(\bar{x}_0\right)=\Delta\bar{y}^i,$$

hence, the reduced uncertainty propagation Eq.(45) can be rewritten as:

$$\mathbf{C}_y\simeq\left[\Delta\bar{y}^1\cdots\Delta\bar{y}^r\right]\left[\Delta\bar{y}^1\cdots\Delta\bar{y}^r\right]^T=\mathbf{R}_y\mathbf{R}_y^T \tag{46}$$

Hence, this process can be viewed as a sort of Karhunen-Loève technique with the neglected component (DoFs) being selected based upon their contribution to the uncertainty and sensitivity. In addition, in **multi-physics** coupled models the important DoF must satisfy one more condition; taking into account the nature of the multi-physics coupled model, any selected DoF must have a **significantly possibility to appear in the interface space between the coupled models**. This down selection will be explained in more details in the following sub-section.

The error in this evaluation can be estimated as follow [4]:

$$\begin{aligned}
E_{C_y}&=\left\|\mathbf{C}_y-\left(\mathbf{S}_{yx}\mathbf{C}_x^{1/2}\mathbf{U}\right)\left(\mathbf{S}_{yx}\mathbf{C}_x^{1/2}\mathbf{U}\right)^T\right\|\\
&=\left\|\left(\mathbf{S}_{yx}\mathbf{C}_x^{1/2}\mathbf{U}^{\perp}\right)\left(\mathbf{S}_{yx}\mathbf{C}_x^{1/2}\mathbf{U}^{\perp}\right)^T\right\|\\
&=\left\|\mathbf{S}_{yx}\mathbf{C}_x^{1/2}\mathbf{U}^{\perp}\mathbf{U}^{\perp T}\mathbf{C}_x^{1/2,T}\mathbf{S}_{yx}^T\right\|\\
&=\left\|\mathbf{S}_{yx}\mathbf{C}_x^{1/2}\left(\mathbf{I}-\mathbf{U}\mathbf{U}^T\right)\mathbf{C}_x^{1/2,T}\mathbf{S}_{yx}^T\right\|.
\end{aligned}$$

The Range Finding Algorithm (RFA) can be used to estimate an error upper bound in the L2-norm of the above error term [29, 30, 34]. This process has two major advantages: **first**, it does not require the accessibility to sensitivity profiles; **second,** it requires only *r* model's execution instead of *n*, where $r \ll n$.

4.2 Efficient Sensitivity Analysis

This dissertation introduces a technique, assuming a linear model, to estimate the individual uncertainty contribution in the overall uncertainty of the RoI using the same snapshots used for the uncertainty quantification process described above. In order to see how this is possible, let's examine Eq.(45) again:

$$\mathbf{S}_{yx}\mathbf{C}_x^{1/2}\mathbf{U} = \left[\mathbf{S}_{yx}\mathbf{C}_x^{1/2}\bar{u}_1 \,|\cdots|\, \mathbf{S}_{yx}\mathbf{C}_x^{1/2}\bar{u}_r\right] = \mathbf{S}_{yx}\left[\mathbf{C}_x^{1/2}\bar{u}_1 \,|\cdots|\, \mathbf{C}_x^{1/2}\bar{u}_r\right] = \mathbf{S}_{yx}\left[\bar{\omega}_1 \,|\cdots|\, \bar{\omega}_r\right]$$

where $\bar{\omega}_i = \mathbf{C}_x^{1/2}\bar{u}_i$. One can think of the vector $\bar{\omega}_i$ as a vector of weights that gives every element a certain contribution in the overall uncertainty. Following this logic one can formulate the following linear system of equations that can be solved to obtain a reduced order estimate of the sensitivity coefficients:

$$\mathbf{R}^T = \mathbf{W}^T\mathbf{S}_{yx}^T, \tag{47}$$

where $\mathbf{W} = \left[\bar{\omega}_1 \,|\cdots|\, \bar{\omega}_r\right]$**.** If we are looking at the uncertainty in a single RoI ($\bar{y}$), then $\mathbf{Y}^T$ and $\mathbf{S}_{yx}^T$ will be vectors instead of matrices. The main issue now is that Eq.(47) represents an underdetermined system, which means that it has infinitely many solutions (if any!). Fortunately, we can construct a full rank system of equations that has a unique solution. In order to do so we have to realize that once we have the active subspace basis (**U**) one can write any input snapshots as a linear combination of the basis vectors:

$$\bar{x}^{nx1} = \sum_{i=1}^{m} \alpha_i \bar{u}_i \approx \sum_{i=1}^{r} \alpha_i \bar{u}_i = \mathbf{U}^{nxr} \bar{\alpha}^{rx1} \tag{48}$$

Now the response variation ($\Delta\bar{y}_i$) can be written in terms of the derivatives of the RoI with respect to the reduced input variable ($\bar{\alpha}^{rx1}$):

$$\Delta\bar{y}^i = \frac{\partial\bar{y}}{\partial\alpha_1}.\Delta\alpha_1^i + \cdots + \frac{\partial\bar{y}}{\partial\alpha_r}.\Delta\alpha_r^i = \mathbf{S}_{y/\alpha}.\Delta\bar{\alpha}^i \,,$$

hence, the variations matrix ($\mathbf{Y}$) can be used to formulate *r* linear equations with *r* unknowns (the sensitivity coefficients $\mathbf{S}_{y_i\alpha}$) where $\mathbf{S}_{y_i\alpha}$ is a vector if the problem has only one RoI. Therefore, the matrix system of equations can be written as follow:

$$\mathbf{R}^T = \mathbf{A}\mathbf{S}_{y\alpha} \,, \tag{49}$$

where,

$$\mathbf{A} = \left[\Delta\bar{\alpha}^1 \cdots \Delta\bar{\alpha}^r \right]^T .$$

The vector $\Delta\bar{\alpha}^i$ can be calculated using Eq. (48):

$$\Delta\bar{\alpha}^i \simeq \mathbf{U}^T \Delta\bar{x}^i = \mathbf{U}^T \mathbf{C}_x^{1/2} u_i \,.$$

Once the system in Eq.(49) is solved for $\mathbf{S}_{y\alpha}$, the reduced order sensitivities $\mathbf{S}_{yx}$ can be estimated using the chain rule and Eq.(48):

$$\mathbf{S}_{yx} = \mathbf{S}_{y\alpha}.\mathbf{S}_{\alpha x} = \mathbf{S}_{y\alpha}.\mathbf{U}^T \,. \tag{50}$$

Once we have a reduced order estimate of the sensitivity profile, the sandwich equation can be used to calculate an estimate of the uncertainty contribution for each source in the input space.

4.3 Efficient Uncertainty Quantification for Multi-Physics Coupled Models

For multi-physics coupled models, consider Figure 21, where the interface between the models has two distinct types of parameters: the dependent parameters ($\bar{x}$ and $\bar{y}$) which are dependent on each other (i.e. $\bar{y}$ is a response of model A and $\bar{\bar{x}}$ is a response of model B) and on the other hand, independent parameters such as $\bar{z}$ which are necessary for model B but their values are not affected by any of the two models. In order to quantify the uncertainty at the interfaces between the coupled models a two steps algorithm will be adapted. The assumption in this section is that the parameters $\bar{x}$ and $\bar{y}$ are high dimensional parameters while the independent parameter $\bar{z}$ is low dimensional (i.e. the corresponding uncertainty can be quantified using the Monte Carlo based uncertainty quantification).

First, the uncertainties due to the high dimensional parameter $\bar{x}$ will be propagated at all coupling steps (i.e. time steps). Consider that the $\mathbf{C}_x^0$ is the initial (0^{th} coupling step) covariance matrix for the *x* parameter. These covariance data are the initial covariance library that is associated with the experimental values of parameter $\bar{x}$ (e.g. uncertainties in the evaluated nuclear data libraries such as ENDF libraries). So the uncertainty in *y* parameter can be expressed, assuming a linear model, via the sandwich equation as follow:

$$\mathbf{C}_y^0 = \mathbf{S}_{yx}^0 \mathbf{C}_x^0 \mathbf{S}_{yx}^{0,T}$$

Hence, for the 1^{st} coupling steps (i.e. time step):

$$\mathbf{C}_x^1 = \mathbf{S}_{xy}^0 \mathbf{C}_y^0 \mathbf{S}_{xy}^{0,T} = \mathbf{S}_{xy}^0 \mathbf{S}_{yx}^0 \mathbf{C}_x^0 \mathbf{S}_{yx}^{0,T} \mathbf{S}_{xy}^{0,T} \tag{51}$$

As explained before, Eq.(51) can be re-written in terms of the singular value decomposition (SVD) of the covariance matrix $\mathbf{C}_x^0 = \mathbf{U}_{\mathbf{C}_x^0} \boldsymbol{\Sigma}_{\mathbf{C}_x^0}^2 \mathbf{U}_{\mathbf{C}_x^0}^T$:

$$\mathbf{C}_x^1 = \mathbf{S}_{xy}^0 \mathbf{S}_{yx}^0 \overbrace{\mathbf{U}_{\mathbf{C}_x} \mathbf{\Sigma}_{\mathbf{C}_x}}^{\mathbf{C}_x^{0,1/2}} \overbrace{\mathbf{\Sigma}_{\mathbf{C}_x} \mathbf{U}_{\mathbf{C}_x}^T}^{\mathbf{C}_x^{0,1/2,T}} \mathbf{S}_{yx}^{0,T} \mathbf{S}_{xy}^{0,T} = \mathbf{S}_{xy}^0 \mathbf{S}_{yx}^0 \mathbf{C}_x^{0,1/2} \mathbf{C}_x^{0,1/2,T} \mathbf{S}_{yx}^{0,T} \mathbf{S}_{xy}^{0,T} \quad (52)$$

Let $\mathbf{U}_x$ denote the matrix with its columns forming the basis vectors representing the lower dimensional subspace approximation of the *x*-space as determined by the ERFA or and MPRFA. If the columns of $\mathbf{U}_x$ are orthonormal then, $\mathbf{U}_x^{\|} \mathbf{U}_x^{\|,T} + \mathbf{U}_x^{\perp} \mathbf{U}_x^{\perp,T} = \mathbf{I}$, where $\mathbf{I}$ is the identity matrix. Eq. (52) can be re-written as:

$$\mathbf{C}_x^1 = \mathbf{S}_{xy}^0 \mathbf{S}_{yx}^0 \mathbf{C}_x^{0,1/2} \left(\mathbf{U}_x^{\|} \mathbf{U}_x^{\|,T} + \mathbf{U}_x^{\perp} \mathbf{U}_x^{\perp,T} \right) \mathbf{C}_x^{0,1/2,T} \mathbf{S}_{yx}^{0,T} \mathbf{S}_{xy}^{0,T} .$$

$$\mathbf{C}_x^1 = \left(\mathbf{S}_{xy}^0 \mathbf{S}_{yx}^0 \mathbf{C}_x^{0,1/2} \mathbf{U}_x^{\|} \mathbf{U}_x^{\|,T} \mathbf{C}_x^{0,1/2,T} \mathbf{S}_{yx}^{0,T} \mathbf{S}_{xy}^{0,T} \right) + \left(\mathbf{S}_{xy}^0 \mathbf{S}_{yx}^0 \mathbf{C}_x^{0,1/2} \mathbf{U}_x^{\perp} \mathbf{U}_x^{\perp,T} \mathbf{C}_x^{0,1/2,T} \mathbf{S}_{yx}^{0,T} \mathbf{S}_{xy}^{0,T} \right). \quad (53)$$

So if the orthogonal component can be ignored, then Eq. (53) can be approximated as:

$$\mathbf{C}_x^1 \simeq \left(\mathbf{S}_{xy}^0 \mathbf{S}_{yx}^0 \mathbf{C}_x^{0,1/2} \mathbf{U}_x^{\|} \mathbf{U}_x^{\|,T} \mathbf{C}_x^{0,1/2,T} \mathbf{S}_{yx}^{0,T} \mathbf{S}_{xy}^{0,T} \right) = \left(\mathbf{S}_{xy}^0 \mathbf{S}_{yx}^0 \mathbf{C}_x^{0,1/2} \mathbf{U}_x^{\|} \right) \left(\mathbf{S}_{xy}^0 \mathbf{S}_{yx}^0 \mathbf{C}_x^{0,1/2} \mathbf{U}_x^{\|} \right)^T$$

$$= \left(\mathbf{S}_{xy}^0 \mathbf{R}_y^0 \right) \left(\mathbf{S}_{xy}^0 \mathbf{R}_y^0 \right)^T = \left(\Delta \mathbf{R}_x^0 \right) \left(\Delta \mathbf{R}_x^0 \right)^T .$$

Hence, for the i^{th} coupling step, the updated covariance matrices ($\mathbf{C}_x^i$ and $\mathbf{C}_y^i$):

$$\mathbf{C}_x^i = \left(\Delta \mathbf{R}_x^{i-1} \right) \left(\Delta \mathbf{R}_x^{i-1} \right)^T$$

$$\mathbf{C}_y^i = \left(\Delta \mathbf{R}_y^i \right) \left(\Delta \mathbf{R}_y^i \right)^T$$

Important note: in the multi-physics application of efficient uncertainty quantification the rank *r* is the minimum rank of the interface spaces (*x*- and *y*- spaces); therefore, the basis vectors used must correspond to the space with the minimum rank. In the analysis before we assumed that the rank of the *x*-space is the minimum rank and that the covariance data in the *x*-space are known a priori. However, if the rank of the *y*-space is the minimum rank, then the

covariance in the *y*-space must be determined first by propagating the uncertainties from the *x*-space towards the *y*-space.

Based on the analysis introduced above and on details in Ref. [4] and for any number of multi-physics coupled models (refer to Figure 21), the Multi-Physics Efficient Uncertainty Quantification algorithm can be summarized as follow (**MP-EUQ**):

A- Use a Monte Carlo based approach to quantify uncertainty due to the independent parameters $\bar{z}$ (i.e. $\mathbf{C}^{i}_{\bar{z}\to\bar{x}}$) for all time steps (assuming that $\bar{y}$ is independent of $\bar{z}$).

B- Use the MPRFA to find the basis of a lower dimensional subspace approximation (active subspace) for the interface parameters i.e. *x* and *y* spaces (**U**).

1- Starting with the *x*-space, Eq. (46) can be used to propagate the uncertainties into the *y*-space.

$$\mathbf{C}^{i}_{y} \simeq \left[\Delta\bar{y}^{1,i}\cdots\Delta\bar{y}^{r,i}\right]\left[\Delta\bar{y}^{1,i}\cdots\Delta\bar{y}^{r,i}\right]^{T} = \mathbf{R}^{i}_{y}\mathbf{R}^{i,T}_{y} \tag{54}$$

2- Calculate the contribution of each uncertainty source using the reduced order sensitivity estimate given by using Eq.(49) and Eq.(50).

3- Then using the same logic in Eq.(46), the uncertainties in the *y*-space ($\mathbf{C}_{y}$) can be propagated towards the *x*-space.

$$\mathbf{C}^{i}_{x} \simeq \left[\Delta\bar{x}^{1,i-1}\cdots\Delta\bar{x}^{r,i-1}\right]\left[\Delta\bar{x}^{1,i-1}\cdots\Delta\bar{x}^{r,i-1}\right]^{T} = \mathbf{R}^{i-1}_{x}\mathbf{R}^{i-1,T}_{x} \tag{55}$$

$$\mathbf{C}^{i}_{\bar{x}} = \mathbf{C}^{i}_{\bar{x}} + \mathbf{C}^{i}_{\bar{z}\to\bar{x}} \tag{56}$$

4- Calculate the contribution of each uncertainty source using the reduced order sensitivity estimate given by Eq. (49) and Eq.(50).

5- Repeat steps 1 through 3 for each coupling step.

The second approach is based on replacing the original model with a surrogate model. For example Eq.(7) is a possible form of a surrogate model that can replace the original model. Therefore, Monte Carlo based uncertainty quantification can be easily applied on the surrogate model by collecting samples of the responses of interest (refer to Ref. [4, 35]).

The following steps represent the **S**urrogate **B**ased **U**ncertainty **Q**uantification (**SBUQ**):

1- Run the model to collect a training set of the response of interest (Δy) and the corresponding input snapshots (Δx) where the input snapshots are generated within the range of the covariance matrix i.e. $\Delta\bar{x} = \mathbf{C}_x^{1/2}\bar{\xi}$ and $\bar{\xi}$ is a random vector.

2- Calculate the coefficients of the reduced order surrogate model via curve fitting (regression analysis). Once the model form and coefficients are determined, calculate the error introduced by the following surrogate form:

$$\Delta y^{surr} = \bar{S}_1^T \overbrace{\mathbf{C}_x^{1/2}\mathbf{U}\mathbf{U}^T\bar{\xi}}^{\Delta\bar{x}} + \left(\bar{S}_2^T \overbrace{\mathbf{C}_x^{1/2}\mathbf{U}\mathbf{U}^T\bar{\xi}}^{\Delta\bar{x}}\right)^2 = \bar{S}_{1,r}^T\Delta\bar{\alpha} + \left(\bar{S}_{2,r}^T\Delta\bar{\alpha}\right)^2 \tag{57}$$

where $\mathbf{U} \in \mathbb{R}^{nxr}$ and $\Delta\bar{\alpha} = \mathbf{U}^T\bar{\xi} \in \mathbb{R}^r$ then $\bar{S}_{1,r}^T = \bar{S}_1^T\mathbf{C}_x^{1/2}\mathbf{U} \in \mathbb{R}^r$ and $\bar{S}_{2,r}^T = \bar{S}_2^T\mathbf{C}_x^{1/2}\mathbf{U} \in \mathbb{R}^r$.

3- Determine the residuals ($\varepsilon_{\Delta y}$) distribution (e.g. normal , independent and identically distribution)

$$\varepsilon_{\Delta y} = \Delta y - \Delta y^{surr}$$

4- Use the surrogate model to collect Monte Carlo based samples of the response of interest. And determine the statistical features of the samples so that the variance and mean are determined.

4.4 Case Study: Lattice Assembly Depletion (CASL Progression Problem 2)

In this section, a simple numerical test is used to demonstrate the **MP-EUQ** algorithm application. CASL VERA progression problem number 2 (refer to Figure 81) is used in a fuel depletion calculation application to demonstrate multi-physics coupled models application. The problem is a single Westinghouse 17x17 fuel lattice. The depletion problem is simulated using the TRITON sequence in the SCALE6.1 package [57]. Figure 24 illustrates the coupled models with the interface parameters. In this numerical test, the uncertainties in the nuclear data cross-sections ($\bar{\Sigma}$) will be propagated through the coupled models via the **MP-EUQ**. First the active subspace of the nuclear data-cross section space ($\bar{\Sigma} \in \mathbb{R}^{21824}$) is identified using the **GB-MPRFA** and then the **MP-EUQ** is used to propagate the uncertainties throughout the depletion sequence to determine the uncertainty in the multiplication factor (k_{eff}) and the one-group neutron flux in the fuel integrated over the fuel region (ϕ_{fuel}) at the End of Cycle (EoC). Figure 32 shows the error upper bound associated with approximating the full dimensional space with a lower dimensional space with different ranks (Eq.(58)):

$$\varepsilon_{upper} = 10\sqrt{\frac{2}{\pi}} \max_{i=1,\cdots p} \left\| \left(\mathbf{I} - \mathbf{U}\mathbf{U}^T \right) \bar{\Sigma}^i \right\| \tag{58}$$

Different subspace ranks are used to propagate the uncertainties and then compared to the uncertainty estimated using the sandwich equation (Table 5).

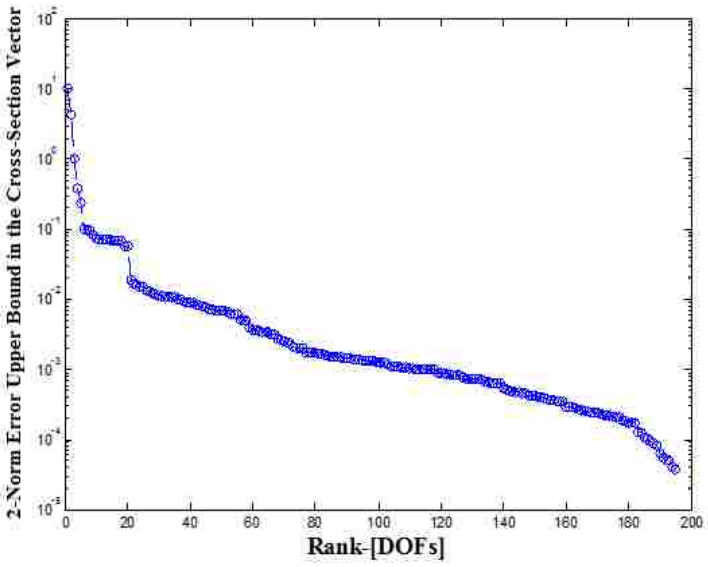

Figure 32. The error upper bound in the 2-norm of the cross-section vector due to representing the lower dimensional subspace approximation of the cross-sections space.

Table 5. Uncertainty propagation via the **MP-EUQ**.

Response	Reference Value (EoC)	Sandwich Equation	MP-EUQ $r = 10$	MP-EUQ $r = 100$	MP-EUQ $r = 190$
k_{eff}	0.95661125	691 pcm	381pcm	602 pcm	669 pcm
ϕ_{fuel}	3.16896E-03	1.0891%	0.5321%	0.8043%	0.9908%

4.5 Case Study: Efficient Uncertainty Quantification for 3-D Assembly Depletion with Thermal-Hydraulics Feedback

The current application deals with an example of depletion calculations with thermal-hydraulics feedback. Figure 6 shows an illustration of the depletion calculations with thermal-hydraulics feedback using VERA-CS [92]. This application will consider the major sources of uncertainty such as: nuclear data cross-sections, thermal conductivity, gap heat conduction. However, due to the huge dimensionality of the nuclear data cross-sections, the **MP-EUQ** will be used to propagate the uncertainties. This approach requires running the model a number of times that is proportional to the dimension of the lower dimensional subspace approximation

(i.e. active subspace) of input parameter space (i.e. nuclear data cross-sections space). This approximation is based on capturing the DoF that have large uncertainty components and large sensitivity components. Moreover, since this is a multi-physics coupled application; there is a certain set of DoF that can appear at the interface between the two models. These DoF can be captured using the Multi-Physics Range Finding Algorithm (**MPRFA**) outlined in Ref. [5] and chapter 3. However, since VERA-CS has no sensitivity calculation capability, the **GF-MPRFA** which was introduced in chapter 3 will be used in this chapter.

Before introducing the details of the application-specific **GF-MPRFA**, let us re-examine Figure 6 and briefly discuss the interface subspaces and their physical interpretation. From Figure 6 one can notice that there are 7 interface parameter spaces which are explained as follow:

a: heat generation spatial distribution.

b: average fuel temperature (T_f), average coolant temperature surrounding the rod (T_c), and average coolant density surrounding the rod (ρ) spatial distribution.

Z: independent thermal-hydraulics parameters.

L: one-group neutron flux distribution and one-group microscopic cross-sections.

Y: ORIGEN's independent parameters (fission product yields and half-lives).

d: isotopic number densities.

X: many group cross-sections.

Assuming that the main source of uncertainty is the **X**-space then first, the important DoF in the **X**-space must be determined. These DoF must satisfy three conditions: first, being possibly generated by ORIGEN; second, has large uncertainty component along them; and third, being effective from MPACT point of view (i.e. large sensitivity component along these

DoF). The VERA-CS depletion sequence first assumes a constant flux which is corrected by the predictor-corrector and sub-step methods. The predictor-corrector method calculates the depletion of the fuel at a time step (t_i) using the 1-group flux and cross-sections at the previous time step (t_{i-1}), which produces a new predicted 1-group flux, cross-sections, and isotopic concentrations using the predicted concentration at t_i, and then averages the two. Once the isotopic concentrations are obtained, a transport calculation is performed to obtain the steady state flux at t_i. The sub-step method is applied to perform multiple depletion calculations between transport calculations.

The **d**-space (which is considered to be the major source of uncertainty in all other spaces) is a high dimensional space, hence a reduction in that space will result in more efficient uncertainty propagation.

In this application we have three distinct sources of uncertainty:

1- **Z:** independent thermal-hydraulics parameters,

2- **Y:** ORIGEN's independent parameters (fission product yields and half-lives),

3- **X:** many group microscopic cross-sections.

The **Z** and **Y** spaces are expected to be low dimensional, hence the associated uncertainty can be propagated efficiently via a Monte Carlo based approach. However, the **X** space is high dimensional, therefore, the **GF-MPRFA** will be applied first to reduce its dimensionality before the propagation of its uncertainty throughout the coupled system.

One important note should be highlighted: the combination of the **d**-space and the **X**-space is the microscopic cross-sections space (Σ -space).

Now let us consider the following application-specific steps of the **GF-MPRFA**:

Stage 1: Gradient-free Reduction of Upstream Model's Outputs.

1. Create *k* random realizations of cross-sections (**X**-space) inputs aggregated in a matrix (the I and Y parameters):

$$\mathbf{X} = [\bar{x}^{(1)} \cdots \bar{x}^{(k)}]$$

where $\bar{x}^{(i)}$ represents the i^{th} random sample of the cross-section vector.

2. Collect the corresponding ORIGEN's responses in a matrix. $\mathbf{d} = [\bar{d}^{(1)} \cdots \bar{d}^{(k)}]$ and the corresponding macroscopic cross-section values $\mathbf{\Sigma} = [\bar{\Sigma}^{(1)} \cdots \bar{\Sigma}^{(k)}]$ use the RFA to construct orthonormal basis for the active subspace using the singular value decomposition (SVD):

$$\mathbf{\Sigma} = \mathbf{U}_{\bar{\Sigma}} \mathbf{S}_{\bar{\Sigma}} \mathbf{V}_{\bar{\Sigma}}^{T}$$

where $\mathbf{U}_{\bar{\Sigma}} \in \mathbb{R}^{r_{\bar{\Sigma}}}$, and $r_{\bar{\Sigma}}$ is the rank of the subspace or the proper number of DoF that approximate the variations generated by ORIGEN as determined by the RFA.

3. Using the singular value decomposition find the DoF with highest component of the uncertainty in the **X**-space.

$$\mathbf{C}_{\mathbf{X}} = \mathbf{U}_{\mathbf{C}_{\mathbf{X}}} \mathbf{S}_{\mathbf{C}_{\mathbf{X}}} \mathbf{U}_{\mathbf{C}_{\mathbf{X}}}^{T} \tag{59}$$

where $\mathbf{U}_{\mathbf{C}_{\mathbf{X}}} \in \mathbb{R}^{r_{\mathbf{C}_{\mathbf{X}}}}$, $r_{\mathbf{C}_{\mathbf{X}}}$ is the rank of the subspace or the proper number of DoF that carry most of the uncertainty components as determined by the RFA. $\mathbf{C}_{\mathbf{X}}$ is the covariance matrix of the **d**-space parameters.

Stage 2. Gradient-Free Reduction of Downstream Model's Inputs.

4. Collect the corresponding MPACT - COBRA-TF responses in a matrix. $\mathbf{L} = [\bar{L}^{(1)} \cdots \bar{L}^{(k)}]$ and use the RFA to construct orthonormal basis for the active subspace using the singular value decomposition (SVD):

$$\mathbf{L} = \mathbf{U}_{\bar{L}\to\bar{d}}\mathbf{S}_{\bar{L}\to\bar{d}}\mathbf{V}^{T}_{\bar{L}\to\bar{d}}$$

5. Generate ($\dim(\mathbf{d}) - k$) extra snapshots in the subspace spanned by the columns of $\mathbf{U}_{\bar{L}\to\bar{d}}$ (response L snapshots-refer to section 3.2, page (94)) **without running the model** and perform the SVD on the snapshots matrix with ($\dim(\mathbf{d})$ snapshots)**:**

$$\mathbf{L} = \left[\bar{L}^{(1)} \cdots \bar{L}^{(\dim(\mathbf{D}))} \right] = \mathbf{U}_{F,\bar{L}\to\bar{d}}\mathbf{S}_{F,\bar{L}\to\bar{d}}\mathbf{V}^{T}_{F,\bar{L}\to\bar{d}}$$

where $\mathbf{V}_{F,\bar{L}\to\bar{d}} \in \mathbb{R}^{nxr_{\bar{L}\to\bar{d}}}$, and $r_{L\to\bar{d}}$ is the rank of the subspace or the proper DoF important to the response of MPACT - COBRA-TF.

Stage 3. Intersection Subspace-Based Reduction at the Model-to-Model Interface.

6. Calculate the intersection between the column spaces of $\mathbf{V}_{\bar{L}\to\bar{d}}$, $\mathbf{U}_{\bar{d}}$ and $\mathbf{U}_{\mathbf{C_d}}$ as follow:

$$\mathbf{N} = \mathbf{U}_{\mathbf{C_X}} \cap \mathbf{U}_{\bar{\Sigma}} \cap \mathbf{V}_{F,\bar{L}\to\bar{d}}$$

7. Construct an orthonormal basis by performing the SVD decomposition:

$$\mathbf{N} = \mathbf{USV},$$

where the columns of matrix **U** represent a basis for the intersection subspace at the first interface between the models in the direction MPACT – COBRA-TF → ORIGEN involving the information carried by the **X**-space, **d**-space**.**

Once the basis of the active subspace is determined (i.e. columns of **U**) one can use it in Eq. (46) to propagate the uncertainties from the nuclear data cross-sections towards the various quantities of interest. Moreover, if **a-** and **b- Z-** or **Y-** spaces (thermal-hydraulics - neutronics interfaces) are high dimensional spaces (which is not the case in this application) then the **GF-MPRFA** (refer to chapter 3) can be used to pursue dimensionality reduction on these spaces.

Once the high dimensional subspaces are approximated by lower dimensional subspaces, the uncertainty in the nuclear data cross-sections(**X**-space), fission yields (**Y**-space) and thermal-hydraulics parameters (**Z**-space) can be propagated through the Quantities of Interest (QoIs) using the following general steps:

1. Run the coupled system of models for the reference case state.
2. Propagate the uncertainty due to the **Z**- and **Y**- spaces via a Monte Carlo approach.
3. Determine the lower dimensional subspace approximation for the high dimensional subspace (**X**-space) using the **GF-MPRFA**.
4. Propagate the uncertainties due to the **X**-space using the MP-EUQ (the macroscopic cross-sections) and the basis **U** through MPACT - COBRA-TF - ORIGEN coupled models.
5. 1 through 3 are repeated for all time steps (fuel depletion steps).

The analysis and algorithms used in this chapter were encoded and implemented in a newly developed tool kit algorithms for Reduced Order Modeling based Uncertainty/Sensitivity Estimator (ROMUSE). In this section and the sections that follow, ROMUSE will be used in conjunction with VERA-CS to verify and test the algorithms developed in this dissertation.

Progression problem 6 is a steady state model of a Westinghouse 17x17 PWR fuel assembly. In this case the assembly is hypothetically operated at 100% of rated power and at 1300 PPM boron concentration with no axial blankets or different enrichment regions. Overall, the total number of fuel rods is 264 fuel rods, with 24 guide tubes, and a single instrument tube at the center. (NOTE: There are no control rods or removable burnable absorber rods in this problem) [68]. For more information about the problem's parameters, refer to Table 2. Figure 33 shows the proximity of the assembly within the core. In this numerical test CASL

progression problem 6 is going to be depleted to 30 GWd/MTU using 24 depletion time-steps (0, 0.1, 0.2, 0.5, 1-10x1, 12-30x2 GWd/MTU).

It is important to emphases here that the nuclear data cross-sections covariance library that will be used in this section is a 44 energy group library while VERA-CS uses a 47 group library. Therefore, it is obvious that the perturbations generated by the 44 group library must be mapped to the 47 group structure. This is achieved via linear interpolation that is based on the assumption of constant lethargy intervals.

295 nuclides, 47 energy groups, 5 reactions are treated (absorption, fission, nu-fission, transport, scattering) besides the fission spectrum and (n,2n) reaction. Taking into account that some reactions are not valid for certain nuclides the full rank of the problem's input is < 295*47*7. Actually, for the problem of interest, the dimension is 49,773 ($\bar{\Sigma} \in \mathbb{R}^{49,773}$). So first the lower dimensional subspace approximation using the **GF-MPRFA** (refer to section 3.2) is applied to the three coupled models here, where the **Z**-space ≡ gap conductivity, fuel thermal conductivity and grid loss coefficient, **Y** – space ≡ k_{eff} , maximum pin power, maximum pin temperature, and **X**-space ≡ nuclear data cross-sections. The problem is run in parallel using 58 cores on the NCSU HPC.

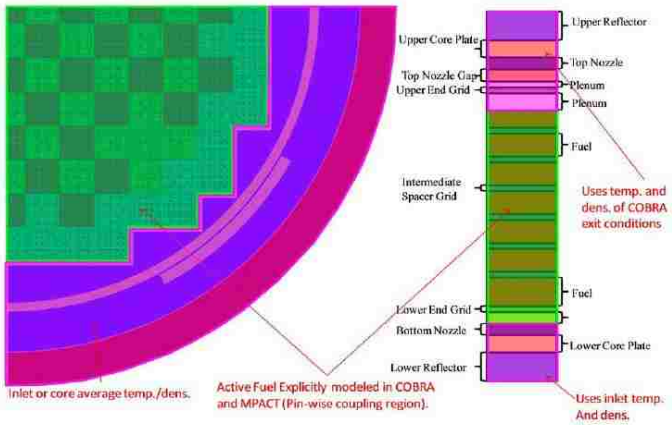

Figure 33. Assembly Configuration.

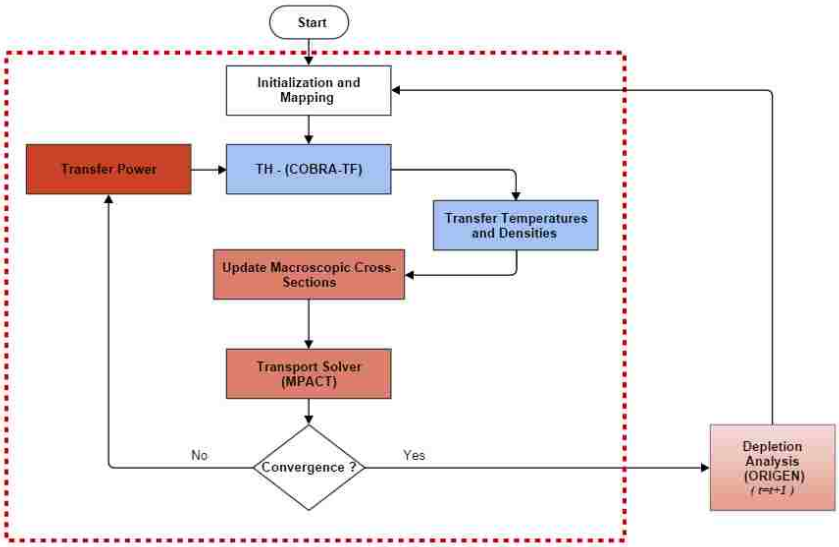

Figure 34. A flow chart illustrating the series of coupled models in VERA-CS Depletion with thermal-hydraulics feedback.

Figure 34 shows a schematic of the coupled modules in VERA-CS. The current case study will estimate the uncertainty in the responses of interest (multiplication factor, maximum pin temperature and maximum pin power) due to the nuclear data cross-sections and few thermal-hydraulics parameters (gap conductivity, fuel thermal conductivity and the grid loss

coefficient). The uncertainty is going to be estimated due to each of the parameters and then the joint uncertainty is estimated.

Three methods will be used to estimate the uncertainties; the Multi-Physics Efficient Uncertainty Quantification **(MP-EUQ)** which is a linear Karhunen Loeve expansion-based approach derived in section **4.3**, Surrogate Based Uncertainty Quantification **(SBUQ)** detailed in section **4.3**, and the brute force forward Monte Carlo uncertainty quantification. The brute force Monte Carlo method is used to verify the results by comparing the Monte Carlo estimated uncertainty with the uncertainty estimated by the **MP-EUQ** and **SBUQ**.

First, the surrogates will be constructed and then evaluated before being used to sample the responses of interest. In this test the surrogate form represented in Eq.(57) is used, however, with the addition of a third order term. Specifically, the following surrogate form is going to be used:

$$\Delta y^{surr} = \bar{S}_{1,r}^{T}\Delta\bar{\alpha} + \left(\bar{S}_{2,r}^{T}\Delta\bar{\alpha}\right)^{2} + \left(\bar{S}_{3,r}^{T}\Delta\bar{\alpha}\right)^{3} \tag{60}$$

where $\mathbf{U} \in \mathbb{R}^{nxr}$, $\Delta\bar{\alpha} = \mathbf{U}^{T}\bar{\xi} \in \mathbb{R}^{r}$, $\bar{S}_{1,r}^{T} = \bar{S}_{1}^{T}\mathbf{C}_{x}^{1/2}\mathbf{U} \in \mathbb{R}^{r}$, $\bar{S}_{2,r}^{T} = \bar{S}_{2}^{T}\mathbf{C}_{x}^{1/2}\mathbf{U} \in \mathbb{R}^{r}$ and $\bar{S}_{3,r}^{T} = \bar{S}_{3}^{T}\mathbf{C}_{x}^{1/2}\mathbf{U} \in \mathbb{R}^{r}$. Hence the unknown elements of $\bar{S}_{1,r}$, $\bar{S}_{2,r}$ and $\bar{S}_{3,r}$ must be determined via regression analysis. For more information about the notations used in Eq.(60) the reader is referred to Eq. (57) and the description therein. Eq.(60) ignores the cross-product terms (correlation terms between model's parameters). Computing these terms requires tremendous computational burden; therefore, Eq. (60) assumes that the reduced parameters are not correlated due to the fact that the reduction processes (i.e. **GF-MPRFA**, **GB-MPRFA** and **ERFA**) remove the **linear** correlations between the original parameters, hence, creating a

reduced set of parameters that have no (or extremely weak) correlation. In the case study represented in this section, a simple test will be implemented to assert this assumption.

First, the **GF-MPRFA** (refer to section 3.2) will be used to determine the basis of the active subspace approximation for the nuclear data cross-sections variations (**U**) after which the perturbations ($\Delta\bar{x}$) are projected on the space spanned by the columns of matrix **U**. Finally, the coefficients ($\bar{S}_{1,r}$, $\bar{S}_{2,r}$, $\bar{S}_{3,r}$) are determined along with the confidence intervals and the surrogate form –related uncertainty.

The surrogate parameters ($\bar{S}_{1,r}$, $\bar{S}_{2,r}$, $\bar{S}_{3,r}$) are statistical parameters that are subjected to variance and standard deviation which can be approximated by Eq.(61) assuming that the residual error is unbiased and an **i**ndependent-**i**dentical **d**istributed random error (**i.i.d**) [15]:

$$V\left(\bar{q}\right) \approx \sigma^2 \left[\chi^T \left(\bar{q}\right) \chi\left(\bar{q}\right) \right]^{-1} , \tag{61}$$

where

$$\bar{q} = \begin{bmatrix} \bar{S}_{1,r} \\ \bar{S}_{2,r} \\ \bar{S}_{3,r} \end{bmatrix} , \quad \chi\left(\bar{q}\right) = \frac{\partial \Delta y^{surr}}{\partial \bar{q}} \text{ and } \sigma^2 = \frac{1}{n-p} R^T R ,$$

and *R* is the residual obtained by comparing the responses obtained by the surrogate and the responses generated by VERA-CS (the original model). On the other hand, $\chi\left(\bar{q}\right)$ is the sensitivity matrix (if the surrogate generates multiple responses) or a vector (for single response case) which can be calculated efficiently using the finite difference method. Finally, *n-p* is the number of DoFs.

Once the uncertainties in the surrogate parameters are determined, they can be used to calculate both confidence intervals and the uncertainties in the responses of interest due to the surrogate form (surrogate form – related uncertainty).

The **GF-MPRFA** was used to obtain the reduced dimensional input parameter space. Table 6 show a comparison between the 2nd and 3rd order surrogates in terms of the surrogate form-related uncertainties, norm of residuals and the residuals distribution. The surrogate form – related uncertainty is calculated by a Monte Carlo approach where the surrogate parameters are sampled based on the uncertainties estimated by Eq.(61). From the GF-MPRFA, a subspace of rank 50 (50 DoFs) is sufficient to capture the variations of the cross-sections in the depletion cycle of interest with an L_2 – norm error upper bound of 1%.

In general, the surrogate quality can be evaluated by examining the residual errors obtained by comparing the responses predicted by the surrogate on one side and the original model on the other side. For example, the current surrogate is constructed for the purpose of uncertainty quantification; therefore, 40 extra random samples generated employing the covariance matrix are used. The perturbations are created in all the parameters simultaneously (cross-sections, fuel thermal conductivity, grid-loss and gap conductivity), hence, testing the assumption introduced within Eq.(60). Figure 35 through Figure 37 shows the residuals associated with the surrogate computed for different parameter sets which are generated by varying all the parameters simultaneously (i.e. the gap conductivity (*hgap*), the fuel thermal conductivity (k_{cond}) and with perturbations generated employing the covariance library which is the "*44groupcov*" library which is distributed with SCALE6.1[57]). The surrogate responses are compared to the responses (multiplication factor, maximum pin power, maximum pin

temperature) generated via VERA-CS. Therefore, the residuals are satisfactory for the purpose of interest (less than 10% of the initial uncertainty in the quantity of interest).

Figure 35 through Figure 37 show that the third order surrogates of the form represented by Eq.(60) can predict the multiplication factor (k_{eff}), maximum pin power, maximum pin temperature with sufficient accuracy relative to the uncertainty estimation application (refer to Table 7 through Table 9).

These surrogates will be used to quantify the uncertainty in the responses on interest (including the surrogate form - related uncertainty) and then compared with the uncertainties estimated via a forward Monte Carlo approach and finally compared with the uncertainty estimated by the **MP-EUQ** (refer to section 4.3).

Figure 38 through Figure 52 and the figures reported in Appendix A compare the performance of the VERA-CS based Monte Carlo approach against the surrogate model based Monte Carlo approach (**SBUQ**). Statistical samples drawn using VERA-CS original models sequences and then compared to samples drawn from the surrogate model replacing the original VERA-CS. First, Appendix A shows the frequency distribution of k_{eff}, maximum fuel pin power and maximum fuel pin temperature due to the gap conductivity uncertainty (±50%), the thermal fuel conductivity (±10%) , grid spacer loss coefficient (±4%), and nuclear data cross-sections (44groupcov). These figures compares the uncertainties in the multiplication factor (k_{eff}), maximum pin power, and maximum pin temperature due to the 4 uncertainty sources of interest: gap conductivity coefficient, fuel thermal conductivity, grid-loss coefficients, nuclear data cross – sections and due to joint samples. Only 8 depletion/time

snapshots are represented by the figures reported in appendix A (0, 5, 10, 14, 18, 22, 26, 30 GWd/MTU). The full comparison is represented by Table 7 through Table 9.

Figure 38, Figure 40, Figure 43, Figure 44, Figure 45, Figure 46, Figure 47, Figure 48, Figure 49, Figure 50, Figure 51 and Figure 52 compare the RoI along with ±σ uncertainty bars as predicted by the original model and the surrogate model at all the depletion steps (mean values ±σ). Details of the uncertainties estimated via the MP-EUQ (linear Karhunen Loeve-based approach), SBUQ (Monte Carlo sampling 3rd order surrogates) and forward MCUQ (Monte Carlo sampling via original model) are shown in Table 7 through Table 9.

One can notice that for the multiplication factor (k_{eff}) the uncertainty estimated via the **MP-EUQ** are within one standard deviation (± σ) of the uncertainties estimated via the Monte Carlo approaches (**MCUQ** and **SBUQ**); however, for the maximum fuel pin power and the maximum fuel pin temperature some of the uncertainty values estimated by the **MP-EUQ** are far away from one standard deviation. The reason for that might be due to the fact that the **MP-EUQ** is a linear approach assuming that the response of interest is a linear function of the parameters. The results in Table 7 indicates that the linear assumption is sufficient for the multiplication factor, while Table 8 and Table 9 indicate that the linear assumption is not sufficient for the maximum pin power and maximum pin temperature.

Table 6. Features of the Surrogate.

Surrogate order	RMS	Number of Construction Data Points	Number of extra Validation Data Points	Residuals distribution	surrogate form – related uncertainty
2nd order	$\varepsilon_{k_{eff}} \rightarrow$ 15.4 pcm	100	40	*iid*	*18.2 pcm*
	$\varepsilon_{P_{max}} \rightarrow$ 0.036 W/cm			*iid*	*0.09* W/cm
	$\varepsilon_{T_{max}} \rightarrow$ 17 C^o			*iid*	*14.36* C^o
3rd order	$\varepsilon_{k_{eff}} \rightarrow$ 13 pcm	150	40	*iid*	*13.0 pcm*
	$\varepsilon_{P_{max}} \rightarrow$ 0.009 W/cm			*iid*	*0.01* W/cm
	$\varepsilon_{T_{max}} \rightarrow$ 8.4 C^o			*iid*	*8.36* C^o

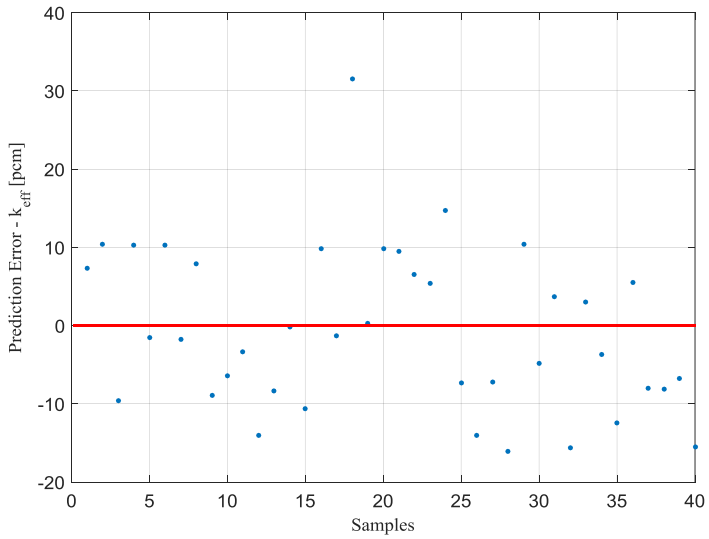

Figure 35. Residuals in predicting the k_{eff} ($\varepsilon_{k_{eff}}$) for a range of the gap conductivity and cross-sections (h_{gap}, k_{cond} and $\overline{\Sigma}$) for 40 samples (surrogate vs. VERA-CS).

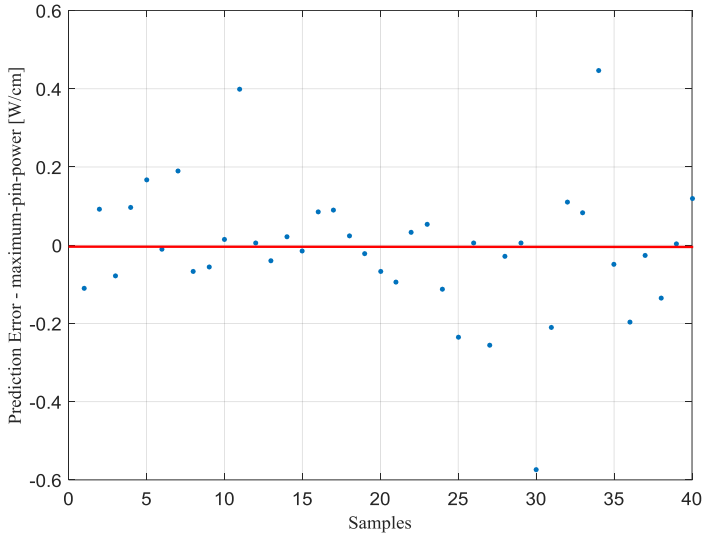

Figure 36. Residuals in predicting the maximum pin power ($\varepsilon_{P_{\max}}$) for a range of the gap conductivity and cross-sections (h_{gap} , k_{cond} and $\bar{\Sigma}$) for 40 samples (surrogate vs. VERA-CS).

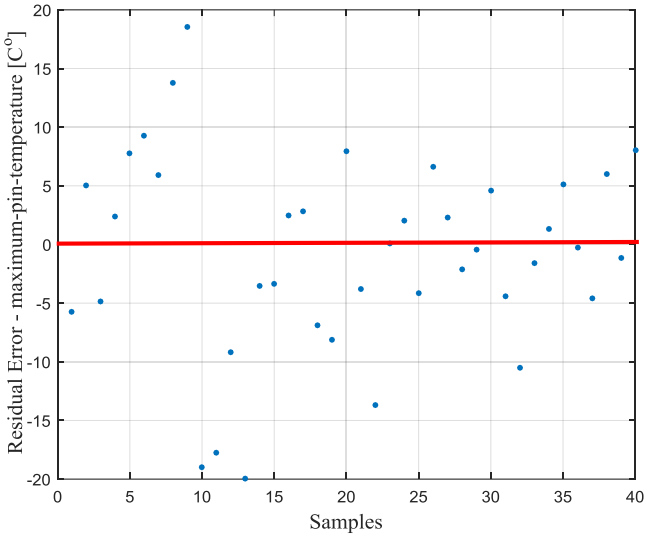

Figure 37. Residuals in predicting the maximum pin temperature ($\varepsilon_{T_{\max}}$)for a range of the gap conductivity and cross-sections (h_{gap} , k_{cond} and $\bar{\Sigma}$) for 40 samples (surrogate vs. VERA-CS).

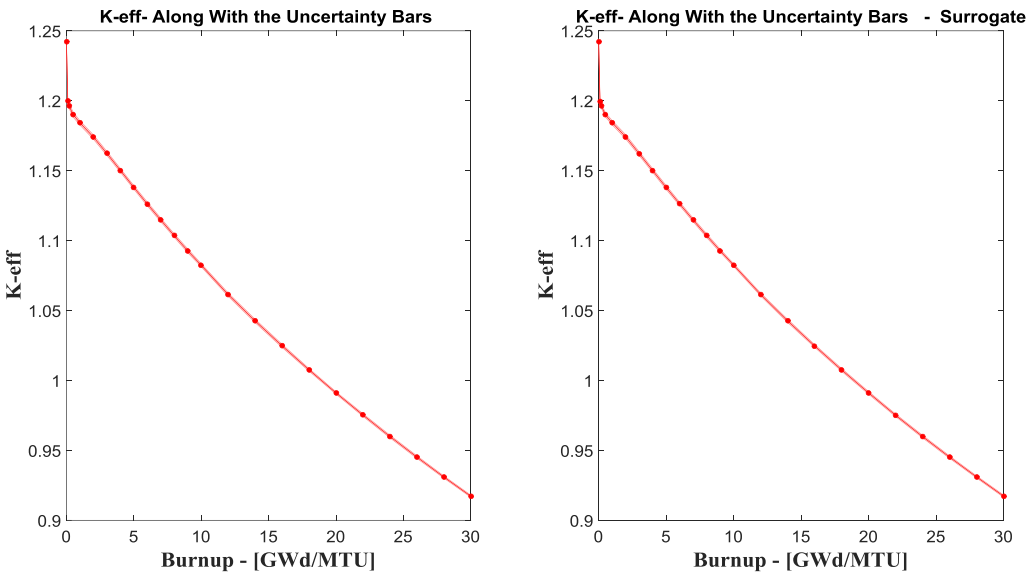

Figure 38. Burnup dependent k_{eff} along with uncertainty ±σ due to the gap conductivity.

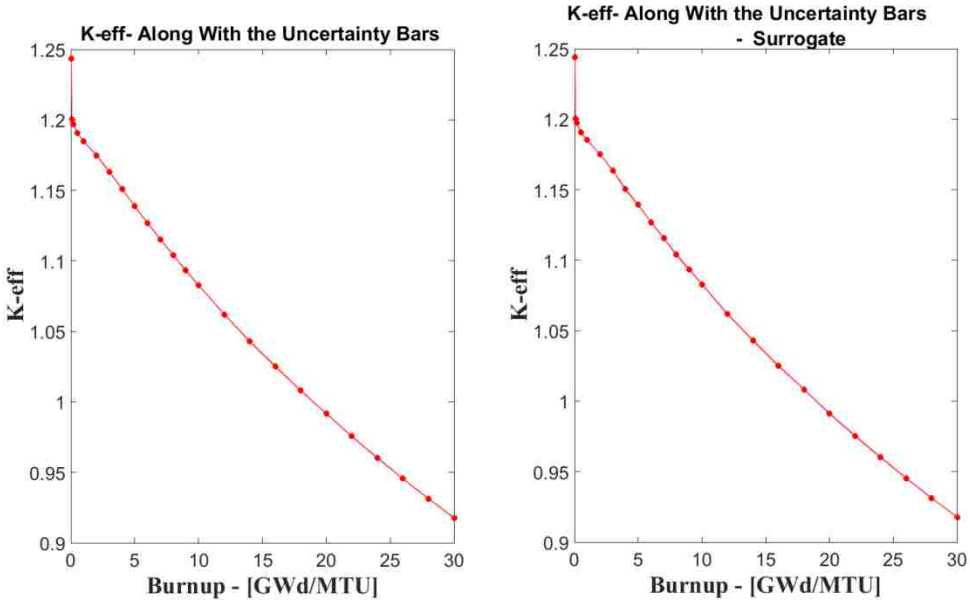

Figure 39. Burnup dependent k_{eff} along with uncertainty ±σ due to the fuel thermal conductivity.

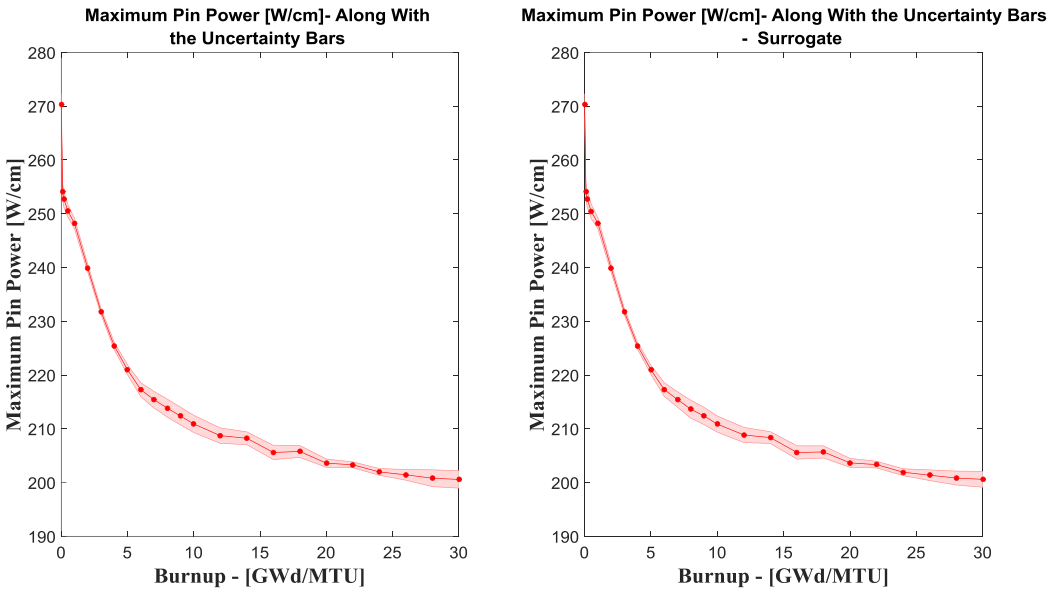

Figure 40. Burnup dependent maximum pin power along with uncertainty ±σ due to the gap conductivity.

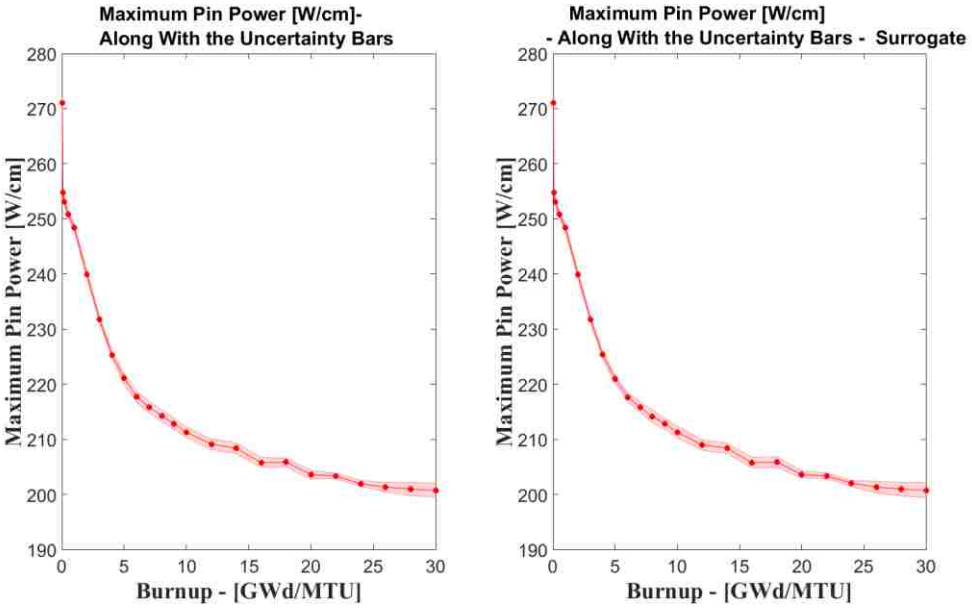

Figure 41. Burnup dependent maximum pin power along with uncertainty ±σ due to the fuel thermal conductivity.

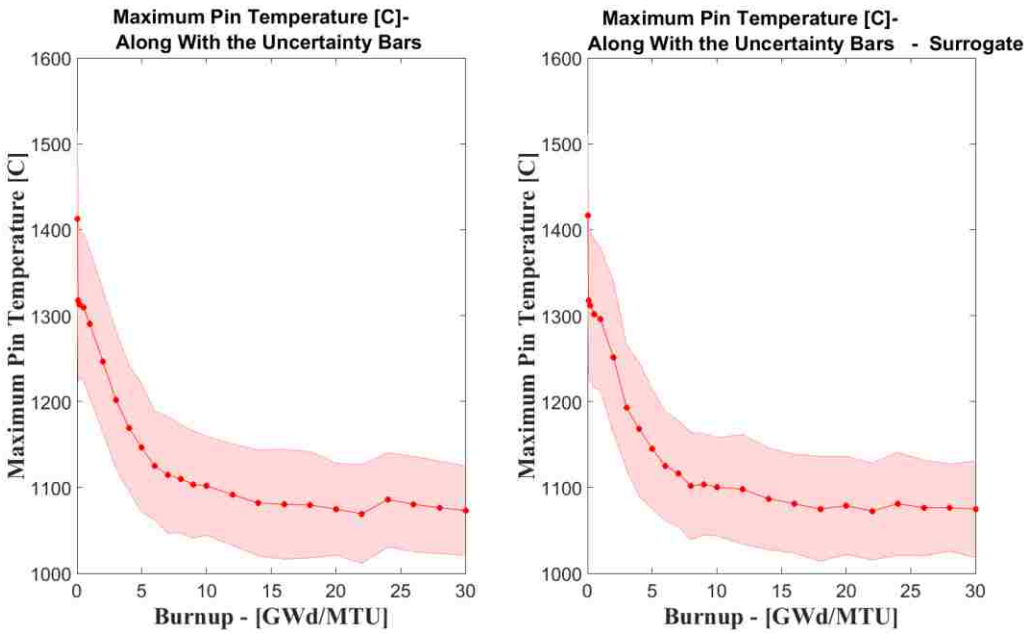

Figure 42. Burnup dependent maximum pin temperature along with uncertainty ±σ due to the fuel thermal conductivity.

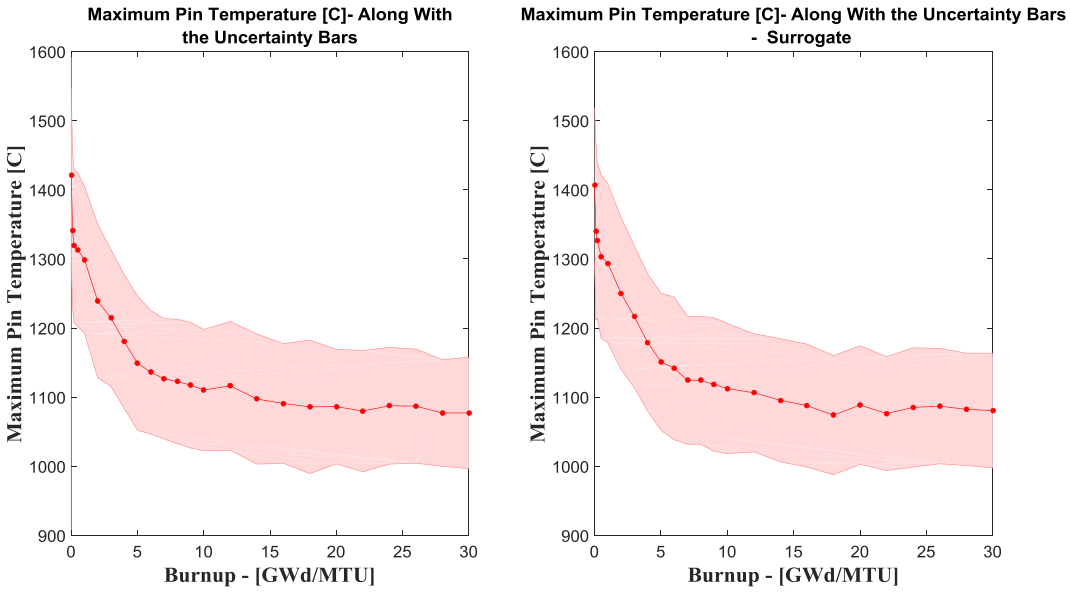

Figure 43. Burnup dependent maximum pin temperature along with uncertainty ±σ due to the gap conductivity.

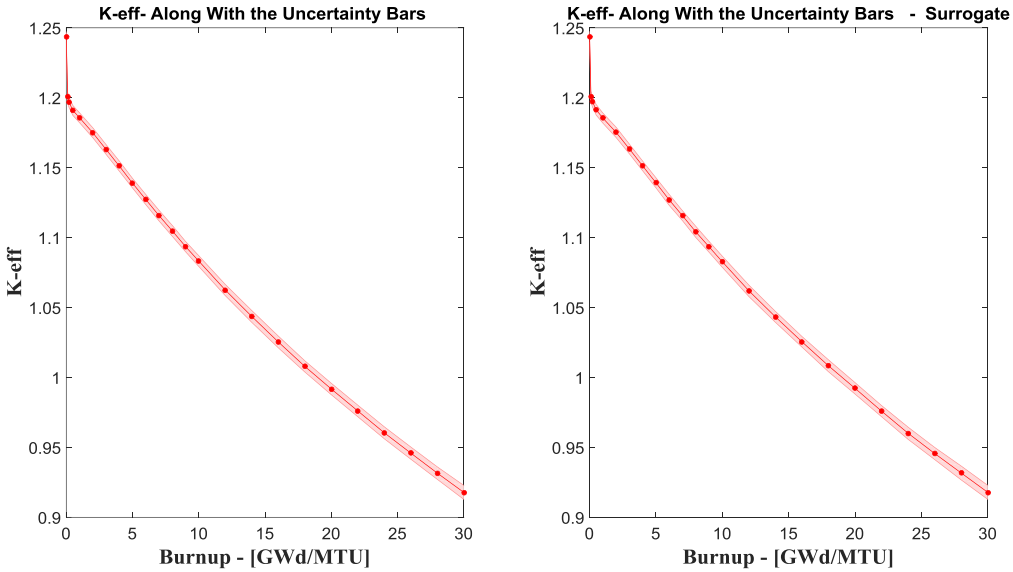

Figure 44. Burnup dependent k_{eff} along with uncertainty ±σ due to the nuclear data cross-sections.

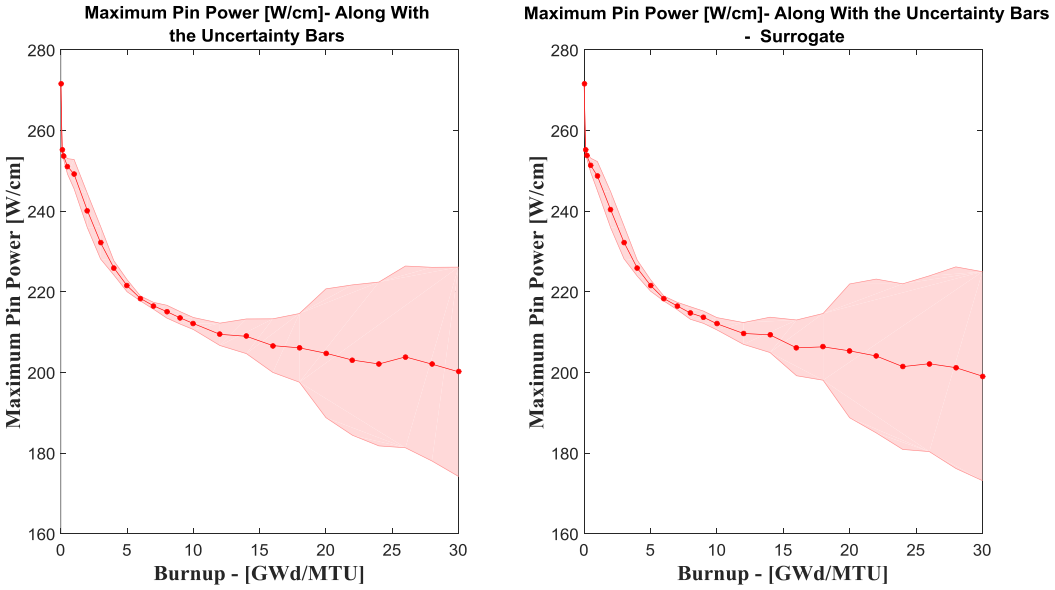

Figure 45. Burnup dependent maximum pin power along with uncertainty ±σ due to the nuclear data cross-sections.

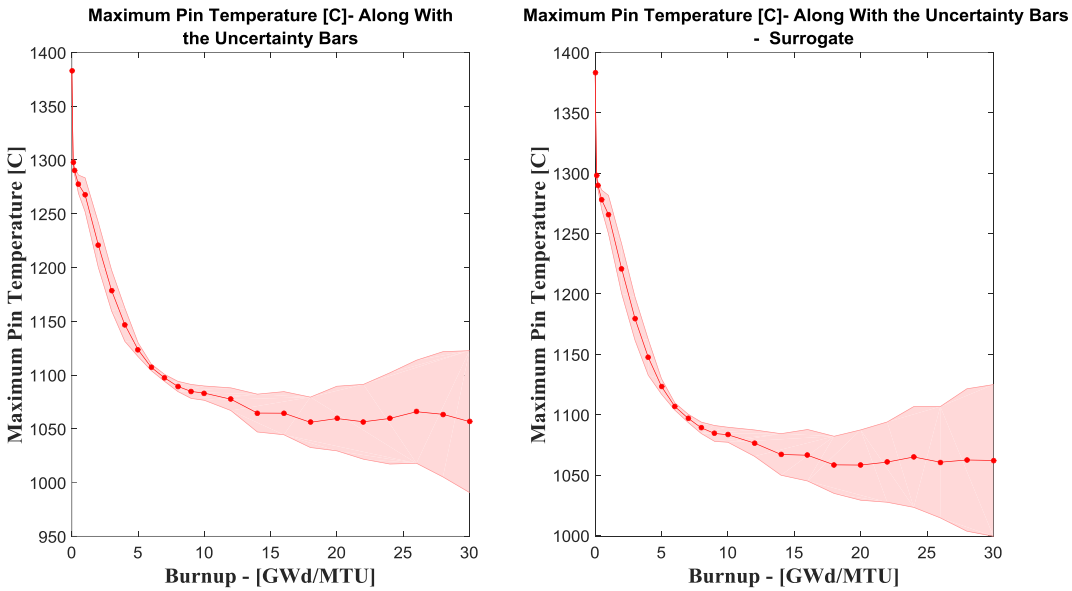

Figure 46. Burnup dependent maximum pin temperature along with uncertainty ±σ due to the nuclear data cross-sections uncertainty.

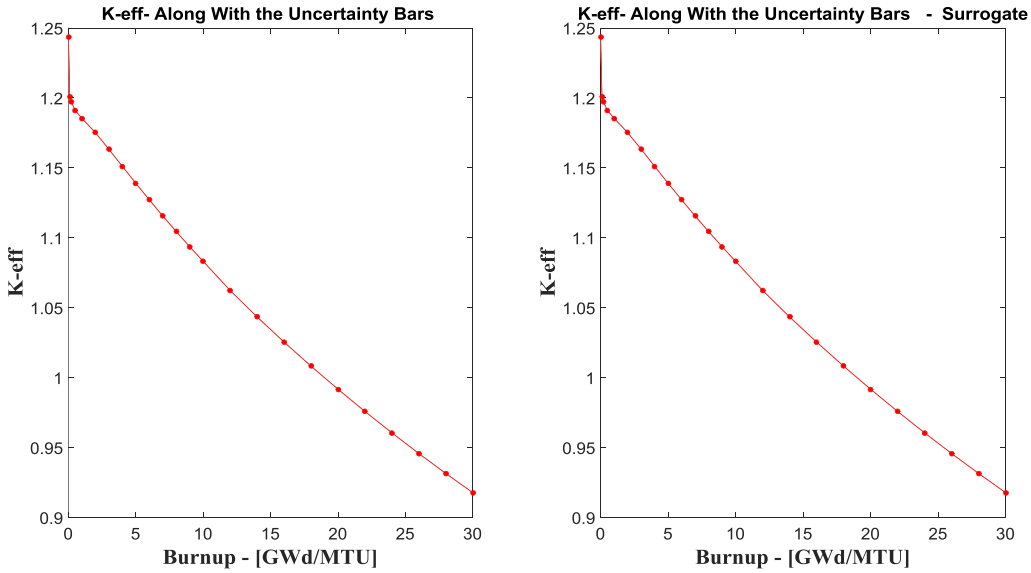

Figure 47. Burnup dependent k_{eff} along with uncertainty ±σ due to the grid-loss coefficient uncertainty.

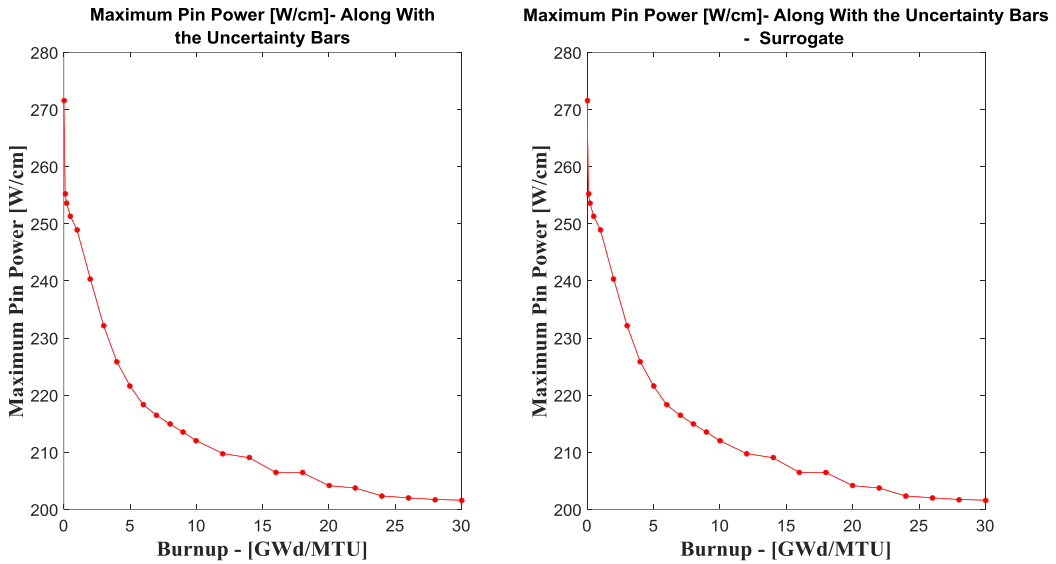

Figure 48. Burnup dependent maximum pin power along with uncertainty ±σ due to the grid-loss coefficient uncertainty.

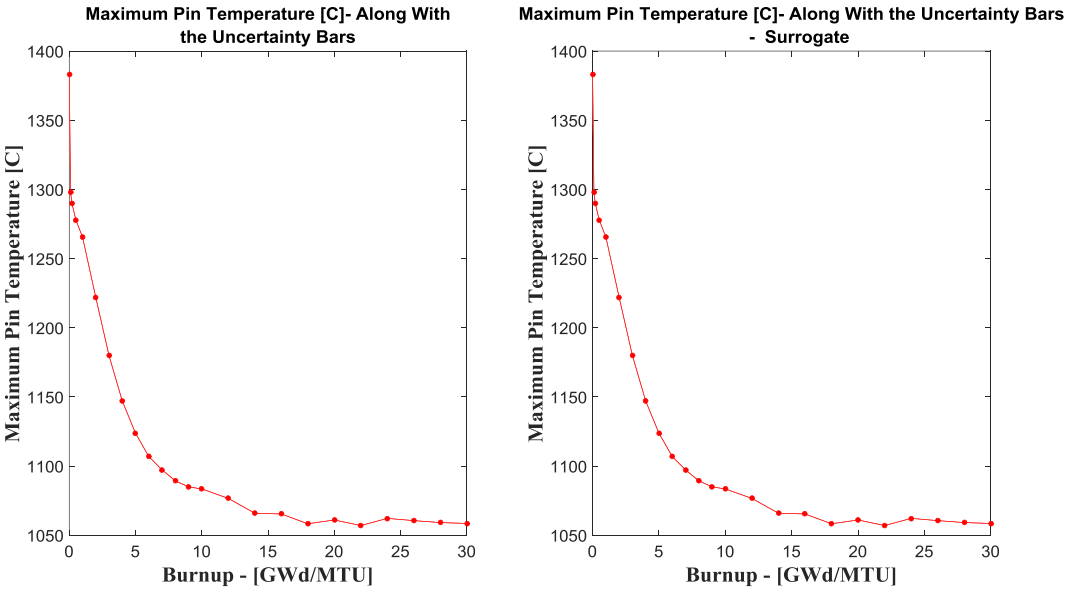

Figure 49. Burnup dependent maximum pin temperature along with uncertainty ±σ due to the grid-loss coefficient uncertainty.

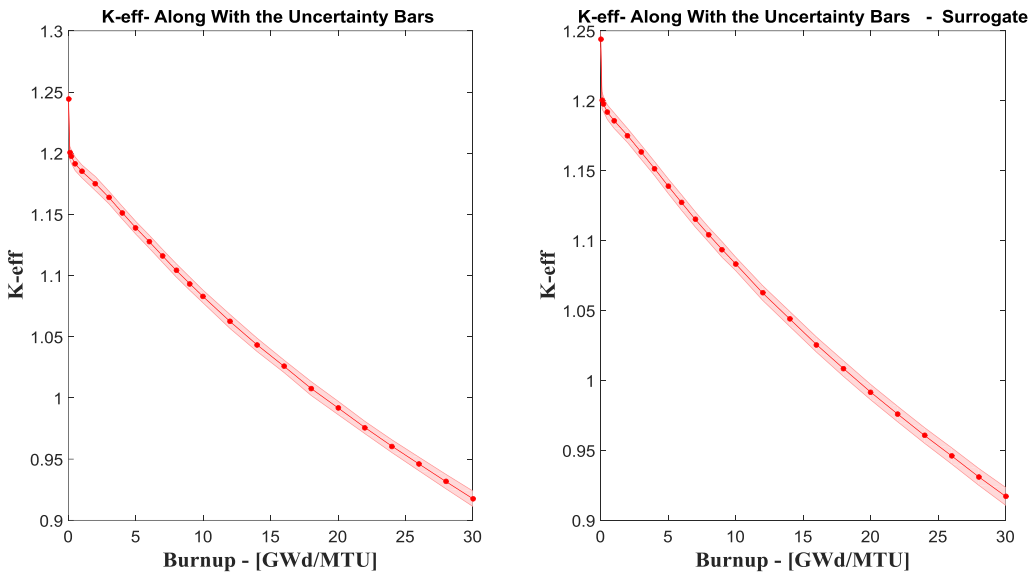

Figure 50. Burnup dependent k_{eff} along with uncertainty ±σ due to joint samples.

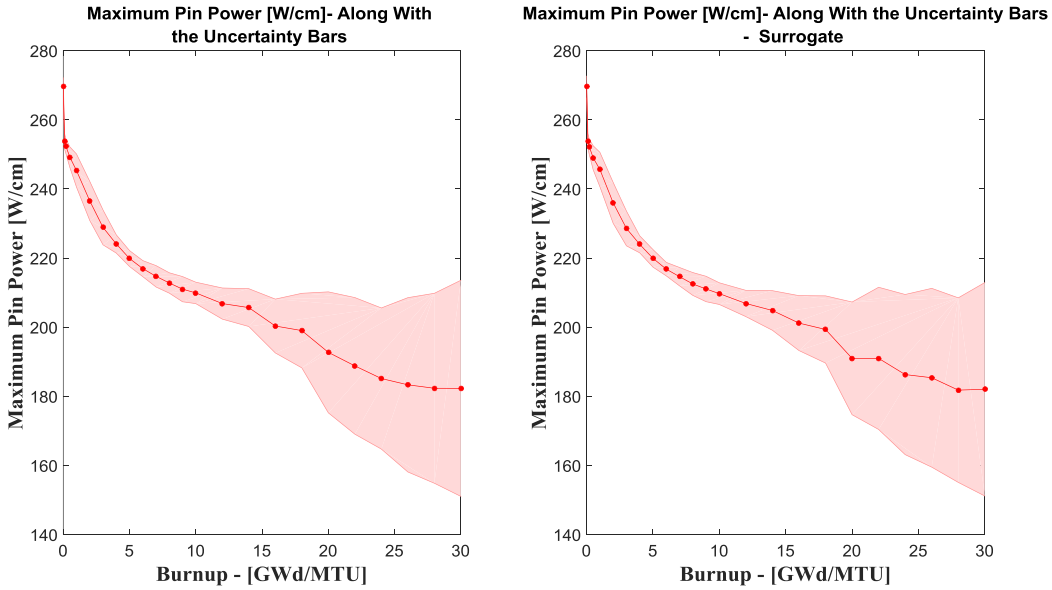

Figure 51. Burnup dependent maximum pin power along with uncertainty ±σ due to joint samples.

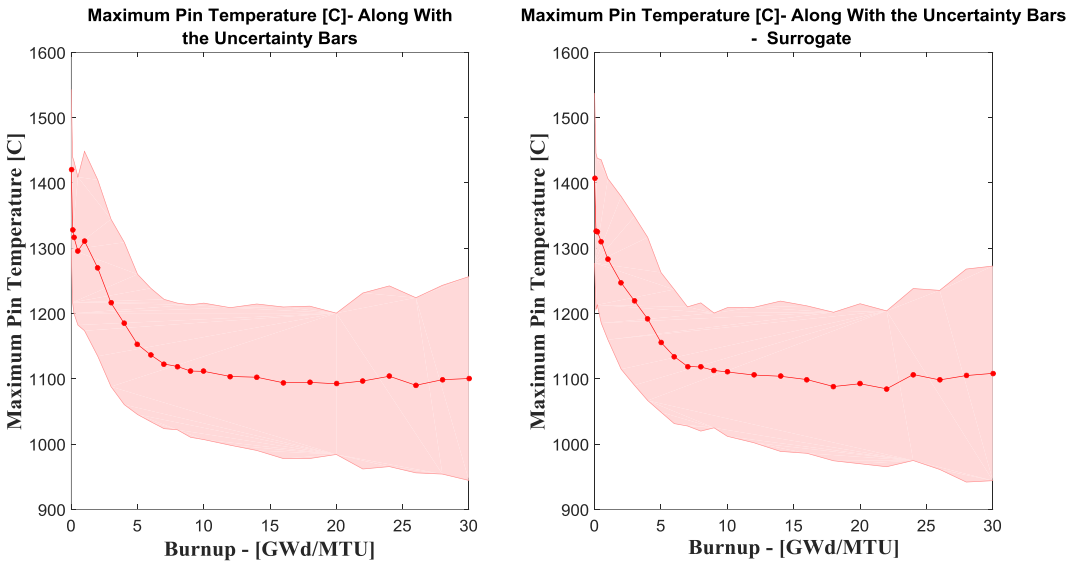

Figure 52. Burnup dependent maximum pin temperature along with uncertainty ±σ due to joint samples

Table 7. Summary of the *k-eff* uncertainty results – joint parameters (MCUQ vs. MP-EUQ vs. SBUQ)

Depletion (irradiation)	STD	MP-EUQ r=50	3rd Order Surrogate 500 samples	Monte Carlo 500 samples
0.0 GWdMTU	σ_k	589 pcm	625 pcm	606cm
	σ_{σ_k}	-	39 pcm	43 pcm
0.1 GWdMTU	σ_k	588 pcm	595 pcm	578 pcm
	σ_{σ_k}	-	21 pcm	36 pcm
0.2 GWdMTU	σ_{σ_k}	523 pcm	557 pcm	565 pcm
	σ_{σ_k}	-	23 pcm	44 pcm
0.5 GWdMTU	σ_k	501 pcm	551 pcm	559 pcm
	σ_{σ_k}	-	43 pcm	42 pcm
1.0 GWdMTU	σ_k	503 pcm	534 pcm	549 pcm
	σ_{σ_k}	-	32 pcm	71 pcm
2.0 GWdMTU	σ_k	511 pcm	542 pcm	541 pcm
	σ_{σ_k}	-	53 pcm	65 pcm
3.0 GWdMTU	σ_k	494 pcm	532 pcm	539 pcm
	σ_{σ_k}	-	43 pcm	62 pcm
4.0 GWdMTU	σ_k	511 pcm	527 pcm	541 pcm
	σ_{σ_k}	-	53 pcm	56 pcm
5.0 GWdMTU	σ_k	523 pcm	525 pcm	531 pcm
	σ_{σ_k}	-	46 pcm	36 pcm
6.0 GWdMTU	σ_k	503 pcm	522 pcm	529 pcm
	σ_{σ_k}	-	54 pcm	67 pcm
7.0 GWdMTU	σ_k	500 pcm	518 pcm	531 pcm
	σ_{σ_k}	-	49 pcm	43 pcm
8.0 GWdMTU	σ_k	512 pcm	530 pcm	532 pcm
	σ_{σ_k}	-	43 pcm	45 pcm
9.0 GWdMTU	σ_k	499 pcm	529 pcm	533 pcm
	σ_{σ_k}	-	41 pcm	32 pcm

Table 7 Continued

10.0 GWdMTU	σ_k	488 pcm	514 pcm	524 pcm
	σ_{σ_k}	-	39 pcm	42 pcm
12.0 GWdMTU	σ_k	491 pcm	526 pcm	538 pcm
	σ_{σ_k}	-	23 pcm	34 pcm
14.0 GWdMTU	σ_k	513 pcm	536 pcm	544 pcm
	σ_{σ_k}	-	41 pcm	39 pcm
16.0 GWdMTU	σ_k	490 pcm	542 pcm	536 pcm
	σ_{σ_k}	-	21 pcm	38 pcm
18.0 GWdMTU	σ_k	509 pcm	545 pcm	544 pcm
	σ_{σ_k}	-	31 pcm	33 pcm
20.0 GWdMTU	σ_k	512 pcm	541 pcm	547 pcm
	σ_{σ_k}	-	36 pcm	39 pcm
22.0 GWdMTU	σ_k	524 pcm	552 pcm	543 pcm
	σ_{σ_k}	-	22 pcm	24 pcm
24.0 GWdMTU	σ_k	528 pcm	567 pcm	565 pcm
	σ_{σ_k}	-	39 pcm	42 pcm
26.0 GWdMTU	σ_k	532 pcm	560 pcm	579 pcm
	σ_{σ_k}	-	45 pcm	51 pcm
28.0 GWdMTU	σ_k	559 pcm	610 pcm	607 pcm
	σ_{σ_k}	-	39 pcm	53 pcm
30.0 GWdMTU	σ_k	591 pcm	622 pcm	641 pcm
	σ_{σ_k}	-	34 pcm	42 pcm

Table 8. Summary of the *Maximum Pin Power* uncertainty results – joint parameters (MCUQ vs. MP-EUQ vs. SBUQ).

Depletion (irradiation)	STD	MP-EUQ r=50	3rd Order Surrogate 500 samples	Monte Carlo 500 samples
0.0 GWdMTU	σ_{mp}	2.03 W/cm	2.76 W/cm	2.32 W/cm
	$\sigma_{\sigma_{mp}}$	-	0.09 W/cm	0.11 W/cm
0.1 GWdMTU	σ_{mp}	1.9 W/cm	2.10 W/cm	2.55 W/cm
	$\sigma_{\sigma_{mp}}$	-	0.05 W/cm	0.09 W/cm
0.2 GWdMTU	σ_{mp}	1.8 W/cm	2.17 W/cm	2.48 W/cm
	$\sigma_{\sigma_{mp}}$	-	0.11 W/cm	0.12 W/cm
0.5 GWdMTU	σ_{mp}	2.9 W/cm	3.26 W/cm	3.13 W/cm
	$\sigma_{\sigma_{mp}}$	-	0.1 W/cm	0.13 W/cm
1.0 GWdMTU	σ_{mp}	3.8 W/cm	4.87 W/cm	5.11 W/cm
	$\sigma_{\sigma_{mp}}$	-	0.08 W/cm	0.09 W/cm
2.0 GWdMTU	σ_{mp}	4.2 W/cm	5.47 W/cm	5.97 W/cm
	$\sigma_{\sigma_{mp}}$	-	0.11 W/cm	0.14 W/cm
3.0 GWdMTU	σ_{mp}	3.7 W/cm	5.08 W/cm	5.99 W/cm
	$\sigma_{\sigma_{mp}}$	-	0.12 W/cm	0.1 W/cm
4.0 GWdMTU	σ_{mp}	2.1 W/cm	2.66 W/cm	3.65 W/cm
	$\sigma_{\sigma_{mp}}$	-	0.06 W/cm	0.08 W/cm
5.0 GWdMTU	σ_{mp}	2.22 W/cm	2.48 W/cm	2.94 W/cm
	$\sigma_{\sigma_{mp}}$	-	0.1 W/cm	0.13 W/cm
6.0 GWdMTU	σ_{mp}	2.1 W/cm	2.20 W/cm	2.64 W/cm
	$\sigma_{\sigma_{mp}}$	-	0.11 W/cm	0.12 W/cm
7.0 GWdMTU	σ_{mp}	2.1 W/cm	2.49 W/cm	3.52 W/cm
	$\sigma_{\sigma_{mp}}$	-	0.09 W/cm	0.11 W/cm
8.0 GWdMTU	σ_{mp}	2.8 W/cm	3.48 W/cm	3.87 W/cm
	$\sigma_{\sigma_{mp}}$	-	0.05 W/cm	0.1 W/cm
9.0 GWdMTU	σ_{mp}	2.9 W/cm	3.45 W/cm	3.99 W/cm
	$\sigma_{\sigma_{mp}}$	-	0.1 W/cm	0.13 W/cm

Table 8 Continued

10.0 GWdMTU	σ_{mp}	2.38 W/cm	3.31 W/cm	3.94 W/cm
	$\sigma_{\sigma_{mp}}$	-	0.11 W/cm	0.13 W/cm
12.0 GWdMTU	σ_{mp}	3.9 W/cm	4.52 W/cm	4.89 W/cm
	$\sigma_{\sigma_{mp}}$	-	0.09 W/cm	0.11 W/cm
14.0 GWdMTU	σ_{mp}	4.1 W/cm	5.73 W/cm	5.76 W/cm
	$\sigma_{\sigma_{mp}}$	-	0.08 W/cm	0.09 W/cm
16.0 GWdMTU	σ_{mp}	5.9 W/cm	8.39 W/cm	8.62 W/cm
	$\sigma_{\sigma_{mp}}$	-	0.07 W/cm	0.11 W/cm
18.0 GWdMTU	σ_{mp}	8.43 W/cm	10.35 W/cm	10.36 W/cm
	$\sigma_{\sigma_{mp}}$	-	0.1 W/cm	0.11 W/cm
20.0 GWdMTU	σ_{mp}	16.2 W/cm	18.59 W/cm	18.55 W/cm
	$\sigma_{\sigma_{mp}}$	-	0.08 W/cm	0.09 W/cm
22.0 GWdMTU	σ_{mp}	15.21 W/cm	20.52 W/cm	20.55 W/cm
	$\sigma_{\sigma_{mp}}$	-	0.09 W/cm	0.1 W/cm
24.0 GWdMTU	σ_{mp}	19.6 W/cm	22.44 W/cm	22.81 W/cm
	$\sigma_{\sigma_{mp}}$	-	0.08 W/cm	0.11 W/cm
26.0 GWdMTU	σ_{mp}	20.7 W/cm	25.00 W/cm	24.99 W/cm
	$\sigma_{\sigma_{mp}}$	-	0.09 W/cm	0.11 W/cm
28.0 GWdMTU	σ_{mp}	21.43 W/cm	27.63 W/cm	28.9 W/cm
	$\sigma_{\sigma_{mp}}$	-	0.07 W/cm	0.12 W/cm
30.0 GWdMTU	σ_{mp}	23.45 W/cm	30.15 W/cm	29.76 W/cm
	$\sigma_{\sigma_{mp}}$	-	0.11 W/cm	0.13 W/cm

Table 9. Summary of the *Maximum Pin Temperature* uncertainty results – joint parameters (MCUQ vs. MP-EUQ vs. SBUQ).

Depletion (irradiation)	STD	MP-EUQ r=50	3rd Order Surrogate 500 samples	Monte Carlo 500 samples
0.0 GWdMTU	σ_{mt}	92 Cº	99 Cº	112 Cº
	$\sigma_{\sigma_{mt}}$	-	8 Cº	10 Cº
0.1 GWdMTU	σ_{mt}	87 Cº	91 Cº	92 Cº
	$\sigma_{\sigma_{mt}}$	-	7 Cº	9 Cº
0.2 GWdMTU	σ_{mt}	85 Cº	94 Cº	92 Cº
	$\sigma_{\sigma_{mt}}$	-	8 Cº	11 Cº
0.5 GWdMTU	σ_{mt}	88 Cº	96 Cº	97 Cº
	$\sigma_{\sigma_{mt}}$	-	8 Cº	9 Cº
1.0 GWdMTU	σ_{mt}	95 Cº	105 Cº	104 Cº
	$\sigma_{\sigma_{mt}}$	-	5 Cº	7 Cº
2.0 GWdMTU	σ_{mt}	94 Cº	106 Cº	105 Cº
	$\sigma_{\sigma_{mt}}$	-	6 Cº	9 Cº
3.0 GWdMTU	σ_{mt}	90 Cº	102 Cº	101 Cº
	$\sigma_{\sigma_{mt}}$	-	9 Cº	10 Cº
4.0 GWdMTU	σ_{mt}	82 Cº	94 Cº	95 Cº
	$\sigma_{\sigma_{mt}}$	-	6 Cº	7 Cº
5.0 GWdMTU	σ_{mt}	79 Cº	90 Cº	95 Cº
	$\sigma_{\sigma_{mt}}$	-	6 Cº	11 Cº
6.0 GWdMTU	σ_{mt}	61 Cº	75 Cº	76 Cº
	$\sigma_{\sigma_{mt}}$	-	5 Cº	11 Cº
7.0 GWdMTU	σ_{mt}	63 Cº	74 Cº	75 Cº
	$\sigma_{\sigma_{mt}}$	-	4 Cº	9 Cº
8.0 GWdMTU	σ_{mt}	60 Cº	75 Cº	75 Cº
	$\sigma_{\sigma_{mt}}$	-	5 Cº	8 Cº
9.0 GWdMTU	σ_{mt}	67 Cº	79 Cº	78 Cº
	$\sigma_{\sigma_{mt}}$	-	8 Cº	9 Cº

Table 9 Continued

10.0 GWdMTU	σ_{mt}	70 C^o	81 C^o	78 C^o
	$\sigma_{\sigma_{mt}}$	-	7 C^o	14 C^o
12.0 GWdMTU	σ_{mt}	68 C^o	80 C^o	81 C^o
	$\sigma_{\sigma_{mt}}$	-	6 C^o	7 C^o
14.0 GWdMTU	σ_{mt}	66 C^o	86 C^o	88 C^o
	$\sigma_{\sigma_{mt}}$	-	11 C^o	12 C^o
16.0 GWdMTU	σ_{mt}	70 C^o	88 C^o	89 C^o
	$\sigma_{\sigma_{mt}}$	-	11 C^o	10 C^o
18.0 GWdMTU	σ_{mt}	70 C^o	92 C^o	91 C^o
	$\sigma_{\sigma_{mt}}$	-	10 C^o	9 C^o
20.0 GWdMTU	σ_{mt}	65 C^o	83 C^o	99 C^o
	$\sigma_{\sigma_{mt}}$	-	11 C^o	13 C^o
22.0 GWdMTU	σ_{mt}	90 C^o	101 C^o	106 C^o
	$\sigma_{\sigma_{mt}}$	-	7 C^o	10 C^o
24.0 GWdMTU	σ_{mt}	79 C^o	107 C^o	109 C^o
	$\sigma_{\sigma_{mt}}$	-	8 C^o	11 C^o
26.0 GWdMTU	σ_{mt}	90 C^o	113 C^o	122 C^o
	$\sigma_{\sigma_{mt}}$	-	9 C^o	10 C^o
28.0 GWdMTU	σ_{mt}	101 C^o	121 C^o	130 C^o
	$\sigma_{\sigma_{mt}}$	-	12 C^o	16 C^o
30.0 GWdMTU	σ_{mt}	101 C^o	119 C^o	139 C^o
	$\sigma_{\sigma_{mt}}$	-	13 C^o	21 C^o

4.6 Case Study: Efficient Uncertainty Quantification for 3-D Core Depletion with Thermal-Hydraulics Feedback (CASL Progression Problem 9)

Problem 9 is a full core Watts Bar Nuclear 1 (WBN1) with neutronics coupled to thermal hydraulics feedback. In this problem both fuel and burnable absorbers are depleted throughout the first cycle. However, due to computational resources limitation, this chapter will perform the uncertainty quantification study upon a part of cycle 1 using a few depletion steps. Specifically, the core is depleted to 160 effective full power days (EFPD) via 9 depletion steps

(0, 9, 32, 45, 60, 80, 100, 120, 160 EFPD). Table 10 shows a summary of the core problem features while Figure 53 represents the layout and enrichment regions of the problem of interest.

As in the previous section [93], the **GF-MPRFA** is used to obtain the reduced dimensional input parameter space in the form of basis of the lower dimensional subspace, which is then used to perform linear uncertainty propagation via the **MP-EUQ.** In addition, the basis is used to construct the surrogate necessary for **SBUQ**. Table 11 show the results of the error test of the 2nd order surrogates in terms of the surrogate form-related uncertainties (defined in Eq.(61)), Root Mean Square (RMS) and the residuals distribution. The surrogate form – related uncertainty is calculated by a Monte Carlo approach where the surrogate parameters are sampled based on the uncertainties estimated by Eq. (61). From the **GF-MPRFA**, a subspace of rank 60 (60 DoFs) is sufficient to capture the variations of the cross-sections in the depletion cycle of interest with an L_2 – norm error upper bound of 1%.

In general, the surrogate quality can be evaluated by examining the residual errors obtained by comparing the responses predicted by the surrogate on one side and the original model on the other side. For example, the current surrogate is constructed for the purpose of uncertainty quantification; therefore, 40 extra random samples generated employing the covariance matrix are used. The perturbations are created in all the parameters simultaneously (cross-sections, grid-loss and gap conductivity), hence, testing the assumption introduced within Eq.(60). Figure 54 through Figure 56 shows the residuals associated with the surrogate computed for different parameter sets which are generated by varying all the parameters simultaneously (i.e. the gap conductivity (h_{gap}), and with perturbations generated employing the covariance library which is the "*44groupcov*" library which is distributed with SCALE6.1[57]). The surrogate

responses are compared to the responses (multiplication factor, maximum pin power, maximum pin temperature) generated via VERA-CS. The figures show that the third order surrogates of the form represented by Eq.(60) can predict the multiplication factor (k_{eff}), maximum pin power, and maximum pin temperature with sufficient accuracy relative to the uncertainty estimation application (refer to Table 12 through Table 14).

Just like the previous section, these surrogates will be used to quantify the uncertainty in the responses on interest (including the surrogate form - related uncertainty) and then compared with the uncertainties estimated via a forward Monte Carlo approach and finally compared with the uncertainty estimated by the **MP-EUQ** (refer to section 4.3).

Figure 57 through Figure 68 and the figures reported in appendix B compare the performance of the VERA-CS based Monte Carlo approach against the surrogate model based Monte Carlo approach (**SBUQ**). Statistical samples are drawn using VERA-CS original models' sequences and then compared to samples drawn from the surrogate model replacing the original VERA-CS. Due to computer resource limitations, Monte Carlo sampling via original model was limited to 50 samples which resulted in large uncertainties associated with limited sampling. First, Appendix B shows the frequency distribution of k_{eff}, maximum fuel pin power and maximum fuel pin temperature due to the gap conductivity uncertainty (±50%) grid spacer loss coefficient (±4%) and nuclear data cross-sections (44groupcov). These figures compares the uncertainties in the multiplication factor (k_{eff}), maximum pin power, and maximum pin temperature due to the four uncertainty sources of interest: gap conductivity coefficient, grid-loss coefficients, nuclear data cross – sections and due to joint samples. Only 3 depletion/time snapshots are presented by the figures reported in Appendix B (0, 80, 160 EFPD). The full comparison is represented by Table 12 through Table 14. Figure 57 through

Figure 68 compare the RoI along with ±σ uncertainty bars as predicted by the original model and the surrogate model at all the depletion steps (mean values ±σ). Details of the uncertainties estimated via the **MP-EUQ** (linear Karhunen Loeve-based approach), **SBUQ** (Monte Carlo sampling 2nd order surrogates) and forward **MCUQ** (Monte Carlo sampling via original model) are shown in Table 12 through Table 14. One can notice that for the multiplication factor (k_{eff}) the uncertainty estimated via the MP-EUQ are within one standard deviation (± σ) of the uncertainties estimated via the Monte Carlo approaches (MCUQ and SBUQ); however, for the maximum fuel pin power and the maximum fuel pin temperature some of the uncertainty values estimated by the **MP-EUQ** are much greater separated than one standard deviation. The reason for that might be due to the fact that the **MP-EUQ** is a linear approach assuming that the response of interest is a linear function of the parameters. The results in Table 12 indicates that the linear assumption is sufficient for the multiplication factor, while Table 13 and Table 14 indicate that the linear assumption is not sufficient for the maximum pin power and maximum pin temperature.

Table 10. Problem 9 features and design properties.

Property	Value	Details
Fuel Assemblies	193	Modeled in quarter symmetry
Enrichment	3.1%, 2.6%, 2.1%	17 Assemblies with 3.1% 19 Assemblies with 2.6% 20 Assemblies with 2.1%
Control Rods	8 banks of B4C	Total of 18 rods in quarter symmetry.
Burnable Inserts	6,12,4,3,2 poison inserts of Pyrex burnable.	These burnable poison inserts consist of 24, 20, 16, 12, 8 rod-lets, respectively.

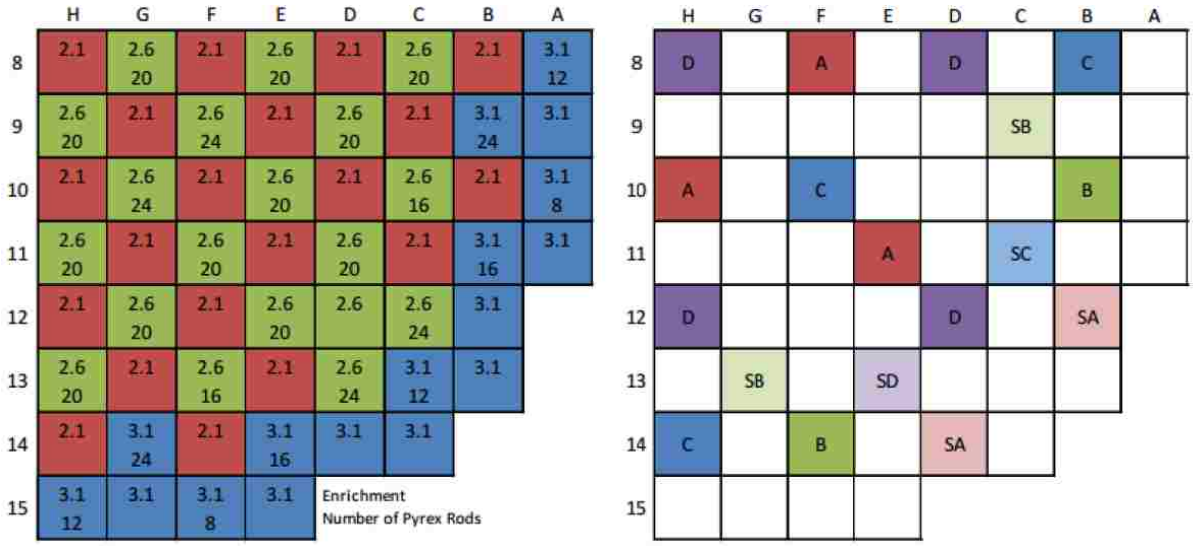

Figure 53. Core layout in quarter symmetry [59].

Table 11. Features of the Surrogate.

Surrogate order	RMS	Number of Construction Data Points	Number of extra Validation Data Points	Residuals distribution	surrogate form – related uncertainty
2nd order	$\varepsilon_{k_{eff}} \rightarrow$ 20.07 pcm	120	30	*iid*	*35.16 pcm*
	$\varepsilon_{P_{max}} \rightarrow$ 0.01 W/cm			*iid*	*0.01* W/cm
	$\varepsilon_{T_{max}} \rightarrow$ 3.0661 C^o			*iid*	*1.12* C^o

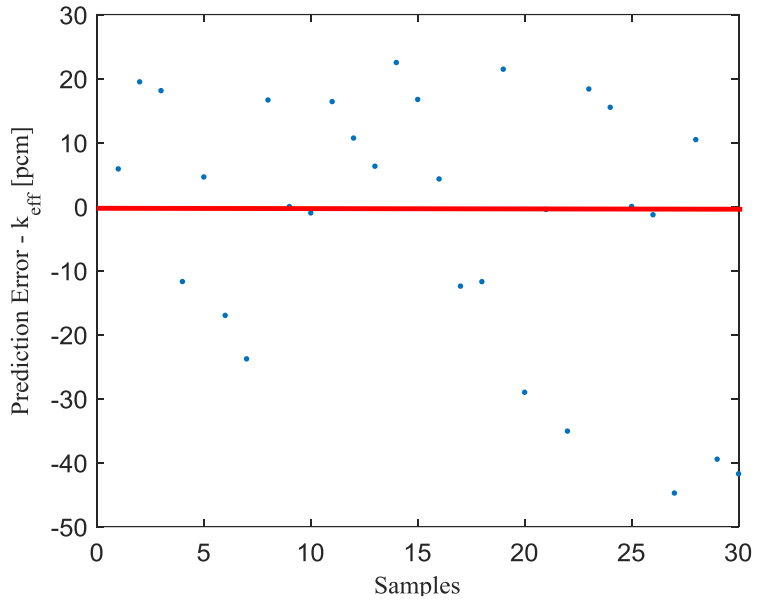

Figure 54. Residuals in predicting the k_{eff} ($\varepsilon_{k_{eff}}$) for a range of the gap conductivity and cross-sections (h_{gap} and $\bar{\Sigma}$) for 30 samples (surrogate vs. VERA-CS).

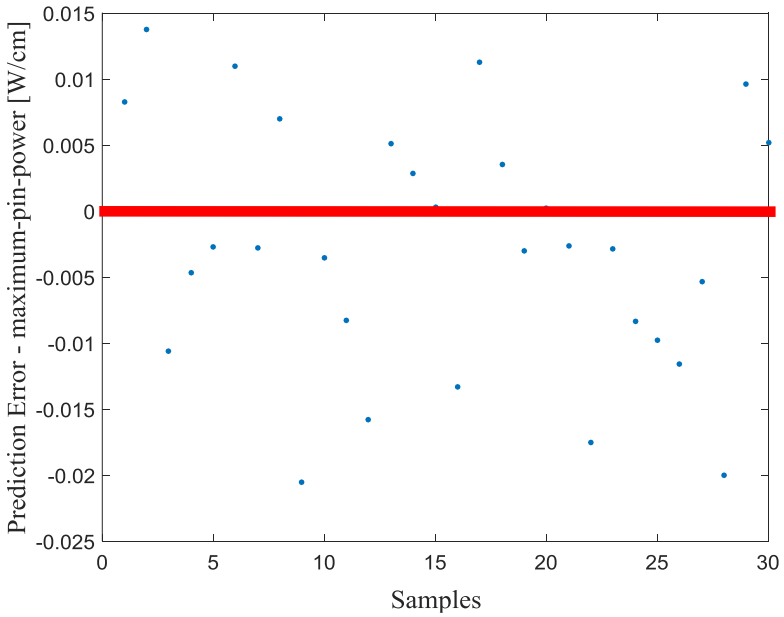

Figure 55. Residuals in predicting the maximum pin power ($\varepsilon_{P_{\max}}$) for a range of the gap conductivity and cross-sections (h_{gap} and $\bar{\Sigma}$) for 30 samples (surrogate vs. VERA-CS).

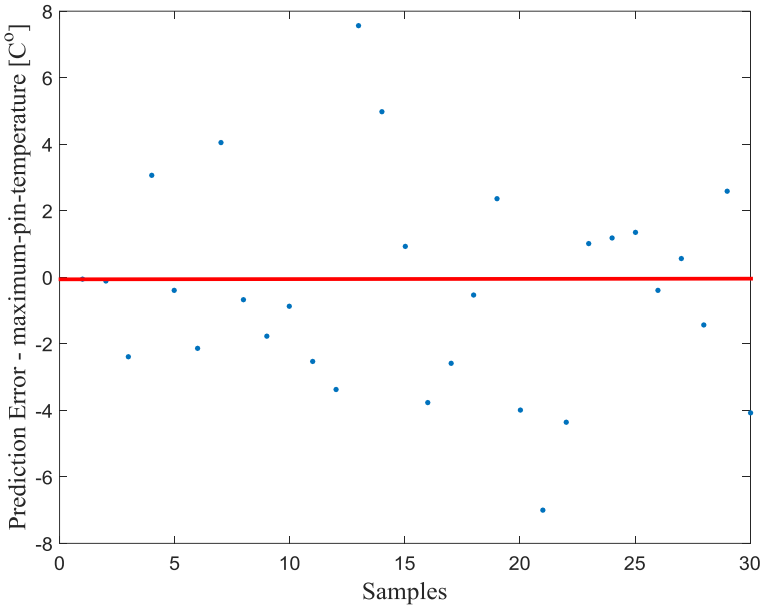

Figure 56. Residuals in predicting the maximum pin temperature ($\varepsilon_{T_{\max}}$) for a range of the gap conductivity and cross-sections (h_{gap} and $\overline{\Sigma}$) for 30 samples (surrogate vs. VERA-CS).

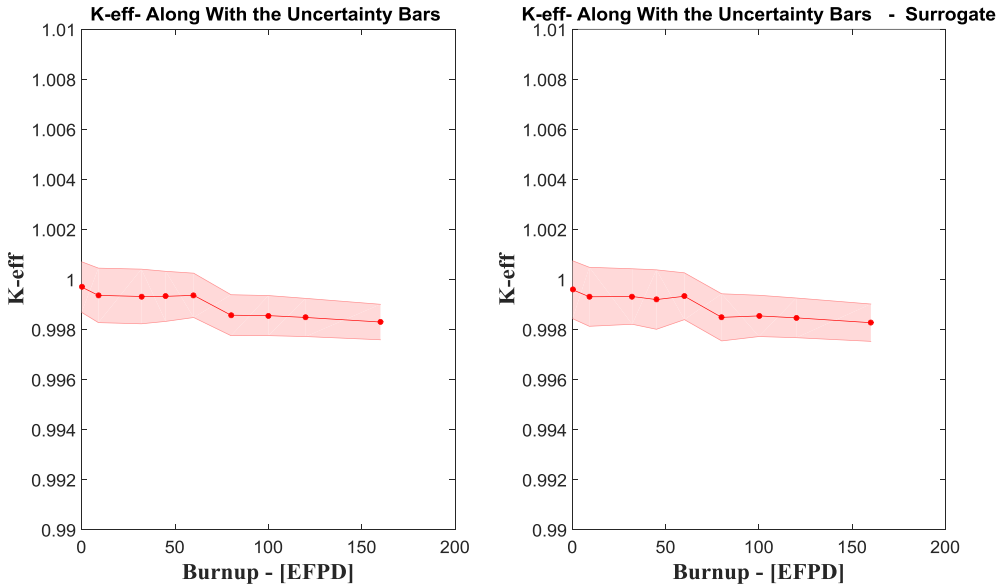

Figure 57. Burnup dependent k_{eff} along with uncertainty ±σ due to the gap conductivity.

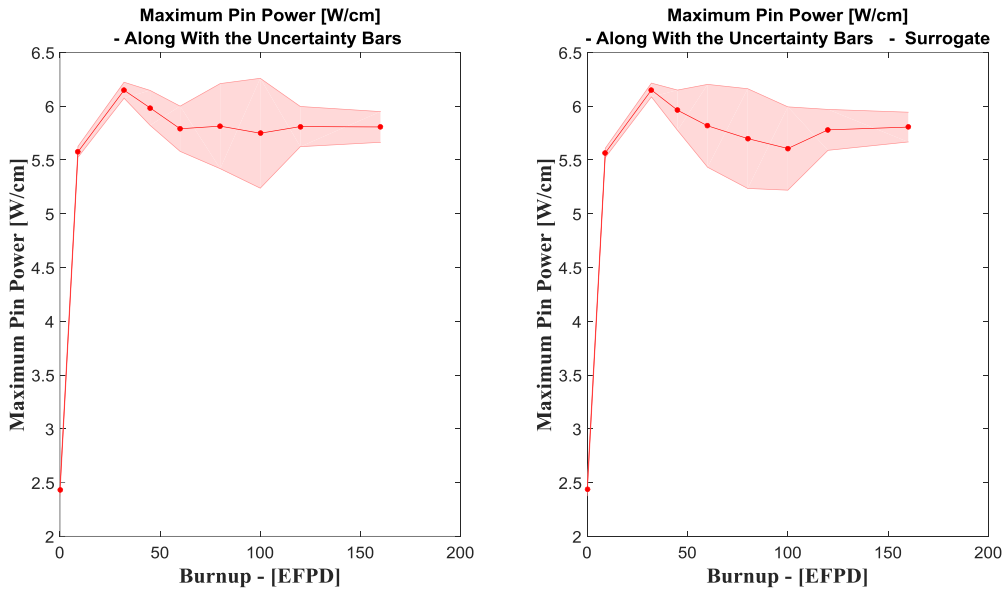

Figure 58. Burnup dependent maximum pin power along with uncertainty ±σ due to the gap conductivity.

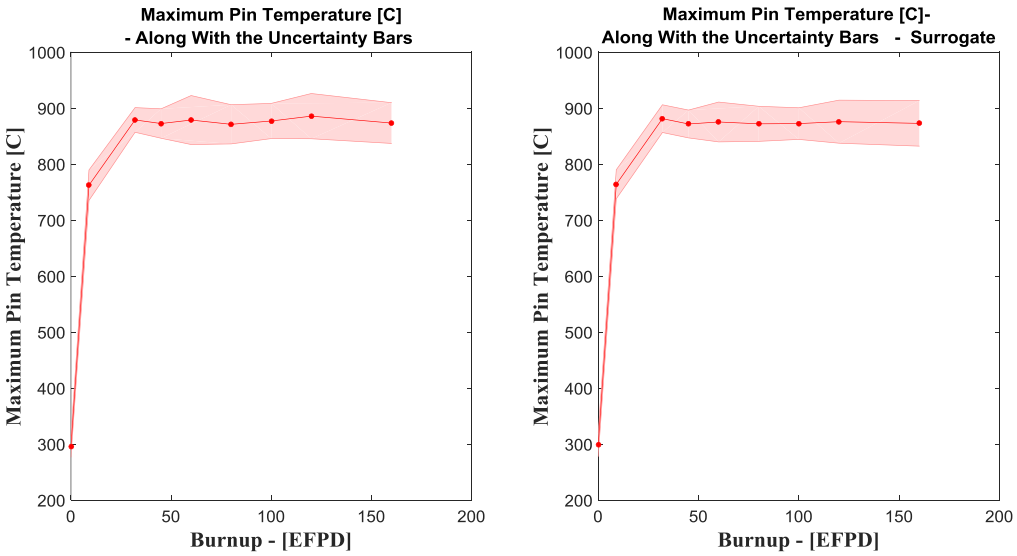

Figure 59. Burnup dependent maximum pin temperature along with uncertainty ±σ due to the gap conductivity.

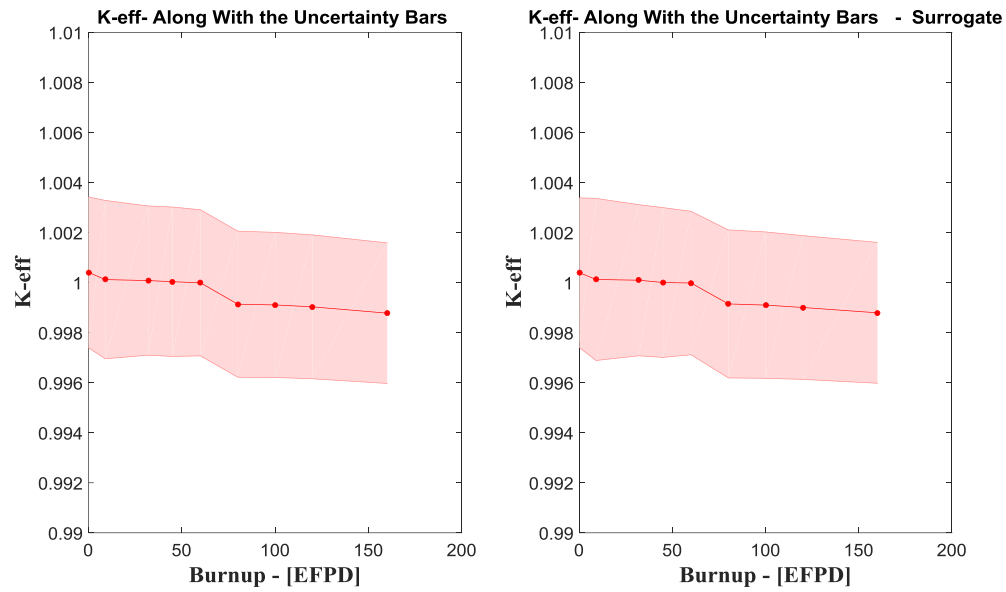

Figure 60. Burnup dependent k_{eff} along with uncertainty ±σ due to the nuclear data cross-sections.

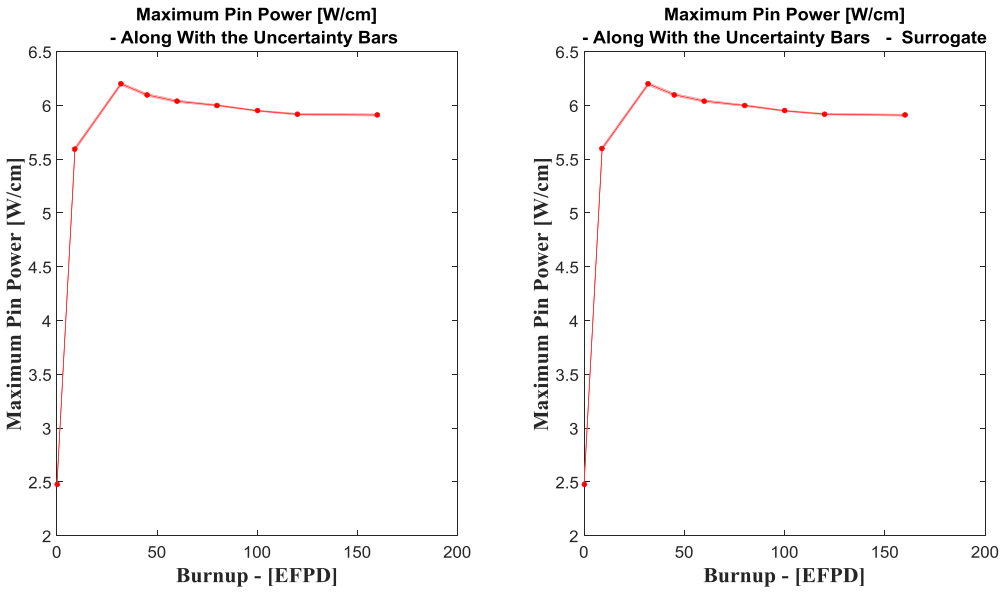

Figure 61. Burnup dependent maximum pin power along with uncertainty ±σ due to the nuclear data cross-sections.

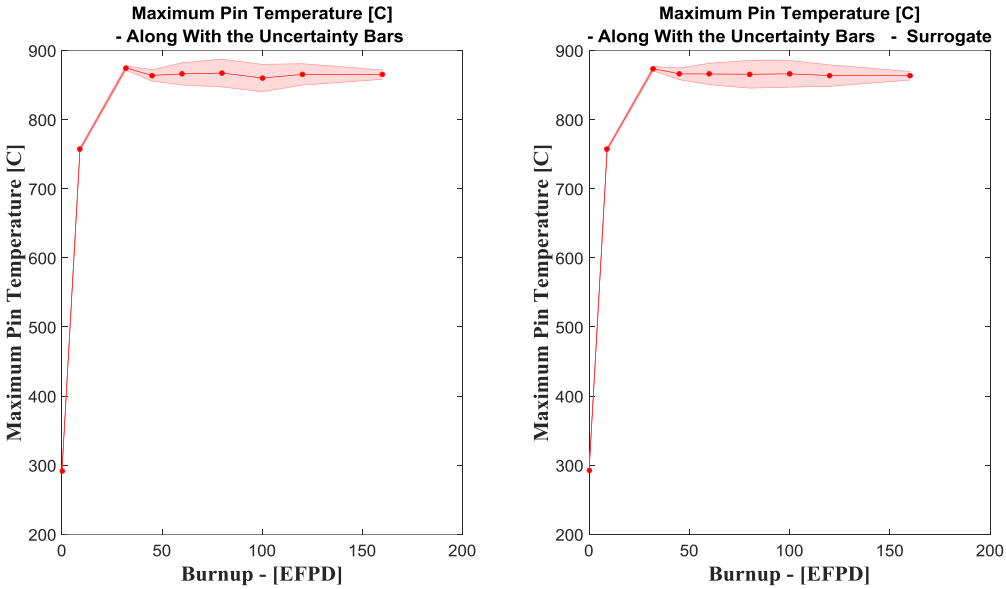

Figure 62. Burnup dependent maximum pin temperature along with uncertainty ±σ due to the nuclear data cross-sections uncertainty.

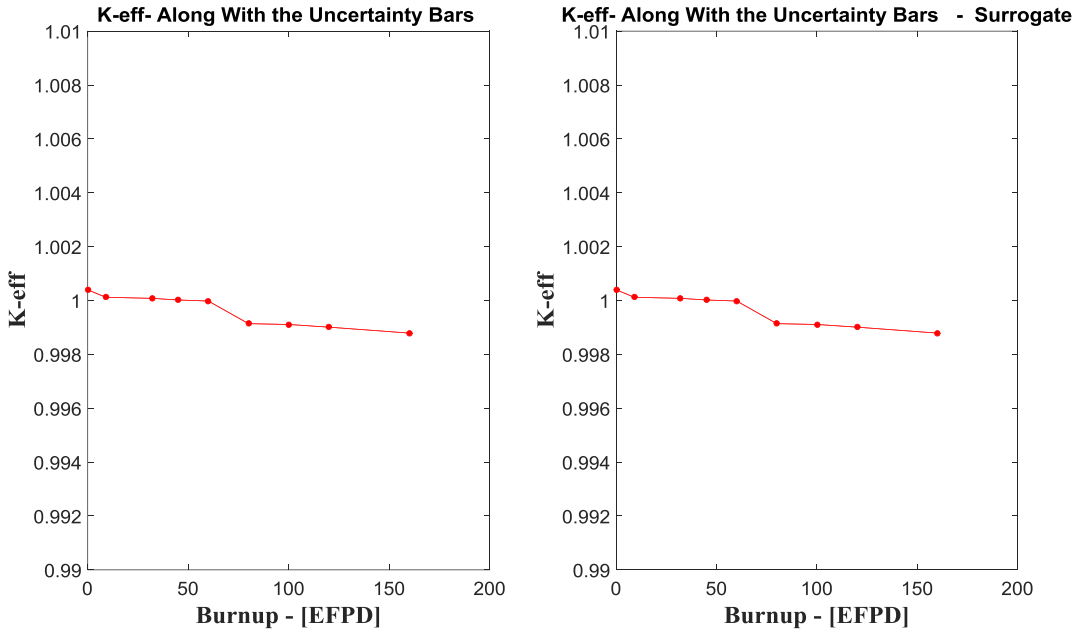

Figure 63. Burnup dependent k_{eff} along with uncertainty ±σ due to the grid-loss coefficient uncertainty.

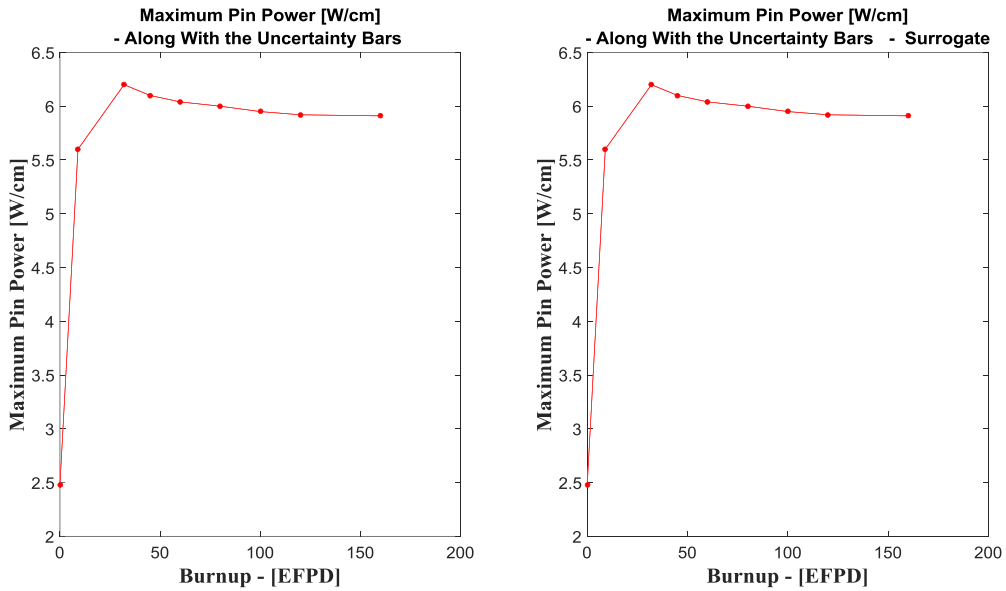

Figure 64. Burnup dependent maximum pin power along with uncertainty ±σ due to the grid-loss coefficient uncertainty.

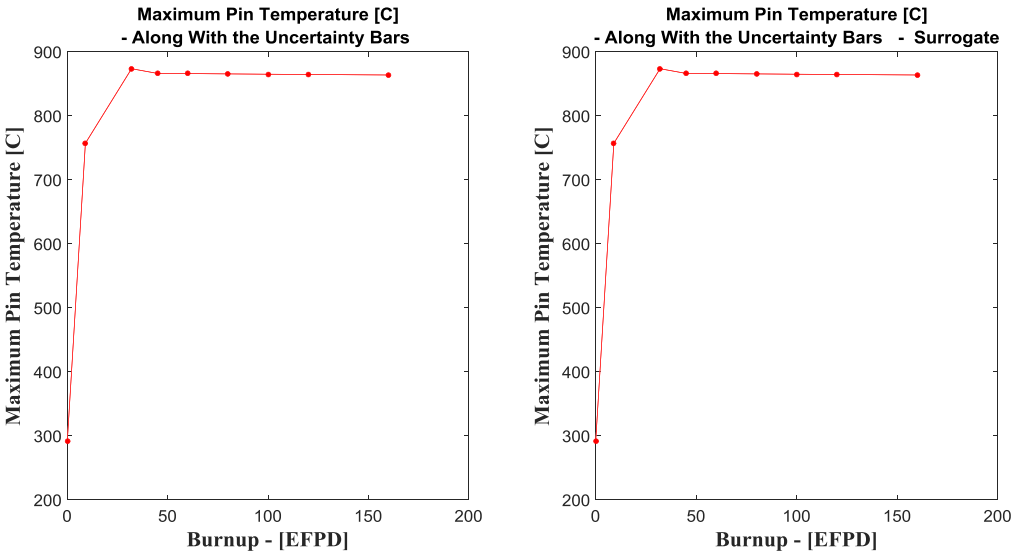

Figure 65. Burnup dependent maximum pin temperature along with uncertainty ±σ due to the grid-loss coefficient uncertainty.

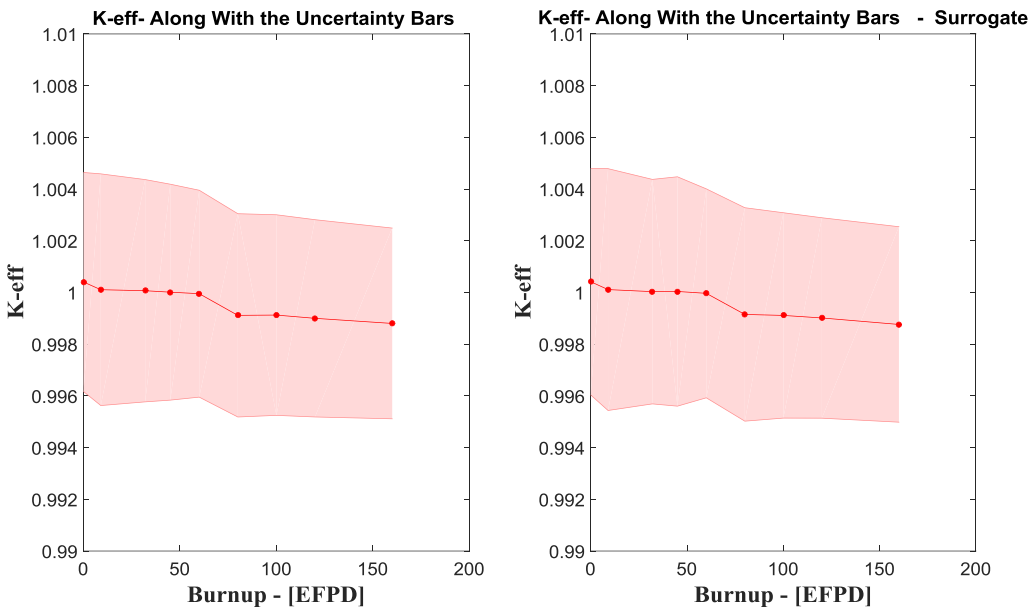

Figure 66. Burnup dependent k_{eff} along with uncertainty ±σ due to joint samples.

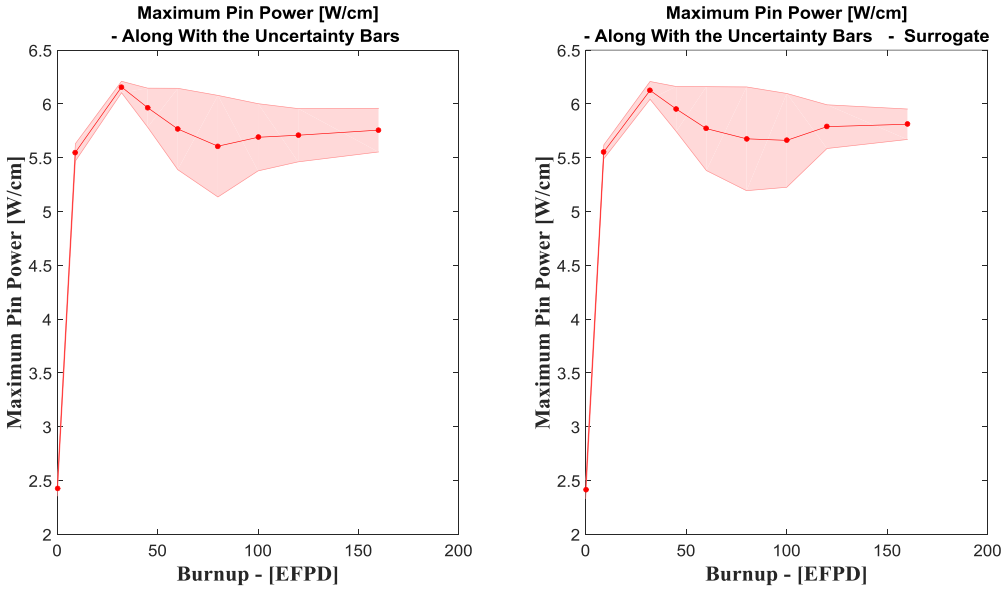

Figure 67. Burnup dependent maximum pin power along with uncertainty ±σ due to joint samples.

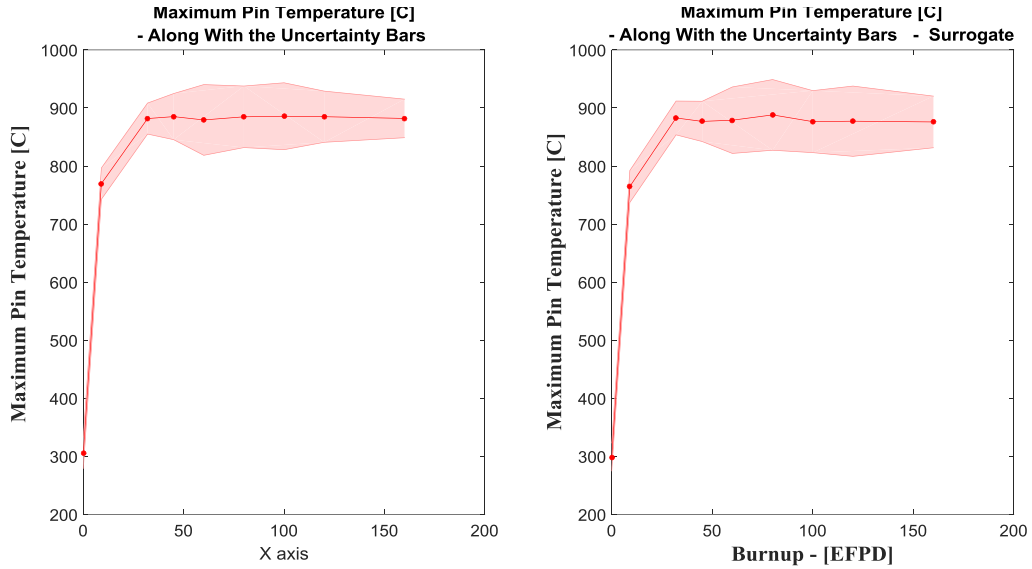

Figure 68. Burnup dependent maximum pin temperature along with uncertainty ±σ due to joint samples

Table 12. Summary of the k_{eff} uncertainty results – joint parameters (MCUQ vs. MP-EUQ vs. SBUQ)

Depletion (irradiation)	STD	MP-EUQ r=60	2nd Order Surrogate 500 samples	Monte Carlo 50 samples
0.0 EFPD	σ_k	389 pcm	425 pcm	401 pcm
	σ_{σ_k}	-	19 pcm	63 pcm
9 EFPD	σ_k	399 pcm	395 pcm	417 pcm
	σ_{σ_k}	-	21 pcm	66 pcm
32 EFPD	σ_k	390 pcm	415 pcm	399 pcm
	σ_{σ_k}	-	25 pcm	74 pcm
45 EFPD	σ_k	380 pcm	420 pcm	398 pcm
	σ_{σ_k}	-	19 pcm	52 pcm
60 EFPD	σ_k	379 pcm	399 pcm	391 pcm
	σ_{σ_k}	-	32 pcm	71 pcm
80 EFPD	σ_k	357 pcm	398 pcm	392 pcm
	σ_{σ_k}	-	23 pcm	65 pcm
100 EFPD	σ_k	351 pcm	394 pcm	390 pcm
	σ_{σ_k}	-	23 pcm	62 pcm
120 EFPD	σ_k	349 pcm	391 pcm	387 pcm
	σ_{σ_k}	-	23 pcm	58 pcm
160 EFPD	σ_k	341 pcm	389 pcm	381 pcm
	σ_{σ_k}	-	26 pcm	46 pcm

Table 13. Summary of the *Maximum Pin Power* uncertainty results – joint parameters (MCUQ vs. MP-EUQ vs. SBUQ).

Depletion (irradiation)	STD	MP-EUQ r=60	2nd Order Surrogate 500 samples	Monte Carlo 50 samples
0.0 EFPD	σ_{mp}	0.06 W/cm	0.081 W/cm	0.083 W/cm
	$\sigma_{\sigma_{mp}}$	-	0.009 W/cm	0.08 W/cm
9 EFPD	σ_{mp}	0.035 W/cm	0.71 W/cm	0.062 W/cm
	$\sigma_{\sigma_{mp}}$	-	0.005 W/cm	0.1 W/cm
32 EFPD	σ_{mp}	0.054 W/cm	0.09 W/cm	0.084 W/cm
	$\sigma_{\sigma_{mp}}$	-	0.011 W/cm	0.12 W/cm
45 EFPD	σ_{mp}	0.16 W/cm	0.21 W/cm	0.186 W/cm
	$\sigma_{\sigma_{mp}}$	-	0.01 W/cm	0.13 W/cm
60 EFPD	σ_{mp}	0.12 W/cm	0.5 W/cm	0.35 W/cm
	$\sigma_{\sigma_{mp}}$	-	0.008 W/cm	0.09 W/cm
80 EFPD	σ_{mp}	0.19 W/cm	0.42 W/cm	0.44 W/cm
	$\sigma_{\sigma_{mp}}$	-	0.011 W/cm	0.14 W/cm
100 EFPD	σ_{mp}	0.21 W/cm	0.38 W/cm	0.42 W/cm
	$\sigma_{\sigma_{mp}}$	-	0.012 W/cm	0.1 W/cm
120 EFPD	σ_{mp}	0.14 W/cm	0.26 W/cm	0.184 W/cm
	$\sigma_{\sigma_{mp}}$	-	0.006 W/cm	0.08 W/cm
160 EFPD	σ_{mp}	0.1 W/cm	0.2 W/cm	0.14 W/cm
	$\sigma_{\sigma_{mp}}$	-	0.001 W/cm	0.05 W/cm

Table 14. Summary of the *Maximum Pin Temperature* uncertainty results – joint parameters (MCUQ vs. MP-EUQ vs. SBUQ).

Depletion (irradiation)	STD	MP-EUQ r=60	2nd Order Surrogate 500 samples	Monte Carlo 50 samples
0.0 EFPD	σ_{mt}	14 C^o	21.7 C^o	19.6 C^o
	$\sigma_{\sigma_{mt}}$	-	0.2 C^o	3 C^o
9 EFPD	σ_{mt}	15 C^o	24.2 C^o	22.7 C^o
	$\sigma_{\sigma_{mt}}$	-	0.19 C^o	3.1 C^o
32 EFPD	σ_{mt}	16 C^o	24 C^o	22.3 C^o
	$\sigma_{\sigma_{mt}}$	-	0.23 C^o	2.9 C^o
45 EFPD	σ_{mt}	18 C^o	28 C^o	26.9 C^o
	$\sigma_{\sigma_{mt}}$	-	0.3 C^o	2.8 C^o
60 EFPD	σ_{mt}	21 C^o	32.1 C^o	32 C^o
	$\sigma_{\sigma_{mt}}$	-	0.7 C^o	3.7 C^o
80 EFPD	σ_{mt}	22 C^o	32 C^o	31 C^o
	$\sigma_{\sigma_{mt}}$	-	0.4 C^o	3.5 C^o
100 EFPD	σ_{mt}	18 C^o	37 C^o	36 C^o
	$\sigma_{\sigma_{mt}}$	-	0.8 C^o	3.9 C^o
120 EFPD	σ_{mt}	19 C^o	40.1 C^o	38 C^o
	$\sigma_{\sigma_{mt}}$	-	0.5 C^o	3.4 C^o
160 EFPD	σ_{mt}	21 C^o	34.8 C^o	33 C^o
	$\sigma_{\sigma_{mt}}$	-	0.6 C^o	2.8 C^o

CHAPTER 5. SURROGATE BASED DATA ASSIMILATION FOR PRESSURIZED WATER REACTORS

Data assimilation is a mathematical methodology used for establishing a connection between experimental and operational data and simulation completed employing mathematical models. Any mathematical model is an approximate representation of the real phenomenon of interest. The purpose of data assimilation is to improve the performance of the mathematical models by calibrating the model's parameters.

Model-based assimilation of experimental measurements (i.e. data assimilation) has been used in various engineering fields for the enhancement of the predictions made by mathematical models and simulations. Section 1.3 reviewed the literature and methodologies commonly used for data assimilation in nuclear engineering and closely related engineering fields [16, 17].

Overall, two major problems were highlighted in section 1.3. First, the computational burden associated with running the high fidelity models (reactor core simulators). Second, the curse of dimensionality associated with the number of model parameters that will need to be calibrated. The computational cost of the data assimilation increases with the number of parameters to be calibrated. In nuclear reactor simulation, the number of neutronics parameters is large due to the fact that the nuclear data cross-sections libraries are detailed for high fidelity modeling and simulation.

Data assimilation utilizing the long operational experience with light water reactors could improve simulation fidelity. In this section the Delayed Rejection Adaptive Metropolis algorithm (DRAM) [15] will be used in conjunction with reduced order modeling, such that

the end result is a practical and applicable algorithm for data assimilation for large scale reactor simulation applications.

Reduced order modeling can facilitate the two major problems noted earlier. Surrogates (such as the reduced order surrogates constructed in chapter 4) can address the first problem (the computational burden associated with running the high fidelity reactor core simulators). On the other hand, reducing the dimensionality of the parameters of interest using the algorithms presented by chapter 2 and chapter 3 will address the second problem (the curse of dimensionality). Ref. [16] introduced high order predictive model calibration algorithm and applied them to relatively large scale applications while Ref. [17] performed data assimilation for few thermal hydraulics parameters of using lower order surrogate to replace the actual thermal hydraulics simulator (i.e. COBRA-TF). This dissertation would use second and third order polynomial surrogate models to substitute for the original coupled models (MPACT-COBRA-TF and ORIGEN). Moreover, in this section, a 3 dimensional depletion problem with thermal-hydraulics feedback considered. Finally, cross-sections (high dimensional parameter) will be calibrated along with the few thermal hydraulics parameters considered here. An assembly problem and a 3 dimensional core problem are used to exemplify the proposed algorithms.

Before discussing the application of ROM in conjunction with DRAM algorithm, a brief summary of the major steps of the DRAM algorithm is represented here as introduced by Ref. [15] (refer to section 1.3 for more details about the notations below):

1. Set an initial state for the parameters of interest (x^0),
2. Determine the number of chain iterates (M),

3. Calculate the term $x^0 = \arg\min_x \sum_{i=1}^{N} \left(v_i - f_i(x)\right)^2$, where v is the observation, f is the representative model, and N the number of observations.

4. Set $SS_{x^0} = \sum_{i=1}^{n} \left(v_i - f_i\left(x^0\right)\right)^2$ and compute the initial variance estimate $s_0^2 = \frac{SS_{x^0}}{n-p}$, and *n-P* is the number of independent DoFs.

5. Estimate the covariance matrix $\mathbf{C} = s_0^2 \left(\chi^T\left(x^0\right)\chi\left(x^0\right)\right)^{-1}$ and $R = chol(\mathbf{C})$ is the Cholesky factorization.

6. For *k=1,..,M*

   a. Sample $z_k \sim N(0,1)$ and update the parameter accordingly $x^* = x^{k-1} + Rz_k$,

   b. Sample $u_\alpha \sim U(0,1)$,

   c. Compute $SS_{x^*} = \sum_{i=1}^{n} \left(v_i - f_i\left(x^*\right)\right)^2$,

   d. Compute $\alpha\left(x^* \mid x^{k-1}\right) = \min\left(1, e^{-\frac{\left(SS_{x^*} - SS_{x^{k-1}}\right)}{2s_{k-1}^2}}\right)$,

   e. If $u_\alpha < \alpha$

   Set $x^k = x^*$ and $SS_{x^k} = SS_{x^*}$,

   Else

   1. Set the design parameter $\gamma_2 = 0.2$,

   2. Sample $z_k \sim N(0,1)$ and update the second stage parameter accordingly

      $x^{*2} = x^{k-1} + \gamma_2 R_k z_k$,

3. Sample $u_\alpha \sim U(0,1)$,

4. Compute $SS_{x^{*2}} = \sum_{i=1}^{N} \left(v_i - f_i\left(x^{*2}\right)\right)^2$,

5. Compute $\alpha_2\left(x^{*2} \mid x^{k-1}, x^*\right) = \min\left(1, \frac{\pi\left(x^{*2} \mid v\right) J\left(x^* \mid x^{*2}\right)\left(1-\alpha\left(x^* \mid x^{*2}\right)\right)}{\pi\left(x^{k-1} \mid v\right) J\left(x^* \mid x^{k-1}\right)\left(1-\alpha\left(x^* \mid x^{k-1}\right)\right)}\right)$,

where *J* is the proposal distribution.

6. If $u_\alpha < \alpha_2$

Set $x^k = x^{*2}$ and $SS_{x^k} = SS_{x^{*2}}$,

Else

Set $x^k = x^{k-1}$ and $SS_{x^k} = SS_{x^{k-1}}$,

End if

End if

f. Update $s_k \sim Inv-gamma\left(a_{val}, b_{val}\right)$, where *Inv-gamma* is the inverse gamma distribution and:

$a_{val} = 0.5\left(n_s + n\right)$ and $b_{val} = 0.5\left(n_s \sigma_s^2 + SS_{q^k}\right)$, where $n_s = 2\alpha$ and n is the number of measurements used.

g. If $\mathrm{mod}\left(k, k_0\right) = 1$

Update $\mathbf{C}_k = s_p \,\mathrm{cov}\left(x^0, x^1, \ldots, x^k\right)$, where s_p is a design parameter that is a function of the dimension (*p*) of the parameter space (2.38^2/p is commonly used)

Else

$\mathbf{C}_k = \mathbf{C}_{k-1}$,

End if

h. Update $R_k = chol\left(\mathbf{C}_k\right)$,

From the algorithm above one can notice that several steps makes DRAM limited to small-medium dimensionality problems with reasonable computational cost. Steps 3, 4, 6.c and 6.e.4 require the evaluation of f (the model of interest). If the model is complex and characterized with high computational cost, then these steps will hinder the practicality of the DRAM algorithm. Therefore, in this section a subspace-based surrogate model ($\tilde{f}$) will be used to replace the model of interest (f). Section 1.5.3 introduced a methodology previously developed for goal-oriented surrogate modeling. In this section the **GF-MPRFA** will be used to construct the basis of the lower dimensional subspace approximation. Once, the basis is determined ($\mathbf{U}$), a 3rd order goal-oriented subspace can be constructed as follow:

$$f \approx \tilde{f} = \bar{S}_1^T \Delta\bar{x} + \left(\bar{S}_2^T \Delta\bar{x}\right)^2 + \left(\bar{S}_3^T \Delta\bar{x}\right)^3$$

where f is the response of interest (e.g. multiplication factor, maximum fuel pin power and maximum fuel pin temperature), a $\Delta\bar{x}$ is the variation in the parameters of interest from the reference values (e.g. cross-sections, gap conductivity and grid loss coefficient).

In order to reduce the number of model runs required to construct the surrogate form, the **GF-MPRFA** is used to calculate the basis matrix ($\mathbf{U}$) of the lower dimensional subspace approximation for the parameters space. The goal of the surrogate here is to perform data assimilation analysis. Therefore, the uncertainty and mean of each parameter might be updated hence the **GF-MPRFA** must take this into consideration. In chapter 4, the goal-oriented surrogate was constructed via perturbations generated along the covariance data (refer to

sections 4.3 and 4.4). In this section, the application of interest implies that the perturbations ($\Delta\bar{x}$) be generated randomly within the interval of interest.

An efficient goal-oriented surrogate can be constructed as follow:

$$f \approx \tilde{f} = \overbrace{\bar{\beta}_1^T}^{\bar{\beta}_{1,r}^T}\mathbf{U}\overbrace{\mathbf{U}^T\Delta\bar{x}_{rand}}^{\Delta\bar{\alpha}} + \left(\overbrace{\bar{\beta}_2^T}^{\bar{\beta}_{2,r}^T}\mathbf{U}\overbrace{\mathbf{U}^T\Delta\bar{x}_{rand}}^{\Delta\bar{\alpha}}\right)^2 + \left(\overbrace{\bar{\beta}_3^T}^{\bar{\beta}_{3,r}^T}\mathbf{U}\overbrace{\mathbf{U}^T\Delta\bar{x}_{rand}}^{\Delta\bar{\alpha}}\right)^3 \\ = \bar{\beta}_{1,r}^T\Delta\bar{\alpha} + \left(\bar{\beta}_{2,r}^T\Delta\bar{\alpha}\right)^2 + \left(\bar{\beta}_{3,r}^T\Delta\bar{\alpha}\right)^3 \tag{62}$$

where $\Delta\bar{x}_{rand}$ is a random input vector sampled to generate a random sample of the input parameter. Given that $\mathbf{U}\in\mathbb{R}^{nxr}$ and $\Delta\bar{\alpha}=\mathbf{U}^T\Delta\bar{x}_{rand}\in\mathbb{R}^r$ then $\bar{\beta}_{1,r}^T=\bar{\beta}_1^T\mathbf{U}\in\mathbb{R}^r$ $\bar{\beta}_{2,r}^T=\bar{\beta}_2^T\mathbf{U}\in\mathbb{R}^r$ and $\bar{\beta}_{3,r}^T=\bar{\beta}_3^T\mathbf{U}\in\mathbb{R}^r$. Hence in order to determine the unknown elements of $\bar{\beta}_{1,r}$, $\bar{\beta}_{2,r}$ and $\bar{\beta}_{3,r}$ the model needs to be run 3*r* times so that the coefficients are determined.

Moreover, in the calculation of the posterior Probability Density Function (PDF) via Eq.(1) , the computational cost of calculating the denominator is dependent on the dimensionality of the parameter space $\mathbb{R}^p$ (i.e. *p*). Hence, by recasting the problem into a lower dimensional subspace approximation (i.e. $\mathbb{R}^r$), the number of calibrated parameters is reduced from *p* to *r*, where the uncertainty information can be mapped from the reduced space to the full dimensional space as follow:

$$\mathbf{C}_x = \mathbf{U}\mathbf{C}_\alpha\mathbf{U}^T \tag{63}$$

where $\mathbf{C}_x$ is the covariance matrix in the full dimensional parameter space and $\mathbf{C}_\alpha$ is the covariance in the reduced space as determined by the assimilation process. In addition to that, running the data assimilation analysis using the surrogate model has a negligible computational

cost compared to the computational cost associated with simulating using the original model (high fidelity simulator).

The following is a summary of the algorithm for Subspace-Based Data Assimilation (**SBDA**):

1. Construct the basis of the lower dimensional subspace approximation of the parameter space (**U**).
2. Construct the goal-oriented surrogate model ($\tilde{f}$).
3. Run DRAM with the surrogate model $\tilde{f}$ and replace the input parameter space ($\mathbb{R}^p$) with the reduced space $\mathbb{R}^r$.

In the following sections, the **SBDA** will be used to perform parameters' calibrations. The parameters of interest are the nuclear data cross-sections (high dimensional parameter) and two thermal-hydraulics parameters (gap conductivity and grid loss coefficients). In this dissertation, we deal with the data assimilation algorithm (i.e. DRAM) as a black box, the real contribution is by replacing the original high fidelity model with a surrogate that has negligible computational cost to run.

5.1 Case Study: Efficient Data Assimilation for 3-Dimensional Assembly Depletion with Thermal-Hydraulics Feedback (CASL Progression Problem 6)

In this case study a few parameters calibration is performed via the **SBDA.** The core simulator of interest is VERA-CS (refer to section 1.7). Figure 6 presents the models that makeup VERA-CS. Referring to the figure; the parameters of interest - in this case study – are the gap conductivity (h_{gap}) and the grid loss coefficient (g_{loss}). These two parameters

represents the **Z**-space in Figure 6. In addition, the nuclear data cross-sections will be calibrated along with the **Z**-space parameters. The cross-section parameters are represented by the **X**-space in Figure 6**.** In this example the cross-sections of interest are the fission, absorption and scattering cross sections for a few isotopes as summarized in Table 18. The number of energy groups used by the VERA-CS cross-sections library is 47. Therefore, the number of parameters to be calibrated is 846 cross-section parameters and two thermal-hydraulics parameters. The DRAM – QUESO algorithm (encoded in DAKOTA 6.2 [78, 79]) will be employed to solve the inverse problem using 100,000 samples per chain.

First, the goal oriented surrogate is constructed in the form represented by Eq.(62). The surrogate is constructed as described in section 4.4 and evaluated via examining the norm of residuals and their distribution. In this case study, the measured attributes are: the multiplication factor (k_{eff}), the coolant inlet temperature (T_{inlet}), the coolant outlet temperature (T_{outlet}), and the fission reaction rate at the fuel assembly center (FR). In this case study, synthetic data will be used instead of real data. Using the synthetic data implies that the actual solution of the data assimilation problem is known a priori enabling the data assimilation method to be verified. Five depletion steps are used to generate the synthetic measurements of interest. Hence, each responses is measured at each of the depletion step (0.0, 0.1, 5, 10, 30 GWd/MTU). Table 16 summarizes the measurements and their uncertainties.

The problem of interest is the same as the assembly problem described in section 4.4. The surrogate will be constructed similarly with the difference that the perturbations are generated randomly within the interval of interest (h_{gap} *(±50%)* g_{loss} *(±4%)* cross-sections (±5%)). The surrogate form-related uncertainty (refer to

Table 15 for details about the surrogate error analysis) is incorporated in the overall measurement uncertainty as follow:

$$\mathbf{C}_f = \mathbf{C}_{q\to f} + \mathbf{C}_{surrogate\to f} \tag{64}$$

where $\mathbf{C}_{surrogate\to f}$ is the surrogate form variance and $\mathbf{C}_{q\to f}$ is the variance in the response due to the parameter set q and $\mathbf{C}_f$ is the overall variance.

Figure 69 through Figure 71 present the residual errors along with their distribution. For the surrogate model to be useful, the residual errors need to be an order of magnitude smaller than the experimental uncertainties.

The surrogate is then used for simultaneous calibration of the thermal-hydraulics parameters along with the cross-sections of interest. The synthetic measurements are generated via the high fidelity simulator (VERA-CS) where specific known parameter's perturbations are used. Therefore, as noted above the ideal solution to the data assimilation problem is known a priori and the performance of the **SBDA** can be evaluated by comparing the known perturbations and the mean variations generated by DRAM in conjunction with the surrogate (**SBDA**). The responses estimated by VERA-CS are considered as synthetic measurements to be assimilated.

For the thermal-hydraulics parameters, a uniform distribution was used as a priori distribution sampled using the uncertainties reported in

Table 19 with the reference values of the parameters. Figure 73 and Figure 74 shows the chains and their distributions for the thermal-hydraulics parameters (grid loss coefficient and gap conductivity). Figure 75 indicates that there is no correlation between the gap conductivity (h_{gap}) and the grid loss coefficient (g_{loss}). From chapter 4, it was noticed that the multiplication factor is not sensitive to the grid loss coefficient. Therefore, the variations in the grid loss coefficient are not identifiable using the current responses of interest. Moreover, it was found that the effect of the grid spacer loss coefficient is the weakest among all other parameters regarding the other responses of interest (coolant inlet temperature, coolant outlet temperature and the fission rate at the reactor center).

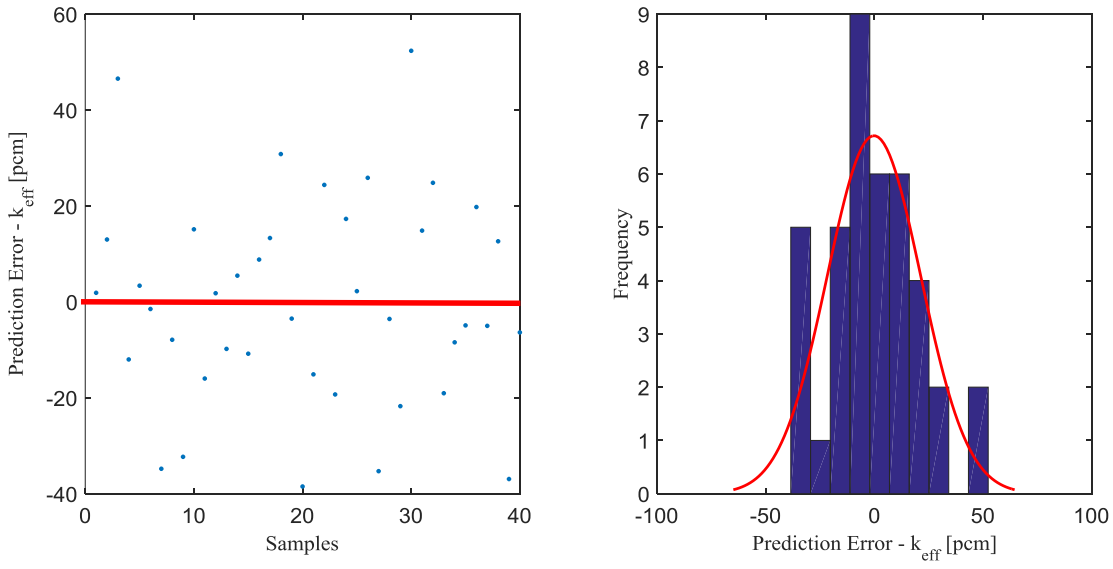

Figure 69. Residual errors along with their distribution - $k_{eff.}$

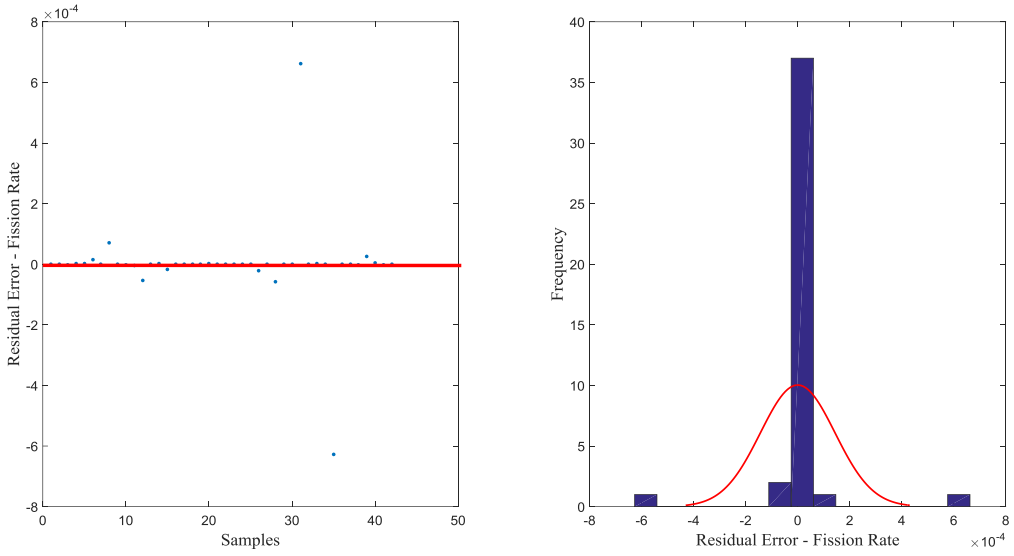

Figure 70. Residual errors along with their distribution – Fission Rate (*FR*).

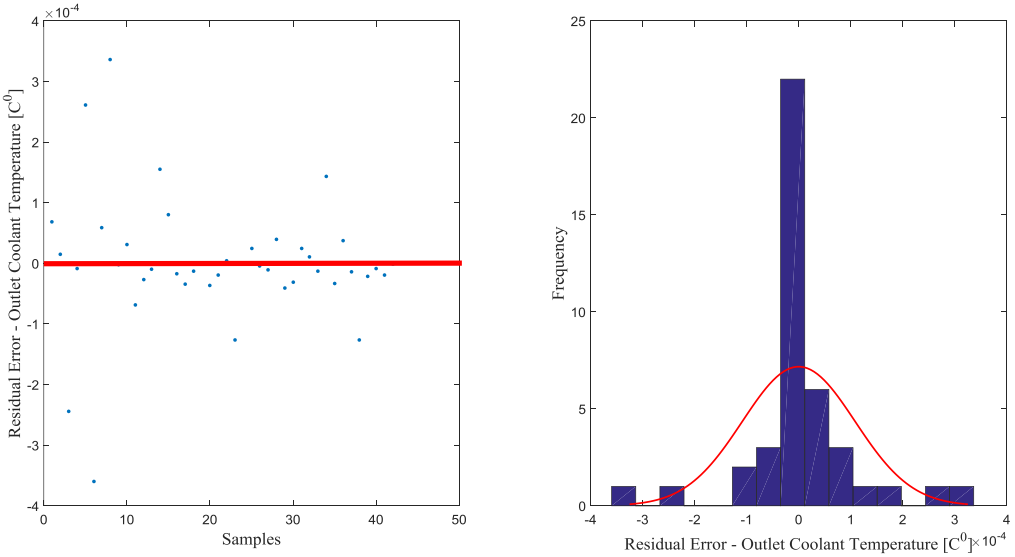

Figure 71. Residual errors along with their distribution – Outlet Coolant Temperature (T_{outlet}).

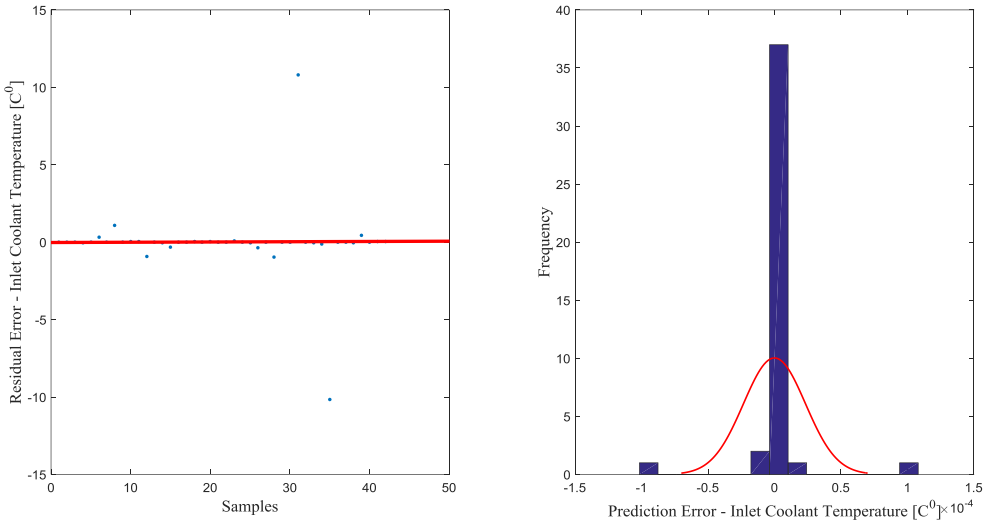

Figure 72. Residual errors along with their distribution – Inlet Coolant Temperature (T_{inlet}).

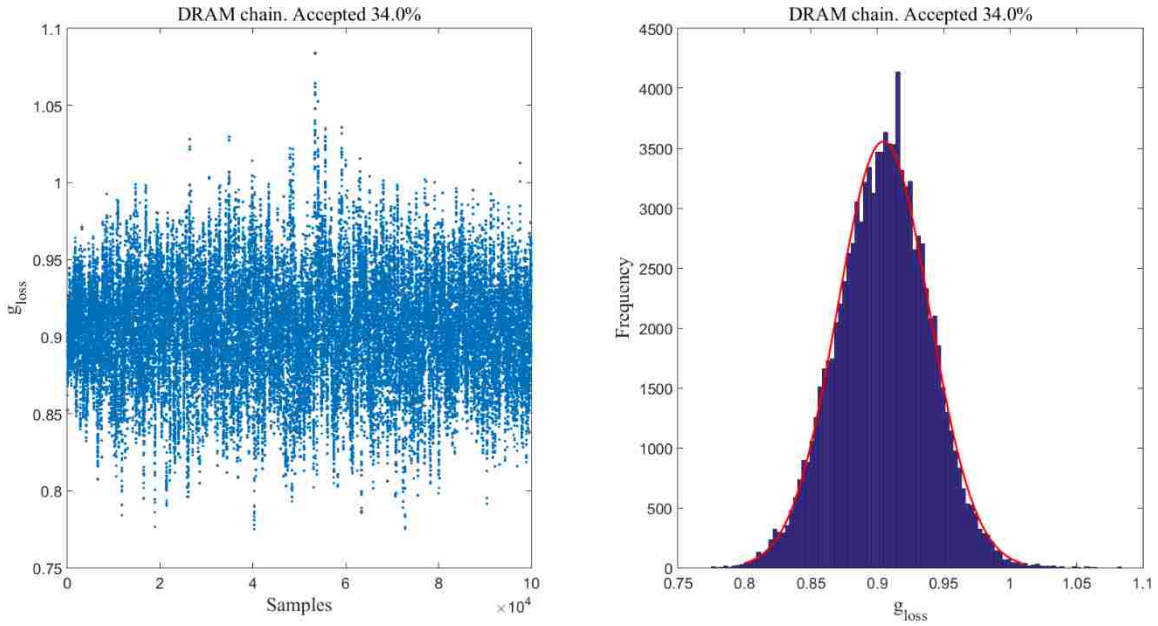

Figure 73. Chain and posterior distribution of the grid loss coefficient (g_{loss}).

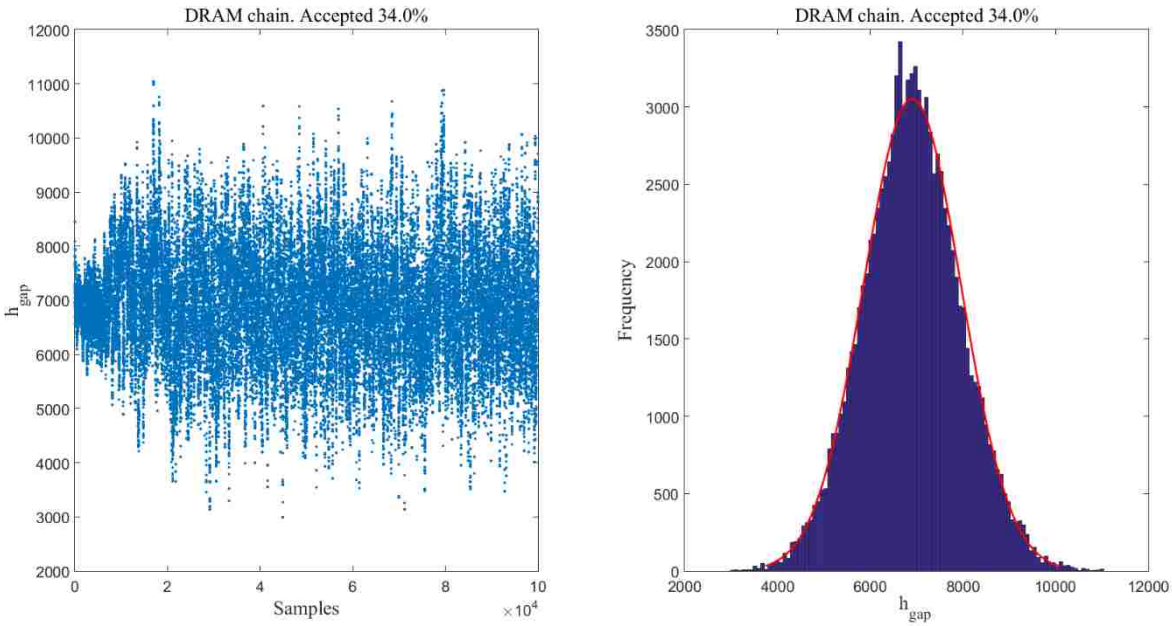

Figure 74. Chain and posterior distribution of the gap conductivity (h_{gap}).

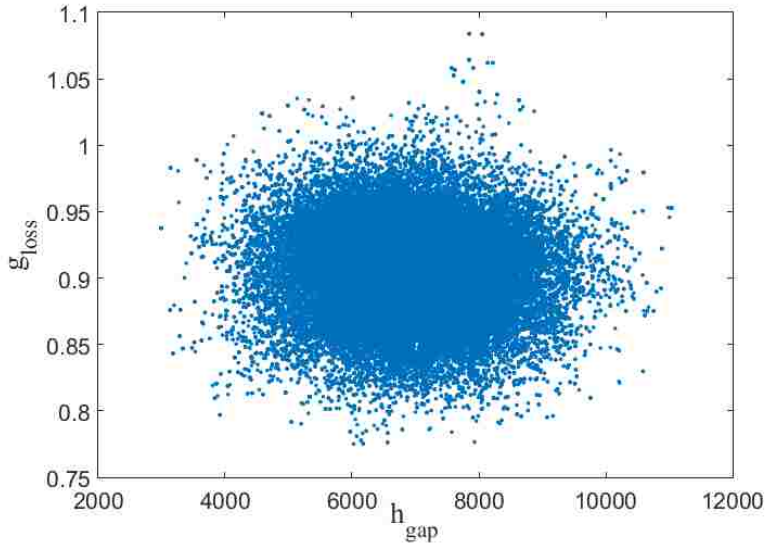

Figure 75. Correlation between the gap conductivity (h_{gap}) and the grid loss coefficient (g_{loss}).

Table 15. Surrogate features.

Surrogate order	RMS	Construction Data Points	Validation Points	Residuals distribution	surrogate form – related uncertainty
3rd order	$\varepsilon_{k_{eff}} \rightarrow$ 22.3 [pcm]	180	40	$k_{eff} \rightarrow$ i.i.d	0.01 [pcm]
	$\varepsilon_{T_{out}} \rightarrow$ 0.000016 [C^o]			$T_{outlet} \rightarrow$ i.i.d	0.00031 [C^o]
	$\varepsilon_{T_{inlet}} \rightarrow$ 0.000004 [C^o]			$T_{inlet} \rightarrow$ i.i.d	0.0021 [C^o]
	$\varepsilon_{FR} \rightarrow$ 0.000022			$FR \rightarrow$ i.i.d	0.008

Table 16. Measurements and their uncertainties

Measurement	0.0 GWd/MTU	0.1 GWd/MTU	5 GWd/MTU	10 GWd/MTU	30 GWd/MTU
k_{eff}	1.243546 ±0.00596	1.2005734 ±0.00568	1.13999 ±0.00531	1.08474 ±0.00524	0.921887 ±0.00641
T_{outlet} [C^0]	325.307 ±0.0077	325.288 ±0.0051	325.263 ±0.00409	325.311 ±0.00473	325.220 ±0.0058
T_{inlet} [C^0]	291.932 ±0.0012	291.942 ±0.00095	291.982 ±0.0008	292.0124 ±0.00143	292.211 ± 0.00101
FR	1.4050 ±0.0102	1.3262 ±0.0071	1.13510 ±0.002	1.07830 ±0.0025	0.872 ±0.0014

In the case of nuclear data cross-sections a Gaussian prior distribution based on the covariance library (44groupcov) [57] is used. A total of 18 different isotope-reaction pairs are considered for calibration. Taking into account that the surrogate uses 47 group structure (refer to Table 17), the number of cross-sections parameters is 18x47 = 846 (refer to Table 18). In

order to evaluate the performance of the **SBDA** the actual perturbation (which is known) is compared with the perturbation expected by the **SBDA**. A consolidated metric is defined to evaluate the performance of the **SBDA** with calibrating the cross-sections parameters. The metric calculates the average difference between the actual and estimated perturbation:

$$\varepsilon_{x,i}^{DA} = \frac{\sum_{g}^{G} \frac{\Delta\Sigma_{x,\mathrm{g}}^{i,syn} - \Delta\Sigma_{x,\mathrm{g}}^{i,DA}}{\Delta\Sigma_{x,\mathrm{g}}^{i,syn}}}{G} \tag{65}$$

where $\varepsilon_{x,i}^{DA}$ is the assimilation performance metric for the interaction x and the i^{th} isotope while $\Delta\Sigma_{x,\mathrm{g}}^{i,syn}$ is the synthetic variation for the x^{th} reaction, the g^{th} energy group and the i^{th} isotope. $\Delta\Sigma_{x,\mathrm{g}}^{i,DA}$ is the variation predicted by the **SBDA**, for x^{th} reaction, g^{th} energy group and i^{th} isotope. G is the number of energy groups considered. Table 18 reports the average difference ($\varepsilon_{x,i}^{DA}$) along with the maximum difference between the actual perturbation and the one estimated by the **SBDA**. The maximum average difference (refer to Eq.(65)) is 3.8% occurring for the Fe-56 absorption cross-sections. Table 19 summarizes the data assimilation results for a few important parameters including the two thermal-hydraulics parameters.

Table 17. 47 group structure.

g	*Energy Boundary*	*g*	*Energy Boundary*	*g*	*Energy Boundary*	*g*	*Energy Boundary*
1	20 MeV	13	78.9 eV	25	2.3824 eV	37	0.5032 eV
2	6.0653 MeV	14	47.8512 eV	26	1.8554 eV	38	0.35767 eV
3	3.6788 MeV	15	29.023 eV	27	1.4574 eV	39	0.2705 eV
4	2.2313 MeV	16	13.71 eV	28	1.2351 eV	40	0.18443 eV
5	1.3534 MeV	17	12.099 eV	29	1.1664 eV	41	0.14572 eV
6	0.8208 MeV	18	8.3153 eV	30	1.1254 eV	42	0.11157 eV
7	4.9787 MeV	19	7.33822 eV	31	1.0722 eV	43	0.08197 eV
8	0.1832 MeV	20	6.47602 eV	32	1.0137 eV	44	0.0569 eV
9	67.38 KeV	21	5.715 eV	33	0.97100 eV	45	0.0428 eV
10	9.119 KeV	22	5.04348 eV	34	0.9099 eV	46	0.0306 eV
11	2.0347 KeV	23	4.4509 eV	35	0.7821 eV	47	0.0124 eV
12	0.13 KeV	24	3.9279 eV	36	0.62506 eV	-	-

Table 18. Assimilation performance measure for the various cross-sections parameters being calibrated.

Parameter	Value	Maximum Estimation Difference $\left(\Delta\Sigma_{x,\mathrm{g}}^{i,syn}-\Delta\Sigma_{x,\mathrm{g}}^{i,DA}\right)/\Delta\Sigma_{x,\mathrm{g}}^{i,syn}$
$\varepsilon_{f,U\text{-}235}^{DA}$	1.7%	1.9% [$g=10$]
$\varepsilon_{f,U\text{-}238}^{DA}$	1.5%	3.1% [$g=14$]
$\varepsilon_{f,Pu\text{-}239}^{DA}$	3%	2.1% [$g=31$]
$\varepsilon_{s,O\text{-}16}^{DA}$	2.3%	2.8%[$g=9$]
$\varepsilon_{s,H\text{-}1}^{DA}$	3.1%	2.1%[$g=37$]
$\varepsilon_{f,Pu\text{-}240}^{DA}$	2.1%	2.3%[g=16]
$\varepsilon_{a,Xe\text{-}134}^{DA}$	1.7%	2.5%[$g=23$]
$\varepsilon_{a,B\text{-}10}^{DA}$	0.89%	1.1% [$g=22$]
$\varepsilon_{a,Xe\text{-}130}^{DA}$	0.9%	1.4%[$g=28$]
$\varepsilon_{a,Y\text{-}90}^{DA}$	3%	2.9%[$g=20$]
$\varepsilon_{a,Y\text{-}91}^{DA}$	2.7%	2.9%[$g=12$]
$\varepsilon_{a,Zr\text{-}90}^{DA}$	3.2%	3.5%[$g=1$]
$\varepsilon_{s,Fe\text{-}56}^{DA}$	1.8%	3.8%[$g=43$]
$\varepsilon_{s,Mn\text{-}55}^{DA}$	1.6%	1.9%[$g=32$]
$\varepsilon_{a,Na\text{-}23}^{DA}$	0.97%	1.9%[$g=40$]
$\varepsilon_{f,Pu\text{-}238}^{DA}$	1.8%	1.9%[$g=45$]
$\varepsilon_{f,Pu\text{-}241}^{DA}$	2.3%	3.4%[$g=24$]
$\varepsilon_{f,U\text{-}236}^{DA}$	2.7%	3.2%[$g=12$]

Table 19. Data assimilation results for a few important parameters.

Parameter	Reference Value	Actual Perturbed Value	SBDA Estimated Perturbation
h_{gap}	5678.3 ± 2250	6835.02	6846.2 ± 901.86
g_{loss}	0.907 ± 0.03628	0.92206	0.909 ± 0.03478
Σ_f^{U-235} [0.0306-0.012396] eV	1125.219 ±2.66	1258.435	1270.231 ± 1.99
Σ_f^{U-238} [2.2313-1.3534] MeV	0.8927011±0.00528	0.93246	0.9013 ± 0.00387
Σ_f^{Pu-239} [0.0306-0.012396] eV	1361.297± 34.51	1441.313	1434.458 ± 27.13
Σ_s^{H-1} [0.0306-0.012396] eV	75.346183±0.07494	82.47610	79.208 ± 0.0569
Σ_s^{O-16} [0.0306-0.012396] eV	4.329821±0.04336	4.629821	4.5891 ± 0.02981

5.2 Case Study: Efficient Data Assimilation for 3-Dimensional Core Wide Depletion with Thermal-Hydraulics Feedback. CASL Progression Problem 9.

In this case study a few parameters calibration is performed via the **SBDA.** The core simulator of interest is VERA-CS (refer to section 1.7). Figure 6 presents the models that makeup VERA-CS. Referring to the figure; the parameters of interest - in this case study – are the gap conductivity (h_{gap}), and the grid loss coefficient (g_{loss}). These two parameters represent the **Z**-space in Figure 6. In addition, the nuclear data cross-sections will be calibrated along with the **Z**-space parameters. The cross-section parameters are represented by the **X**-space in Figure 6**.** In this example the cross-sections of interest are the fission, absorption and scattering cross-sections for a few isotopes as summarized in Table 22 . The number of energy groups in the VERA-CS cross-sections library is 47 (refer to Table 17). Therefore, the number of parameters to be calibrated is 846 cross-section parameters and two thermal-hydraulics

parameters. The DRAM – QUESO algorithm (encoded in DAKOTA 6.2 [78, 79]) will be employed to solve the inverse problem using 100,000 samples per chain.

First, the goal oriented surrogate is constructed in the form represented by Eq.(62). The surrogate is constructed as described in section 4.4 and evaluated via examining the norm of residuals and their distribution. In this case study, the measured attributes are: the multiplication factor (k_{eff}), and the relative fission reaction rate 3 dimensional distribution at the ($\mathbf{FR}$). The matrix **FR** is 49*17*17 equivalent to measuring the fission rate over 49 axial levels (within the 56 axial levels). Synthetic data will be used instead of real data. Using the synthetic data implies that the actual solution of the data assimilation problem is known a priori enabling the data assimilation method to be verified. Five depletion steps are used to generate the synthetic measurements of interest. Hence, each response is measured at each of the depletion step (0, 9, 32, 45, 120, 160 EFPD). Table 16 summarizes the measurements and their uncertainties.

The problem of interest is the same as the assembly problem described in section 4.4. The surrogate will be constructed similarly with the difference that the perturbations are generated randomly within the interval of interest (h_{gap} *(±50%),* g_{loss} *(±4%)* , cross-sections (±5%)). The surrogate form-related uncertainty is obtained by Eq.(64) (refer to Table 20 for details about the surrogate error analysis). Note that the RMS for the **FR** reflects the RMS of a vector formed from the 49*17*17 matrix mentioned earlier; that is:

$$\varepsilon_{\mathbf{FR}} = RMS\left(vec\left\{\mathbf{FR}\right\}\right),$$

where *vec* is a process that transfers a matrix into a vector. Due to the computational resources limitation, a 2nd polynomial surrogate is used, hence the surrogate form-related uncertainty is

higher than the case of a 3rd order surrogate. The effect of a higher surrogate form-related uncertainty is a larger error in calibrating the parameters of interest along with higher uncertainty. Therefore, in this section the DA problem will be solved twice; once with including the surrogate form-related uncertainty and then without including the surrogate form-related uncertainty. Comparing the results of the two cases will indicate the effect of the surrogate errors on the calibration study. Figure 76 and Figure 77 present the residual errors along with their distribution. Figure 77 is a sample figure showing the residual error distribution for the fission rate at the core central point. For the surrogate model to be useful, the residual errors need to be an order of magnitude smaller than the experimental uncertainties.

The surrogate is then used for simultaneous calibration of the thermal-hydraulics parameters along with the cross-sections of interest. The synthetic measurements are generated via the high fidelity simulator (VERA-CS) where specific known parameters' perturbations are used. Therefore, as noted above the ideal solution to the data assimilation problem is known a priori and the performance of the **SBDA** can be evaluated by comparing the known perturbations and the mean variations generated by DRAM in conjunction with the surrogate (**SBDA**). The responses estimated by VERA-CS are considered as synthetic measurements to be assimilated.

For the thermal-hydraulics parameters, a uniform distribution was used as a priori distribution sampled using the uncertainties reported in Table 19 with the reference values of the parameters. Figure 78 and Figure 79 shows the chains and their distributions for the thermal-hydraulics parameters (grid loss coefficient and gap conductivity). Figure 80 indicates that there is no correlation between the gap conductivity (h_{gap}) and the grid spacer loss

coefficient (g_{loss}). From chapter 4, it was noted that the multiplication factor is not sensitive to the grid loss coefficient. Therefore, the variations in the grid spacer loss coefficient are not identifiable using the current responses of interest. Moreover, it was found that the effect of the grid spacer loss coefficient is the weakest among all other parameters regarding the the fission rate at the reactor center.

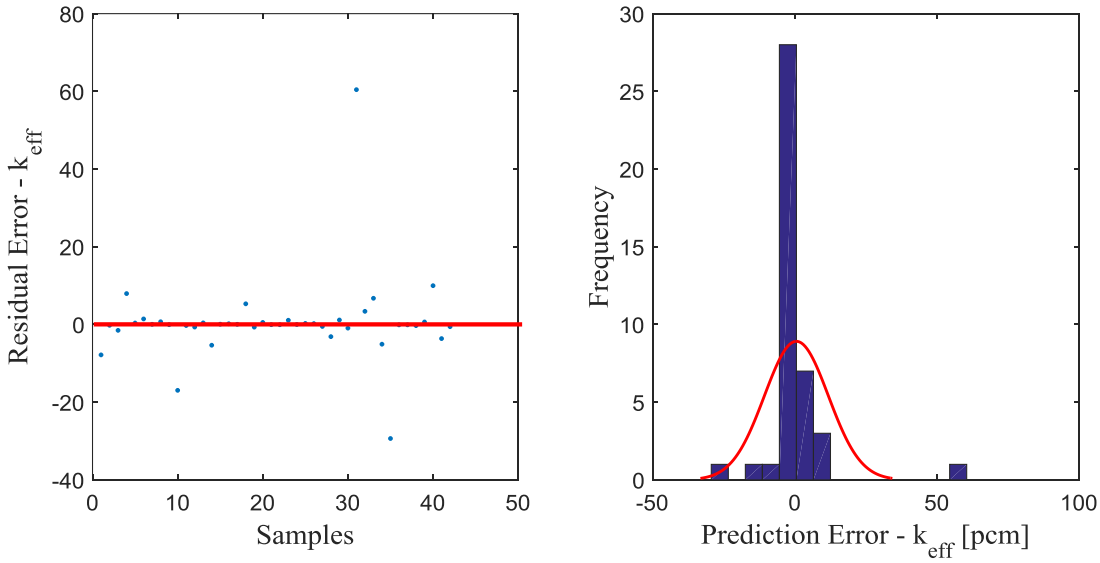

Figure 76. Residual errors along with their distribution - k_{eff}

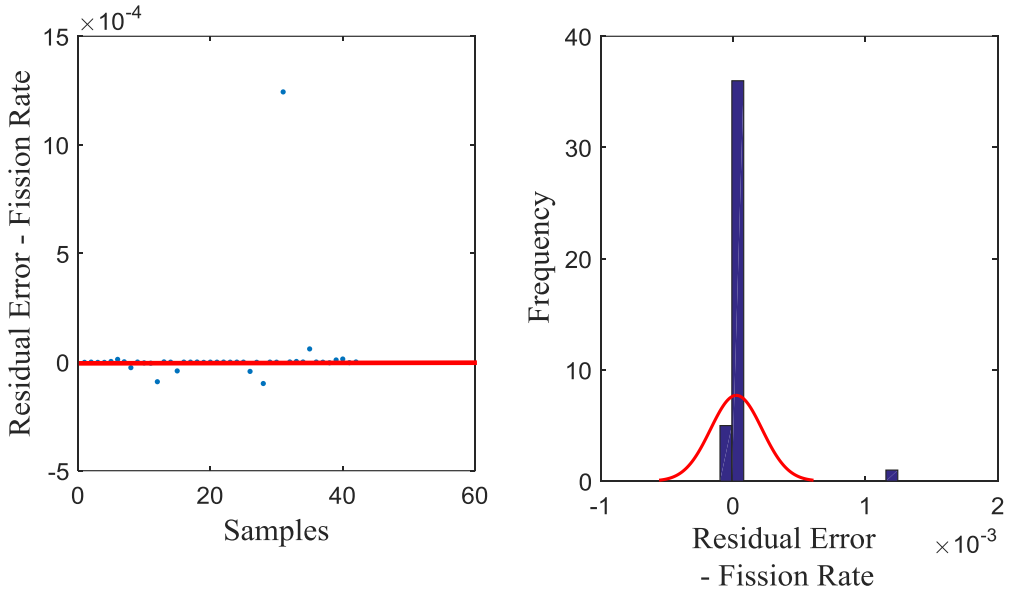

Figure 77. Residual errors along with their distribution – Fission Rate at the core center.

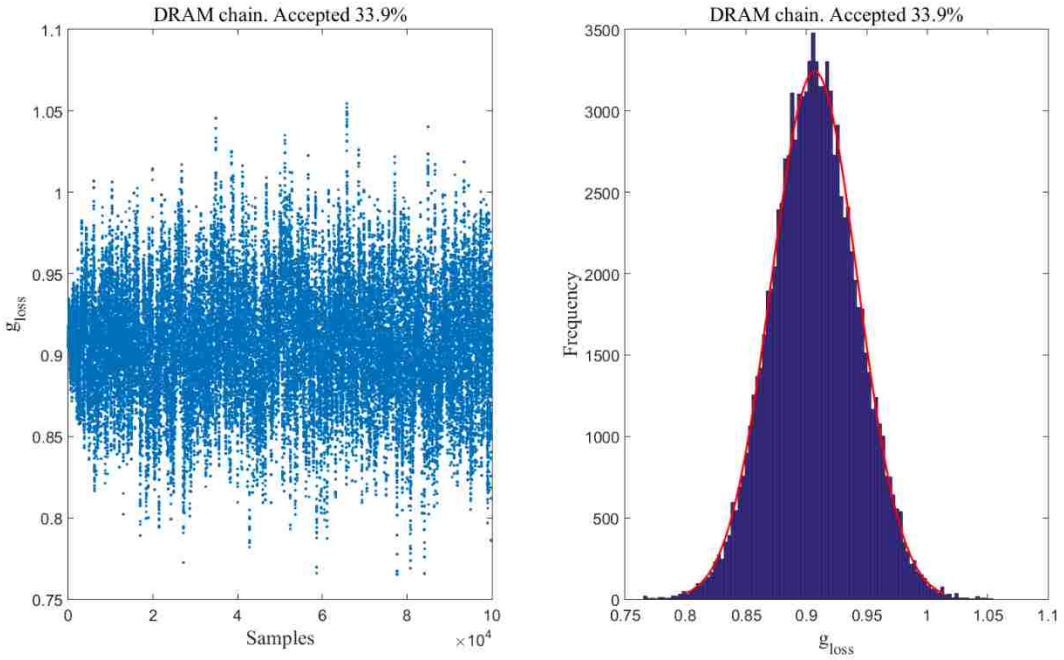

Figure 78. Chain and posterior distribution of the grid spacer loss coefficient (g_{loss}).[Including $\mathbf{C}_{surrogate \rightarrow f}$].

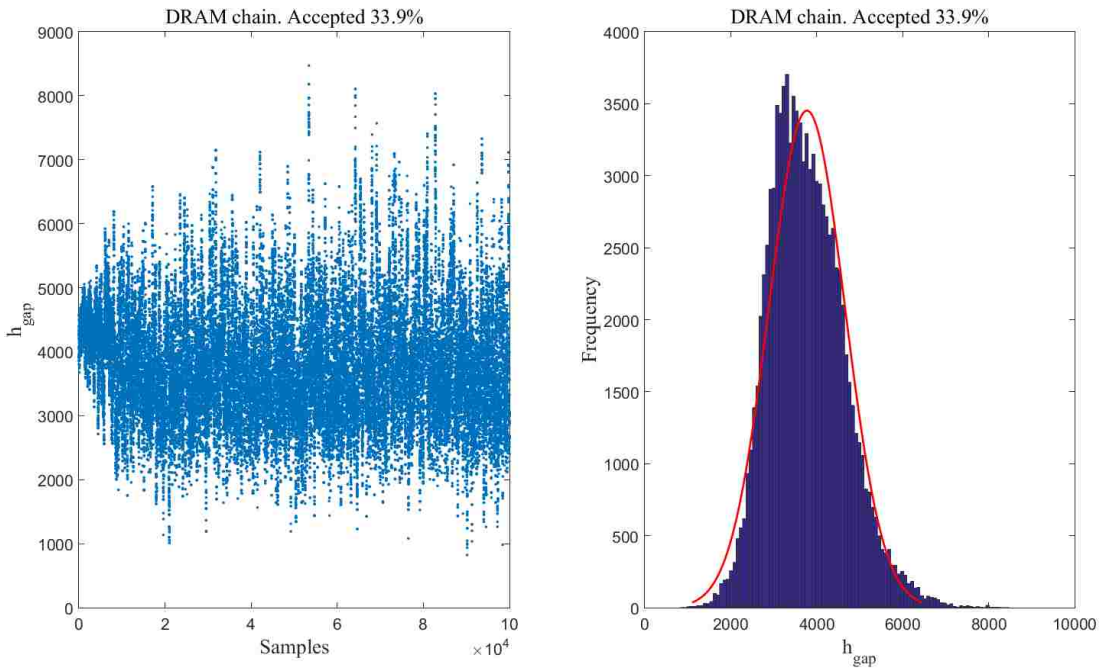

Figure 79. Chain and posterior distribution of the gap conductivity (h_{gap}). [Including $\mathbf{C}_{surrogate \rightarrow f}$].

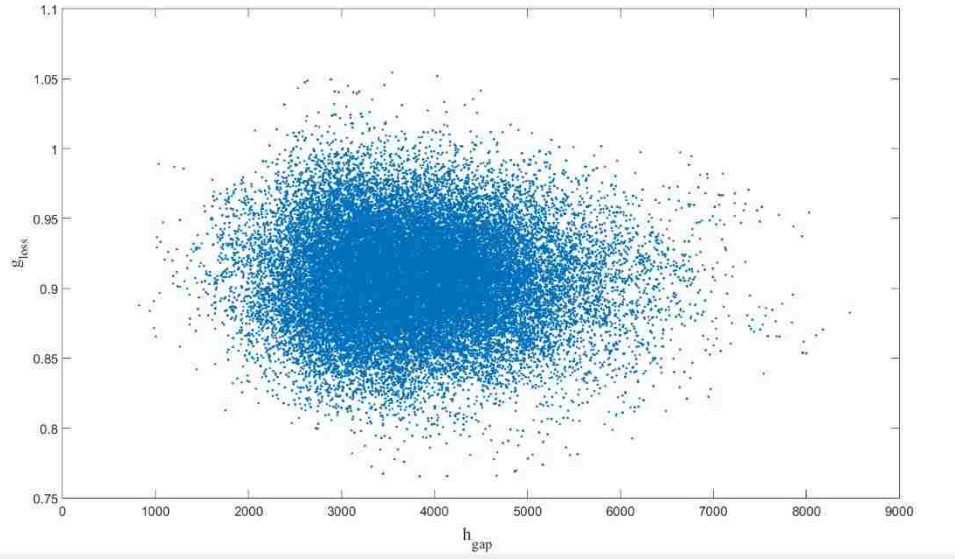

Figure 80. Correlation between the gap conductivity (h_{gap}) and the grid loss coefficient (g_{loss}). Including $\mathbf{C}_{surrogate \rightarrow f}$.

Table 20. Surrogate features.

Surrogate order	RMS	Construction Data Points	Validation Points	Residuals distribution	surrogate form – related uncertainty
2nd order	$\varepsilon_{k_{eff}} \rightarrow 14.4$ [pcm]	120	30	$k_{eff} \rightarrow$ i.i.d	35.0 [pcm]
	$\varepsilon_{\mathbf{FR}} \rightarrow 0.0332$			$FR \rightarrow$ i.i.d	0.93% [Maximum]

Table 21. Measurements and their uncertainties

Measurement	0.0 EFPD	9.0 EFPD	32.0 EFPD	120.0 EFPD	160.0 EFPD
k_{eff}	1.000443 ±0.00401	1.000121 ±0.00417	1.00013 ±0.00399	0.999951 ±0.00387	0.99991 ±0.00381
FR (at the core central point)	1.9321 ±0.021	1.8962 ±0.019	1.8212 ±0.0169	1.7612 ±0.0187	1.7312 ±0.0179

In the case of nuclear data cross-sections a Gaussian prior distribution based on the covariance library (44groupcov) [57] is used. A total of 18 different isotope-reaction pairs are considered for calibration. Taking into account that the surrogate uses a 47 group structure (refer to Table 17), the number of cross-sections parameters is 18x47 = 846 (refer to Table 18).

In order to evaluate the performance of the **SBDA**, the actual perturbation (which is known) is compared with the perturbation determined by the **SBDA**. A consolidated metric is defined to evaluate the performance of the **SBDA** with calibrating the cross-sections parameters (refer to Eq.(65)). Table 22 reports the average difference ($\varepsilon_{x,i}^{DA}$) along with the maximum difference between the actual perturbation and the one estimated by the **SBDA**. The maximum average error (refer to Eq.(65)) difference is 6.2% occurring for the Pu-240 absorption cross-sections (when the surrogate form uncertainty is included i.e. $\mathbf{C}_{surrogate \to f}$). In the case of ignoring the surrogate form –related uncertainty the maximum average difference is 6.1% occurring for the O-16 scattering cross-sections. Table 19 summarizes the data assimilation results for a few important parameters including the two thermal-hydraulics parameters.

Table 22. Assimilation performance measure for the various cross-sections parameters being calibrated.

Parameter	Value With $\mathbf{C}_{surrogate\to f}$	Value Without $\mathbf{C}_{surrogate\to f}$	Maximum Estimation Difference $\left(\Delta\Sigma_{x,\mathrm{g}}^{i,syn}-\Delta\Sigma_{x,\mathrm{g}}^{i,DA}\right)/\Delta\Sigma_{x,\mathrm{g}}^{i,syn}$ with $\mathbf{C}_{surrogate\to f}$	Maximum Estimation Difference $\left(\Delta\Sigma_{x,\mathrm{g}}^{i,syn}-\Delta\Sigma_{x,\mathrm{g}}^{i,DA}\right)/\Delta\Sigma_{x,\mathrm{g}}^{i,syn}$ without $\mathbf{C}_{surrogate\to f}$
$\varepsilon_{f,U\text{-}235}^{DA}$	2.2%	2.1%	2.8% [*g=2*]	2.2% [*g=8*]
$\varepsilon_{f,U\text{-}238}^{DA}$	1.9%	1.8%	4.1% [*g=5*]	3.2% [*g=4*]
$\varepsilon_{f,Pu\text{-}239}^{DA}$	6.2 %	5.8%	5.1% [*g=41*]	6.2% [*g=34*]
$\varepsilon_{s,O\text{-}16}^{DA}$	6.1%	6.1%	12.4%[*g=11*]	3.2%[*g=8*]
$\varepsilon_{s,H\text{-}1}^{DA}$	2.3%	2.1%	6.1%[*g=37*]	4.0% [*g=40*]
$\varepsilon_{f,Pu\text{-}240}^{DA}$	4.1%	4.2%	4.2%[*g=25*]	3.5% [*g=18*]
$\varepsilon_{a,Xe\text{-}134}^{DA}$	2.7%	2.5%	4.5%[*g=26*]	2.5% [*g=26*]
$\varepsilon_{a,B\text{-}10}^{DA}$	1.5%	1.3%	4.1% [*g=10*]	2.1% [*g=12*]
$\varepsilon_{a,Xe\text{-}130}^{DA}$	1.1%	0.92%	5.2%[*g=8*]	3.4%[*g=10*]
$\varepsilon_{a,Y\text{-}90}^{DA}$	3.1%	3.3%	4.3%[*g=12*]	2.9%[*g=10*]
$\varepsilon_{a,Y\text{-}91}^{DA}$	3.3%	3.1%	6.1%[*g=15*]	4.2%[*g=16*]
$\varepsilon_{a,Zr\text{-}90}^{DA}$	3.3%	3.0%	3.9%[*g=3*]	4.5%[*g=4*]
$\varepsilon_{s,Fe\text{-}56}^{DA}$	2.7%	1.3%	4.8%[*g=41*]	2.6%[*g=40*]
$\varepsilon_{s,Mn\text{-}55}^{DA}$	2.5%	1.4%	4.9%[*g=30*]	3.8%[*g=29*]
$\varepsilon_{a,Na\text{-}23}^{DA}$	2.1 %	1.5%	2.9%[*g=41*]	1.8%[*g=34*]
$\varepsilon_{f,Pu\text{-}238}^{DA}$	3.3%	2.2%	5.9%[*g=47*]	2.2%[*g=42*]
$\varepsilon_{f,Pu\text{-}241}^{DA}$	4.9%	2.4%	7.4%[*g=41*]	4.2%[*g=43*]
$\varepsilon_{f,U\text{-}236}^{DA}$	1.9%	3.3%	5.2%[*g=13*]	2.1%[*g=15*]

Table 23. Data assimilation results for a few important parameters.

Parameter	Reference Value	Actual Perturbed Value	SBDA Estimated Perturbation With $\mathbf{C}_{surrogate \to f}$	SBDA Estimated Perturbation Without $\mathbf{C}_{surrogate \to f}$
h_{gap}	4500 ± 2250	4359.91	4114.2 ± 903.21	4008.3 ± 699.56
g_{loss}	0.907 ± 0.03628	0.9123	0.9088 ± 0.035	0.9088 ± 0.035
Σ_f^{U-235} [g=47]	1125.219 ±2.66	1258.435	1270.01 ± 2.01	1281.45 ± 1.81
Σ_f^{U-238} [g=27]	0.8927011±0.00528	0.93246	0.9230 ± 0.00489	0.9013 ± 0.00401
Σ_f^{Pu-239} [g=1]	1361.297± 34.51	1441.313	1431.18 ± 28.21	1444.87 ± 21.34
Σ_s^{H-1} [g=47]	75.346183±0.07494	82.47610	81.72 ± 0.0591	81.208 ± 0.0411
Σ_s^{O-16} [g=47]	4.329821±0.04336	4.629821	4.612 ± 0.0406	4.742 ± 0.0331

CHAPTER 6. TARGET ACCURACY ASSESSMENT FOR HIGH DIMENSIONAL LIGHT WATER REACTOR SIMULATION PROBLEMS

Examples of Target Accuracy Assessment (TAA) analysis in nuclear engineering applications include a variety of problems that are important to both the safety and design of nuclear reactors. Nuclear data assimilation and target accuracy assessment are among the most important examples of the so called Inverse Uncertainty Quantification (IUQ) applications. Data assimilation methods are used to obtain best estimate of key parameters (e.g. nuclear data cross-sections) with the aim of improving the simulation for nuclear reactor designs. Data assimilation aims to find the true state or the best estimate of the true state of a certain set of key parameters utilizing experimental measurements of certain system attributes to learn more about the true state of the key parameters. For example, given a certain uncertainty in a measured attribute, data assimilation can provide more information about key sources of uncertainty through the so-called IUQ analysis [54,250 95]. On the other hand, target accuracy assessment aims to estimate the requirements on the uncertainty sources such that the target accuracy in the attributes of interest can be met. Mathematically, both data assimilation and target accuracy assessment are similar except that data assimilation uses measurement uncertainties while the target accuracy uses uncertainty targets specified by the safety and design constraints to obtain the requirements on the covariance library of the key uncertainty sources (model's parameters and other sources of uncertainty) [19, 20]. In sections 6.1, 6.2 and 6.3.2 the Target Accuracy Assessment (TAA) problem is solved for single and multi-physics problems via deterministic methods (i.e. Sequential Quadratic Programming

(SQP) algorithm) while in section 6.3.3 a 3 dimensional depletion problem is used to illustrate a non-linear and surrogate based methodology for the target accuracy assessment problem.

In this chapter, four improvements are introduced to the IUQ problem analysis. **First**, the problem's identifiability is improved through a regularization technique that confines the solution into a certain subspace determined a prior to the problem solution. **Second**, the IUQ scheme is made efficient for high dimensional constrained problems through dimensionality reduction, which facilitates both the sensitivity analysis and reduces the number of active constraints significantly. **Third**, the IUQ problem is extended to loosely coupled multi-physics models where two cases are considered; gradient-based and gradient-free IUQ algorithms. The gradient based algorithm assumes the availability of sensitivity information prior to the problem's solution while, the gradient-free approach pursues the solution of the IUQ problem without a prior knowledge of the sensitivity information. **Finally**, section 6.3.3 introduces a TAA formalism that is based on replacing the original high fidelity model by a more efficient surrogate model. This makes possible to perform TAA via non-linear uncertainty propagation through Monte Carlo sampling. The analysis therein aims to determine a set of integral response measurements such that the required parameters' uncertainties are achieved.

The target accuracy assessment analysis helps to evaluate the impact of each neutron cross-section or other parameter uncertainty on the most important integral responses related to the core and/or nuclear fuel cycle (forward/inverse uncertainty quantification of the depletion calculations in specific). Therefore, this chapter is a contribution to enabling the feasibility assessment of reactor and fuel cycle systems for current and Generation IV reactors.

6.1 Regularization of the Inverse Uncertainty Quantification Problem

Given the stringent requirements on the accuracy of nuclear design and safety calculations, new developments in uncertainty reduction are paramount to improving the competitiveness of nuclear energy against other energy sources. Focusing on neutronics calculations, many studies have shown that nuclear data constitute a major source of uncertainties in the calculated reactor attributes of interest, which are used to judge the performance of the associated reactor system. Therefore, it is natural to seek algorithms that identify the key parameters whose reduced uncertainties would have the highest impact on the uncertainties of reactor attributes of interest. Nuclear data experiments could then be established to reduce the uncertainty of the key parameters. Given that the cost of experiments, which noticeably vary from one parameter to another, one must take into account both the cost of the experiment and the potential benefit of uncertainty reduction on the attributes of interest. This is possible via a constrained optimization problem that minimizes a cost function, representing the cost of the experiments, while being constrained by the reduced uncertainty sought for the attribute(s) of interest. Note that the true cost function to be minimized is defined by the cost of experiments, minus the economic benefit associated with the reduced uncertainties obtained from executing the experiments with no constraints imposed via target attributes uncertainties. Since maximizing the economic benefit given reduced uncertainties involves optimization, the true optimization problem involves joint optimization; that is, optimization of both the experiments to be conducted and optimization of the system design are linked due to their interdependence. This more challenging optimization problem will be discussed later.

The constrained optimization problem has been previously tackled by many researchers as early as the 1970s. The problem appeared under the name of ‘nuclear data target accuracy

assessment', initially developed by Uschev in 1970s [16]. We refer to this problem as the inverse uncertainty quantification (IUQ) problem. This is because it first employs basic uncertainty quantification to estimate the uncertainties of reactor attributes of interest, and then via an inverse analysis, it solves the optimization problem for the key parameters of largest impact on the uncertainties of attributes of interest. This IUQ algorithm has been applied for current and future reactors [86]. These studies considered different integral quantities such as the multiplication factor, reactivity coefficients and various important reaction rates, as the attributes of interest whose uncertainties are to be reduced. Based on a target uncertainty for the attributes as defined by design/safety/economic consideration, these studies have shown that the current cross-sections evaluations need further improvements; see Ref. [19] for an example of a comprehensive study.

The IUQ suffers two problems: first, the identifiably; where several solutions might satisfy the target accuracy. Second, the Curse of Dimensionality; where the computational cost is a strong function in the dimensionality of the solution space and the constraint space. The identifiability of the IUQ problem depends on the effective dimensionality of the input parameter space which is often a rank deficient space [80]. In problems involving a high dimensional input parameter space the input parameters tends to be correlated, which means that the space is rank deficient and hence the inverse problem is not identifiable unless the observables (attributes) are measured with unrealistically high accuracy. On the other hand, in theory, all parameters that might contribute significantly to the overall uncertainty must be included in the IUQ analysis, for example: nuclear fuel and structural material cross-sections, fission products concentrations, and any other potentially important sources of uncertainty. Hence the number of parameters might grow very large, which increases the computational

cost of the IUQ analysis. Such a challenge is usually addressed by the elimination of parameters that do not contribute significantly to the overall uncertainty [19]. The sensitivity of each response is calculated at the reference values for the input parameters and then influential parameters are selected based on these sensitivities. However, there is little guarantee that the sensitivity profile remains constant over a range of inputs around the reference case. Hence the contribution might change as the input parameters change. This means that eliminating parameters that do not significantly contribute to the uncertainty relies on the assumption that the model is linear and therefore that the uncertainty contribution is constant. Therefore, in this subsection we introduce an algorithm to identify an active subspace a prior to the problem's solution. This subspace is based on sampling the sensitivity coefficients at different point in the phase space which can account for changes in the sensitivity coefficients in the region of interest (i.e. non-linearity). Moreover, this subspace can be used to regularize the problem by confining the solution to a physics-based lower dimensional subspace. This regularization might take the form of Tikhonov regularization [89]. Moreover, by confining the solution to a specific subspace, the Curse of Dimensionality problem is relaxed by the fact that searching along the DoF involved in the active subspace is more efficient than searching the whole solution space. Hence, both identifiability and computational cost are expected to be improved.

In order to solve the optimization problem, many algorithms might be used. Among these is the Sequential Quadratic Programming (SQP) which is the most popular optimization algorithm used in nuclear data assessment applications including the IUQ. SQP solves a set of sub-problems, each of which optimizes a quadratic model over a certain Lagrangian function. Such a method is reliable but computationally expensive and has slow convergence characteristics. Therefore, most optimization algorithms are either slow or need a feasible

starting point which is as hard as finding a solution to the problem, especially when huge number of uncertainty sources are considered. The computational burden of solving realistic optimization problems commands the attention to techniques that can restrict the search to a small sub-region or feasible directions in the domain [81]. For example, an active subspace can be identified in order to replace the full dimensional trust region with a lower dimensional active subspace [81]. Another example of implementing subspace techniques for optimization problems is the reduced Hessian method used in an interior-point algorithm. These techniques are abbreviated as SESOP (Sequential Subspace Optimization) [81-85].

Section 1.4 reviewed the efforts in the nuclear engineering community to apply the TAA in determining the experimental requirements such that safety margins are met. The most important efforts are represented in the following references [19, 51, 22, 20]. Ref. [19] has been primarily limited to integral benchmark critical experiments, exhibiting no feedback or depletion effects, and applied to relatively small problems. In addition to that, Ref. [51, 87] introduced an early exploration and application of the inverse methods to develop adaptive core simulation.

In this dissertation we seek to generalize the application of the IUQ algorithm to core-wide models simulating at power reactor conditions through the so called subspace methods. This goal implies one has to solve an optimization problem with a large number of parameters, currently impossible with a brute force application of any given optimization technique. Therefore, in support of our overarching goal, we propose an algorithm that can render practical the solution of a high dimensional optimization problem of applied to reducing the uncertainties of cross-sections. The proposed algorithm is based on the replacement of the full dimensional space of all possible solutions (i.e. the searching domain) by a subspace that is

smaller and of lower dimension (i.e. a target subspace) tailored by the model's physics. A low fidelity solution of the optimization problem is used to build the target subspace. The proposed algorithm can reduce the computational cost of the targeted cross-sections assessment and hence allowing the designer to study a wider range of uncertainty sources and include finer energy groups. The algorithm is applied to a quarter PWR lattice model, where a target accuracy of the multiplication factor has been defined and the performance of the proposed algorithm was investigated and compared against the conventional IUQ approach. In this work, the differential cross-section and covariance values of the constituent isotopes are those distributed in SCALE 6.1 [57]. In addition, the proposed algorithm may be used in various analysis such as the impact of uncertainties in cross-sections on the transmutation of actinides [19], Gen. IV reactors design and safety calculations [86], and statistical adjustments of cross-sections using post-irradiation experiments to enhance the prediction accuracy of the experimental data.

In the following sections the term **T**-subspace will be used to refer to the lower dimensional target subspace while the term **SIUQ** will be used to refer to the proposed subspace based inverse sensitivity/uncertainty quantification algorithm.

6.1.1 Algorithm

In this section an extension of the classical IUQ methods used in Ref. [19, 86] to high dimensional problems will be presented. The IUQ formalism implemented in this section is outlined in Ref. [19, 86]. In Section 6.3.3 a new, more realistic formalism will be introduced.

The formalism therein utilizes a more realistic cost function and replaces the linearity assumption introduced in this section by a higher order goal-oriented surrogate.

The IUQ problem is an inequality-nonlinear-constrained optimization problem. The starting point when considering cross-sections as parameters is the prior covariance matrix **C** of multi-group cross sections, whose diagonal elements are the variances of cross-sections. The target is to calculate the updated covariance matrix $\mathbf{C}'$ by updating its elements as follows:

$$C'_{ij} = d_i C_{ij} d_j \ , \tag{66}$$

where d_i's are the adjustment parameters. More precisely one would write $C'_{ij} = d_{ij} C_{ij}$, which when constrained with Eq.(66) reveals the assumption that $d_{ij}=d_i \, .d_j$. This assumption assumes that the posterior correlation of parameters *i* and *j* is unchanged from the prior correlation. To show this, note that the correlation terms can be expressed as follow:

$$C_{ij} = \rho_{ij} \sigma_i \sigma_j$$

where ρ_{ij} is the correlation coefficient. Therefore, the adjustment of $\sigma_i = \sqrt{C_{ii}}$ by d_i and $\sigma_j = \sqrt{C_{jj}}$ by d_j implies that σ_{ij} is adjusted by a factor of $d_i.d_j$:

$$C'_{ij} = \rho_{ij} \sigma'_i \sigma'_j = \rho_{ij} d_i \sigma_i \sigma_j d_j = d_i C_{ij} d_j$$

Let us assume that the cost to be minimized can be defined as:

$$\text{Cost}[\mathbf{C}'] = \sum_i \frac{w_i}{\sigma'^{,2}_{ii}} = \sum_i \frac{w_i}{d_i \sigma^2_{ii} d_i} \tag{67}$$

where w_i's are user-defined weights corresponding to cost of measuring various cross sections in different energy ranges. The constraint that must be satisfied by the optimal solution is:

$$\bar{\sigma}^2_{\mathbf{R}} = \text{diag}\left\{\mathbf{S}\mathbf{C}'\mathbf{S}^{\mathbf{T}}\right\} \le \tau \tag{68}$$

where $\bar{\sigma}_{\mathbf{R}}^2$ denotes the response variance vector and the "diag." function forms a vector from the matrix diagonal, $\bar{\hat{\sigma}}_{\mathbf{R}}^2$ is a vector of maximum allowed variances of the application's bounding responses, and $\mathbf{S}$ is the application's sensitivity profile with respect to the cross-sections at the reference case. Note that the expression in Eq.(68) includes the covariance terms. The covariance terms reflect the correlations between different parameters; hence they effect the magnitude of the responses' variance reduction. It has been shown that the correlation terms are important in targeted cross-sections assessment [86].

In order to guide the optimization algorithm to search along certain directions we build these directions based on the subspace determined by an approximate solution to the optimization problem. If the covariance terms (correlation terms) are neglected, the problem can be solved using a Lagrange multipliers analysis.

For a single response *R* that is a function of a vector ξ*;* where:

$$R = f(\xi_1, ..., \xi_N).$$

Then the uncertainty in the response can be calculated by propagating the input parameter uncertainties, neglecting the covariance terms, by:

$$\sigma_R^{',2} = \sum_{i=1}^{N} s_i^2 \sigma_{\xi_i}^{',2} \tag{69}$$

Now assume a general objective (cost) function obj. We can solve the constrained optimization problem by defining a Lagrangian function F as follow:

$$F = obj - \lambda(\sigma_R^{',2} - \tau)$$

$$F = obj - \lambda(\sum_{i=1}^{N} s_i^2 \sigma_{\xi_i}^{',2} - \tau),$$

where *obj* is to be minimized by selection of the optimum $\{\sigma'^{,2}_{\xi_i}\}$, and τ is the variance tolerance in the response to be constrained. In order to solve the constrained minimization problem, one needs to satisfy:

$$\nabla_{\sigma_{\xi_j}} F = \nabla_{\sigma_{\xi_j}} obj - 2\lambda s_j^2 \sigma'_{\xi_j} = 0 \text{ , for } j=1,2,\ldots N \tag{70}$$

Also, the derivative with respect to the Lagrange multiplier must satisfy:

$$\nabla_{\lambda} F = \sum_{i=1}^{N} s_i^2 \sigma'^{,2}_{\xi_i} - \tau = 0 \tag{71}$$

If the cost function is linear then Eq.(70) and Eq.(71) can be solved explicitly for $\{\sigma'_{\xi_i}\}$

$$\sigma'_{\xi_i} = \frac{\nabla_{\sigma_{\xi_j}} obj}{-2s_j^2 \left[\frac{1}{\tau} \sum_i s_i^2 \left(\frac{\nabla_{\sigma_{\xi_j}} obj}{2s_i^2} \right)^2 \right]^{1/2}} = d_j \sigma_{\xi_i}$$

where the adjustment parameter d_j:

$$d_j = \frac{\nabla_{\sigma_{\xi_j}} obj}{-2\sigma_{\xi_j} s_j^2 \left[\frac{1}{\tau} \sum_i s_i^2 \left(\frac{\nabla_{\sigma_{\xi_j}} obj}{2s_i^2} \right)^2 \right]^{1/2}} \tag{72}$$

So if the cost function is linear, e.g. $obj = \sum_i w_i \left(\sigma_{\xi_j} - \sigma'_{\xi_j} \right)$, Eq.(72) can be used to show that:

$$d_j = \frac{w_i}{2\sigma_{\xi_j} s_j^2 \left[\frac{1}{\tau} \sum_i s_i^2 \left(\frac{-w_i}{2s_i^2} \right)^2 \right]^{1/2}}$$

where s_i is the sensitivity coefficient for the response with respect to the i^{th} parameter. If the cost function is non-linear, Eq.(70) and Eq.(71) still apply. For example, if we define the cost function as [16-20]:

$$obj = \sum_{i=1}^{N} \frac{w_i}{(\sigma_{\xi_i})^2}, \tag{73}$$

the constrained minimization problem can be analytically solved. The updated uncertainties can be shown to be:

$$\sigma'_{\xi_j} = \left(\frac{w_j(\tau)^2}{\left(\sum_{i=1}^{N} |s_i| \sqrt{w_i} \right)^2 s_j^2} \right)^{1/4} = d_j \sigma_{\xi_j}.$$

So the adjustment parameter d_j indicated in eq.(66) is:

$$d_j = \frac{1}{\sigma^0_{\xi j}} \left(\frac{w_i(\tau)^2}{\left(\sum_{i=1}^{N} |s_i| \sqrt{w_i} \right)^2 s_j^2} \right)^{1/4}. \tag{74}$$

So if the cost function is linear then Eq.(72) can be used to obtain the values of $\{d_i\}$ sample the low fidelity solution of the optimization problem. Otherwise, if the function is non-linear then Eq.(70) and (71) must be solved simultaneously for $\{\sigma_{\xi_j}\}$. Note that this solution assumes that the covariance terms do not affect the values of the responses which is not generally true. However, this solution (i.e. $\{d_i\}$) can be used to define a lower dimensional subspace which can searched during the optimization with the jut noted assumption removed. This lower dimensional subspace will be denoted the Target Subspace (**T**-subspace), where the IUQ analysis seeks a solution for the target accuracy assessment problem. The following steps

summarize the process of constructing the subspace and hence solving the Subspace Inverse Uncertainty Quantification (**SIUQ**):

1- Determine the sources of uncertainty (parameter uncertainties to be considered),

2- Sample *k* perturbations of the model's input parameters and for each sample determine the responses sensitivity (i.e. $\{s_i\}$). Then solve Eq.(70) and Eq.(71) simultaneously for each sample to construct the corresponding adjustment parameter samples:

$$\Xi = [\bar{d}_1, \cdots, \bar{d}_i, \cdots, \bar{d}_k]$$

3- Build an orthonormal basis of the **T**-subspace spanned by the samples:

$$\Xi = \mathbf{USV}^T$$

4- Calculate the error upper bound using associated with each subspace size, using Eq.(75) by taking additional samples [30]:

$$\varepsilon_{tol} \geq 10\sqrt{\frac{2}{\pi}} \max_{i=1,..s} \| (\mathbf{I} - \mathbf{UU}^T)\bar{d}_i \|_2 = \varepsilon_{upper} \tag{75}$$

s = 10 is a reasonable choice.

5- If the inequality in step 4 is not satisfied; increase the number of samples and repeat steps 2-5,

$$k = k + 1$$

6- Tune the optimization algorithm to search along the directions represented by the basis (columns of $\mathbf{U}$ matrix), where:

$$\mathbf{U} \in \mathbb{R}^k,\ k < N\ .$$

So matrix $\mathbf{U}$ contains the basis of the **T-**subspace. The basis will direct the optimization algorithm to search along certain directions. So instead of investigating the whole space, only

the **T**-subspace will be investigated. The directions of search are limited to those that belong to the subset determined by the proposed algorithm. Therefore, the search is restricted to a subset of the full dimensional space. However, note that if the correlation terms have a strong effect on the problem of interest, then the **T**-subspace solution will be invalid and hence the search along the directions proposed by this algorithm will not be applicable. In Section 6.3.3 a more general and practical method will be introduced.

6.1.2 Case Study: CASL Progression Problem 2 – Lattice Model

In this section, the goal is to demonstrate the proposed algorithm using a practical example. CASL VERA progression problem number 2 [90] is modeled using the SCALE6.1-TSUNAMI module [57]. Problem number 2 analyzes a fuel lattice typical of the central axial region of PWR fuel lattices (refer to Figure 81) and is two-dimensional. TSUNAMI calculates the first order sensitivity coefficients and hence can estimate the uncertainty in the responses of interest. Target accuracy of the multiplication factor and the fission rate are defined, and the IUQ formalism is then used to estimate the required experimental accuracy and the proper prioritization to reduce cross-section uncertainties to values determined by the constrained optimization.

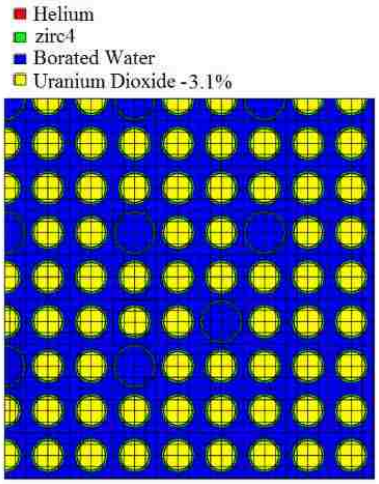

Figure 81. CASL progression problem number 2.

The conventional IUQ algorithm was used to solve the optimization problem. Then the problem was solved using the SIUQ algorithm. In order to choose the important directions in the full dimensional domain, the approximate analytic solution as previously defined was sampled and used to build the **T**-subspace as indicated in the algorithm outlined in the previous section. The base cross-sections parameters were perturbed ($\pm 30\%$) and the size of the **T**-subspace was defined using the error metric tool presented by Eq.(75). The **T**-subspace is then used to regularize the solution of the IUQ problem to be confined to those DoF represented by the basis of the **T**-subspace.

The size of the subspace is increased until the subspace represents the approximate solution within a negligible error upper bound. Figure 82 shows the absolute error. Based on this, a subspace of dimension (rank) equals to 60 is a reasonable choice to attain the target subspace; therefore, the SIUQ has only 60 directions (degrees of freedom) to search for the optimized solution compared with the IUQ which searches along 8140 directions. The original uncertainty in k_{eff} is about 504 pcm which is intended to be reduced to 250 pcm; moreover,

the uncertainty in the normalized fission rate in the fuel mixture (Eq.(76)) is 1.6% and is to be reduced to 0.5% while minimizing the financial effort represented by the cost function defined by Eq. (77), where:

$$FR_{fuel} = \frac{\sum_{i,i\in fuel} V_i \sum_g \Sigma_f^g \phi_{i,g}}{\sum_i V_i \sum_g \phi_{i,g}} \tag{76}$$

$$\text{Cost}\left(\bar{d}\right) = \frac{\left(\sum_{i=1}^{n} \frac{w_i}{\sigma_i^{',2}\left(\bar{d}\right)} - \sum_{i=1}^{n} \frac{w_i}{\sigma_i^2}\right) - \sum_{j=1}^{m} \mu_j \left(\sigma_{R_j}^2 - \sigma_{R_j}^{',2}\left(\bar{d}\right)\right)}{\sum_{i=1}^{n} \frac{w_i}{\sigma_i^2}} \tag{77}$$

In this study the values of $\{w_i\}$ and $\{\mu_j\}$ are set to 1.0 hence all the parameters and responses are assumed to be equivalent. Table 24 summarizes the results and compare the behavior of the proposed algorithm and the conventional one given certain convergence conditions. Since sequential quadratic programming (SQP) is the most reliable and common optimization algorithm used in such applications, it is used for both the IUQ and SIUQ via MATLAB function FMINCON and CONMIN NASA software [96]. Both algorithms converge to the specified target accuracies and minimizes the costs to within a 1% difference. However, the SIUQ converges faster (423 function evaluations), while the IUQ required 3500 function evaluations to fall within the range of the target accuracies. In other words, the introduction of the **T**-subspace will reduce the complexity of the optimization problem. The SIUQ algorithm will always search in a smaller space, a situation that gives it an advantage over the IUQ. The running time per function evaluation is much smaller due to the fact that the SIUQ searches in a smaller subspace and hence the derivatives, cost and constraints need to be evaluated at less number of points and have smaller number of searching directions per

iteration per region in the parameter space. The convergence thickness (constraint violation) and the termination tolerance on the solution were set to 10^{-10}. Usually, such tight tolerances on the constraint and solution are not used. However, since the goal of this work is to compare the asymptotic performance of the two algorithms, these harsh convergence conditions were used. This explains the relatively long CPU run times observed in Table 24.

Table 24. Summary of the numerical results and comparison of the two algorithms.

Algorithm	DoF	CPU time (hours)	$Cost^{opt}$
SIUQ	60	0.45	10.37%
IUQ	8140	6.1	10.12%

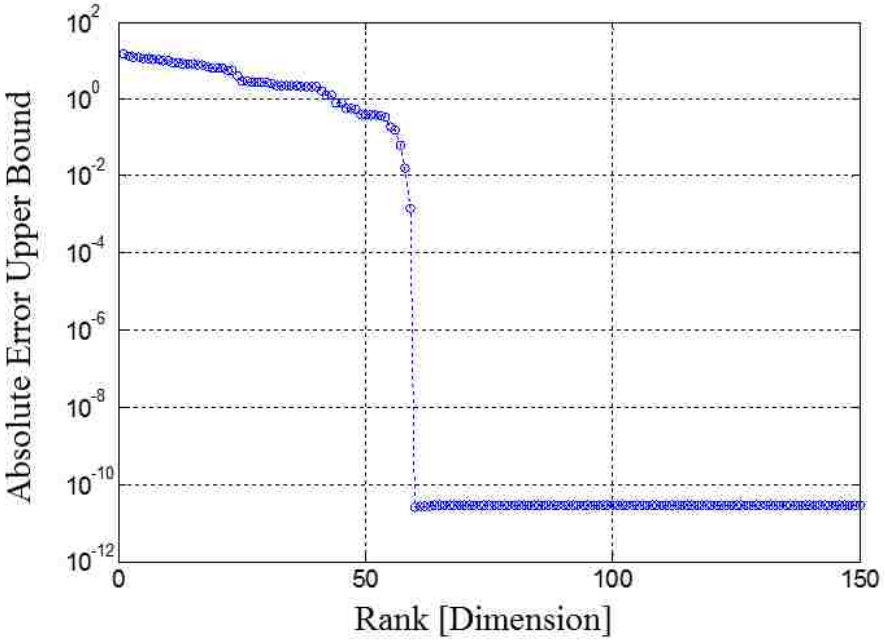

Figure 82. Direction importance in terms of absolute error in adjustment parameter.

In order to prioritize among alternative experiments, the previous formulation can be generalized such that Eq.(78) sorts the experiments based on two factors; first the contribution of each experiment to the overall uncertainty reduction and second the financial saving associated with each experiment:

$$\mathrm{I}_l = \frac{\sum_{j=1}^{m} \mu_j \left(\sigma_{R_j}^2 - \sigma_{l\to R_j}^{',2} \right) - \left(\frac{\omega_l}{\sigma_l^{',2}} - \frac{\omega_l}{\sigma_l^2} \right)}{\mathrm{Cost}\left(\bar{d}^{\,opt} \right)} \,, \tag{78}$$

where $\mathrm{Cost}\left(\bar{d}^{\,opt} \right)$ is the cost evaluated at the optimum adjustment set (i.e. $\bar{d}^{\,opt}$). $\sigma_{l\to R_j}^{',2}$ is the variance in the response y_j due to the l^{th} experiment. Note that it has been assumed that the l^{th} experiment only reduces the uncertainty of a single cross-section which may be true for differential measurements but not integral experiments. Hence, the experiments are prioritized according to the value of I_l; the larger the value of I_l the more important the experiment is. Using the same logic one can quantify the effect of performing the first L experiments using the following expression:

$$\chi_L = \frac{\sum_{j=1}^{m} \mu_j \left(\sigma_{R_j}^2 - \sigma_{L\to R_j}^{',2} \right) - \left(\sum_{l=1}^{L} \frac{\omega_l}{\sigma_l^{',2}} - \sum_{l=1}^{L} \frac{\omega_l}{\sigma_l^2} \right)}{\mathrm{Cost}\left(\bar{d}^{\,opt} \right)} \tag{79}$$

Table 25 and Table 26 show the 10 most important experiments to be performed along with their initial and require uncertainties, I_l, χ_L. σ^0 denotes the initial relative uncertainty and σ' denotes the required uncertainty. Comparing the solution from both SIUQ and the IUQ, the similarity of the solution between the two schemes is obvious. Furthermore, note that the depleted MOX fuel has a relatively high concentration of ${}^{239}_{94}Pu$; therefore, the sensitivities of the responses with respect to this isotope are expected to be higher for the MOX fuel than for the UO_2 fuel. This expectation was verified numerically by calculating the sensitivities using each fuel type separately.

The identifiability of the inverse problem can be tested by the rank of the Fisher matrix. The Fisher matrix represents the information carried by the model from the parameter space towards the response or observables space [91-94]. Figure 83 depicts the rank of the Fisher matrix for the full dimensional problem; one can see that the Fisher matrix is rank deficient even for unrealistically high measurement precision. However, Figure 84 shows that for the reduced problem (SIUQ algorithm) the Fisher matrix is full ranked at a measurement precision of 10^{-4}.

Table 27 shows the identifiability test for the full dimensional IUQ formalism. One can see that for a different initial guess, the problem converges to different solutions with different adjustment parameters and experiments. Table 28 shows that the reduced dimensional problem is fully identifiable regardless of the initial guess (refer to Figure 84).

Table 25. Summary of the results. The 10 most affected reactions: IUQ algorithm.

Parameter	σ^0 %	$\sigma^{'}$ %	χ_L
$^{238}_{92}\mathrm{U}\ (n,n')$ [3.0-4.8]MeV	20.0	6.3	46%
$^{238}_{92}\mathrm{U}\ (n,n')$ [1.85-2.35]MeV	19.7	7.44	58%
$^{238}_{92}\mathrm{U}\ (n,n')$ [2.479-3.000]MeV	19.1	7.42	72%
$^{238}_{92}\mathrm{U}\ (n,n')$ [1.4-1.85]MeV	21.1	10.4	84%
$^{238}_{92}\mathrm{U}\ (n,n')$ [6.434-8.1873]MeV	20.9	12.1	87%
$^{238}_{92}\mathrm{U}\ (n,n')$ [0.9-1.4]MeV	19.3	11.6	89%
$^{238}_{92}\mathrm{U}\ (n,\gamma)$ [6-8.099]eV	2.28	1.39	91%
$^{238}_{92}\mathrm{U}\ (n,\gamma)$ [4.75-6]eV	3.00	1.83	92%
$^{238}_{92}\mathrm{U}\ (n,\gamma)$ [8.099-10]eV	2.39	1.48	94%
$^{235}_{92}\mathrm{U}\ (\chi)$ [3.0-4.8]MeV	3.14	1.89	95%

Table 26. Summary of the results. The 10 most affected reactions: SIUQ algorithm.

Parameter	σ^0 %	$\sigma^{'}$ %	χ_L
$^{238}_{92}\mathrm{U}\ (n,n')$ [3.0-4.8]MeV	20.0	7.16	45%
$^{238}_{92}\mathrm{U}\ (n,n')$ [1.4-1.85]MeV	21.1	8.52	63%
$^{238}_{92}\mathrm{U}\ (n,n')$ [1.85-2.35]MeV	19.7	7.99	79%
$^{238}_{92}\mathrm{U}\ (n,n')$ [2.479-3.000]MeV	19.1	7.89	90%
$^{238}_{92}\mathrm{U}\ (n,n')$ [6.434-8.1873]MeV	20.9	8.69	93%
$^{235}_{92}\mathrm{U}\ (\chi)$ [6.434-8.1873]MeV	8.34	3.52	95%
$^{235}_{92}\mathrm{U}\ (\chi)$ [8.1873-20.0]MeV	11.6	5.23	98%
$^{238}_{92}\mathrm{U}\ (n,n')$ [2.354-2.479]MeV	19.4	9.42	99%
$^{238}_{92}\mathrm{U}\ (n,\gamma)$ [8.099-10]eV	2.39	1.32	99.7%
$^{235}_{92}\mathrm{U}\ (n,\gamma)$ [17.0-3.0]KeV	34.0	19.1	99.8%

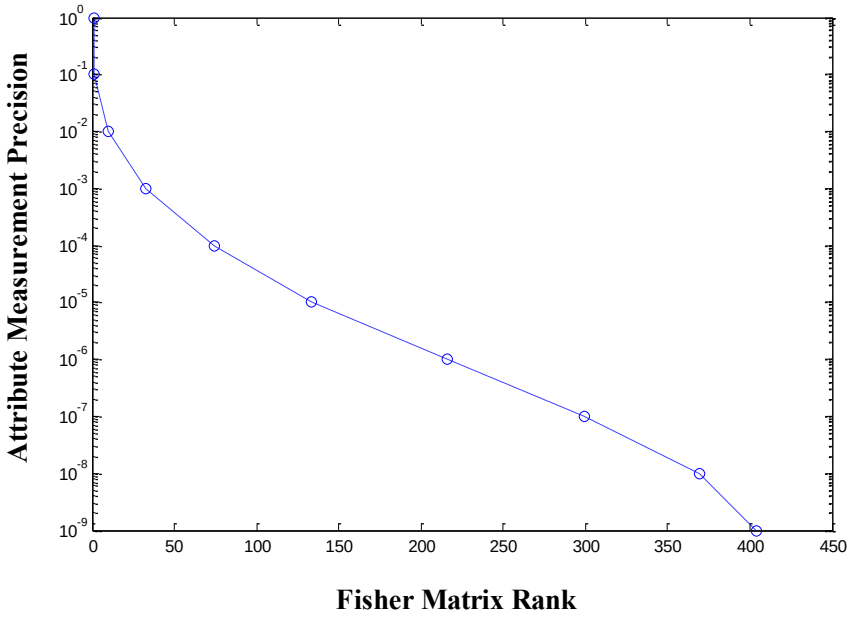

Figure 83. The rank of Fisher matrix for different attribute measurement precisions (full dimensional problem).

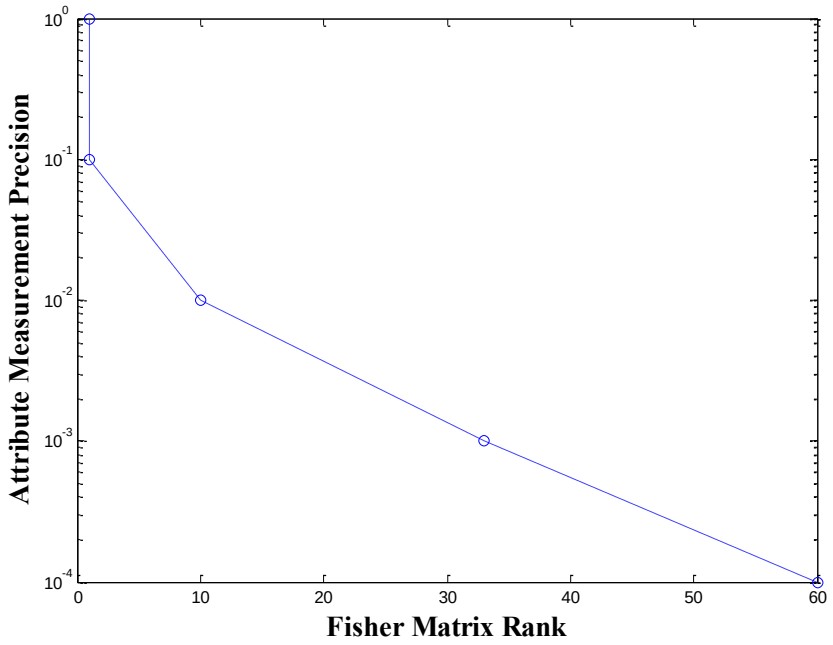

Figure 84. The rank of the Fisher matrix for different attribute measurement precisions (reduced problem).

Table 27. Identifiability test - Full dimensional space analysis.

	$\bar{d}_{initial} = \mathbf{0.1}$	$\bar{d}_{initial} = \mathbf{0.5}$	$\bar{d}_{initial} = \mathbf{0.9}$
Cost Function	11.02%	10.49%	10.12%
CPU (hours)	0.58	5.89	6.1
d_1	1.23E-01	1.21E-01	1.11E-01
d_2	1.29E-01	1.65E-01	1.52E-01
d_3	1.43E-01	1.55E-01	1.54E-01
d_4	1.50E-01	1.62E-01	2.55E-01
d_5	1.50E-01	1.65E-01	2.63E-01
d_6	1.50E-01	1.72E-01	3.06E-01
d_7	1.50E-01	1.82E-01	3.17E-01
d_8	1.50E-01	2.14E-01	3.12E-01
d_9	1.50E-01	2.36E-01	3.16E-01
d_{10}	1.50E-01	2.32E-01	3.62E-01

Table 28. Identifiability test - Reduced dimensional space analysis (SIUQ algorithm).

	$\bar{d}_{initial} = \mathbf{0.1}$	$\bar{d}_{initial} = \mathbf{0.5}$	$\bar{d}_{initial} = \mathbf{0.9}$
Cost Function	10.41%	10.38%	10.37%
CPU (hours)	0.28	0.37	0.45
d_1	1.01E-01	1.03E-01	1.05E-01
d_2	1.51E-01	1.50E-01	1.52E-01
d_3	1.57E-01	1.58E-01	1.59E-01
d_4	2.62E-01	2.62E-01	2.57E-01
d_5	2.69E-01	2.63E-01	2.68E-01
d_6	3.11E-01	3.16E-01	3.16E-01
d_7	3.11E-01	3.12E-01	3.14E-01
d_8	3.14E-01	3.13E-01	3.12E-01
d_9	3.25E-01	3.25E-01	3.17E-01
d_{10}	3.83E-01	3.93E-01	3.98E-01

6.2 Inverse Uncertainty Quantification for High Dimensional Constrained Problems

The inverse uncertainty quantification problem or IUQ deals with the following question: which and by how much each parameter uncertainty should be reduced to meet the target uncertainties for the responses of interest? This provides a useful analysis tool for both new and existing reactors, as it allows one to identify the experimental needs to support the reactor application of interest. IUQ is set up as a constrained minimization problem in terms of a cost function that measures the cost of the experiments required to reduce cross-section uncertainties (focusing on nuclear data uncertainties only), with the target uncertainties for the responses serving as constraints.

This section introduces another development to the IUQ formalism; this development reduces the computational cost of high dimensional constrained problems. The approach enables the IUQ to be extended to applications of this method to models with a high number

of constraints (e.g., flux field) whose respective uncertainties are to meet target values. Direct solution of the minimization problem with many constraints is difficult. To address this challenge, this section introduces an efficient algorithm that reduces the dimensionality of the response space prior to the application of the minimization search. Numerical experiments employing PWR lattice models demonstrate the computational efficiency of the proposed algorithm.

As mentioned earlier, the SQP algorithm is used in the IUQ formalism adapted here. SQP algorithms are often at an advantage over other methods whenever the number of uncertainty sources is not large while the evaluation of the constraint functions is computationally expensive. Hence the improvement introduced in the previous section (section 5.1) solves the problem of a large number of uncertainties, while the improvement introduced here addresses the issue of a huge number of constraints. Therefore, this section takes us one step further towards the application of the IUQ formalism on multi-physics coupled problems which are expected to encounter a large number of constraints.

6.2.1 Algorithm

Consider the following radiation transport model:

$$\bar{R} = f\left(\bar{\xi}\right),\ \bar{\xi} \in \mathbb{R}^n \text{ and } \bar{R} \in \mathbb{R}^m,$$

where $\bar{\xi}$ represents the input parameters (e.g. nuclear data cross-sections) and $\bar{R}$ is the response vector (e.g. the neutron flux field) whose uncertainties are to be reduced. Earlier work has shown that neutronics models typically used in reactor design calculations are inherently reducible, implying a large degree of correlation exists between the spatially-energy-dependent

flux values. This means that the flux variations could be described using a lower number of degrees of freedom. The range finding algorithm (RFA) [30], introduced in earlier chapters, can be used to determine these degrees of freedom, described mathematically by a lower dimensional subspace (i.e. the active subspace). The implication is that response variations orthogonal to the active subspace are negligible, and hence could be discarded by the analysis. The proposed algorithm is used to recast the minimization search in terms of the active subspace prior to the execution of the minimization search, which results in a significant reduction in the number of constraints.

Assume that the RFA yielded the basis of the active subspace as the columns of matrix $\mathbf{U}$:

$$\mathbf{U} = \left[\bar{u}_1 \,|\, \bar{u}_2 \,|\, \cdots \,|\, \bar{u}_r \right]$$

The implication is that any response variation can be approximated by:

$$\bar{R}^{m\times 1} \simeq \sum_{i=1}^{r} \alpha_i \bar{u}_i = \mathbf{U}^{m\text{x}r} \bar{\alpha}^{r\text{x}1} \tag{80}$$

where r is the rank of the active subspace and is typically much smaller than the original dimension of the response space, i.e., $r \ll n$. The above equation may be used to recast the minimization search as follows:

Eq. (80) may be re-written as follows:

$$\bar{\alpha} = \mathbf{U}^T \bar{R},$$

where $\bar{\alpha}$ is denoted hereinafter as the active responses. The target uncertainties for the responses are determined by the user, denoted by the diagonal elements of a matrix $\mathbf{C}_R$. The

above equation can be used to calculate the corresponding target uncertainties for the active responses.

$$\mathbf{C}_{\alpha} = \mathbf{U}^{T}\mathbf{C}_{R}\mathbf{U} \tag{81}$$

The IUQ formalism requires the sensitivities of the responses with respect to the input cross-sections, which can be expressed in terms of the active responses as follows:

$$\frac{d\bar{R}^{m\text{x}1}}{d\xi_i} = \mathbf{U}^{m\text{x}r}\,\frac{d\bar{\alpha}^{r\text{x}1}}{d\xi_i} \tag{82}$$

With the active responses much fewer in number than the original responses, the adjoint-based sensitivity analysis is the best candidate to evaluate the sensitivity profiles for the *r* active responses. This follows as *r* is expected to be much smaller than the number of input cross-sections, which renders a forward-based sensitivity analysis computationally intractable for neutronics models. The active response can be used in conjunction with Eqs.(82) and Eq.(42) to recast the problem's constraints as follows:

$$diag\left\{\mathbf{S}_{\alpha\xi}\mathbf{C}'_{\xi}\mathbf{S}^{T}_{\alpha\xi}\right\} \le \bar{\tau}_{\alpha} \tag{83}$$

where $\mathbf{S}_{\alpha\xi}$ is the matrix of the sensitivity profiles of the active responses ($\bar{\alpha}$). At each cost function calculation the parameter $\bar{\alpha}$ is mapped back to the full dimensional response $\bar{y}$; hence, the cost function remains the same. The algorithm might be summarized as follows:

1- Determine a basis for the active subspace described by a matrix ($\mathbf{U}^{m\text{x}r}$) using the range finding algorithm (RFA) to identify the active responses.

2- Calculate the sensitivity profile for the active responses ($\bar{\alpha}$) using the adjoint approach.

3- Calculate the new constraints in terms of the active responses using Eq. (81). Execute the IUQ optimization problem to determine the search parameters.

6.2.2 Case Study: High Dimensional Single Physics Target Accuracy Assessment– Lattice/Depletion

Motivated by the need for multi-physics coupling in many nuclear systems modeling, this section introduces a numerical test that illustrates the use of the proposed technique on coupled multi-physics models. A depletion-transport sequence is used for demonstration. A PWR quarter fuel lattice is modeled using SCALE6.1 (H. B Robinson Assembly 05, Rod N-9, Sample N-9B-S, First Cycle [57]) where the TRITON sequence is used to perform the depletion calculations through three key steps: the first step is the transport calculations and the flux post processing calculation (mainly NEWT) where the transport flux solution is used to prepare region-averaged multi-group cross sections and multi-group flux values for each depletion material. Additionally, the energy-integrated power for each depletion material is determined by normalizing the model power density to equal a user defined power level. Second, COUPLE module generates a one-group cross-section library for each material assigned for depletion. Finally, ORIGEN module is used to deplete material using the normalized material power or the normalized flux

In this numerical test the NEWT transport solver is used to calculate the corresponding neutron flux distribution and the multiplication factor and hence considered as one physics model (denoted as Transport Calculations in Figure 85), while the rest of calculations are considered another separate physics (denoted as Depletion Calculations in Figure 85). The target is to constrain the uncertainties of the flux solution and the critical eigenvalue at all depletion steps to be below some specified target values. The transport calculations takes the neutron macroscopic cross-sections ($\bar{\Sigma}$) as input and generates the flux and eigenvalue as responses. On the other hand, the depletion calculations takes the neutron flux distribution as

an input to predict isotopic concentrations, as well as to generate many-group spatially dependent cross-sections for nodal core calculations [57].

The goal is to constrain the uncertainty in the 44 group neutron scalar flux in the fuel mixture and the multiplication factor over 5 depletion steps (4 intervals).

In order to find the reduced space, an augmented vector ($\bar{\lambda}$) is defined and the RFA is used to find the basis of the active subspace:

$$\lambda = \begin{pmatrix} \bar{\phi} \\ k \end{pmatrix} \tag{84}$$

Assume that matrix $\mathbf{U}_{\lambda} \in \mathbb{R}^{mxr}$ is the basis matrix which is used to transform the reduced space uncertainties into the full space using Eq.(81). Hence, the response ($\bar{\lambda}$) can be transformed into the lower dimensional subspace as follow:

$$\bar{\lambda} = \mathbf{U}_{\lambda} \bar{\alpha} \tag{85}$$

where the constraint can be defined as follow:

$$diag\left[\mathbf{S}_{\alpha\xi}\mathbf{C}_{\xi}\mathbf{S}_{\alpha\xi}^{T}\right] < \bar{\tau}_{\alpha} \tag{86}$$

where $\bar{\tau}_{\alpha}$ is the vector of the user defined constraint tolerances (i.e. target variance). Figure 86 shows the relative error upper bound predicted when approximating the full dimensional space of the augmented parameter ($\bar{\lambda}$) with a lower dimensional subspace using Eq.(87). Previous work has demonstrated that, for loosely coupled models, the active subspace can be estimated using a gradient-free RFA and yet be inclusive of that obtained from the gradient-based RFA (**GB-MPRFA**) (refer to chapter 2 and 3). Hence, in this numerical test we employ the subspace obtained by the gradient-free RFA applied on the transport model (only) to obtain the subspace

characterized by the error metric in Figure 86. The RFA uses the following equation to predict the error upper bound:

$$\varepsilon_{upper} = 10\sqrt{\frac{2}{\pi}} \max_{i=1,\dots p} \| (\mathbf{I} - \mathbf{U}_\lambda \mathbf{U}_\lambda^T)\bar{\lambda}^i \|_2 \tag{87}$$

where this result is guaranteed with a probability of $1-10^{-p}$ [30, 34]. Moreover, *p* is the number of extra snapshots used to verify this upper bound.

For demonstration, in this numerical test, a subspace with dimension (r = 10) is used, Figure 86 suggests that this subspace can approximate the variations of the response vector ($\bar{\lambda}$) with a relative error upper bound less than 1%. Keeping in mind that the number of responses $\bar{\lambda}$ per transport calculation is 45 = (44 +1) vs. 10 degrees of freedom per depletion step for the reduced order problem.

Table 29 shows the summary of the calculations and the result. The reduced formalism computes in less than 2% of the time required to solve the full dimensional space problem (using the objective function presented by Eq.(88)). Figure 87 shows a comparison of the uncertainty in the neutron flux over the 5 depletion steps burning the fuel to 33 GWD/MTHM. The figure depicts the comparison between the target accuracy violation as calculated by the full dimensional analysis and the reduced dimensional analysis.

Table 30 provides the required experiments along with the required uncertainties; the experiments were prioritized according to the expression given by Eq.(79) . Note that all the factors $\{\omega_i\}$ and $\{\mu_j\}$ are set to 1.0. On the other hand, Table 31 compares the target accuracy violation in the multiplication factor (k_{eff}) as obtained by both the full dimensional analysis

and the reduced dimensional analysis. Moreover, Figure 87 compares the constraint violations in the 44-group neutron flux distribution over the depletion steps (from fresh fuel to 33 GWD/MTHM). In this numerical example the objective (cost) function is defined by Eq.(88), denoting the relative financial effort reported in the table:

$$\text{Cost}\left(\bar{d}\right)=\frac{\left(\sum_{i=1}^{n}\frac{\omega_i}{\sigma_i^{',2}}-\sum_{i=1}^{n}\frac{\omega_i}{\sigma_i^{2}}\right)}{\sum_{i=1}^{n}\frac{\omega_i}{\sigma_i^{2}}} \tag{88}$$

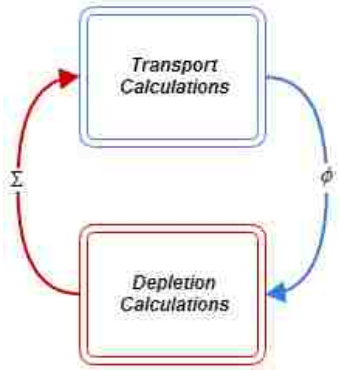

Figure 85. The Depletion Sequence

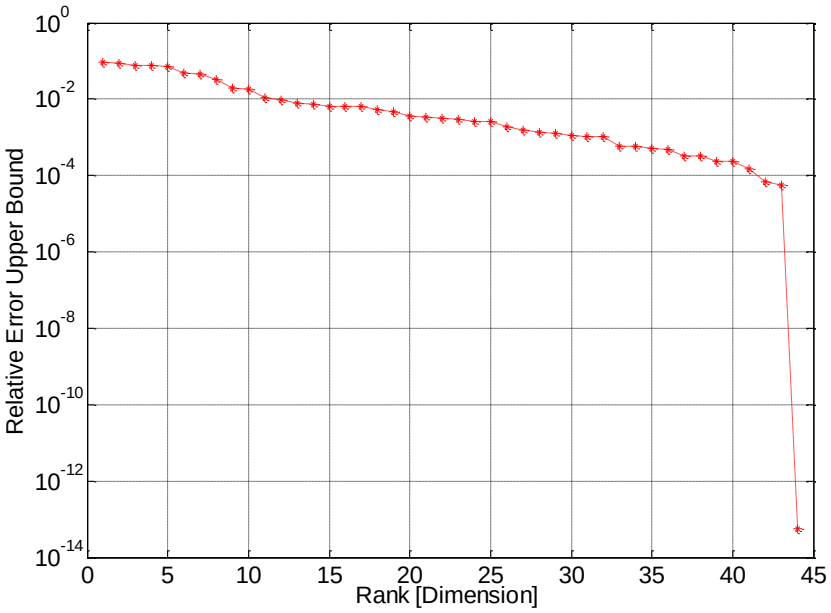

Figure 86. Error upper bound –scalar flux.

Table 29. Summary of the results.

	Number of Constraints	Relative Financial Effort Eq.(88)
Full Space	45	0.325%
Reduced Space	10	0.326%

Table 30.The required experiments along with the required uncertainties.

Parameter	σ^0 %	$\sigma^{'}$ %	χ_L
$^{238}_{92}\mathrm{U}\ (n,n')$ [3.0-4.8]MeV	20.04%	2.83%	57%
$^{238}_{92}\mathrm{U}\ (n,n')$ [1.85-2.35]MeV	19.71%	12.34%	65%
$^{238}_{92}\mathrm{U}\ (n,n')$ [2.48-3.00]MeV	19.13%	12.15%	73%
$^{238}_{92}\mathrm{U}\ (n,n')$ [1.4-1.85]MeV	21.06%	13.87%	79%
$^{239}_{94}Pu\ (\bar{\nu})$ [0.275-0.325]eV	1.03%	0.50%	83%
$^{239}_{94}Pu\ (\bar{\nu})$ [0.1-0.15]eV	1.03%	0.52%	86%
$^{238}_{92}\mathrm{U}\ (n,\gamma)$ [0.03-0.1]KeV	3.00%	1.67%	88%
$^{238}_{92}\mathrm{U}\ (n,n')$ [0.9-1.4]MeV	19.33%	14.76%	91%
$^{239}_{94}Pu\ (\bar{\nu})$ [0.15-0.20]eV	1.03%	0.62%	92%
$^{238}_{92}\mathrm{U}\ (n,n')$ [4.80-6.43]MeV	20.85%	16.07%	94%

Table 31. Uncertainty in the multiplication factor.

Depletion Step (GWD/MTHT)	Initial $\sigma_{k_{eff}}$	Target $\sigma_{k_{eff}}$	$\sigma_{k_{eff}}$ (Full space)	$\sigma_{k_{eff}}$ (Reduced space)
0.00	0.0054	0.0038	0.0036	0.0036
5.44	0.0065	0.0046	0.0043	0.0042
15.7	0.0073	0.0052	0.0044	0.0044
25.1	0.0080	0.0057	0.0049	0.0049
33.7	0.0084	0.0059	0.0051	0.0051

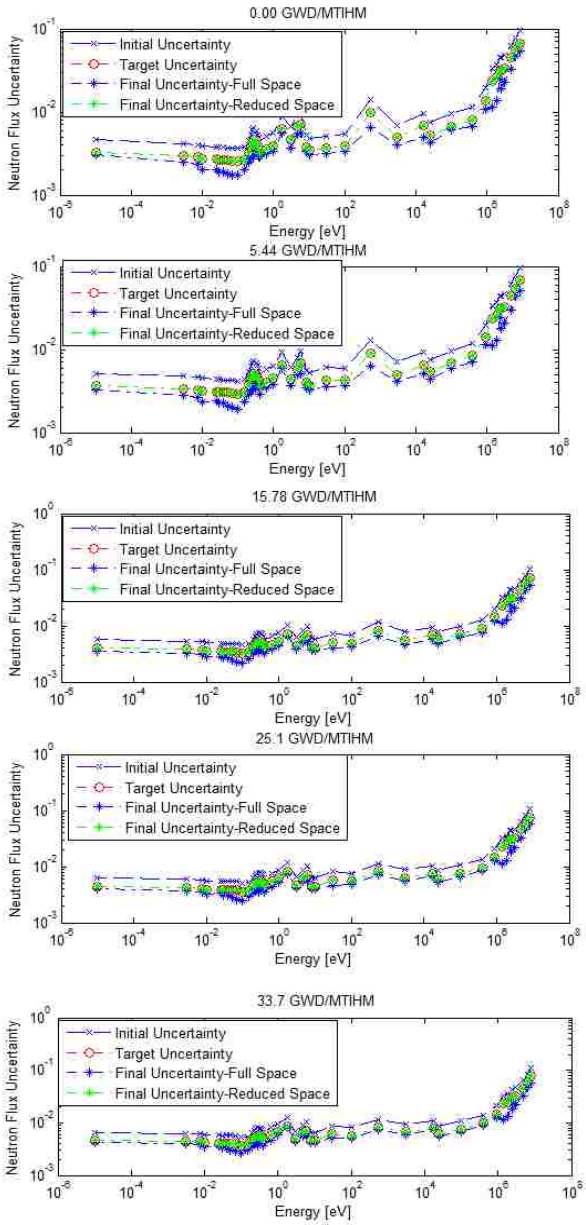

Figure 87. Uncertainty (standard deviation) in the 44 group flux in the fuel mixture (normalized to the sum of fluxes in all mixtures) as obtained from the full and reduced space.

This section introduces an efficient technique for performing the inverse uncertainty quantification (IUQ) in reactor physics calculations. This work deals with the case when the IUQ aims to constraint many responses. In this case the computational cost of the IUQ problem is expected to be high and the problem might become intractable. Therefore, this section

illustrates that computational savings are possible via reduction of the dimensionality of the response space by transforming it into a lower dimensional active subspace.

6.3 Multi-Physics Target Accuracy Assessment

In recent years, there has been an increasing demand from nuclear research, safety, regulation and industrial communities for best estimate predictions to be provided with enhanced confidence bounds for many important attributes such as neutron multiplicity, power distribution and reaction rates. Therefore, the inverse uncertainty quantification (IUQ) problem can be defined and solved to assess the requirements on the sources of uncertainty such that the uncertainty in the attributes of interest can be met. The resultant of this inverse problem can, subsequently, guide the experimental effort to further reduce the uncertainty associated with these sources in the most efficient and optimized manner.

As pointed out in chapter 1, nuclear reactor modeling and simulation involve neutronics, fuel thermo-mechanics and thermal hydraulics. Therefore, multi-physics coupling is needed to account for the feedback from these different effects. Such coupling is important for reactor design and safety analysis and should result in an integrated high-fidelity system of software tools describing the overall Nuclear Power Plant (NPP) behavior and taking into account interactions among the different systems and physical phenomena during reactor operation and safety related transients. Hence, multi-physics coupled modeling is at the heart of the most important research problems being perused in the nuclear engineering modeling and simulation field. Previous chapters introduced gradient-based and gradient-free reduction algorithms for single physics and multi-physics coupled models. Moreover, Efficient UQ and IUQ formalisms

were introduced and discussed. In this chapter the IUQ analysis will be extended to multi-physics coupled models in gradient-free and gradient-based manners.

The computational cost of the inverse uncertainty quantification problem depends, mainly, on the dimensionality of the uncertainty sources space and the constraint space. Fortunately, these spaces can be often replaced by lower dimensional subspaces approximations that are believed to represent the actual subspaces within certain user-defined upper error bounds [30]. Moreover, previous sections have demonstrated and implemented subspace based improvements to enhance the identifiabiltiy and the computational cost of the IUQ formalism.

As demonstrated previously, reducing the dimensionality in the uncertainty sources space allows the analyst to consider a larger number of uncertainty sources because the computational cost is dependent of the number of DoF which represent the major uncertainty/sensitivity components, unlike the conventional formalism where the computational cost is dependent on the number of uncertainty sources.

In this section, the algorithms developed previously are used to extract the influential DoF efficiently for two loosely coupled models. Extracting the important DoF represented by the basis of the lower dimensional subspace approximation (active subspace) reduces the complexity and computational cost of the analysis. Dimensionality reduction in the constraint space is introduced and used to reduce the computational cost of the IUQ formalism. A multi-physics problem represented by a PWR fuel lattice depletion problem (CASL VERA progression problem 2) is modeled and the accuracy of the multiplication factor and the group dependent neutron flux (spatially averaged) are used as reactor attributes whose uncertainties are to be reduced. The goal is to determine the required covariance in the nuclear data cross

sections such that the target accuracies are achieved. Numerical experiments are used to demonstrate the implementation and the computational efficiency of the proposed algorithm.

6.3.1 Algorithm

The complexity of IUQ problem (as defined in previous sections) depends on the number of uncertainty sources to be reckoned with (the dimensionality of the uncertainty sources space) and the number of constraints to be satisfied (the dimensionality of the constraints space). Other complications might arise if the model is to be considered as a non-linear model. In this case the linear uncertainty propagation (the sandwich equation) is no longer valid. Moreover, if higher than the second order moment is required to describe the uncertainty distribution (e.g. non-Gaussian) then the method fails. However, in this work the linear assumption is to be tolerated for relatively small intervals in the input parameter range.

Section 6.1.1 suggested a subspace based approach to deal with the case of huge dimensionality in the uncertainty sources space [88]. That approach considered single-physics problem with few constraints and high dimensional uncertainty source space. However, in this work high dimensional multi-physics coupled problems will be considered.

To begin with the analysis, consider the two loosely coupled multi-physics models illustrated in Figure 85. First let us focus on model **A** and assume that the model can be represented mathematically as follow:

$$\bar{y} = f\left(\bar{x}\right),\ \bar{x} \in \mathbb{R}^n \text{ and } \bar{R} \in \mathbb{R}^m$$

The multi-physics range finding algorithm (MPRFA) introduced in chapter 3 can be used to approximate the full dimensional space representing the model's response (i.e. $\bar{y}$) by a lower dimensional subspace (active subspace). For example, for the two loosely coupled multi-

physics models in Figure 89 there are two interface parameters where each is characterized by a space that can be approximated using a lower dimensional subspace (active subspace) using the RFA. Let $\mathbf{U}_x$ and $\mathbf{U}_y$ be the basis of the active subspaces of the x and y – spaces, respectively, as calculated by the MPRFA. MPRFA uses a combination of gradient-free and gradient-based versions of the RFA. It is important to notice that the RFA can be used to calculate the basis of the lower dimensional subspace approximation of the *x*- and *y*-subspaces; however, as demonstrated in Chapter 3, comparing the RFA and the MPRFA illustrated the superiority of the MPRFA over the RFA. Whenever the gradient information is not available, the MPRFA cannot be used, hence the RFA can be used to perform the gradient-free dimensionality reduction using the Efficient Range Finding Algorithm, i.e. ERFA (Refer to Chapter 2). For more details about the RFAs Ref. [30, 34] might be consulted.

For example, the response $\bar{y} \in \mathbb{R}^m$ can be represented by a lower dimensional subspace characterized with the basis matrix $\mathbf{U}_y$. Therefore, any response vector can be written as a linear combination of the basis vectors as follow:

$$\bar{y} = \sum_{i=1}^{m} \alpha_{y,i} \bar{u}_{y,i} \approx \sum_{i=1}^{r_y} \alpha_{y,i} \bar{u}_{y,i} \tag{89}$$

where r_y is the rank of the lower dimension subspace approximation (active subspace):

$$\bar{y}^{m\text{x}1} = \mathbf{U}_y^{m\text{x}r_y} \bar{\alpha}_y^{r_y\text{x}1} \tag{90}$$

where $r_y \ll m$. The following paragraphs discuss an approach which can be used to perform the uncertainty quantification analysis efficiently utilizing the lower dimensional spaces.

From Eq.(90), if the uncertainties in the reduced order parameters (α_y's) are determined, Eq.(91) can be used to propagate the uncertainty towards the full dimensional response as follow:

$$\mathbf{C}_y = \mathbf{U}_y \mathbf{C}_{\alpha_y} \mathbf{U}_y^T, \tag{91}$$

hence, one can propagate the uncertainties along the reduced space and map them back towards the full space. Note that in this case the number of responses is reduced from $m \to r_y$, hence the computational cost of estimating the uncertainties is reduced.

Moreover, the IUQ formalism entails the calculation of the sensitivity profiles which often involves models characterized with large input parameter dimensionality (e.g. nuclear cross-sections) and/or high dimensional response space. Generally, there are two approaches to evaluate the sensitivities; the forward approach and the adjoint approach. The adjoint (variational) approach is preferred whenever the model is characterized with a high dimensional input parameter space. The adjoint approach entails the calculation of *m* adjoint profiles, each corresponding to one of the responses (observables). Therefore, the computational cost of applying the adjoint approach depends on the number of responses (the dimensionality of the *y*-space). Nevertheless, if the dimensionality of the *y*-space is high and/or the adjoint model is not available, then the forward approach (brute force) might be used. Although the forward approach is always available to use, its computational cost depends on the number of inputs (dimensionality of *x*-space). Unfortunately, neutronics applications can be characterized with a huge dimensionality in the input space (e.g. nuclear data cross-section data) and in certain applications huge dimensionality in the response space (e.g. spatial mesh wise angular flux distribution). If the response space is also characterized with huge

dimensionality, then even the adjoint method might be computationally expensive; in this case the MPRFA can provide a way to ease the analysis and make the computational cost reasonable. A reduction in the response space provides an efficient way to calculate the sensitivities in the lower dimensional space and map them back towards the full dimensional space as follow:

$$\overline{s}_{yx} = \mathbf{U}_{y}^{m\mathrm{x}r_y}\overline{s}_{\alpha_y x} \tag{92}$$

For instance, using the adjoint method to calculate the sensitivity coefficients of a general response requires $r_y + 2$ model runs (1 forward run + 1 adjoint runs and r_y GPT run). On the other hand, the corresponding computational cost of calculating the sensitivity profiles on the full dimensional space is $m+2$. Hence, the IUQ formalism can be tuned to constrain the reduced dimensional variance ($\mathbf{C}_{\alpha_y}$) instead of the full dimensional variance ($\mathbf{C}_y$) which can be related to that of the reduced dimensional variance using Eq.(91).

Whenever the adjoint model is not available, a similar approach can be used to make the forward approach more efficient. This approach was first proposed in Ref. [51] under the title Efficient Subspace Method (ESM). Assume that the parameter space can be approximated by a lower dimensional subspace with the orthonormal basis $\mathbf{U}_{x}^{n\mathrm{x}r_x}$. Then any snapshot of the parameter space can be represented, approximately, by a linear combination of the basis vectors (columns of matrix $\mathbf{U}_{x}^{n\mathrm{x}r_x}$) :

$$\overline{x} = \sum_{i=1}^{n}\alpha_{x,i}\overline{u}_{x,i} \approx \sum_{i=1}^{r_x}\alpha_{x,i}\overline{u}_{x,i} \tag{93}$$

where r_x is the rank of the lower dimension approximation of the parameter space:

$$\overline{x}^{m\mathrm{x}1} = \mathbf{U}_{x}^{m\mathrm{x}r_x}\overline{\alpha}_{x}^{r_x\mathrm{x}1} \tag{94}$$

Now consider a multi-physics coupled system (consult Figure 2). In this case the IUQ problem must be solved repeatedly to make sure that the variance (or the standard deviation) on the interface parameters (e.g. $\bar{x}$ and $\bar{y}$) are constrained on each coupling step.

Assume that the two models are coupled over *t* steps (e.g. time steps). For example, if the focus is turned onto the *y*-space interface, then at each coupling step the sensitivity profile must be updated ($\mathbf{s}_{yx}^{j}$):

$$\mathbf{S}_{yx}^{j},\ j=1,\cdots,t$$

The IUQ formalism can be reformulated to constrain the variance on the *y*-space as follow:

$$diag\left\{\mathbf{S}_{yx}^{j}\mathbf{C}_{x}^{'}\mathbf{S}_{yx}^{j,T}\right\}\leq\bar{\tau}_{y}$$

A dimensionality reduction on the interface space can help in making this formalism efficient, so that the IUQ problem is solved along the influential directions (DoF) in the interface space. As mentioned before, the problem can be recast in terms of the reduced variable. This transformation simplifies the problem in two aspects: first, the sensitivity profiles can be calculated efficiently along only r_y responses instead of *m* responses; this makes the adjoint sensitivity analysis more efficient. Moreover, the forward sensitivity approach might be simplified as explained before. Second, the number of constraints to deal with it is transformed from *m* to r_y. In this case the constraint can be reformulated as follow:

$$diag\left\{\mathbf{S}_{\alpha_y x}^{j}\mathbf{C}_{x}^{'}\mathbf{S}_{\alpha_y x}^{j,T}\right\}\leq\bar{\tau}_{\alpha_y}$$

To avoid repetition, it is obvious that the same argument applies on the *x*-space interface between the two models. The proposed algorithm (Multi-Physics Subspace based Inverse Uncertainty Quantification) can be summarized as follows (**MP-SIUQ**):

Step 1: Finding the active subspace approximation (MPRFA)

1- Using the MPRFA, find the lower dimensional subspace approximation of the interface parameters of interest ($\mathbf{U}_y^{nxr}$ and $\mathbf{U}_x^{mxl}$).

2- Calculate the sensitivities on the reduced space and at each coupling step for each interface parameter:

$$\mathbf{s}_{\alpha_y x}^{j},\ j=1,\cdots,t$$

$$\mathbf{s}_{\alpha_x \mathrm{y}}^{j},\ j=1,\cdots,t$$

where *t* is the total number of coupling steps.

Step 2 : Use the SIUQ algorithm to obtain the regularization subspace (T-subspace).

Step 3 : Solve the IUQ problem in the reduced space.

1- Outer optimization: Starting from $j = t;$ Using Eq. (46) to determine the target accuracy in the lower dimensional space for model **A**.

2- Solve the IUQ problem for model **A** using the following reduced constraint:

$$diag\left\{\mathbf{s}_{\alpha_y x}^{j}\mathbf{C}_x^{'}\mathbf{s}_{\alpha_y x}^{j,T}\right\} \le \bar{\tau}_{\alpha_y}$$

Minimize the corresponding objective function (e.g. Eq.(77)) for the decision variable $\bar{d}_y$

3- From the solution of the outer minimization problem, determine the target accuracy for model **B**:

$$\bar{\tau}_x^{j} = \min\left\{diag\left[\mathbf{C}_x^{'}\right], \bar{\tau}_x^{j}\right\}$$

Using the following equation, determine the target accuracy in the lower dimensional space:

$$\mathbf{C}_x = \mathbf{U}_x\mathbf{C}_\alpha\ \mathbf{U}_x^T$$

a- Solve the IUQ formalism for model **B** using the following constraint**:**

$$diag\left\{\mathbf{s}^{j}_{\alpha_x y}\mathbf{C}'_{y}\mathbf{s}^{j,T}_{\alpha_x y}\right\} \le \bar{\tau}^{j}_{\alpha_x}$$

Minimize the corresponding objective function (e.g. Eq. (88)) for the decision variable $\bar{d}_x$

b- Determine the target accuracy for the outer optimization step:

$$\bar{\tau}^{j-1}_{y} = \min\left\{diag\left[\mathbf{C}'_{y}\right], \bar{\tau}^{j-1}_{y}\right\}$$

4- *j=j-1*, if *j = 0*, go to next step , otherwise repeat steps 1 to 4.

5- Report the initial covariance library (*j*=0) as the library required to attain the target accuracy throughout the coupling process.

6.3.2 Case Study: CASL Progression Problem 2 – Lattice/Depletion

Motivated by the existence of strong multi-physics coupling in many computational nuclear engineering applications, this section introduces a numerical test that illustrates the use of the proposed algorithm on coupled multi-physics models. A depletion application can serve as an example where the transport calculations are considered to be coupled with the rest of the depletion sequence. SCALE6.1, TRITON sequence is used to simulate the depletion of a PWR fuel lattice model [57]. More specifically, the 2-D TRITON sequence T-DEPL is used. T-DEPL sequence consists of three main modules: NEWT, COUPLE and ORIGEN. NEWT generates the transport flux distribution which is then used to compute the region-averaged, multi-group cross-sections along with the multi-group flux for each of the depletion materials. COUPLE generates the 1-group cross-section for each of the depletion materials. Finally, ORIGEN depletes each of the isotopes based on the normalized material flux (or power) using the 1-group cross-sections computed by COUPLE.

This section will solve the target accuracy assessment problem using the classical problem formulation [16, 19] while in Section 6.3.3 a new problem formalism is proposed. The formalism entails a new cost function combined with a more realistic list of experiments.

In this numerical example, the transport calculations represented by NEWT are considered as a separate physics (Transport calculation block in Figure 89) while COUPLE and ORIGEN are considered another separate physics (depletion calculations in Figure 89). The interface parameters are the neutron flux distribution ($\bar{\phi}$) and the multiplication factor (k_{eff}) which are the output of the transport calculations model ($\bar{\lambda}$) and the macroscopic cross-sections ($\bar{\Sigma}$), which are considered to be the output of the depletion calculation sequence.

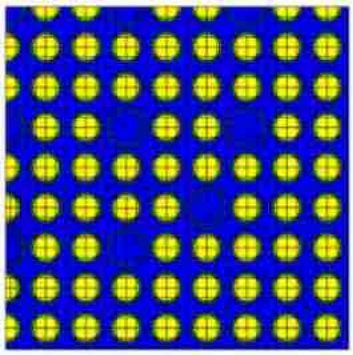

Figure 88. CASL Progression Problem 2: lattice Model.

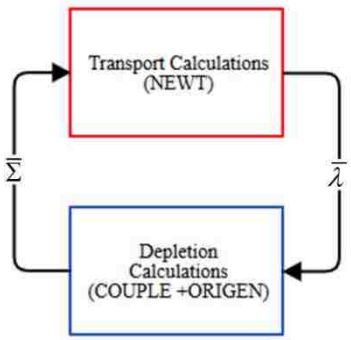

Figure 89. Depletion sequence.

The goal is to constrain the uncertainty in the mesh-wise-spatially dependent 44 energy group neutron scalar flux and the multiplication factor over 5 depletion steps (4 intervals). In order to find the reduced space, an augmented vector ($\bar{\lambda}$) is defined as the vector containing the transport flux and the multiplication factor:

$$\bar{\lambda} = \left(\bar{\phi}_i \cdots k_i\right)^T,$$

where $\bar{\phi}_i$ is the vector of multi-group transport flux as calculated after the i^{th} depletion step and k_i is the multiplication factor characterizing the system after the i^{th} depletion step. Assume that the columns of matrix $\mathbf{Q}_\lambda \in \mathbb{R}^{nxm}$ form the basis for the interface parameter $\bar{\lambda}_i$. While the basis of the other interface, the microscopic nuclear data cross-sections ($\bar{\Sigma}$), is represented by the columns of matrix $\mathbf{Q}_\Sigma$. The basis of the low dimensional subspace approximation can be calculated using either Algorithm I (ERFA) or (MPRFA). Figure 90 and Figure 91 compare the performance of the lower dimensional subspace approximation for the $\bar{\lambda}$ interface parameter and $\bar{\Sigma}$ interface, respectively. Each figure compares the performance of the **ERFA** and **MPRFA**. The relative error upper bound in the two figures suggests that the performance

of the basis calculated by the MPRFA is superior to those calculated via the ERFA. Therefore, in the remainder of this text the MPRFA will be used to calculate the basis of the lower dimensional subspace ($\mathbf{Q}_\lambda$ and $\mathbf{Q}_\Sigma$). However, for an application where running the coupled models is computationally impractical, then the ERFA can offer a computationally practical technique to performed dimensionality reduction. For example, for the transport calculation model (first physics), these bases are used to transform the reduced space uncertainties into the full space using Eq.(91). Hence, the response ($\bar{\lambda}$) can be transformed into the lower dimensional subspace as follow:

$$\bar{\lambda} = \mathbf{Q}_\lambda \bar{\alpha}_\lambda$$

where the constraint can be defined as follow:

$$diag\left\{\mathbf{S}^T_{\alpha_\lambda x}\mathbf{C}_x\mathbf{S}_{\alpha_\lambda x}\right\} < \bar{\tau}_{\alpha_\lambda}$$

Previous work demonstrated that the active subspace can be estimated using a single physics based RFA and yet be inclusive of that obtained from the multi-physics based RFA. The RFA uses the following equation to predict the error upper bound:

$$\varepsilon_{upper} = 10\sqrt{\frac{2}{\pi}}\max_{i=1,\dots p} \| (\mathbf{I} - \mathbf{Q}_\lambda \mathbf{Q}^T_\lambda)\bar{\lambda}_i \|_2$$

where this result is guaranteed with a probability of $1-10^{-p}$.

First the sensitivities are calculated using the adjoint approach applied at the reduced space ($\mathbf{S}_{\alpha_\lambda / x}$) and then Eq.(92) is used to map the sensitivity back to the full dimensional space. The same procedure is applied on the other interface parameter (microscopic cross-sections $\bar{\Sigma}$).

In this numerical test, the scalar neutron flux is being calculated on 52 spatial mesh points for 44 energy groups which makes the full dimension of the scalar neutron flux (52 x 44 =

2288); however, the multiplication factor at each depletion step is augmented in the vector $\bar{\lambda}$ which makes its dimension (2288 + 1 = 2289). To keep the error upper bound below 1%, a subspace of rank 300 is used for $\bar{\lambda}$ (Figure 90) and 220 for the cross-sections (Figure 91).

Table 32 shows the summary of the calculations and the results. The reduced formalism runs within a reasonable time scale compared to that required by the full dimensional problem, yet the reduced formalism produced similar results as depicted by Table 33 and Table 34. Both algorithms converge to similar solutions, as the transformation from the full to lower dimensional space preserves the important directions in the response space. Therefore, the uncertainty requirements on the sources (nuclear cross-sections) are similar.

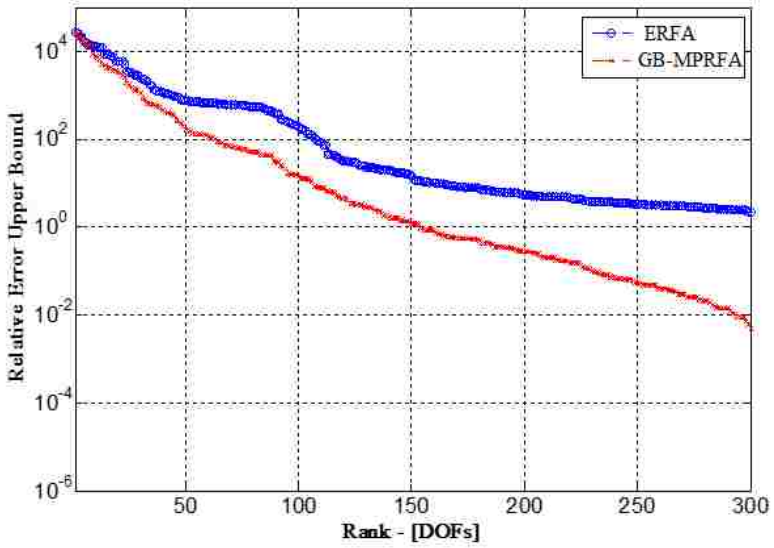

Figure 90. Single-Physics vs. Multi-Physics Active Subspace ($\bar{\lambda}$).

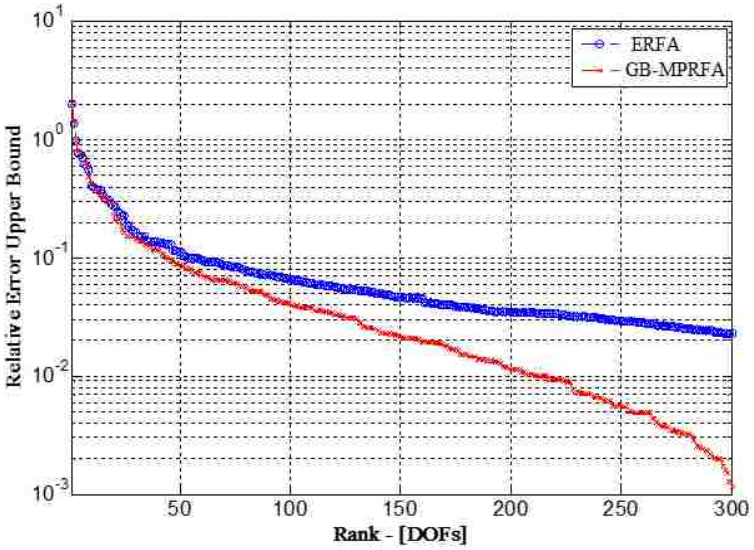

Figure 91. Cross section subspace as obtained from the single physics examination compared to the one obtained from the multi-physics examination ($\overline{\Sigma}$).

Table 32. Summary of the numerical results and comparison of the two algorithms.

Algorithm	DoF	CPU time (hours)	Cost^{opt} (BoC) - Eq.(77)	Cost^{opt} (EoC) - Eq.(77)
MP-SIUQ	250	1.1	3.64%	18.1%
IUQ	36,144	-	-	-

Table 33. The experimental requirements along with their required uncertainties – (EoC).

Parameter	σ^0 %	$\sigma^{'}$ %	χ_L
${}^{238}_{92}\text{U}\ (n,n')$ [3.0-4.8]MeV	20.04%	3.27%	54%
${}^{239}_{94}Pu\ (\bar{\nu})$ [0.1-0.15]eV	1.03%	0.36%	59%
${}^{239}_{94}Pu\ (\bar{\nu})$ [0.275-0.325]eV	1.03%	0.39%	64%
${}^{239}_{94}Pu\ (\bar{\nu})$ [0.15-0.20]eV	1.03%	0.52%	66%
${}^{239}_{94}Pu\ (\bar{\nu})$ [0.07-0.1]eV	1.03%	0.55%	69%
${}^{238}_{92}\text{U}\ (n,\gamma)$ [0.03-0.1]KeV	3.00%	1.68%	71%
${}^{238}_{92}\text{U}\ (n,n')$ [1.85-2.35]MeV	19.71%	12.49%	78%
${}^{239}_{94}Pu\ (\bar{\nu})$ [0.05-0.07]eV	1.03%	0.66%	79%
${}^{238}_{92}\text{U}\ (n,n')$ [2.48-3.00]MeV	19.13%	12.29%	86%
${}^{238}_{92}\text{U}\ (n,n')$ [1.4-1.85]MeV	21.0%	14.03%	92%

Table 34. The experimental requirements along with their required uncertainties – (BoC).

Parameter	σ^0 %	$\sigma^{'}$ %	χ_L
$^{238}_{92}\mathrm{U}\ (n,n')$ [3.0-4.8]MeV	20.04%	6.66%	43%
$^{238}_{92}\mathrm{U}\ (n,n')$ [1.85-2.35]MeV	19.71%	9.92%	55%
$^{238}_{92}\mathrm{U}\ (n,n')$ [2.48-3.00]MeV	19.13%	9.66%	66%
$^{238}_{92}\mathrm{U}\ (n,n')$ [1.4-1.85]MeV	21.06%	12.46%	74%
$^{238}_{92}\mathrm{U}\ (n,\gamma)$ [0.03-0.1]KeV	3.00%	1.47%	82%
$^{238}_{92}\mathrm{U}\ (n,\gamma)$ [0.1-0.55]KeV	2.28%	1.30%	84%
$^{238}_{92}\mathrm{U}\ (n,\gamma)$ [0.01-0.03]KeV	2.69%	1.48%	87%
$^{238}_{92}\mathrm{U}\ (n,\gamma)$ [0.55-3.00]KeV	2.39%	1.39%	88%
$^{235}_{92}\mathrm{U}\ (\chi)$ [3.0-4.8]MeV	3.14%	2.14%	90%
$^{238}_{92}\mathrm{U}\ (n,n')$ [4.8-6.43]MeV	20.85%	15.12%	92%

6.3.3 Case Study: Target Accuracy Assessment for 3-D Assembly Depletion Problem (CASL Progression Problem 6)

Two differences distinguish the TAA methodology used in this case study from the ones used in previous sections:

1- The assumption that the uncertainty can be propagated linearly is removed by using a forward Monte Carlo sampling of a surrogate model that replaces the original model. Therefore, at each iteration, the uncertainty is estimated by Monte Carlo samples drawn from the surrogate model.

2- The goal of the previous TAA methodology is to determine the optimum set of the adjustment parameters for the parameters' uncertainties (cross-sections) using differential experiments. However, in reality the uncertainty in the parameters can be improved by also assimilation of measurements of integral responses. Therefore, in this section the goal of

the TAA analysis is to provide the required integral response measurement uncertainty required to improve the knowledge of the parameters uncertainties.

MP-SIUQ (refer to section 6.3.1) is used to solve the target accuracy assessment problem for the 3 dimensional depletion problem. Hence, the cost function that will be used in this case study is:

$$\text{Cost}\left(\bar{d}\right)=\sum_{j=1}^{m}\mu_j\left(\sigma_{R,j}^{2}-\sigma_{R,j}^{',2}\left(\bar{d}\right)\right)-\left(\sum_{i=1}^{M}\frac{w_i}{\sigma_i^{',2,IR}\left(\bar{d}\right)}-\sum_{i=1}^{M}\frac{w_i}{\sigma_i^{2,IR}}\right) \tag{95}$$

$$\sigma_{R,j}^{',2}\left(\bar{d}\right)\le\tau_j \tag{96}$$

where $\sigma_{R,j}^{2}$ is the initial uncertainty in the j^{th} target response of interest and $\sigma_{R,j}^{',2}$ is its updated uncertainty. $\sigma_i^{2,IR}$ is the integral response measured to enhance the knowledge of the differential parameters uncertainty ($\mathbf{C}_x$) via data assimilation. $\sigma_i^{',2,IR}\left(\bar{d}\right)$ is the updated integral responses uncertainty required to update the covariance data of the differential parameter according to the required adjustment parameter ($\bar{d}$). τ_j is the target variance ty to be achieved in the j^{th} response of interests. All values of { μ_j } and { w_i } were set to 1.0

The process can be summarized as follow:

1- Construct the surrogate (for example of the form represented by Eq. (62)) replacing the original model with a more efficient surrogate model.

2- Solve the optimization problem using the cost function defined on Eq.(95) and the constraint defined by Eq.(96). At each optimization step the uncertainty in the target responses ($\sigma_{R,j}^{2}$) are obtained by Monte Carlo Sampling via the surrogate model. At each

step the information carried by the adjustment parameters vector ($\bar{d}$) are transformed into required uncertainty in the integral response of interest.

The uncertainty is propagated non-linearly via Monte Carlo sampling through the computationally efficient surrogate model; Thereby dropping the linearity assumption endorsed in previous sections within chapter 6. Moreover, the end result is a set of required uncertainties in the measurable integral responses to be measured so that the target accuracies in the responses of interest are met.

In this case study a 3 dimensional depletion problem will be subjected for a target accuracy assessment study. The problem described in section 0 is used in this case study to perform target accuracy assessment on a few measurable responses (the multiplication factor (k_{eff}) and the fission reaction rate at the reactor assembly geometrical center (FR)) are used as integral responses that can be used to enhance the parameters uncertainties via data assimilation. On the other hand, the target responses are the maximum fuel pin power ($P_{\max}$) and the maximum fuel pin temperature ($T_{\max}$). From results introduced in chapter 4, the maximum pin power and maximum pin temperature are functions of the gap conductivity and nuclear cross-sections. Moreover, the multiplication factor and fission rate are both affected by the nuclear cross-sections and gap conductivity. Hence, reducing the uncertainty in the multiplication factor and the fission rate would reduce the uncertainty in the parameters of interest (cross-sections and gap conductivity) through data assimilation.

The simulator used is VERA-CS (refer to section 1.7) which does not have a sensitivity capability. Therefore, instead of using a linear constraint (defined by Eq.(86)) samples from a computationally efficient surrogate will be used to estimate the uncertainty in both the

responses of interests ($T_{\max}$ and $P_{\max}$) and the integral responses used for the improvement of the parameters' uncertainties (k_{eff} and FR).

Table 35 shows the initial and target accuracies of the responses of interest. First a 3rd order surrogate of the form defined in Eq. (62) is constructed and tested. Table 36 shows the accuracy tests of the 3rd order surrogate of the form defined by Eq. (62). Table 37 and Table 38 illustrates the target accuracies along with the required integral responses measurement uncertainties at the Beginning of Cycle (BoC) and the End of Cycle (EoC), respectively. Note that the requirements at the EoC are stricter than those at the BoC which means that constraining the uncertainty in the responses of interest over the fuel depletion requires rigorous knowledge of the integral responses. Finally, this section introduced the capability of performing TAA via reduced order models efficiently. This use of the surrogate removes the linearity assumption and provides a mean of using the integral experiments rather than the differential experiments.

Table 35. Initial and target accuracies for the responses of interest.

Entry	Value BoC	Value EoC
$\sigma_{T_{\max}}$	98 C^o [7%]	129 C^o [11.72%]
$\sqrt{\tau_{T_{\max}}}$	28 C^o [2%]	56 C^o [4%]
$\sigma_{P_{\max}}$	2.7 W/cm [1.2%]	29.6 W/cm [16.03%]
$\sqrt{\tau_{P_{\max}}}$	1 W/cm [0.37%]	5 W/cm [2.7%]

Table 36. Target accuracy assessment - surrogate accuracy features.

Surrogate order	RMS	Construction Data Points	Validation Points	Residuals distribution	surrogate form – related uncertainty
3rd order	$\varepsilon_{k_{eff}} \rightarrow 5$ [pcm]	150	40	$k_{eff} \rightarrow$ i.i.d	14.7 [pcm]
	$\varepsilon_{P_{\max}} \rightarrow$ 0.0098 [W/cm]			$P_{\max} \rightarrow$ i.i.d	0.01 [C^o]
	$\varepsilon_{T_{\max}} \rightarrow$ 7.4 [C^o]			$T_{\max} \rightarrow$ i.i.d	9.1 [C^o]
	$\varepsilon_{FR} \rightarrow$ 0.00021			$FR \rightarrow$ i.i.d	0.0009

Table 37. The target accuracies along with the required experimental uncertainties for the measurable integral parameters – (BoC).

$\sqrt{\tau_{T_{\max}}}$ %	$\sqrt{\tau_{P_{\max}}}$ %	$\sqrt{C'_{k_{eff}}}$	$\sqrt{C'_{FR}}$
6 %	1 %	432 pcm	0.0063
4 %	0.5 %	369 pcm	0.0031
2 %	0.37%	314 pcm	0.0020

Table 38. The target accuracies along with the required experimental uncertainties for the measurable integral parameters – (EoC – 30 GWd/MTU).

$\sqrt{\tau_{T_{\max}}}$ %	$\sqrt{\tau_{P_{\max}}}$ %	$\sqrt{C'_{k_{eff}}}$ %	$\sqrt{C'_{FR}}$ %
10 %	10 %	411 pcm	0.0047
8 %	8 %	341pcm	0.0023
4%	2.70%	286 pcm	0.0012

CHAPTER 7. SUMMARY, CONCLUSIONS AND RECOMMENDATIONS

The goal of this work is to develop scalable algorithms for the uncertainty quantification, data assimilation and target accuracy assessment for large scale multi-physics simulation of nuclear reactor cores. This dissertation builds upon previous efforts for adaptive core simulation developed and reduced order modeling that appeared in various engineering fields along with efforts developed within the nuclear research community.

First, an efficient algorithm for Reduced Order Modeling (ROM) was developed in chapter 2. The algorithm is an **E**fficient version of the so called **R**ange **F**inding **A**lgorithm (**ERFA**), which utilizes loosely converged snapshots of the quantity of interest to capture the variations of these quantities of interest. The proposed algorithm enables the nuclear analysts to approximate the Quantities of Interest (QoI) via lower dimensional subspaces efficiently; therefore, enabling the replacement of complex and computational expensive models with efficient reduced order models in the form of surrogates.

For coupled multi-physics models, chapter 3 improves a previously developed gradient-based Range Finding Algorithm (RFA) and extends it to multi-physics coupled models (i.e. closed loop coupling) with feedback effect. A **G**radient **B**ased **M**ulti-**P**hysics **R**ange **F**inding **A**lgorithm (**GB-MPRFA)** is developed and utilized to construct reduced order models of coupled multi-physics models whenever the sensitivity capability is available via adjoint or forward approaches. On the other hand, for coupled models without a sensitivity capability, a **G**radient **F**ree **M**ulti-**P**hysics **R**ange **F**inding **A**lgorithm (**GB-MPRFA)** was developed to offer a method for the construction of lower dimensional subspace approximations and hence

reduced order models to replace the coupled models of interest whenever sensitivity capability is not available.

The algorithms described above are used to facilitate large scale analysis of reactor physics calculations such as uncertainty quantification and data assimilation. Chapter 4 introduces efficient algorithms for uncertainty quantification. First, the Karhunen-Loeve approach is extended for multi-physics coupled models (**MP-EUQ**) and then compared with a **S**urrogate **B**ased **U**ncertainty **Q**uantification (**SBUQ**) approach. Both methods are then verified via comparison with brute force Monte Carlo estimated uncertainty values obtained by sampling from the original high fidelity model (i.e. VERA-CS). The surrogate approach was further utilized to perform Data Assimilation (DA). Chapter 5 and the case studies therein show that data assimilation can be performed efficiently by replacing the original high fidelity models with surrogate models that has negligible computational cost to run.

Finally, chapter 6 utilizes the developed RFAs in another type of inverse problems used in nuclear reactor safety and design optimization studies, namely, the Target Accuracy Assessment (TAA). ROM is used to enhance the identifiability and efficiency of target accuracy assessment studies through the **M**ulti-**P**hysics **S**ubspace based **I**nverse **U**ncertainty **Q**uantification (**MP-SIUQ**) which reduces the dimensionality of the parameters and/or responses of interest through the proposed RFAs. Moreover, the efficiency of the problems is enhanced by replacing the original high fidelity model with a lower order surrogate; therefore, solving the inverse problem (TAA) which requires multiple model runs becomes computationally efficient.

Overall, this dissertation develops a framework that can address large scale forward problems (i.e. uncertainty quantification), and inverse problems (i.e. data assimilation and

target accuracy assessment). The algorithms introduced in this dissertation have been developed, verified and tested on lattice physics assembly models (modeled via SCALE6.1) and 3 dimensional assembly and core wide models (modeled via VERA-CS). The verification and case study tests are mainly of Light Water Reactor (LWR) type represented by CASL Progression Problem number 2 (lattice physics), CASL Progression Problem number 6 (3 dimensional assembly depletion model with thermal hydraulics feedback), and CASL Progression Problem number 9 (3 dimensional core wide depletion problem with thermal-hydraulics feedback).

The algorithms developed in this dissertation opens the way towards more detailed analysis of high fidelity models and facilitates the calibration of these models for depletion problems. In other words, the proposed algorithms formulate a model-based and general method to provide best-estimates of the Quantities of Interest (QoI) accompanied with an uncertainty evaluation, so that the conservative design assumptions are replaced by model based estimates of the margins. Moreover, in the past applications with rigorous uncertainty quantification were not possible due to computational resources requirements, hence, necessitating the excessive use of conservative engineering judgement which can now be rigorously addressed avoiding the need for excessive conservatism.

Establishing a unified framework to estimate uncertainties, safety margins and parameter calibration is important and fundamental for the improvement of reactor modeling and simulation. This would provide a more realistic and physics-based measure of reactor safety and design calculations, which help the practical implementation of risk informed regulations. Moreover, having simulation-based margins helps in expediting the licensing process when using high fidelity computer codes in safety analysis. For example, design margins can be

improved by reducing predictive uncertainty in key reactor attributes. However, the improvement of the uncertainties in such important attributes requires a robust experimental effort with potentially a huge investment in time and/or money. Nevertheless, with the availability of trusted and efficient simulation tools, the experimental effort can be directed in the most efficient and optimized manner so that the time-financial investment is minimized and the safety-competitiveness gain is maximized.

This work represents a comprehensive study for the usage of ROM techniques in nuclear engineering applications. However, room for improvement is available and further investigations are required in order to improve the efficiency and competitiveness of the ROM methods in nuclear reactor analysis. Future work, might consider more rigorous mathematical proof to support the gradient based multi-physics dimensionality reduction approach introduced in chapter 3. In this context, future work will consider developing such proofs to insure that the gradient based approach is applicable and sufficient for nuclear reactor design and safety analysis along with improving the gradient free ROM algorithms performance such that it matches the performance of the gradient based ROM algorithms. On the other hand, more surrogate forms can be tried such as the Gaussian process based surrogates and simplified physics based surrogates (e.g. sub-channel versus CFD). In addition, the surrogates can be constructed more efficiently by considering each of the coupled physics separately and then compared with the performance of the surrogates constructed for the overall coupled system.

Regarding the Data Assimilation analysis, other accelerated MCMC algorithms should be evaluated with regard to computational performance. In this dissertation, Delayed Rejection Adaptive Metropolis (DRAM) was used in conjunction with the surrogate, however, other algorithms such as DiffeRential Evolution Adaptive Metropolis (DREAM) must be tested too.

Ultimately, more case studies are needed for the consideration of other types of light water reactors (e.g. Boiling Water Reactors) which are characterized by a considerably different reactor environment which might affect the performance of the proposed algorithms. Moreover, other transient scenarios such as the Loss Of Coolant Accident (LOCA) and Loss Of Flow Accident (LOFA) can benefit from such methods as long as the required accuracy is preserved.

REFERENCES

1. Koebke, K. (1980). A new approach to homogenization and group condensation. *IAEA-TECDOC, 231*, 303.

2. Abdel-Khalik, H. S. (2004). *Adaptive core simulation*. PhD Dissertation, North Carolina State University.

3. Jessee, M. A. (2008). *Cross-section adjustment techniques for BWR adaptive simulation*. PhD Dissertation, North Carolina State University.

4. Bang, Y. (2012). *Hybrid Reduced Order Modeling Algorithms for Reactor Physics Calculations*. PhD Dissertation, North Carolina State University.

5. Boyack, B. E., & Lellouche, G. S. (1990). Quantifying reactor safety margins part 1: an overview of the code scaling, applicability, and uncertainty evaluation methodology. *Nuclear Engineering and Design, 119*(1), 1-15.

6. Hochreiter, L. E. (1992). Comments on 'quantifying reactor safety margins'. *Nuclear Engineering and Design, 132*(3), 409-410.

7. Young, M. Y., Bajorek, S. M., Nissley, M. E., & Hochreiter, L. E. (1998). Application of code scaling applicability and uncertainty methodology to the large break loss of coolant. *Nuclear Engineering and Design, 186*(1), 39-52.

8. Avramova, Maria N., and Kostadin N. Ivanov. "Verification, validation and uncertainty quantification in multi-physics modeling for nuclear reactor design and safety analysis." *Progress in Nuclear Energy* 52.7 (2010): 601-614.

9. Gaston, D., Newman, C., Hansen, G., & Lebrun-Grandié, D. (2009). MOOSE: A parallel computational framework for coupled systems of nonlinear equations. *Nuclear Engineering and Design, 239*(10), 1768-1778.

10. Constantine, P. G. (2015). *Active Subspaces: Emerging Ideas for Dimension Reduction in Parameter Studies* (Vol. 2). SIAM.

11. Constantine, P. G., & Wang, Q. (2012). Input subspace detection for dimension reduction in high dimensional approximation. *arXiv preprint arXiv:1202.3508*.

12. Constantine, P. G., & Iaccarino, G. (2012). Reduced order models for parameterized hyperbolic conservations laws with shock reconstruction. *Center for Turbulence Research*.

13. Chadwick, M. B., Obložinský, P., Herman, M., Greene, N. M., McKnight, R. D., Smith, D. L., ... & Van der Marck, S. C. (2006). ENDF/B-VII. 0: Next generation evaluated nuclear data library for nuclear science and technology. *Nuclear data sheets*, *107*(12), 2931-3060.

14. Cacuci, D. G., & Ionescu-Bujor, M. (2004). A comparative review of sensitivity and uncertainty analysis of large-scale systems. II: statistical methods. *Nuclear Science and Engineering*, *147*(3), 204-217.

15. Smith, R. C. (2013). *Uncertainty Quantification: Theory, Implementation, and Applications* (Vol. 12). SIAM.

16. Proctor, W. C. (2012). *Elements of high-order predictive model calibration algorithms with applications to large-scale reactor physics systems*. North Carolina State University.

17. Hite, J. M., Abdel-Khalik, H. S., Smith, R. C., Wentworth, M., Prudencio, E., & Williams, B. (2013). Uncertainty Quantification and Data Assimilation (UQ/DA) Study on a VERA Core Simulator Component for CRUD Analysis CASL-I-2013-0184-000.

18. Usachev, L. N., & Bobkov, Y. G. (1972). Planning an optimum set of microscopic experiments and evaluation to obtain a given accuracy in reactor parameter calculations (No. INDC (CCP)--19/U). International Nuclear Data Committee.

19. Aliberti, G., Palmiotti, G., Salvatores, M., Kim, T. K., Taiwo, T. A., Anitescu, M., ... & Tommasi, J. (2006). Nuclear data sensitivity, uncertainty and target accuracy assessment for future nuclear systems. *Annals of Nuclear Energy*, *33*(8), 700-733.

20. Arbanas, G., Dunn, M. E., & Williams, M. L. (2014). Inverse Sensitivity/Uncertainty Methods Development for Nuclear Fuel Cycle Applications. *Nuclear Data Sheets*, *118*, 374-377.

21. Abdel-Khalik, H., Turinsky, P., Jessee, M., Elkins, J., Stover, T., & Iqbal, M. (2008). Uncertainty quantification, sensitivity analysis, and data assimilation for nuclear systems simulation. *Nuclear Data Sheets*, *109*(12), 2785-2790.

22. Gandini, A. (1973). *Nuclear data and integral measurements correlation for fast reactors*. Comitato Nazionale per l'Energia Nucleare, Rome (Italy).

23. d'Angelo, A., Oliva, A., Palmiotti, G., Salvatores, M., & Zero, S. (1978). Consistent utilization of shielding benchmark experiments. *Nuclear Science and Engineering*, *65*(3), 477-491.

24. Salvatores, M., Palmiotti, G., Derrien, H., Fort, E., & Oliva, G. (1981). *Resonance parameter data uncertainty effects on integral characteristic of fast reactors*. CEA Centre d'Etudes Nucleaires de Cadarache, 13-Saint-Paul-les-Durance (France).

25. Palmiotti, G., Herman, M., Palmiotti, G., Hiruta, H., Salvatores, M., Herman, M., ... & Pigni, M. T. (2011). Use of Covariance Matrices in a Consistent (Multiscale) Data Assimilation for Improvement of Basic Nuclear Parameters in Nuclear Reactor Applications: from Meters to Femtometers. *Journal of the Korean Physical Society*, *59*(BNL--96322-2011-JA).

26. Cacuci, D. G., & Ionescu-Bujor, M. (2010). Sensitivity and Uncertainty Analysis, Data Assimilation, and Predictive Best-Estimate Model Calibration. In *Handbook of Nuclear Engineering* (pp. 1913-2051). Springer US.

27. Haario, H., Laine, M., Mira, A., & Saksman, E. (2006). DRAM: efficient adaptive MCMC. *Statistics and Computing*, *16*(4), 339-354.

28. Vrugt, J. A., & Ter Braak, C. J. (2011). DREAM (D): an adaptive Markov Chain Monte Carlo simulation algorithm to solve discrete, noncontinuous, and combinatorial posterior parameter estimation problems. *Hydrology and Earth System Sciences*, *15*(12), 3701-3713.

29. Dixon, J. D. (1983). Estimating extremal eigenvalues and condition numbers of matrices. *SIAM Journal on Numerical Analysis*, *20*(4), 812-814.

30. Halko, N., Martinsson, P., & Tropp, J. A. (2011). Finding structure with randomness: Probabilistic algorithms for constructing approximate matrix decompositions. *SIAM Review*, *53*(2), 217-288.

31. Lieu, T., Farhat, C., & Lesoinne, M. (2005). POD-based aeroelastic analysis of a complete F-16 configuration: ROM adaptation and demonstration. *AIAA Paper*, *2295*, 2005.

32. Sirovich, L. (1987). Turbulence and the dynamics of coherent structures. I-coherent structures. II-symmetries and transformations. III-dynamics and scaling. *Quarterly of Applied Mathematics*, *45*, 561-571.

33. Schilders, W. H., Van der Vorst, H. A., & Rommes, J. (2008). *Model order reduction: theory, research aspects and applications* (Vol. 13). Berlin, Germany:: Springer.

34. Bang, Y., Abdel-Khalik, H. S., & Hite, J. M. (2012). Hybrid reduced order modeling applied to nonlinear models. *International Journal for Numerical Methods in Engineering*, *91*(9), 929-949.

35. Constantine, P. G., Phipps, E. T., & Wildey, T. M. (2014). Efficient uncertainty propagation for network multiphysics systems. *International Journal for Numerical Methods in Engineering*, *99*(3), 183-202.

36. Jefferson, J. L., Gilbert, J. M., Constantine, P. G., & Maxwell, R. M. (2015). Active subspaces for sensitivity analysis and dimension reduction of an integrated hydrologic model. *Computers & Geosciences, 83*, 127-138.

37. Eldred, M. S., Giunta, A. A., van Bloemen Waanders, Bart G, Wojtkiewicz, S. F., Hart, W. E., & Alleva, M. P. (2007). *DAKOTA, a multilevel parallel object-oriented framework for design optimization, parameter estimation, uncertainty quantification, and sensitivity analysis: Version 4.1 reference manual* Sandia National Laboratories Albuquerque, NM.

38. Ghanem, R. G., & Spanos, P. D. (1991). *Stochastic finite elements: a spectral approach* (Vol. 41). New York: Springer-Verlag.

39. Xiu, D. (2010). *Numerical methods for stochastic computations: a spectral method approach*. Princeton University Press.

40. Chaturantabut, S., & Sorensen, D. C. (2010). Nonlinear model reduction via discrete empirical interpolation. *SIAM Journal on Scientific Computing, 32*(5), 2737-2764.

41. Liberty, E., Woolfe, F., Martinsson, P., Rokhlin, V., & Tygert, M. (2007). Randomized algorithms for the low-rank approximation of matrices. *Proceedings of the National Academy of Sciences, 104*(51), 20167-20172.

42. Reddy, J. N. (1993). *An introduction to the finite element method* (Vol. 2, No. 2.2). New York: McGraw-Hill.

43. Penzl, T. (2006). Algorithms for model reduction of large dynamical systems. *Linear Algebra and its Applications, 415*(2), 322-343.

44. Gallivan, K., Grimme, E., & Van Dooren, P. (1994). Padé approximation of large-scale dynamic systems with lanczos methods. Paper presented at the *Decision and Control, 1994., Proceedings of the 33rd IEEE Conference on, , 1.* pp. 443-448.

45. Ipsen, I. C. F., & Meyer, C. D. (1998). The idea behind krylov methods. *The American Mathematical Monthly, 105*(10), 889-899. Retrieved from http://www.jstor.org/stable/2589281.

46. Carlberg, K., Bou-Mosleh, C., & Farhat, C. (2011). Efficient non-linear model reduction via a least-squares Petrov–Galerkin projection and compressive tensor approximations. *International Journal for Numerical Methods in Engineering, 86*(2), 155-181.

47. Chaturantabut, S., & Sorensen, D. C. (2010). Nonlinear model reduction via discrete empirical interpolation. *SIAM Journal on Scientific Computing, 32*(5), 2737-2764.

48. Willcox, K., & Peraire, J. (2002). Balanced model reduction via the proper orthogonal decomposition. *AIAA Journal, 40*(11), 2323-2330.

49. Davison B (1957). Neutron transport theory. New York: Oxford University Press.

50. Bang, Y. and H. S. Abdel-Khalik. (2013). Hybrid reduced order modeling for coupled code systems. Internationa Conference on Mathmatics and Computational Methods Applied to Nuclear Science & Engineering (M&C 2013), Sun Valley, Idaho, USA.

51. Abdel-Khalik, H. S., Turinsky, P. J., & Jessee, M. A. (2008). Efficient subspace methods-based algorithms for performing sensitivity, uncertainty, and adaptive simulation of large-scale computational models. *Nuclear science and engineering*, *159*(3), 256-272.

52. Bang, Y. and H. S. Abdel-Khalik. (2014). Sensitivity analysis via reduced order adjoint method. *PHYSOR 2014 – The Role of Reactor Physics Toward a Sustainable Future.*

53. Eldred, M. S., Giunta, A. A., Collis, S. S., Alexandrov, N. A., & Lewis, R. M. (2004, August). Second-order corrections for surrogate-based optimization with model hierarchies. In *Proceedings of the 10th AIAA/ISSMO Multidisciplinary Analysis and Optimization Conference, Albany, NY, Aug*.

54. Kennedy, M. C., & O'Hagan, A. (2001). Bayesian calibration of computer models. *Journal of the Royal Statistical Society: Series B (Statistical Methodology)*, *63*(3), 425-464.

55. Bui-Thanh, T., Willcox, K., Ghattas, O., & van Bloemen Waanders, B. (2007). Goal-oriented, model-constrained optimization for reduction of large-scale systems. *Journal of Computational Physics*, *224*(2), 880-896.

56. Wang C, Abdel-Khalik HS. Exact-to-precision generalized perturbation theory for eigenvalue problems. Nucl Eng Des 2013;256:130-40.

57. Scale (2011): A Comprehensive Modeling and Simulation Suite for Nuclear Safety Analysis and Design, ORNL/ TM-2005/39, Version 6.1, Oak Ridge National Laboratory, Oak Ridge, Tennessee. Available from Scale: A Comprehensive Modeling and Simulation Suite for Nuclear Safety Analysis.

58. Godfrey, A., *VERA-CS Validation Plan*, CASL Technical Report: CASL-U-2014–0185–000-b, October 21, 2014.

59. Godfrey, A., *VERA Core Physics Benchmark Progression Problem Specifications, Revision 4*, CASL Technical Report: CASL-U-2012–0131–004, August 29, 2014.

60. Meyer, C. D. (2000). *Matrix analysis and applied linear algebra*. Siam.

61. Taylor, J. B., Knott, D., & Baratta, A. J. (2007). A method of characteristics solution to the OECD/NEA 3D Neutron Transport Benchmark problem. In *Joint International Topical*

Meeting on Mathematics & Computation and Supercomputing in Nuclear Applications (M&C+ SNA 2007) (pp. 15-19).

62. Bell, G. I., & Glasstone, S. (1970). *Nuclear reactor theory* (Vol. 252). New York: Van Nostrand Reinhold.

63. Hermann, O. W., & Westfall, R. M. (1995). ORIGEN-S: SCALE system module to calculate fuel depletion, actinide transmutation, fission product buildup and decay, and associated radiation source terms. *Vol. II, Sect. F7 of SCALE: A Modular Code System for Performing Standardized Computer Analyses for Licensing Evaluation, NUREG/CR-0200, Rev, 6*.

64. Palmtag, S., Clarno, K., Davidson, G., Salko, R., Evans, T., Turner, J., ... & Schmidt, R. (2014). Coupled Neutronics and Therma-Hydraulic Solution of a Full Core PWR Using VERA-CS. PHYSOR.

65. MPACT (2013): "Theory Manual", University of Michigan.

66. Collins, B., Kochunas, B., & Downar, T. (2013). *Assessment of the 2D MOC solver in MPACT: Michigan parallel characteristics transport code*. American Nuclear Society, 555 North Kensington Avenue, La Grange Park, IL 60526 (United States).

67. COBRA-TF (2014): "CTF Theory Manual", Pennsylvania State University.

68. Kochunas, B., D. Jabaay, B. Collins and T. Downar. (2013). *Coupled Single Assembly Solution with COBRA-TF/MPACT (Problem 6)*. CASL Technical Report: CASL-U-2013–0280–000.

69. Patankar, S. V., & Spalding, D. B. (1972). A calculation procedure for heat, mass and momentum transfer in three-dimensional parabolic flows. *International Journal of Heat and Mass Transfer*, *15*(10), 1787-1806.

70. Xue, F., & Elman, H. C. (2011). Fast inexact subspace iteration for generalized eigenvalue problems with spectral transformation. *Linear Algebra and its Applications*, *435*(3), 601-622.

71. Khuwaileh, Bassam A., Hite J. and Abdel-Khalik, Hany S. (2014). Subspace Methods For Multi-Physics Reduced Order Modeling In Nuclear Engineering Applications. Proceedings of *PHYSOR 2014-The Role of Reactor Physics Toward a Sustainable Future*. Kyoto-Japan.

72. Khuwaileh, Bassam A and Abdel-Khalik, Hany S. (2014). Efficient Subspace Construction for Reduced Order Modeling in Reactor Analysis. Proceedings of *PHYSOR 2014-The Role of Reactor Physics Toward a Sustainable Future*. Kyoto-Japan.

73. Khuwaileh, Bassam A and Abdel-Khalik, Hany S. (2014). "A New Importance Measure for Reduced Order Modeling", Transactions of American Nuclear Society.

74. Godfrey, A. T. (2013). VERA Core Physics Benchmark Progression Problem Specifications. CASL-U-2012-0131-002.

75. Courcelle, A., Santamarina, A., Bocquet, F., Combes, G., Mounier, C., & Willermoz, G. (2004). JEF-2.2 Nuclear Data Statistical Adjustment Using Post-irradiation Experiments. *The Physics of Fuel Cycles and Advanced Nuclear Systems: Global Developments (PHYSOR 2004).*

76. Trakas, C., & Daudin, L. (2004, April). Benchmarking of MONTEBURNS against measurements on irradiated UOX and MOX fuels. In *Proceedings of International Conference PHYSOR-2004* (pp. 25-29).

77. Galbally, D., Fidkowski, K., Willcox, K., & Ghattas, O. (2010). Non-linear model reduction for uncertainty quantification in large-scale inverse problems. *International journal for numerical methods in engineering*, *81*(12), 1581-1608.

78. Adams, B. M., Bohnhoff, W. J., Dalbey, K. R., Eddy, J. P., Eldred, M. S., Gay, D. M., ... & Swiler, L. P. (2009). DAKOTA, a multilevel parallel object-oriented framework for design optimization, parameter estimation, uncertainty quantification, and sensitivity analysis: version 5.0 user's manual. *Sandia National Laboratories, Tech. Rep. SAND2010-2183*.

79. Estacio-Hiroms, K. C., & Prudencio, E. E. Quantification of Uncertainty for Estimation, Simulation, and Optimization (QUESO).

80. Fisher, F. M. (1961). Identifiability criteria in nonlinear systems. *Econometrica: Journal of the Econometric Society*, 574-590.

81. Branch, M. A., Coleman, T. F., & Li, Y. (1999). A subspace, interior, and conjugate gradient method for large-scale bound-constrained minimization problems. *SIAM Journal on Scientific Computing*, *21*(1), 1-23.

82. Xu, Y., Sun, W., & Qi, L. (2011). A feasible direction method for the semidefinite program with box constraints. *Applied Mathematics Letters*, *24*(11), 1874-1881.

83. Chouzenoux, E., Idier, J., & Moussaoui, S. (2011). A majorize–minimize strategy for subspace optimization applied to image restoration. *Image Processing, IEEE Transactions on*, *20*(6), 1517-1528.

84. Narkiss, G., & Zibulevsky, M. (2005). *Sequential subspace optimization method for large-scale unconstrained problems*. Technion-IIT, Department of Electrical Engineering.

85. Schöpfer, F., & Schuster, T. (2009). Fast regularizing sequential subspace optimization in Banach spaces. *Inverse Problems*, *25*(1), 015013.

86. Palmiotti, G., Salvatores, M., Assawaroongruengchot, M., Herman, M., Oblozinsky, P., & Mattoon, C. (2010, April). Nuclear data target accuracies for generation-IV systems based on

the use of new covariance data. In *Proc. Int. Conf. ND2010, International Conference on Nuclear Data for Science and Technology 2010*.

87. Abdel-Khalik, H. S. (2002). Inverse Method Applied to Adaptive Core Simulation. Master Thesis, NCSU.

88. Khuwaileh, Bassam A. and H.S. Abdel-khalik. (2014) "Subspace Based Inverse Uncertainty Quantification for Nuclear Data Assessment". *Accepted for publication at Journal of Nuclear Data Sheets* (in press 2014).

89. Tikhonov, A. N., Leonov, A. S., & Yagola, A. G. (1996, May). Nonlinear ill-posed problems. In *Proceedings of the first world congress on World congress of nonlinear analysts' 92, volume I* (pp. 505-511). Walter de Gruyter & Co.

90. Godfrey, A. T. (2013, March). VERA Core Physics Benchmark Progression Problem Specifications. CASL-U-2012-0131-002, Rev.2.

91. Fisher, F. M. (1961). Identifiability criteria in nonlinear systems. *Econometrica: Journal of the Econometric Society*, 574-590.

92. Franceschini, F., Kromar, M., Ćalić, D., Godfrey, A., Collins, B., Evans, T., & Gehin, J. (2014). SIMULATION OF THE NPP KRSKO STARTUP CORE WITH CASL CORE SIMULATOR, VERA-CS.

93. Khuwaileh, B. A., Hooper, R., Turinsky, P. J., & Mousseau, V. A. (2015). Uncertainty Quantification Analysis Using VERA-CS for a PWR Fuel Assembly with Depletion CASL-I-2015-0328-000.

94. Jacquez, J. A., & Greif, P. (1985). Numerical parameter identifiability and estimability: Integrating identifiability, estimability, and optimal sampling design. *Mathematical Biosciences*, *77*(1), 201-227.

95. Heo, J., Turinsky, P. J., & Michael Doster, J. (2013). Optimization of Thermal-Hydraulic Reactor System for SMRs via Data Assimilation and Uncertainty Quantification. *Nuclear Science and Engineering*, *173*(3), 293-311.

96. Vanderplaats, G. N. (1973). *CONMIN, a FORTRAN Program for Constrained Function Minimization: User's Manual* (Vol. 62282). Ames Research Center and US Army Air Mobility R&D Laboratory.

APPENDICES

Appendix A

Frequency Distributions for the Multiplication Factor, Maximum Fuel Pin Power, Maximum Fuel Pin Temperature – CASL Progression Problem 6

Figure 92. Statistical sampling of *k-eff* corresponding to samples of the fuel thermal conductivity. Left: obtained via running VERA-CS right: obtained via the surrogate model.

(**Fuel Thermal Conductivity [k_{cond} W/m^2K] → k_{eff}**)

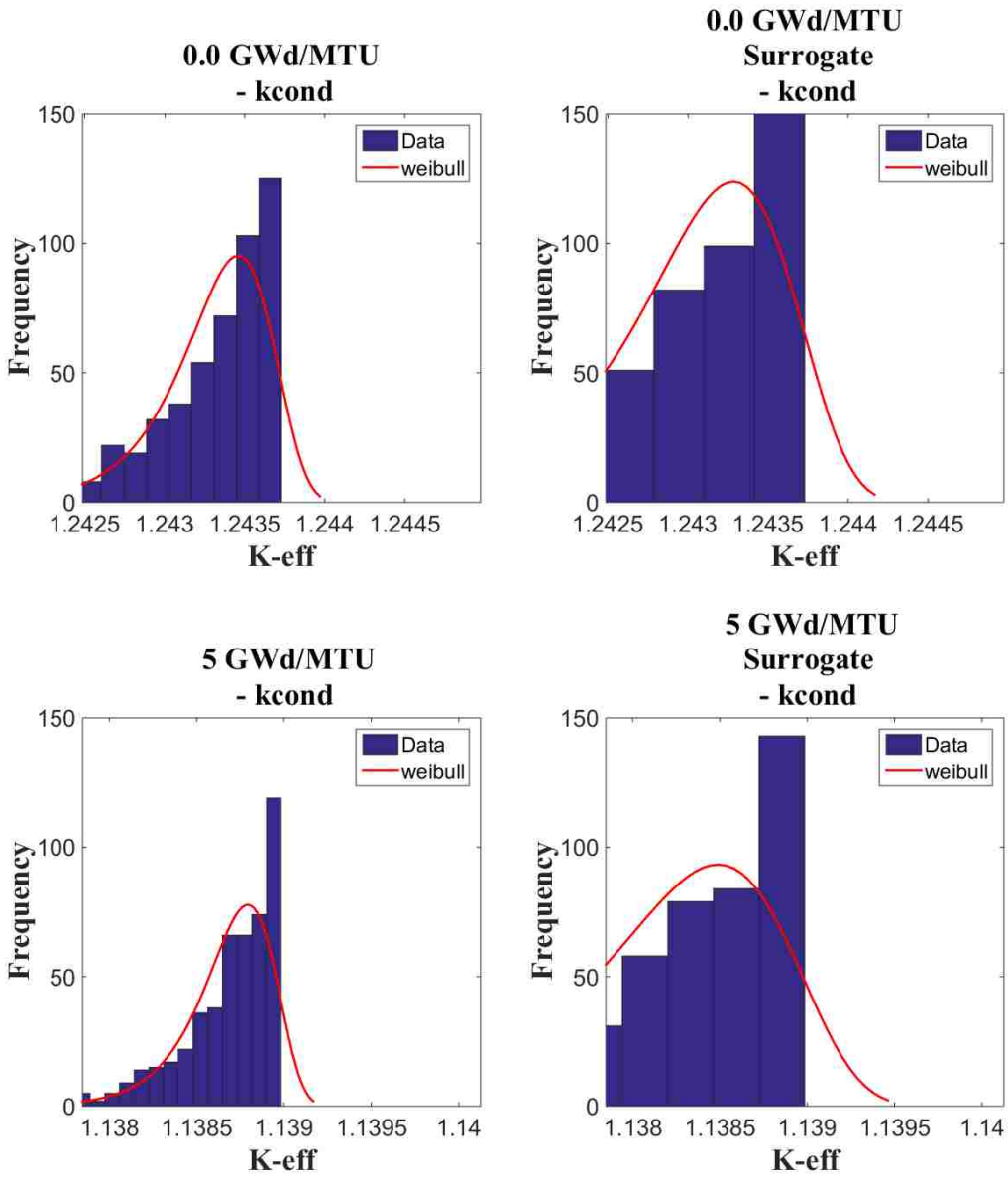
0.0 GWd/MTU
- kcond
Data
weibull
Frequency
150
100
50
0
1.2425
1.243
1.2435
1.244
1.2445
K-eff
0.0 GWd/MTU
Surrogate
- kcond
Data
weibull
Frequency
150
100
50
0
1.2425
1.243
1.2435
1.244
1.2445
K-eff
5 GWd/MTU
- kcond
Data
weibull
Frequency
150
100
50
0
1.138
1.1385
1.139
1.1395
1.14
K-eff
5 GWd/MTU
Surrogate
- kcond
Data
weibull
Frequency
150
100
50
0
1.138
1.1385
1.139
1.1395
1.14
K-eff

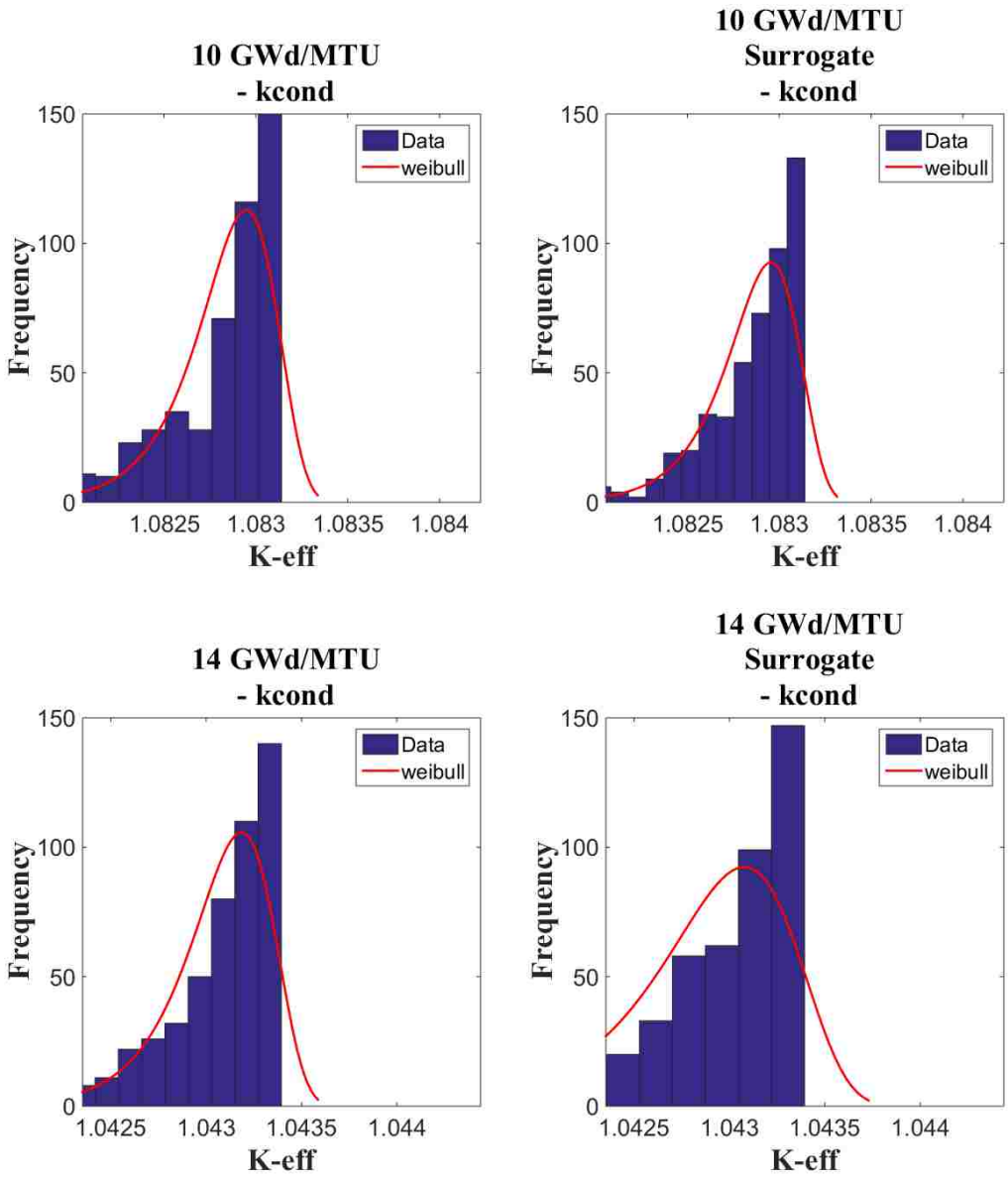
10 GWd/MTU
- kcond
Data
weibull
Frequency
K-eff
10 GWd/MTU
Surrogate
- kcond
Data
weibull
Frequency
K-eff
14 GWd/MTU
- kcond
Data
weibull
Frequency
K-eff
14 GWd/MTU
Surrogate
- kcond
Data
weibull
Frequency
K-eff

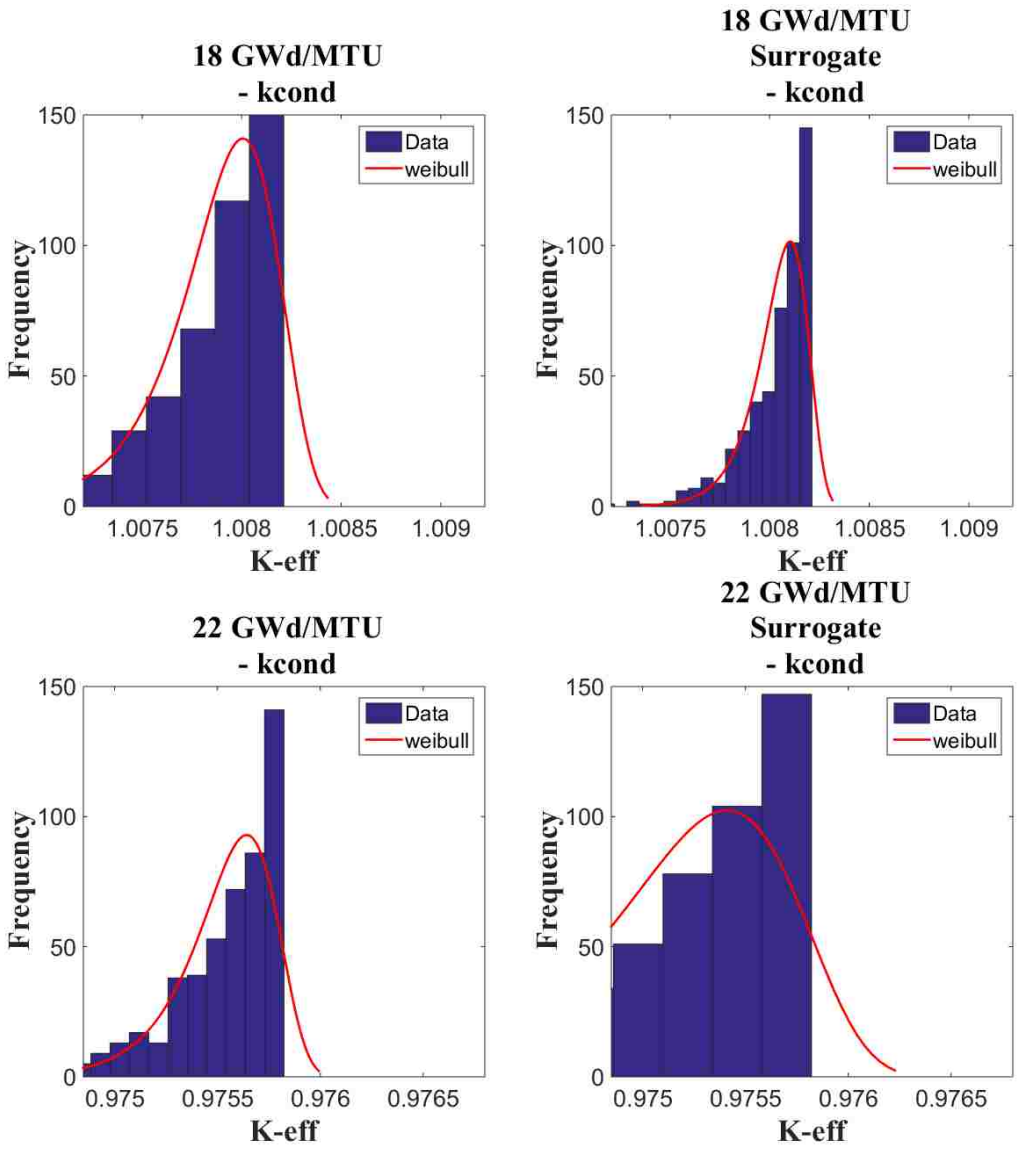
18 GWd/MTU
- kcond
Data
weibull
Frequency
K-eff
18 GWd/MTU
Surrogate
- kcond
Data
weibull
Frequency
K-eff
22 GWd/MTU
- kcond
Data
weibull
Frequency
K-eff
22 GWd/MTU
Surrogate
- kcond
Data
weibull
Frequency
K-eff

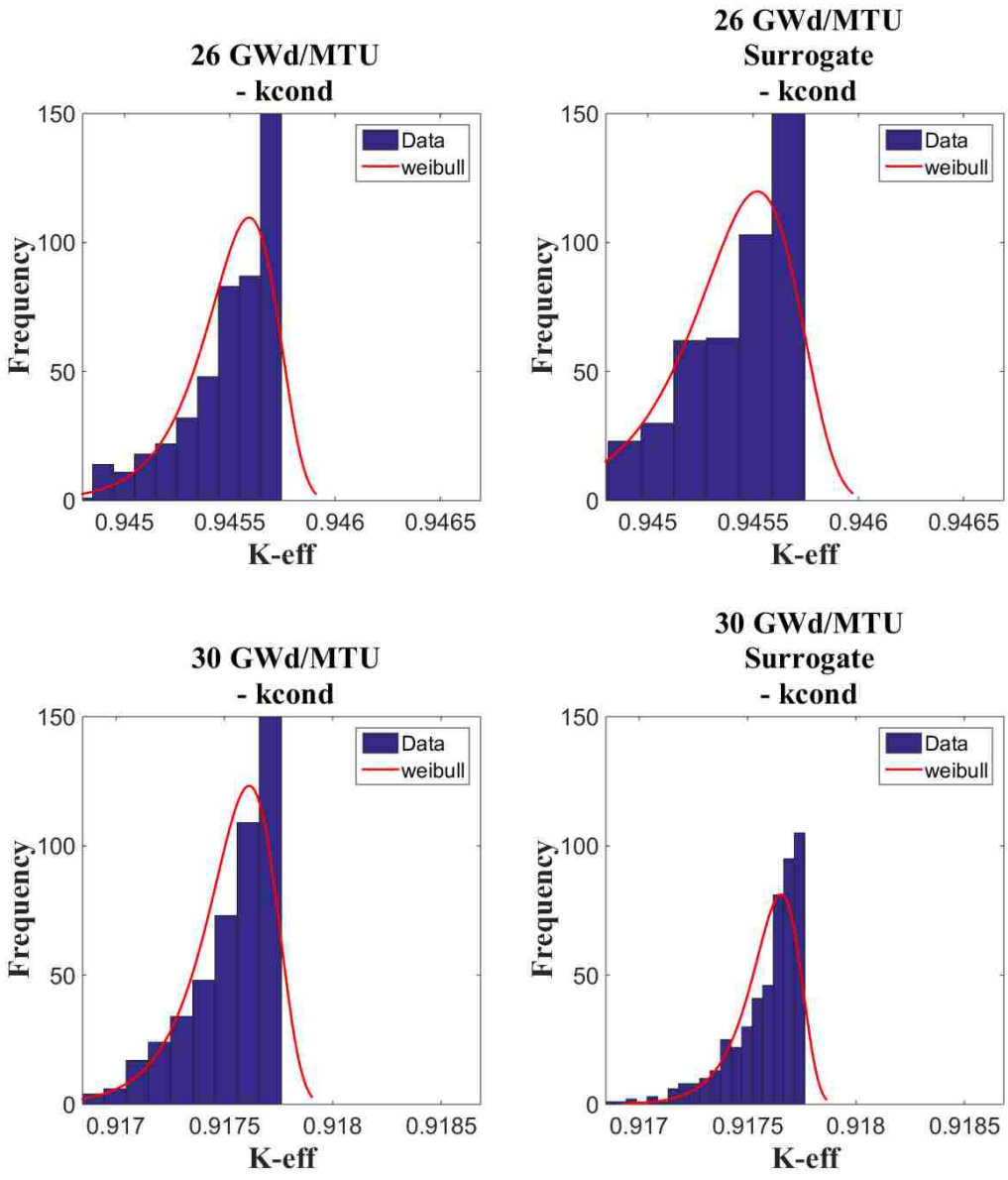
26 GWd/MTU
- kcond
Data
weibull
Frequency
K-eff
150
100
50
0
0.945
0.9455
0.946
0.9465
26 GWd/MTU
Surrogate
- kcond
Data
weibull
Frequency
K-eff
150
100
50
0
0.945
0.9455
0.946
0.9465
30 GWd/MTU
- kcond
Data
weibull
Frequency
K-eff
150
100
50
0
0.917
0.9175
0.918
0.9185
30 GWd/MTU
Surrogate
- kcond
Data
weibull
Frequency
K-eff
150
100
50
0
0.917
0.9175
0.918
0.9185

Figure 93. Statistical sampling of *maximum fuel pin power* corresponding to samples of the fuel thermal conductivity. Left: obtained via running VERA-CS right: obtained via the surrogate model.

(**Fuel Thermal Conductivity [k_{cond} W/m^2K]** $\rightarrow$ P_{max})

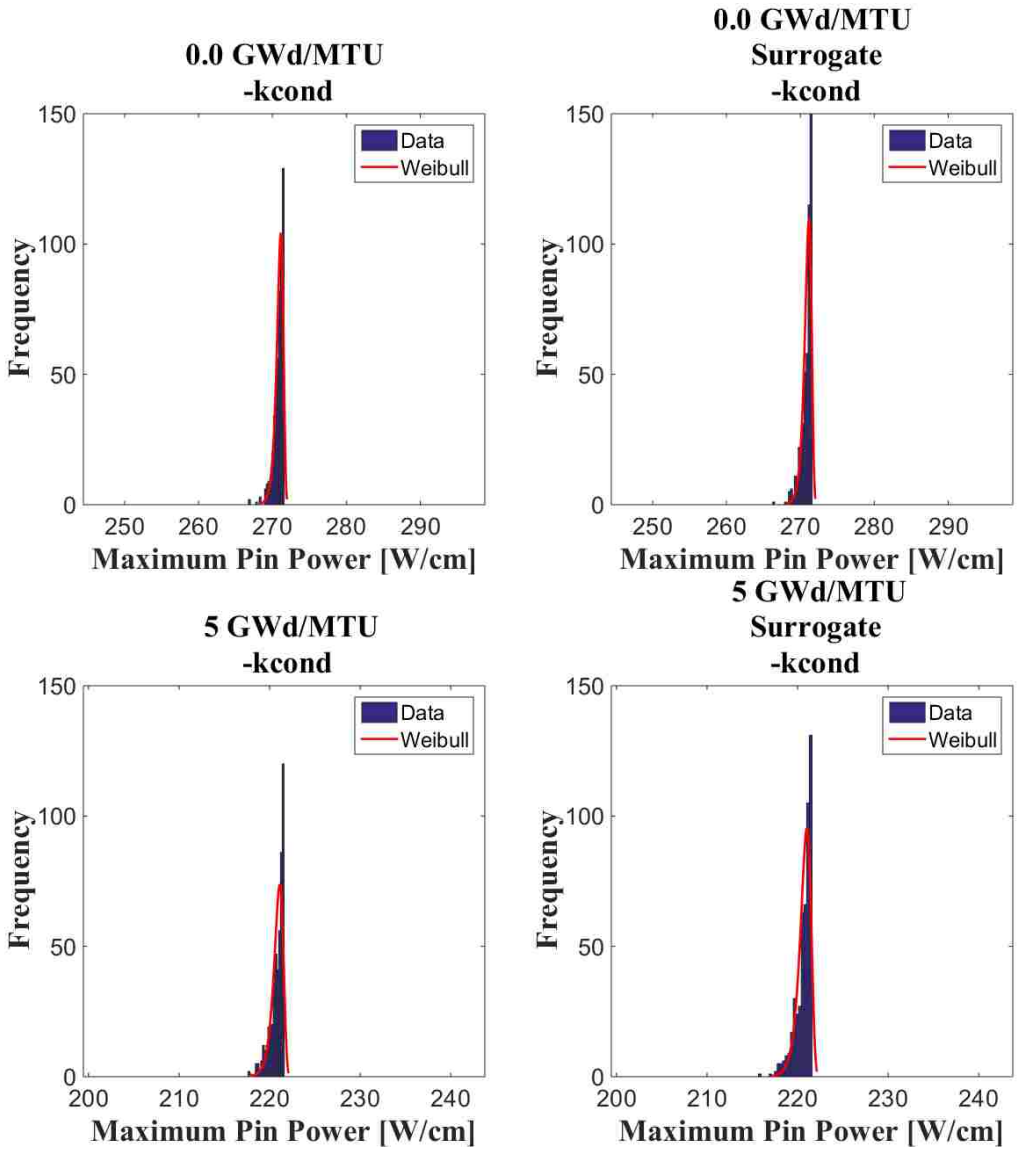
0.0 GWd/MTU
-kcond
Data
Weibull
Frequency
Maximum Pin Power [W/cm]
0.0 GWd/MTU
Surrogate
-kcond
Data
Weibull
Frequency
Maximum Pin Power [W/cm]
5 GWd/MTU
-kcond
Data
Weibull
Frequency
Maximum Pin Power [W/cm]
5 GWd/MTU
Surrogate
-kcond
Data
Weibull
Frequency
Maximum Pin Power [W/cm]

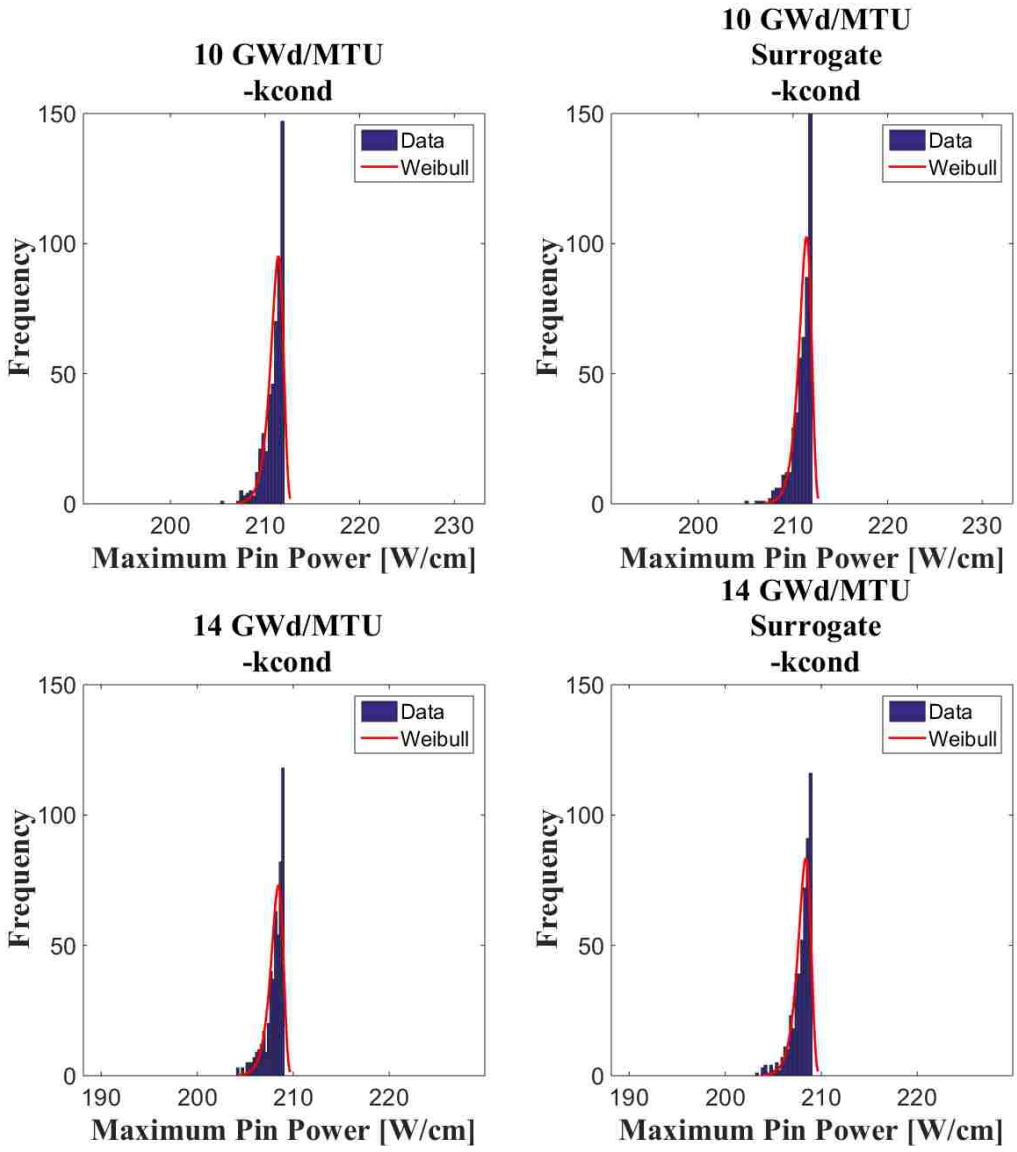
10 GWd/MTU
-kcond
Data
Weibull
Frequency
Maximum Pin Power [W/cm]
10 GWd/MTU
Surrogate
-kcond
Data
Weibull
Frequency
Maximum Pin Power [W/cm]
14 GWd/MTU
-kcond
Data
Weibull
Frequency
Maximum Pin Power [W/cm]
14 GWd/MTU
Surrogate
-kcond
Data
Weibull
Frequency
Maximum Pin Power [W/cm]

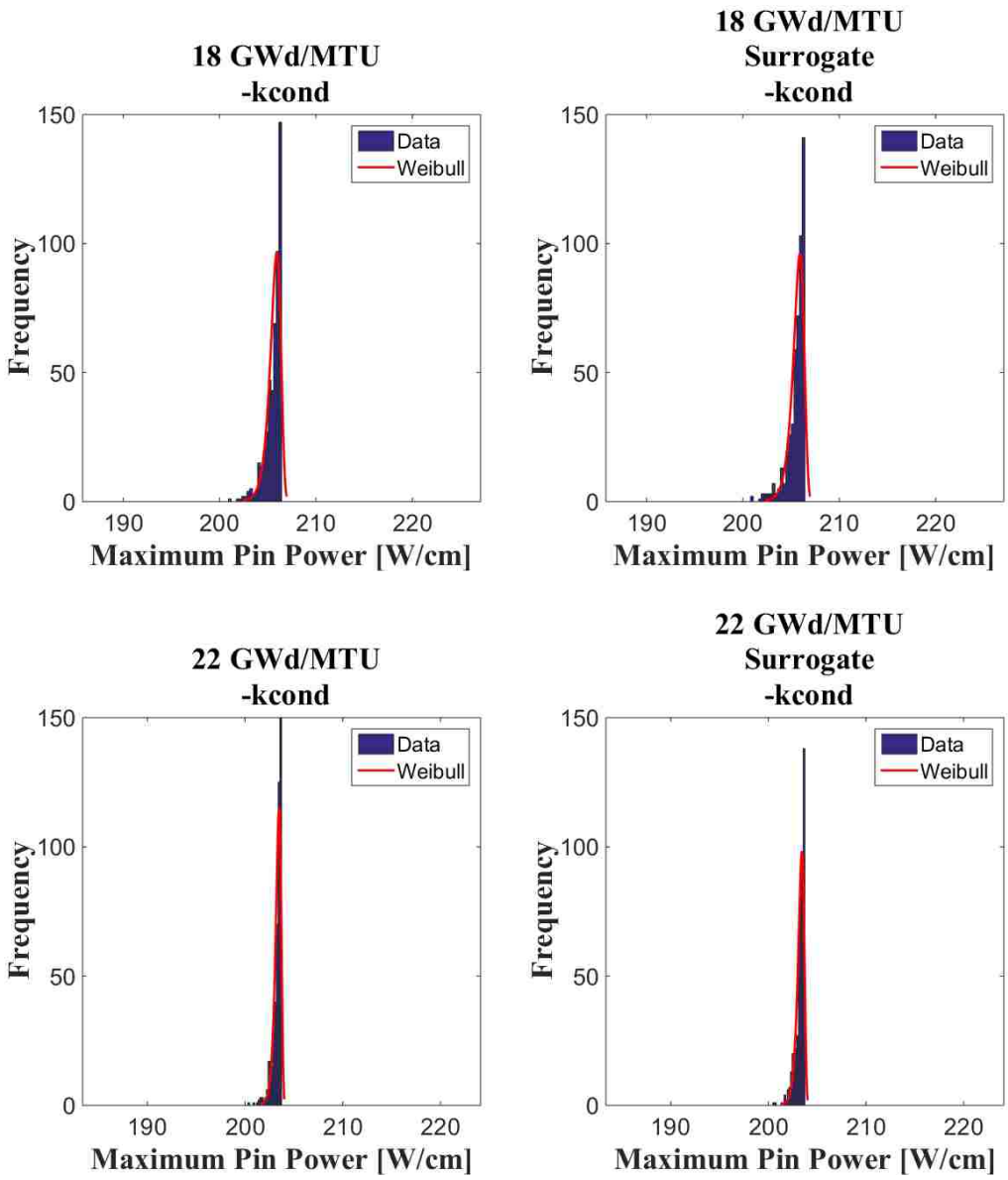
18 GWd/MTU
-kcond
18 GWd/MTU
Surrogate
-kcond
22 GWd/MTU
-kcond
22 GWd/MTU
Surrogate
-kcond
Data
Weibull
Frequency
Maximum Pin Power [W/cm]
0
50
100
150
190
200
210
220

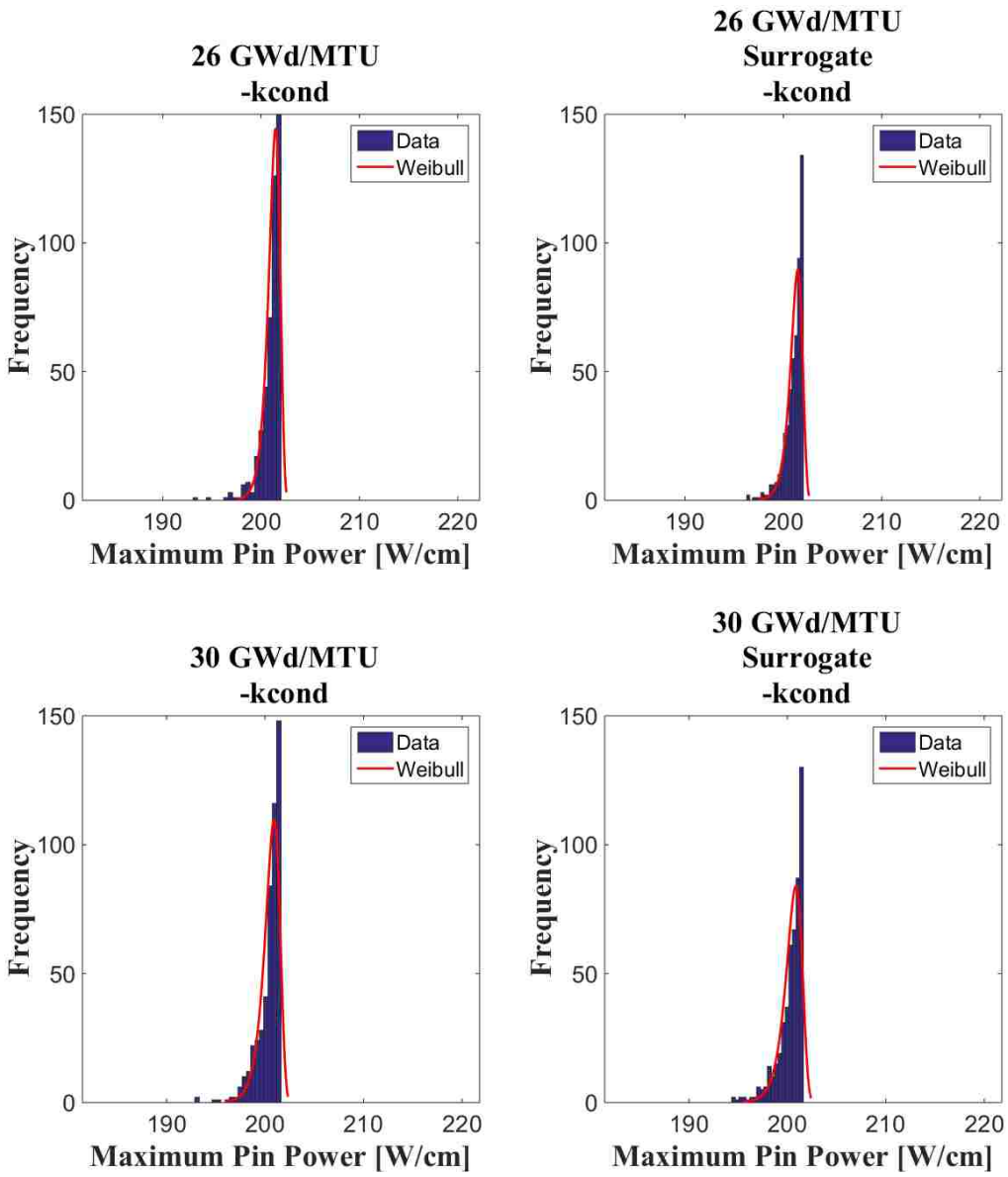
26 GWd/MTU
-kcond
Data
Weibull
Frequency
Maximum Pin Power [W/cm]
26 GWd/MTU
Surrogate
-kcond
Data
Weibull
Frequency
Maximum Pin Power [W/cm]
30 GWd/MTU
-kcond
Data
Weibull
Frequency
Maximum Pin Power [W/cm]
30 GWd/MTU
Surrogate
-kcond
Data
Weibull
Frequency
Maximum Pin Power [W/cm]

Figure 94. Statistical sampling of *maximum fuel pin temperature* corresponding to samples of the fuel thermal conductivity. Left: obtained via running VERA-CS right: obtained via the surrogate model.

(**Fuel Thermal Conductivity [k_{cond} W/m^2K]** $\rightarrow$ T_{max})

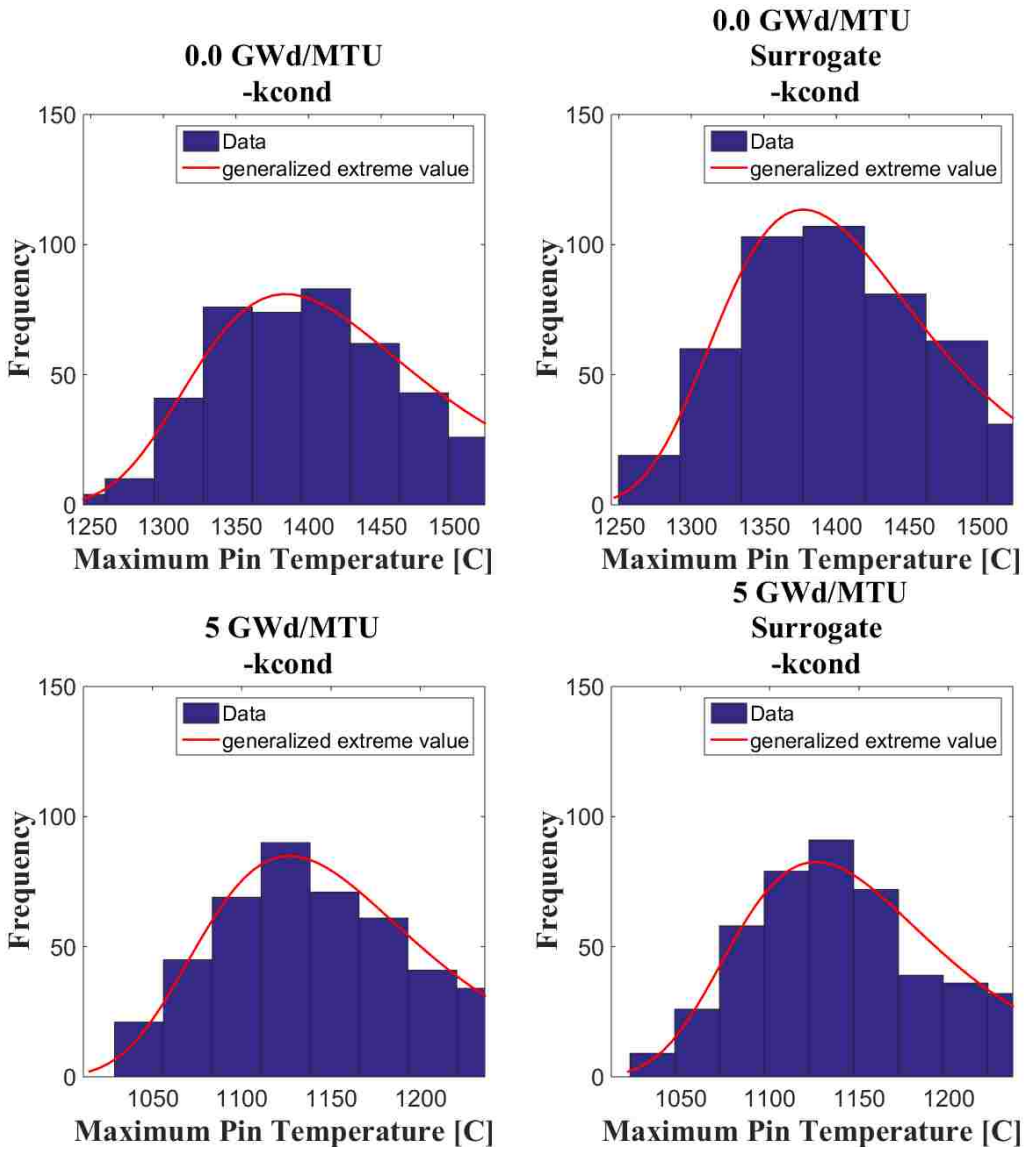
0.0 GWd/MTU
-kcond
Data
generalized extreme value
Frequency
Maximum Pin Temperature [C]
0.0 GWd/MTU
Surrogate
-kcond
Data
generalized extreme value
Frequency
Maximum Pin Temperature [C]
5 GWd/MTU
-kcond
Data
generalized extreme value
Frequency
Maximum Pin Temperature [C]
5 GWd/MTU
Surrogate
-kcond
Data
generalized extreme value
Frequency
Maximum Pin Temperature [C]

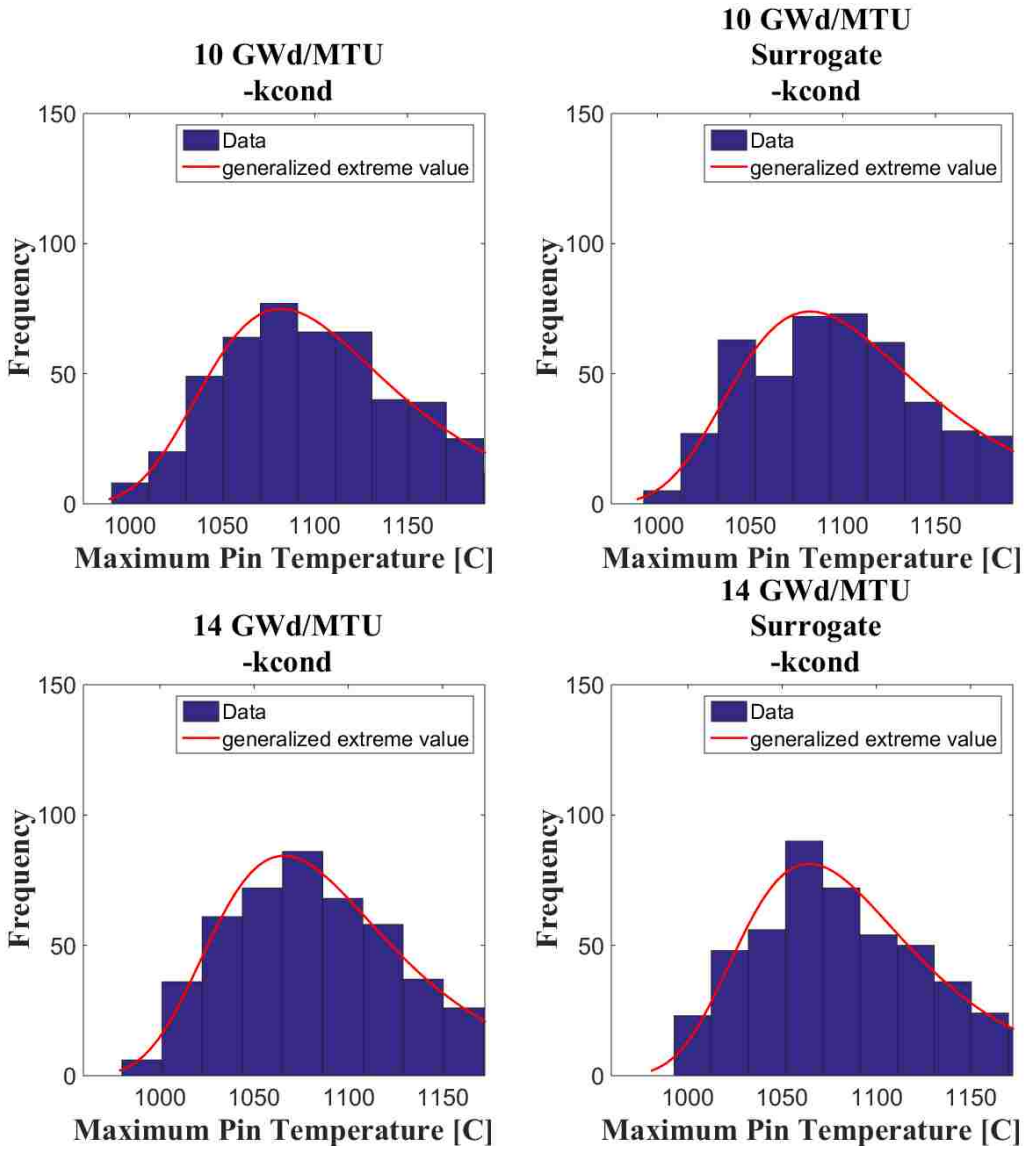
10 GWd/MTU
-kcond
Data
generalized extreme value
Frequency
Maximum Pin Temperature [C]
10 GWd/MTU
Surrogate
-kcond
Data
generalized extreme value
Frequency
Maximum Pin Temperature [C]
14 GWd/MTU
-kcond
Data
generalized extreme value
Frequency
Maximum Pin Temperature [C]
14 GWd/MTU
Surrogate
-kcond
Data
generalized extreme value
Frequency
Maximum Pin Temperature [C]

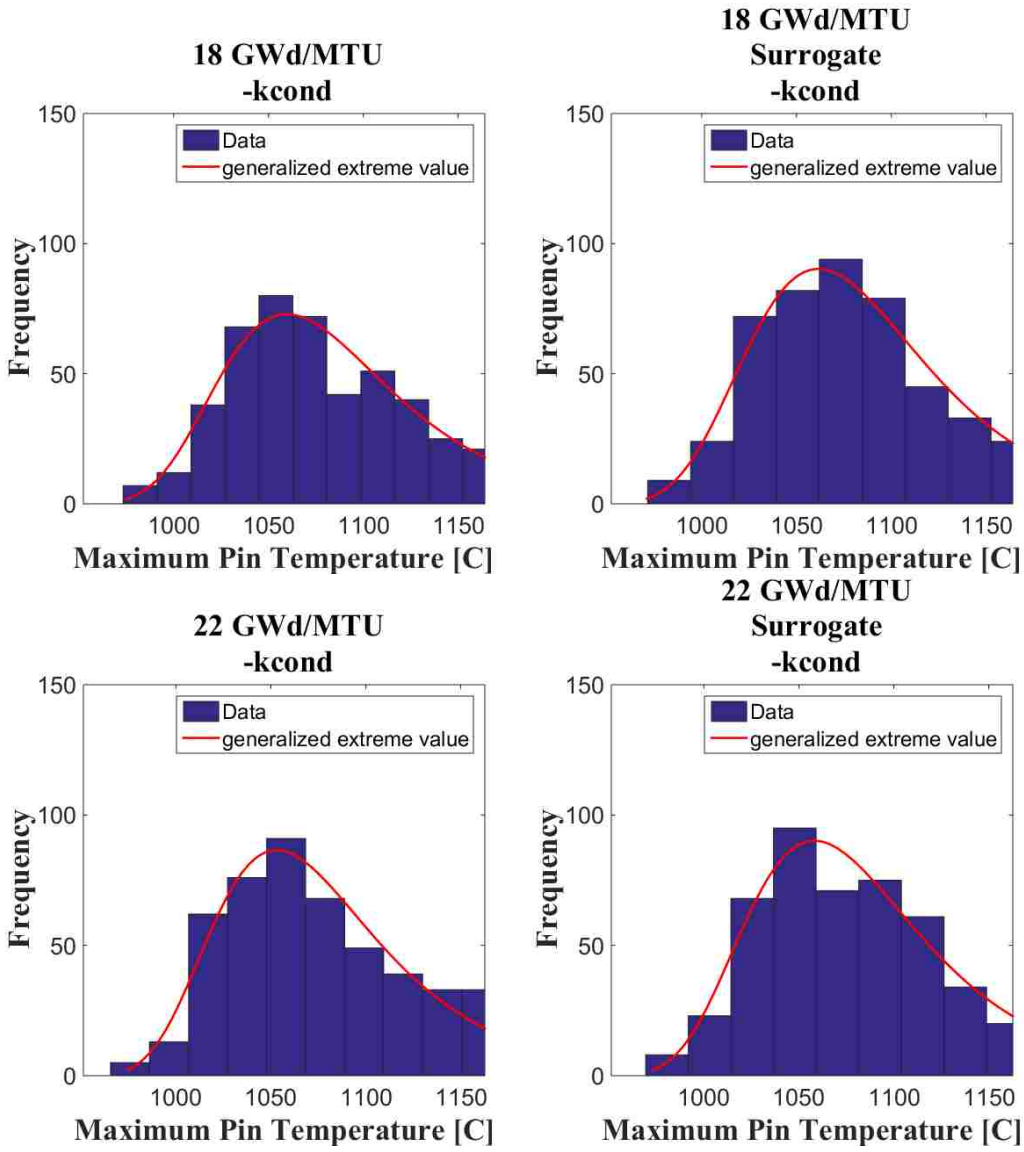
18 GWd/MTU
-kcond
Data
generalized extreme value
Frequency
Maximum Pin Temperature [C]
18 GWd/MTU
Surrogate
-kcond
Data
generalized extreme value
Frequency
Maximum Pin Temperature [C]
22 GWd/MTU
-kcond
Data
generalized extreme value
Frequency
Maximum Pin Temperature [C]
22 GWd/MTU
Surrogate
-kcond
Data
generalized extreme value
Frequency
Maximum Pin Temperature [C]

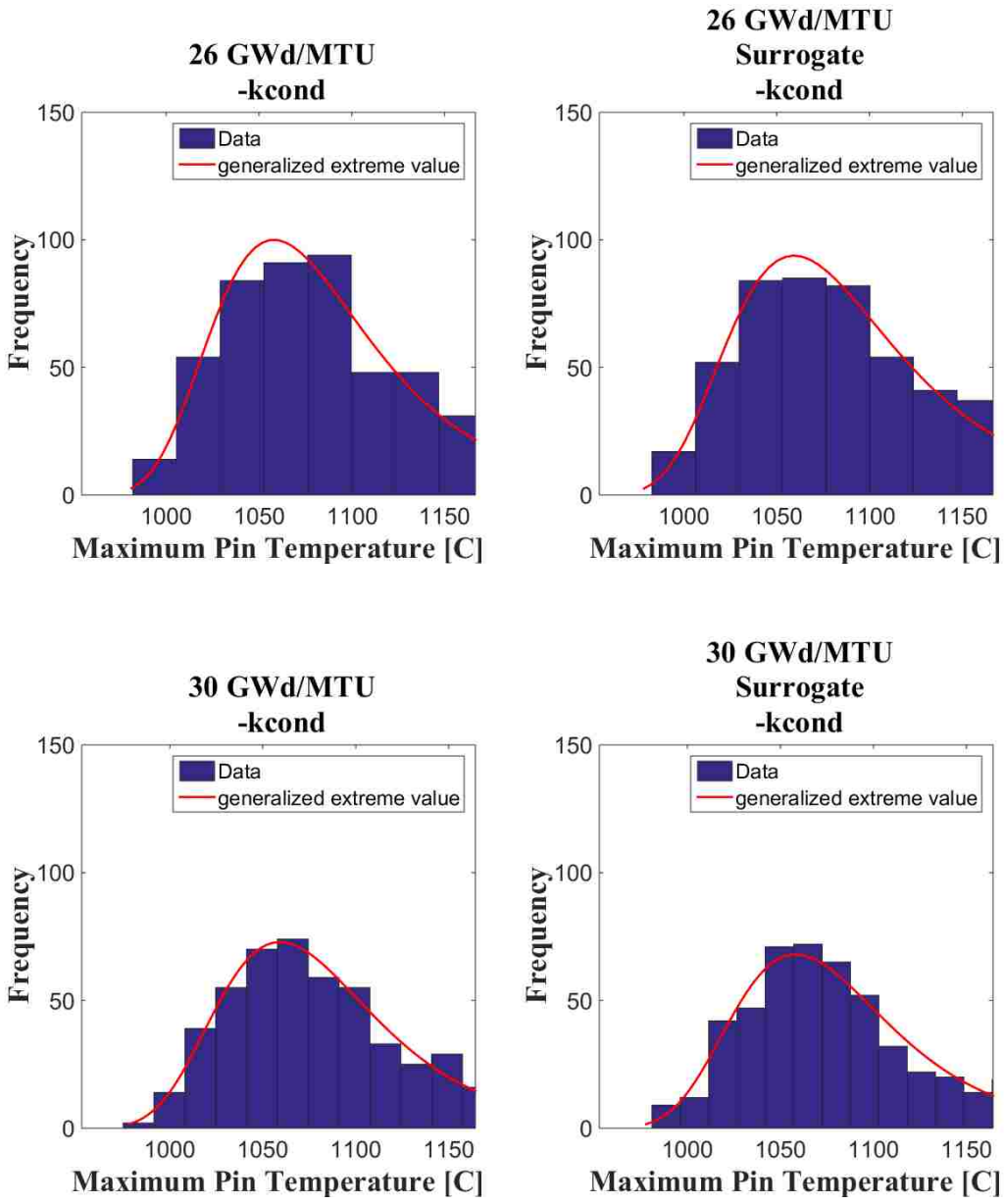
26 GWd/MTU
-kcond
Data
generalized extreme value
Frequency
Maximum Pin Temperature [C]
26 GWd/MTU
Surrogate
-kcond
Data
generalized extreme value
Frequency
Maximum Pin Temperature [C]
30 GWd/MTU
-kcond
Data
generalized extreme value
Frequency
Maximum Pin Temperature [C]
30 GWd/MTU
Surrogate
-kcond
Data
generalized extreme value
Frequency
Maximum Pin Temperature [C]

Figure 95. Statistical sampling of *k-eff* corresponding to samples of the gap conductivity. Left: obtained via running VERA-CS right: obtained via the surrogate model.

(**Gap Conductivity [*hgap W/m*^{2}*K*] $\rightarrow$ k_{eff}**)

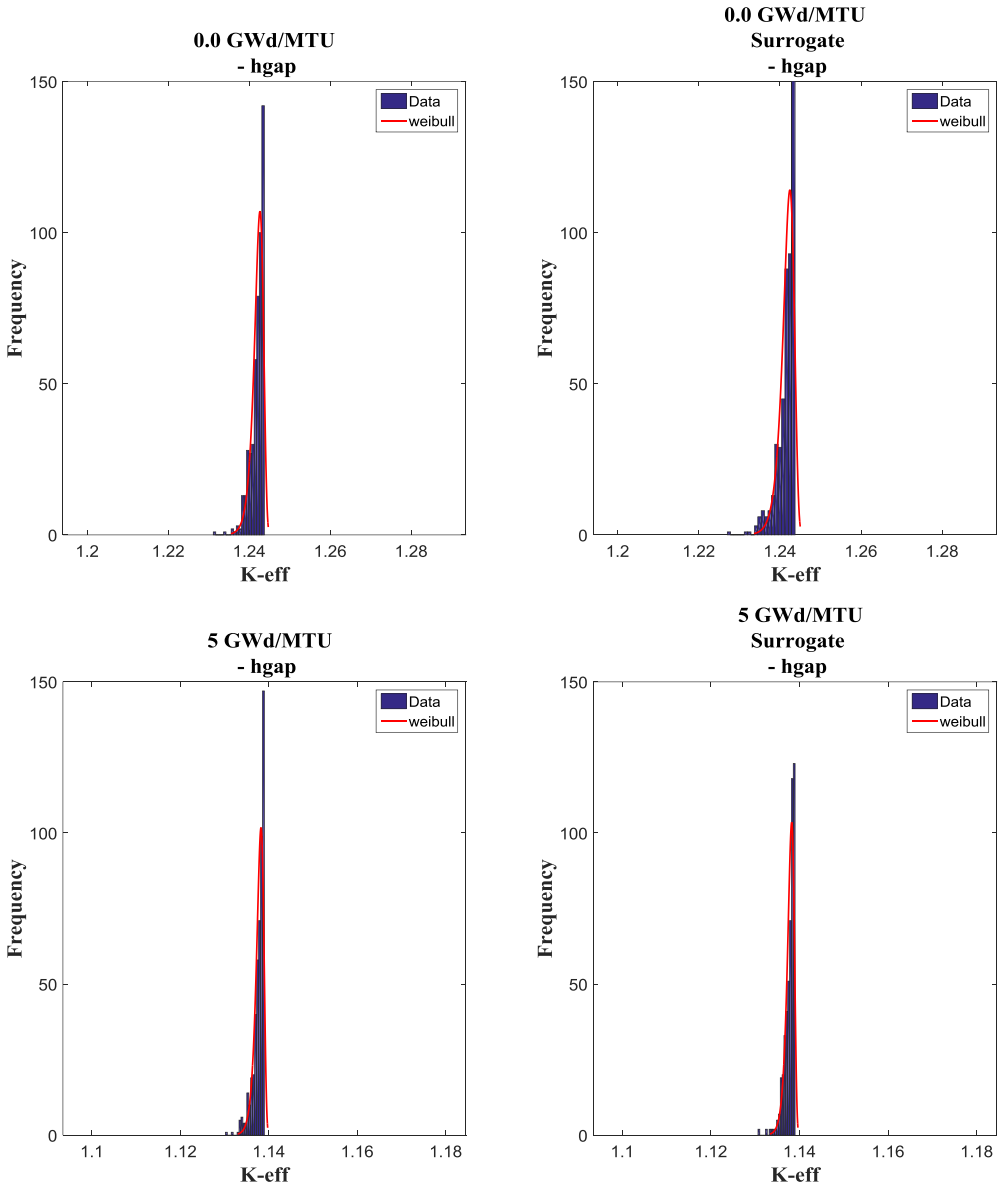
0.0 GWd/MTU
- hgap
Data
weibull
Frequency
K-eff
0.0 GWd/MTU
Surrogate
- hgap
Data
weibull
Frequency
K-eff
5 GWd/MTU
- hgap
Data
weibull
Frequency
K-eff
5 GWd/MTU
Surrogate
- hgap
Data
weibull
Frequency
K-eff

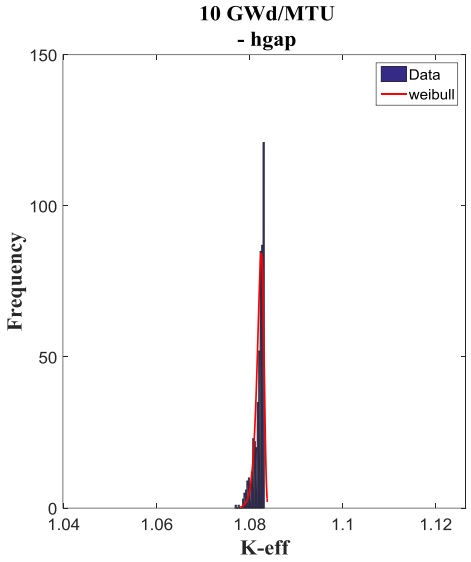
10 GWd/MTU
- hgap
Data
weibull
Frequency
K-eff
0
50
100
150
1.04
1.06
1.08
1.1
1.12

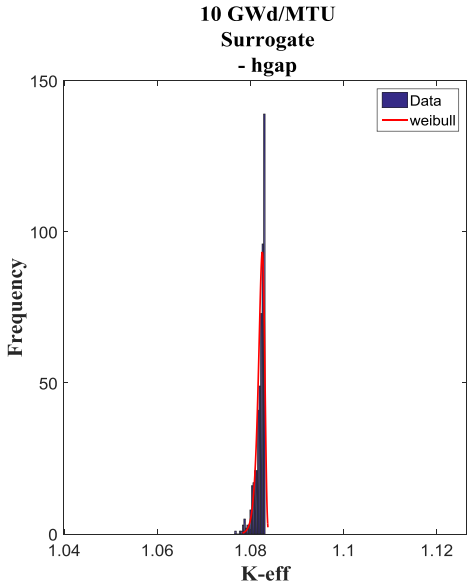
10 GWd/MTU
Surrogate
- hgap
Data
weibull
Frequency
K-eff
0
50
100
150
1.04
1.06
1.08
1.1
1.12

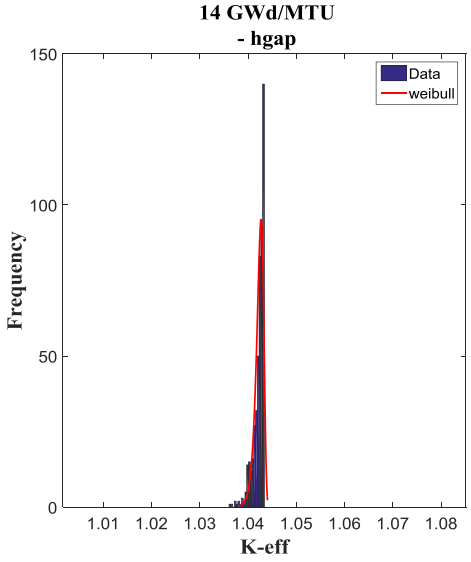
14 GWd/MTU
- hgap
Data
weibull
Frequency
K-eff
0
50
100
150
1.01
1.02
1.03
1.04
1.05
1.06
1.07
1.08

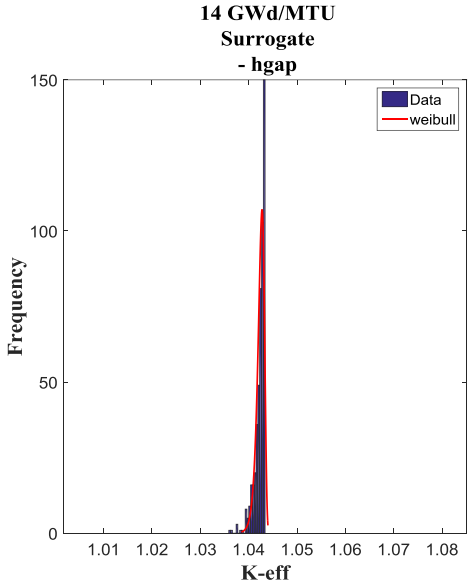
14 GWd/MTU
Surrogate
- hgap
Data
weibull
Frequency
K-eff
0
50
100
150
1.01
1.02
1.03
1.04
1.05
1.06
1.07
1.08

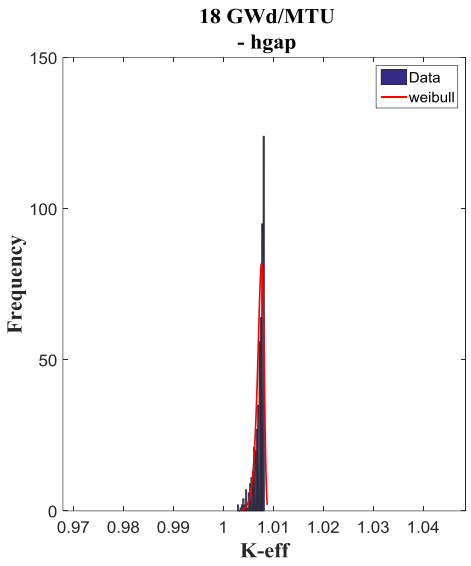
18 GWd/MTU
- hgap
Data
weibull
Frequency
K-eff
0
50
100
150
0.97
0.98
0.99
1
1.01
1.02
1.03
1.04

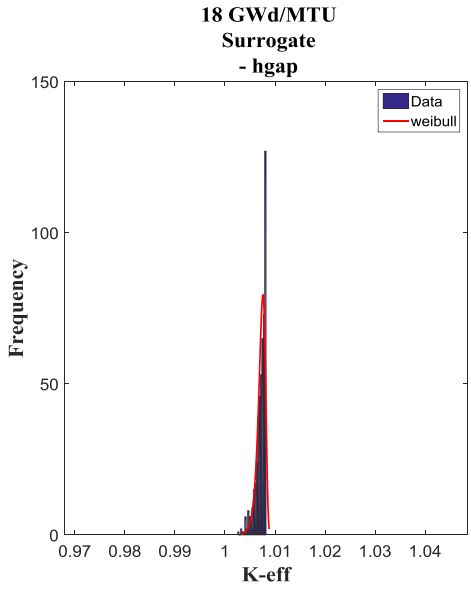
18 GWd/MTU
Surrogate
- hgap
Data
weibull
Frequency
K-eff
0
50
100
150
0.97
0.98
0.99
1
1.01
1.02
1.03
1.04

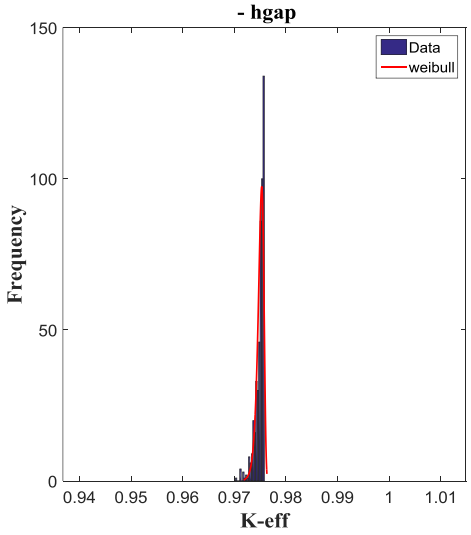
22 GWd/MTU
- hgap
Data
weibull
Frequency
K-eff
0
50
100
150
0.94
0.95
0.96
0.97
0.98
0.99
1
1.01

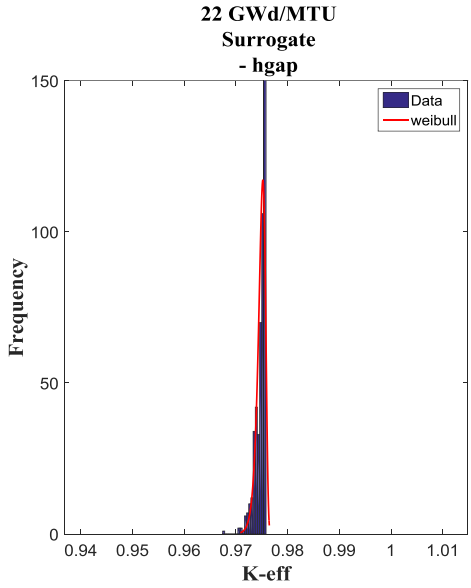
22 GWd/MTU
Surrogate
- hgap
Data
weibull
Frequency
K-eff
0
50
100
150
0.94
0.95
0.96
0.97
0.98
0.99
1
1.01

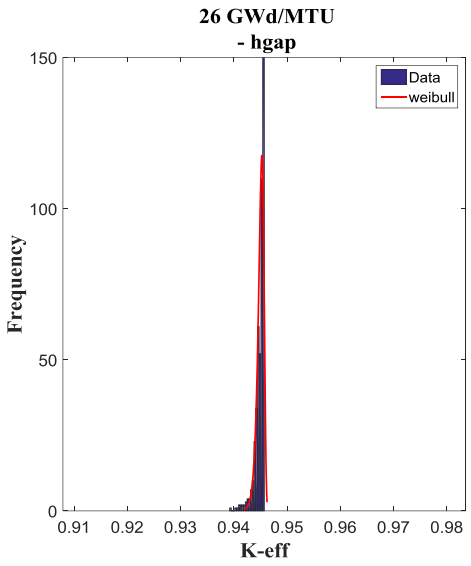
26 GWd/MTU
- hgap
Data
weibull
Frequency
K-eff
0
50
100
150
0.91
0.92
0.93
0.94
0.95
0.96
0.97
0.98

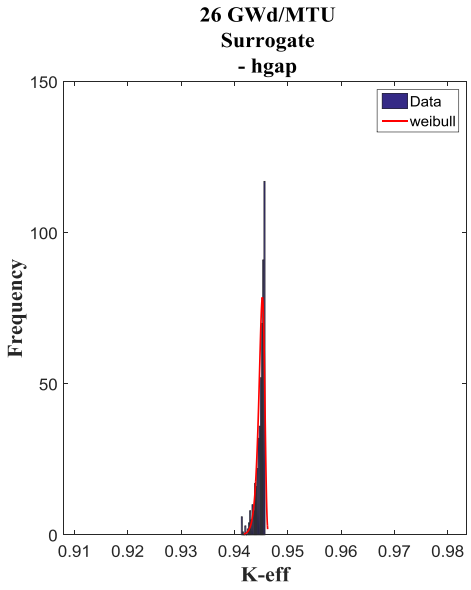
26 GWd/MTU
Surrogate
- hgap
Data
weibull
Frequency
K-eff
0
50
100
150
0.91
0.92
0.93
0.94
0.95
0.96
0.97
0.98

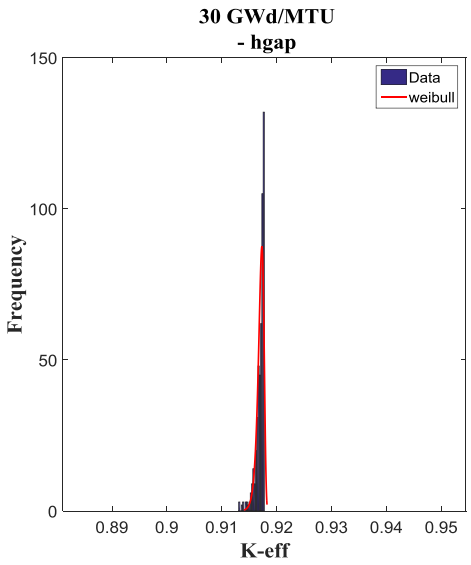
30 GWd/MTU
- hgap
Data
weibull
Frequency
K-eff
0
50
100
150
0.89
0.9
0.91
0.92
0.93
0.94
0.95

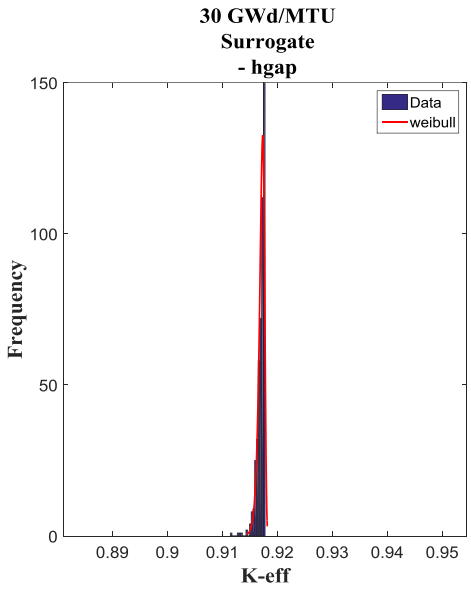
30 GWd/MTU
Surrogate
- hgap
Data
weibull
Frequency
K-eff
0
50
100
150
0.89
0.9
0.91
0.92
0.93
0.94
0.95

Figure 96. Statistical sampling maximum pin power corresponding to samples of the gap conductivity. Left: obtained via running VERA-CS right: obtained via the surrogate model.

Gap Conductivity [*hgap W/m^{2}K*] →*Maximum Pin Power*

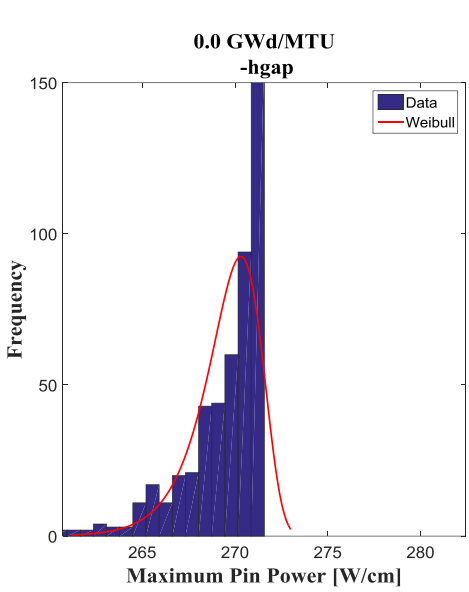
0.0 GWd/MTU
-hgap
Data
Weibull
Frequency
Maximum Pin Power [W/cm]
0
50
100
150
265
270
275
280

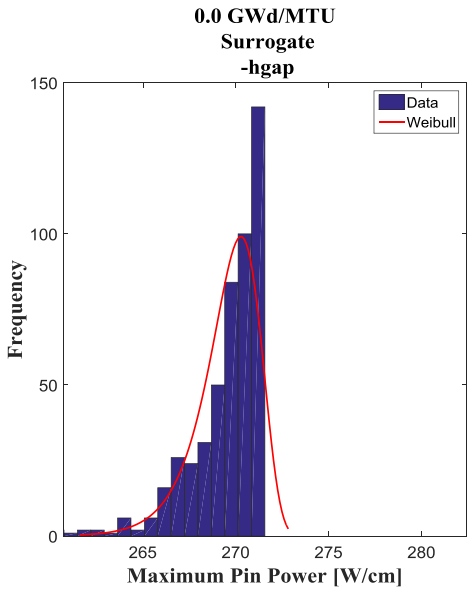
0.0 GWd/MTU
Surrogate
-hgap
Data
Weibull
Frequency
Maximum Pin Power [W/cm]
0
50
100
150
265
270
275
280

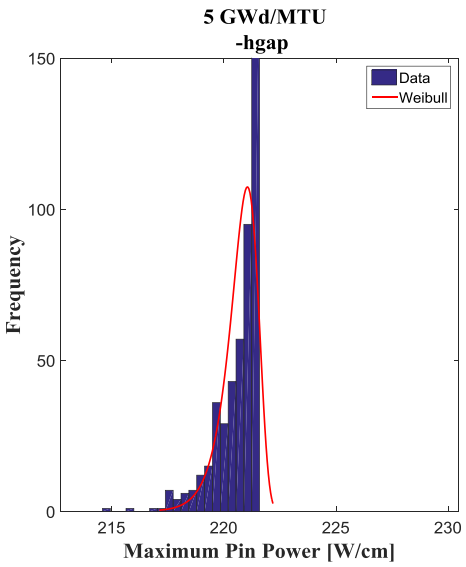
5 GWd/MTU
-hgap
Data
Weibull
Frequency
Maximum Pin Power [W/cm]
0
50
100
150
215
220
225
230

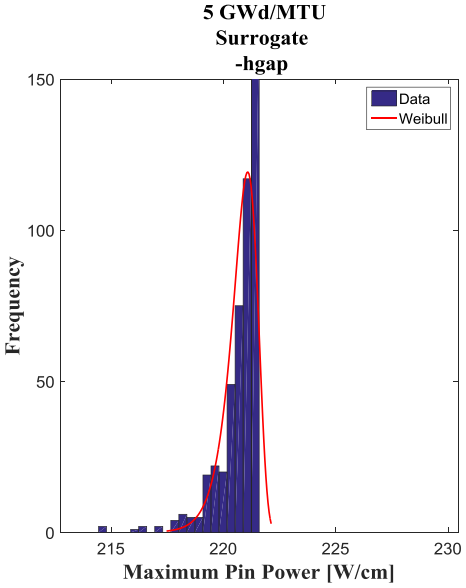
5 GWd/MTU
Surrogate
-hgap
Data
Weibull
Frequency
Maximum Pin Power [W/cm]
0
50
100
150
215
220
225
230

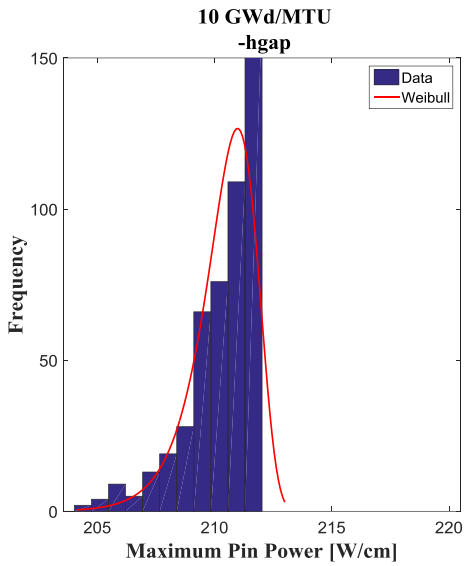
10 GWd/MTU
-hgap
Data
Weibull
Frequency
Maximum Pin Power [W/cm]
0
50
100
150
205
210
215
220

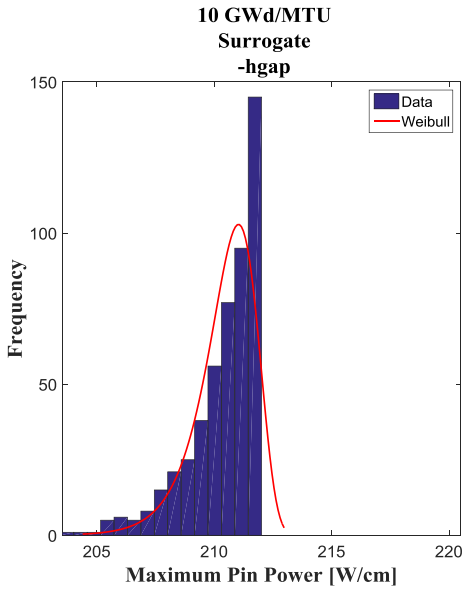
10 GWd/MTU
Surrogate
-hgap
Data
Weibull
Frequency
Maximum Pin Power [W/cm]
0
50
100
150
205
210
215
220

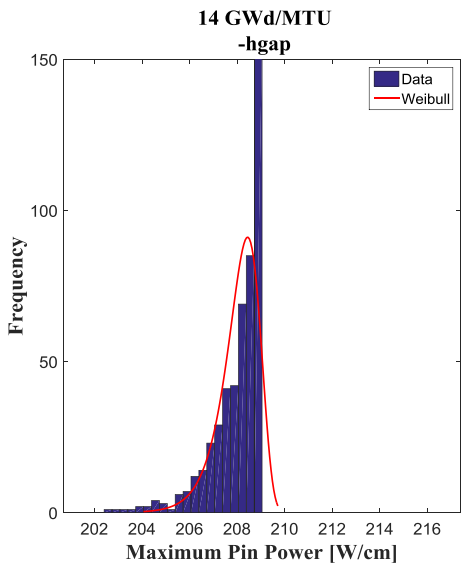
14 GWd/MTU
-hgap
Data
Weibull
Frequency
Maximum Pin Power [W/cm]
0
50
100
150
202
204
206
208
210
212
214
216

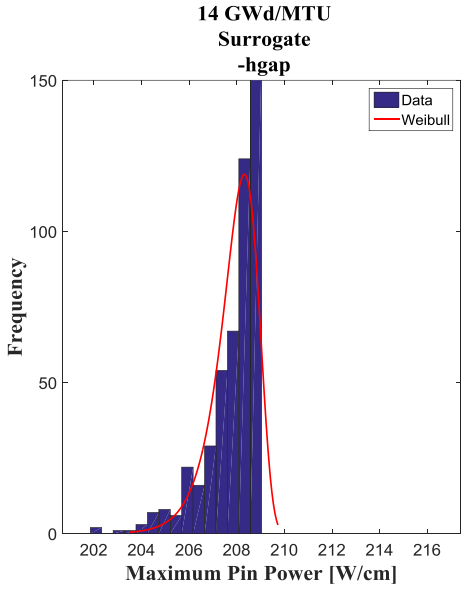
14 GWd/MTU
Surrogate
-hgap
Data
Weibull
Frequency
Maximum Pin Power [W/cm]
0
50
100
150
202
204
206
208
210
212
214
216

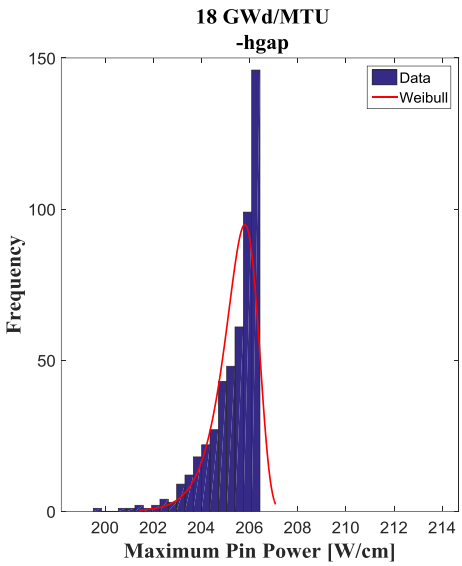
18 GWd/MTU
-hgap
Data
Weibull
Frequency
Maximum Pin Power [W/cm]
0
50
100
150
200
202
204
206
208
210
212
214

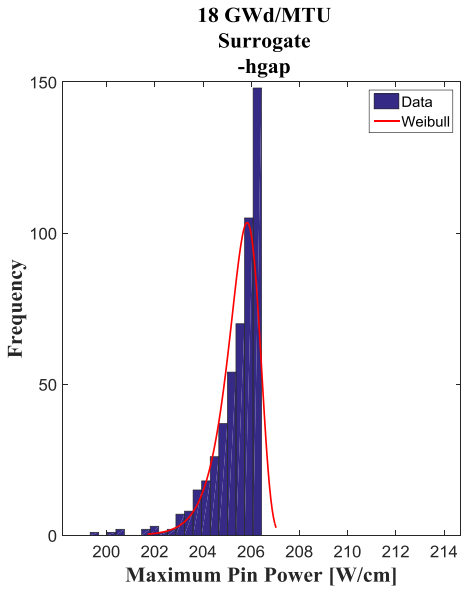
18 GWd/MTU
Surrogate
-hgap
Data
Weibull
Frequency
Maximum Pin Power [W/cm]
0
50
100
150
200
202
204
206
208
210
212
214

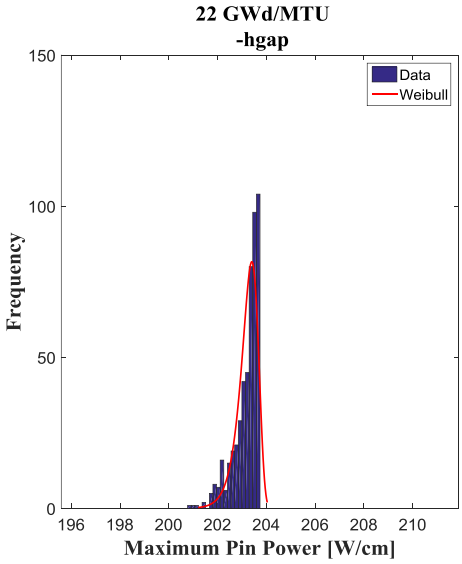
22 GWd/MTU
-hgap
Data
Weibull
Frequency
Maximum Pin Power [W/cm]
0
50
100
150
196
198
200
202
204
206
208
210

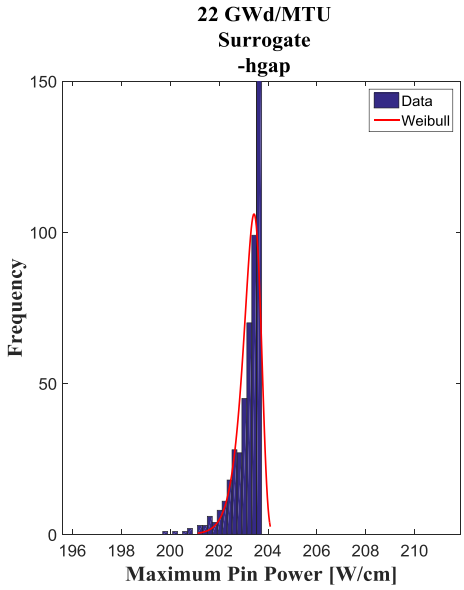
22 GWd/MTU
Surrogate
-hgap
Data
Weibull
Frequency
Maximum Pin Power [W/cm]
0
50
100
150
196
198
200
202
204
206
208
210

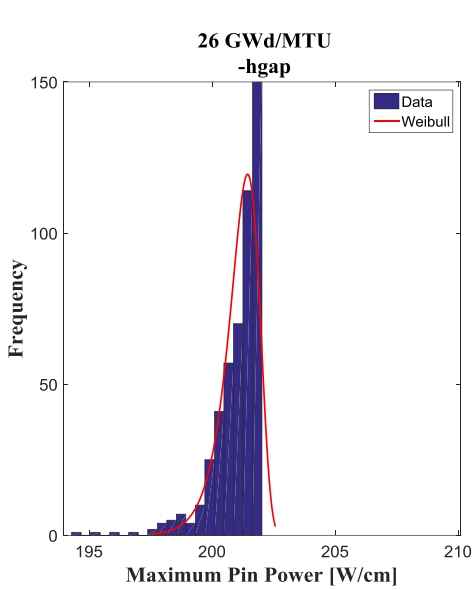
26 GWd/MTU
-hgap
Data
Weibull
Frequency
Maximum Pin Power [W/cm]
0
50
100
150
195
200
205
210

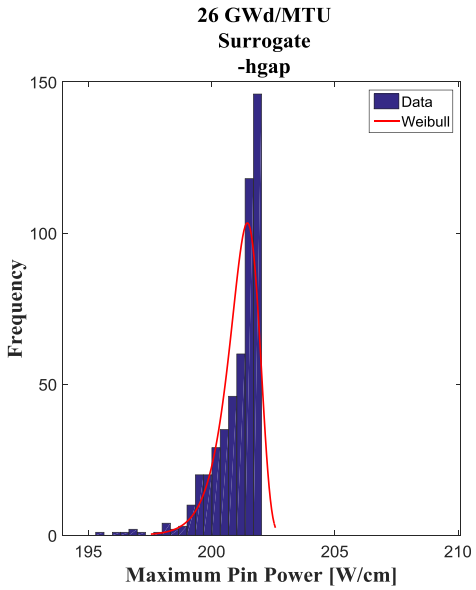
26 GWd/MTU
Surrogate
-hgap
Data
Weibull
Frequency
Maximum Pin Power [W/cm]
0
50
100
150
195
200
205
210

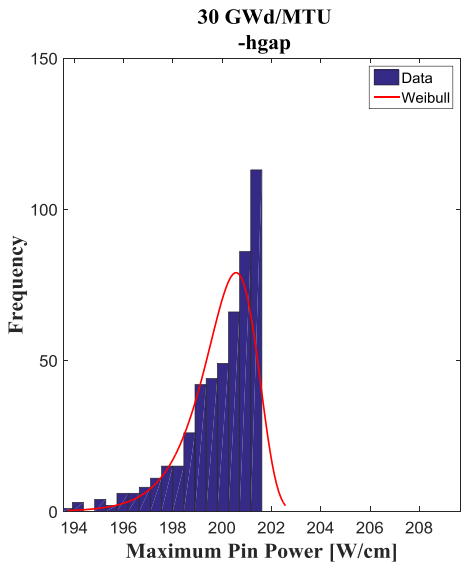
30 GWd/MTU
-hgap
Data
Weibull
Frequency
Maximum Pin Power [W/cm]
0
50
100
150
194
196
198
200
202
204
206
208

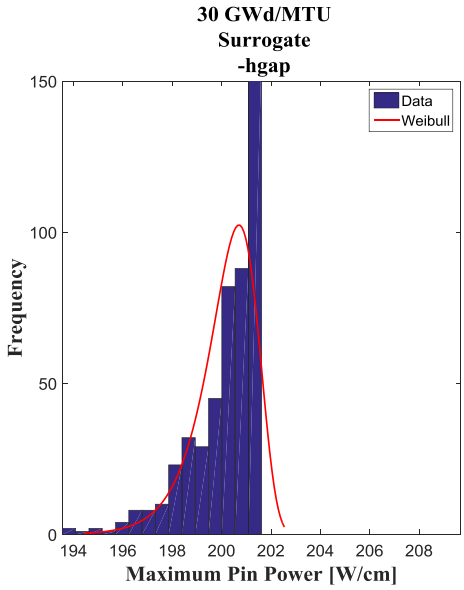
30 GWd/MTU
Surrogate
-hgap
Data
Weibull
Frequency
Maximum Pin Power [W/cm]
0
50
100
150
194
196
198
200
202
204
206
208

Figure 97. Statistical sampling maximum pin temperature corresponding to samples of the gap conductivity. Left: obtained via running VERA-CS right: obtained via the surrogate model.

Gap Conductivity [*hgap* W/m^2K] → *Maximum Pin Temperature*

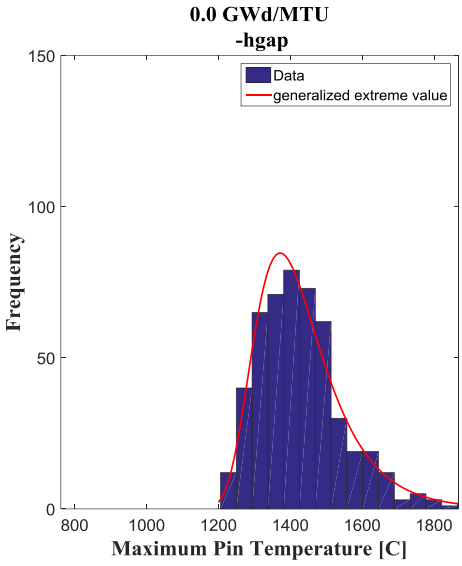
0.0 GWd/MTU
-hgap
Data
generalized extreme value
Frequency
Maximum Pin Temperature [C]

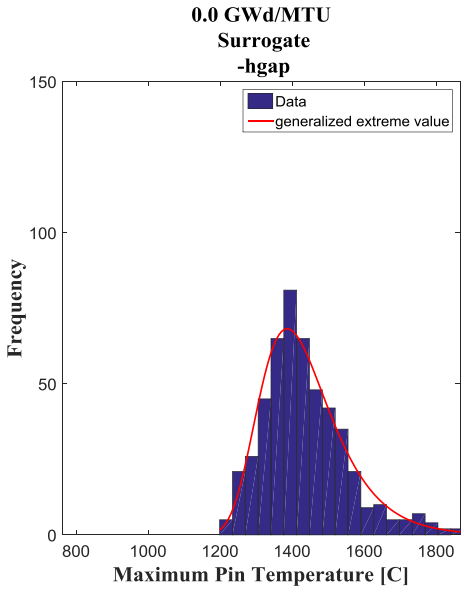
0.0 GWd/MTU
Surrogate
-hgap
Data
generalized extreme value
Frequency
Maximum Pin Temperature [C]

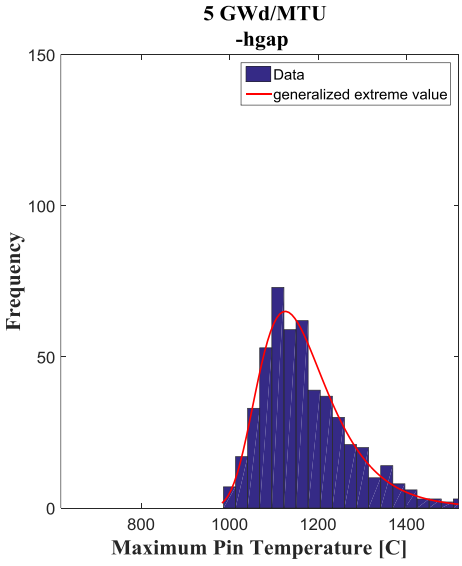
5 GWd/MTU
-hgap
Data
generalized extreme value
Frequency
Maximum Pin Temperature [C]

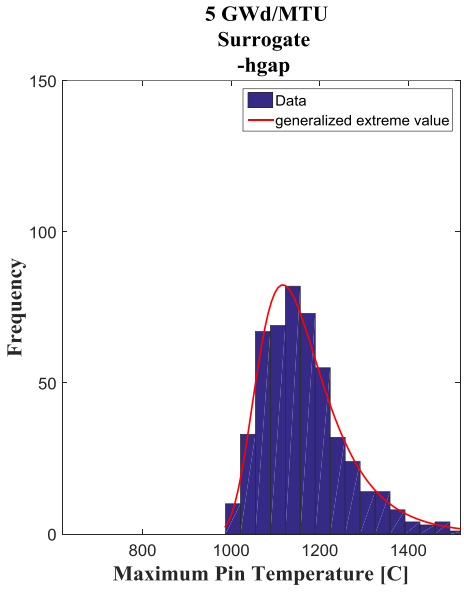
5 GWd/MTU
Surrogate
-hgap
Data
generalized extreme value
Frequency
Maximum Pin Temperature [C]

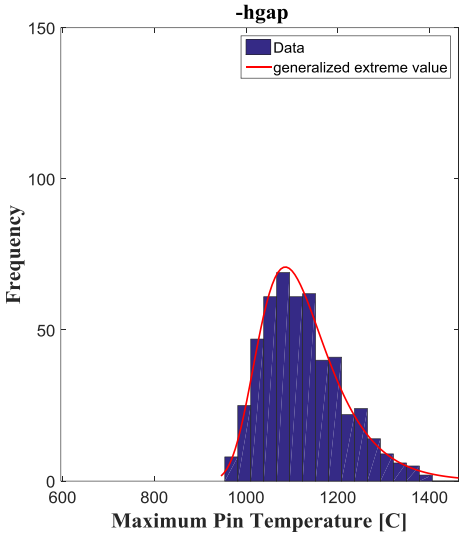
10 GWd/MTU
-hgap
Data
generalized extreme value
Frequency
Maximum Pin Temperature [C]
0
50
100
150
600
800
1000
1200
1400

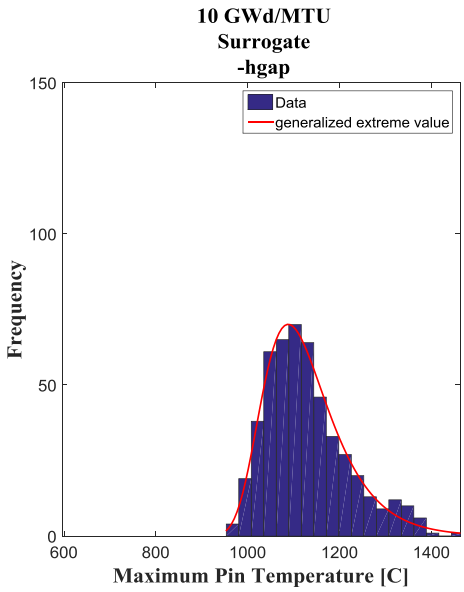
10 GWd/MTU
Surrogate
-hgap
Data
generalized extreme value
Frequency
Maximum Pin Temperature [C]
0
50
100
150
600
800
1000
1200
1400

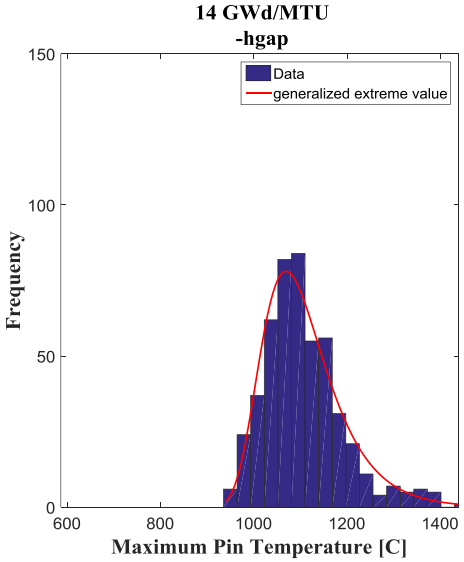
14 GWd/MTU
-hgap
Data
generalized extreme value
Frequency
Maximum Pin Temperature [C]
0
50
100
150
600
800
1000
1200
1400

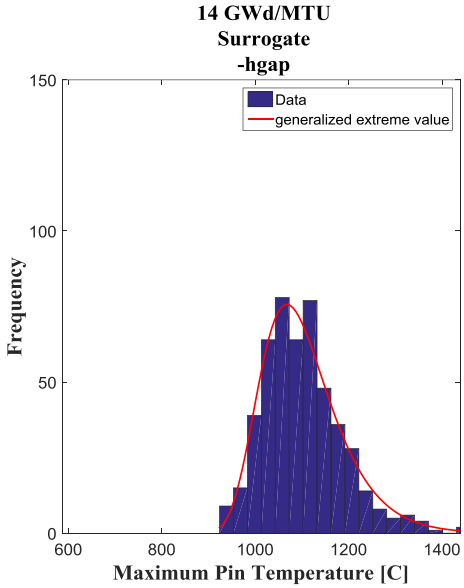
14 GWd/MTU
Surrogate
-hgap
Data
generalized extreme value
Frequency
Maximum Pin Temperature [C]
0
50
100
150
600
800
1000
1200
1400

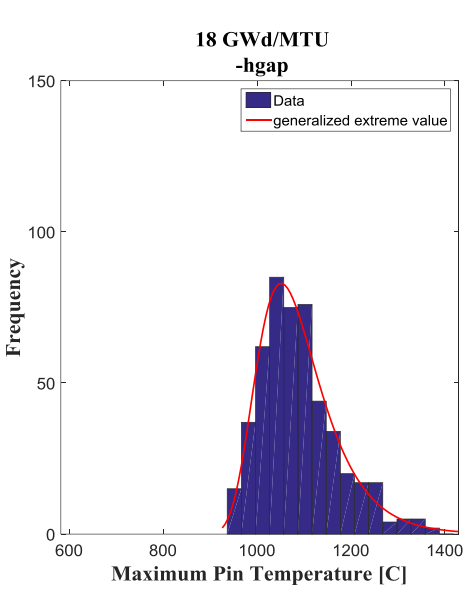
18 GWd/MTU
-hgap
Data
generalized extreme value
Frequency
Maximum Pin Temperature [C]
0
50
100
150
600
800
1000
1200
1400

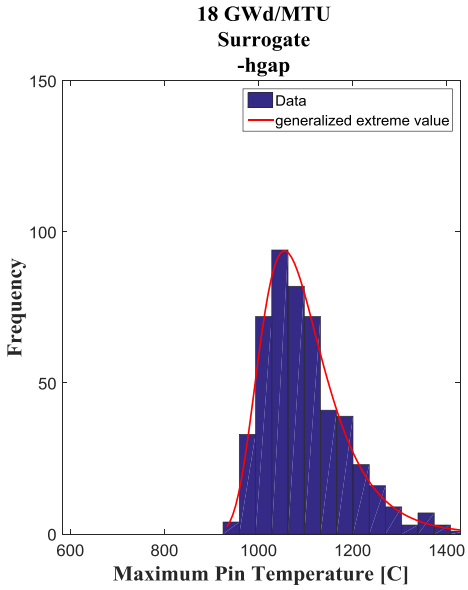
18 GWd/MTU
Surrogate
-hgap
Data
generalized extreme value
Frequency
Maximum Pin Temperature [C]
0
50
100
150
600
800
1000
1200
1400

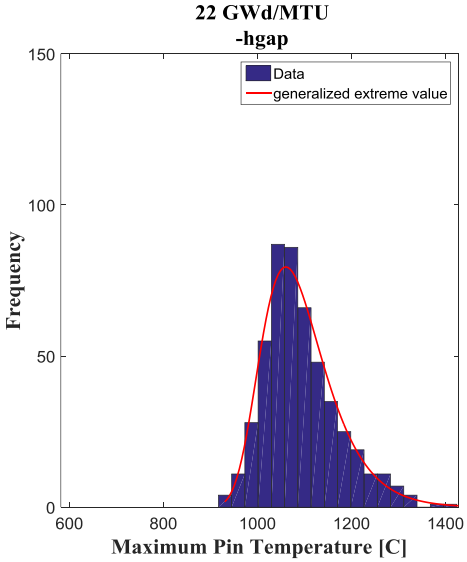
22 GWd/MTU
-hgap
Data
generalized extreme value
Frequency
Maximum Pin Temperature [C]
0
50
100
150
600
800
1000
1200
1400

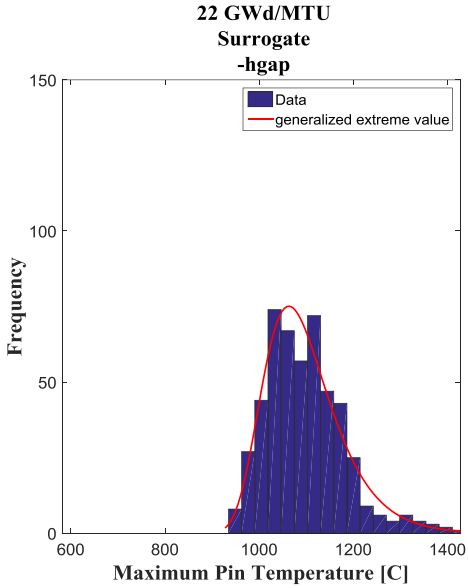
22 GWd/MTU
Surrogate
-hgap
Data
generalized extreme value
Frequency
Maximum Pin Temperature [C]
0
50
100
150
600
800
1000
1200
1400

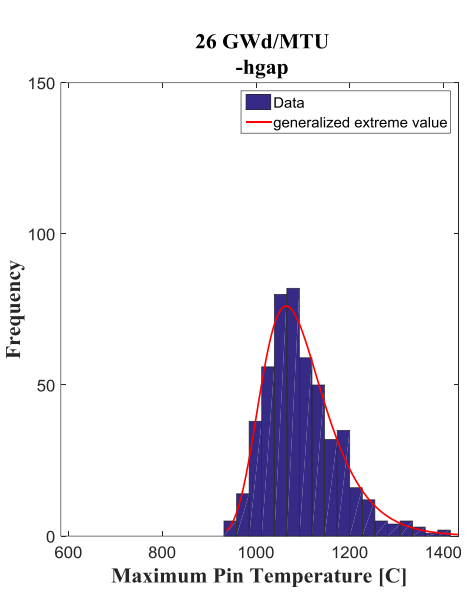
26 GWd/MTU
-hgap
Data
generalized extreme value
Frequency
Maximum Pin Temperature [C]
0
50
100
150
600
800
1000
1200
1400

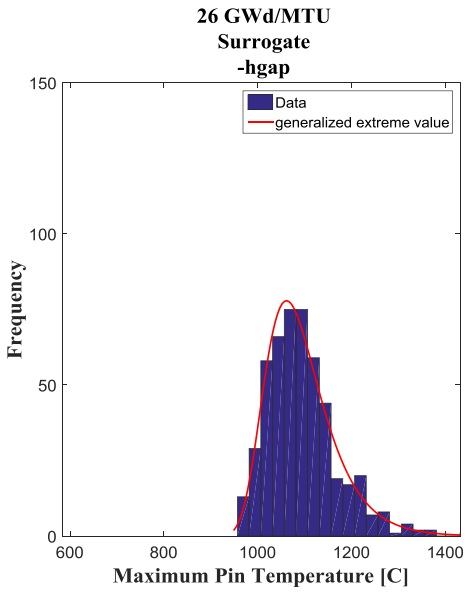
26 GWd/MTU
Surrogate
-hgap
Data
generalized extreme value
Frequency
Maximum Pin Temperature [C]
0
50
100
150
600
800
1000
1200
1400

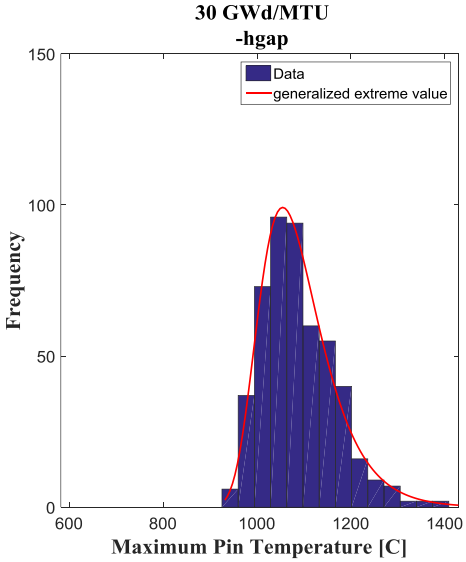
30 GWd/MTU
-hgap
Data
generalized extreme value
Frequency
Maximum Pin Temperature [C]
0
50
100
150
600
800
1000
1200
1400

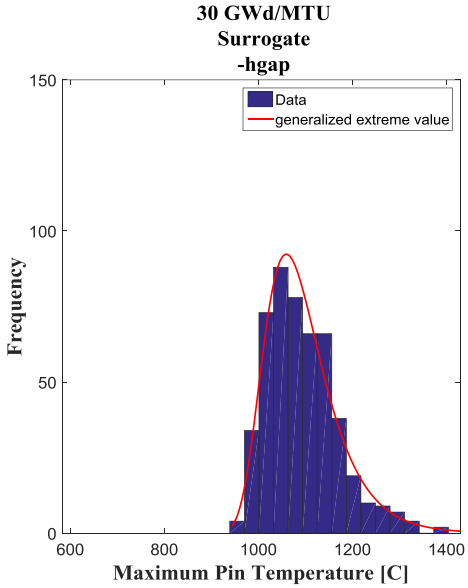
30 GWd/MTU
Surrogate
-hgap
Data
generalized extreme value
Frequency
Maximum Pin Temperature [C]
0
50
100
150
600
800
1000
1200
1400

Figure 98. Statistical sampling of the k_{eff} corresponding to samples of the nuclear data cross-sections. Left: obtained via running VERA-CS right: obtained via the surrogate model.

Nuclear Data Cross-Sections [44groupcov] $\rightarrow$ k_{eff}

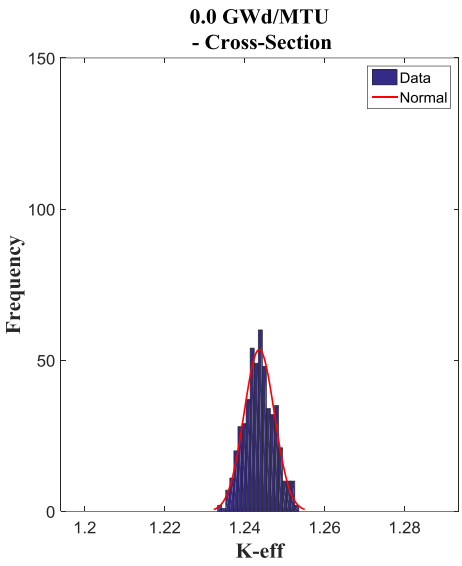
0.0 GWd/MTU
- Cross-Section
Data
Normal
Frequency
K-eff
150
100
50
0
1.2
1.22
1.24
1.26
1.28

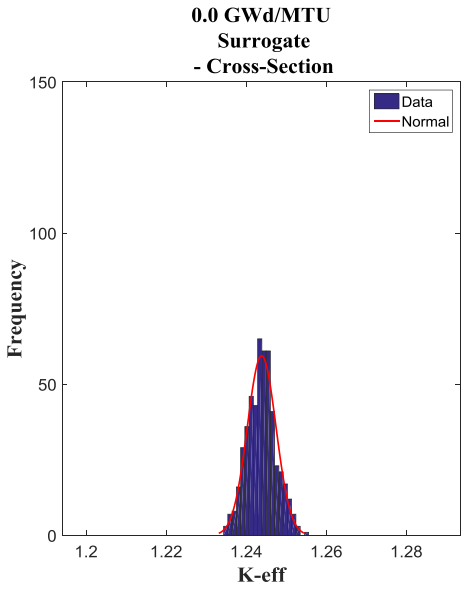
0.0 GWd/MTU
Surrogate
- Cross-Section
Data
Normal
Frequency
K-eff
150
100
50
0
1.2
1.22
1.24
1.26
1.28

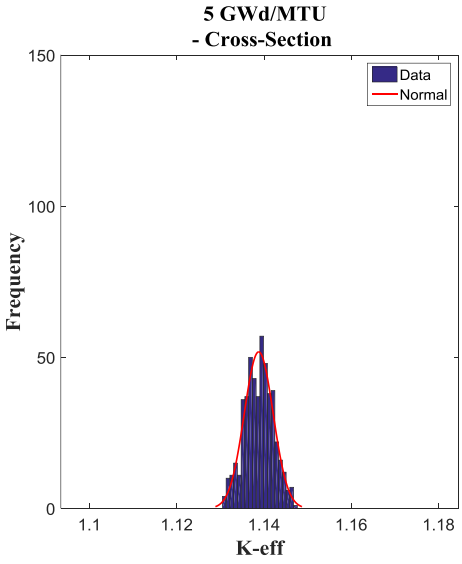
5 GWd/MTU
- Cross-Section
Data
Normal
Frequency
K-eff
150
100
50
0
1.1
1.12
1.14
1.16
1.18

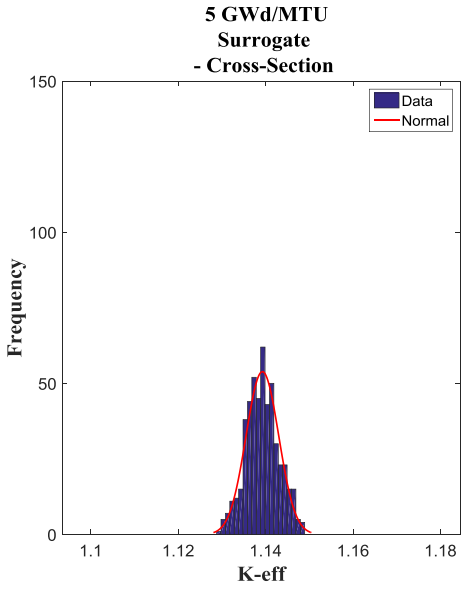
5 GWd/MTU
Surrogate
- Cross-Section
Data
Normal
Frequency
K-eff
150
100
50
0
1.1
1.12
1.14
1.16
1.18

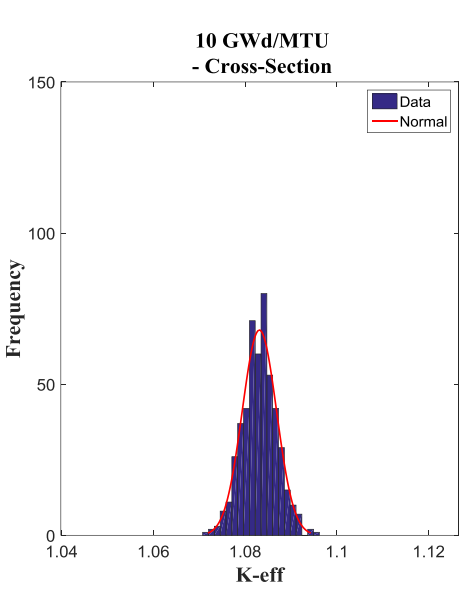
10 GWd/MTU
- Cross-Section
Data
Normal
Frequency
K-eff
0
50
100
150
1.04
1.06
1.08
1.1
1.12

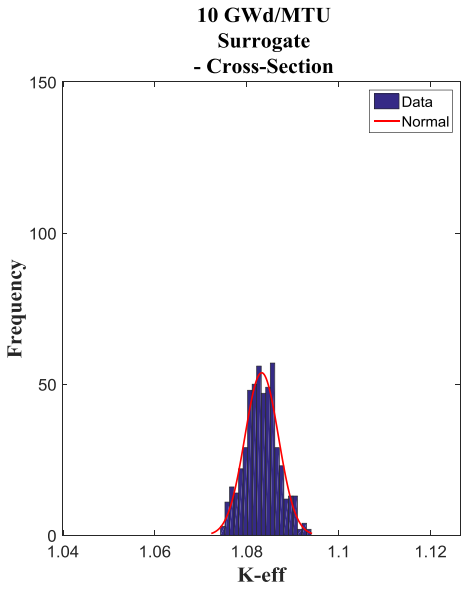
10 GWd/MTU
Surrogate
- Cross-Section
Data
Normal
Frequency
K-eff
0
50
100
150
1.04
1.06
1.08
1.1
1.12

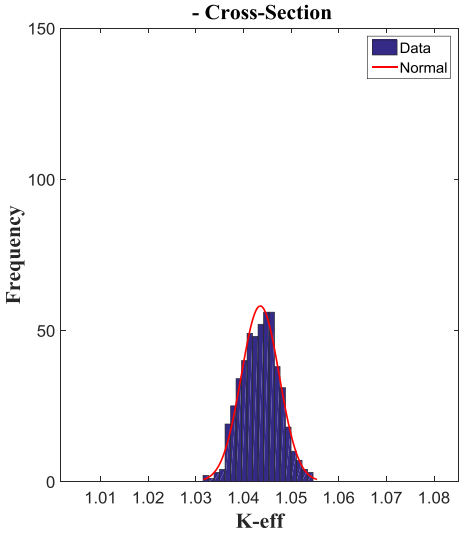
14 GWd/MTU
- Cross-Section
Data
Normal
Frequency
K-eff
0
50
100
150
1.01
1.02
1.03
1.04
1.05
1.06
1.07
1.08

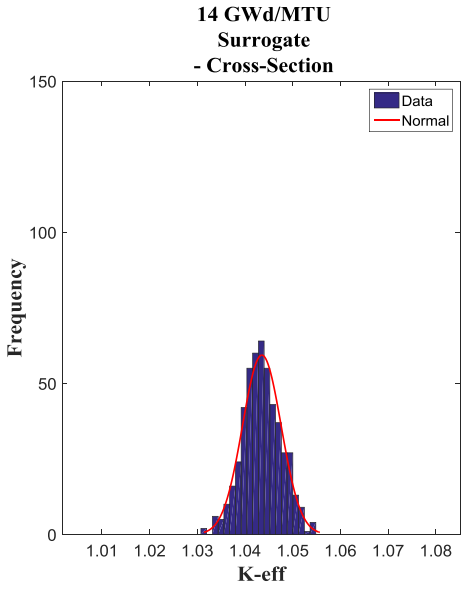
14 GWd/MTU
Surrogate
- Cross-Section
Data
Normal
Frequency
K-eff
0
50
100
150
1.01
1.02
1.03
1.04
1.05
1.06
1.07
1.08

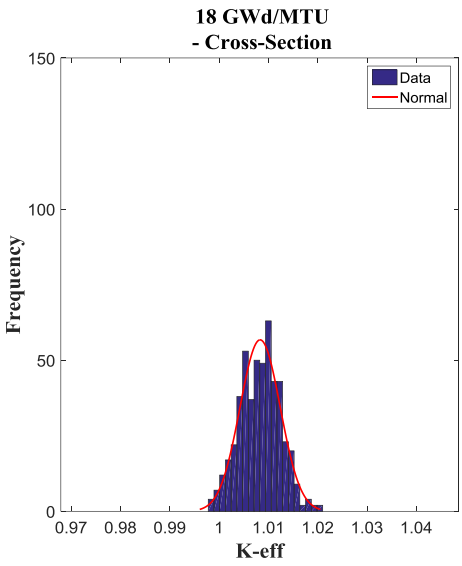
18 GWd/MTU
- Cross-Section
Data
Normal
Frequency
K-eff
0
50
100
150
0.97
0.98
0.99
1
1.01
1.02
1.03
1.04

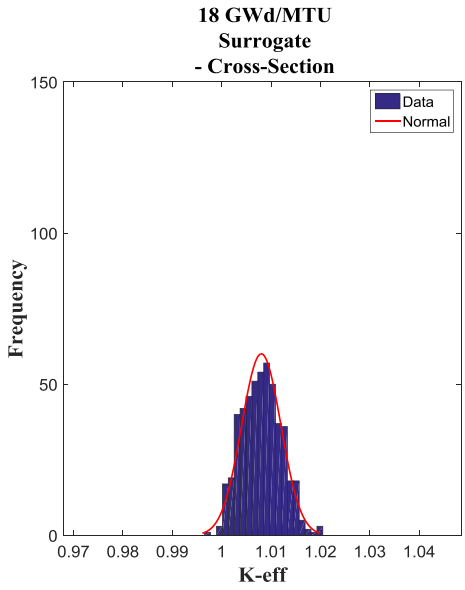
18 GWd/MTU
Surrogate
- Cross-Section
Data
Normal
Frequency
K-eff
0
50
100
150
0.97
0.98
0.99
1
1.01
1.02
1.03
1.04

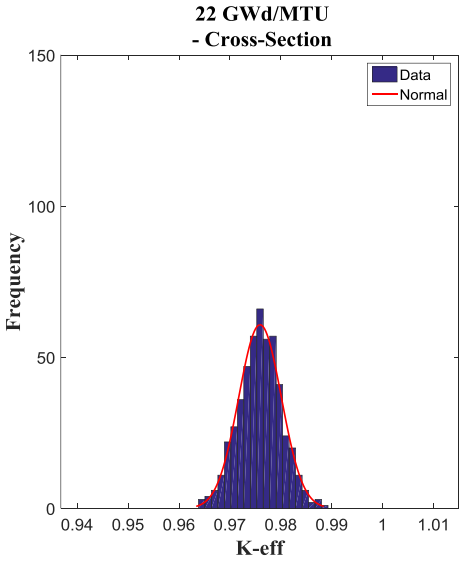
22 GWd/MTU
- Cross-Section
Data
Normal
Frequency
K-eff
0
50
100
150
0.94
0.95
0.96
0.97
0.98
0.99
1
1.01

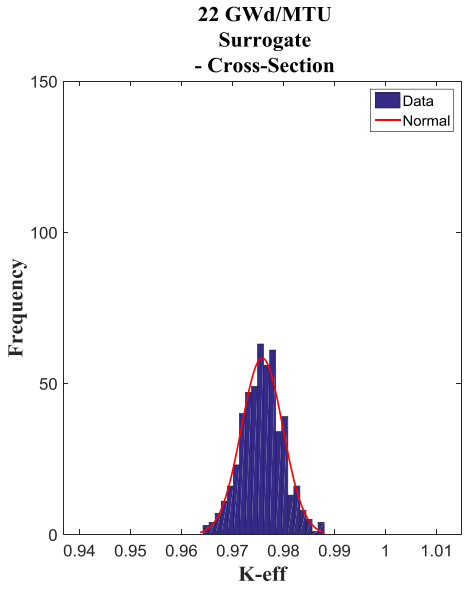
22 GWd/MTU
Surrogate
- Cross-Section
Data
Normal
Frequency
K-eff
0
50
100
150
0.94
0.95
0.96
0.97
0.98
0.99
1
1.01

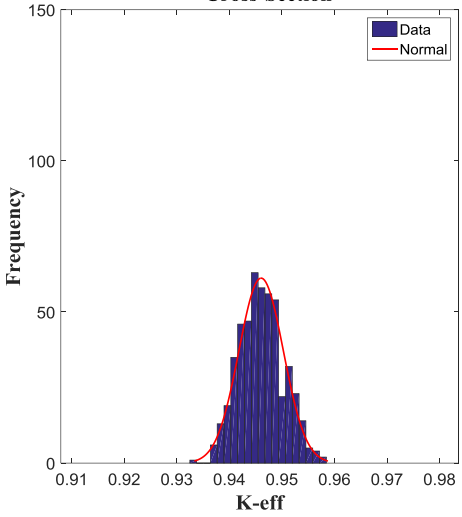
26 GWd/MTU
- Cross-Section
Data
Normal
Frequency
K-eff
0
50
100
150
0.91
0.92
0.93
0.94
0.95
0.96
0.97
0.98

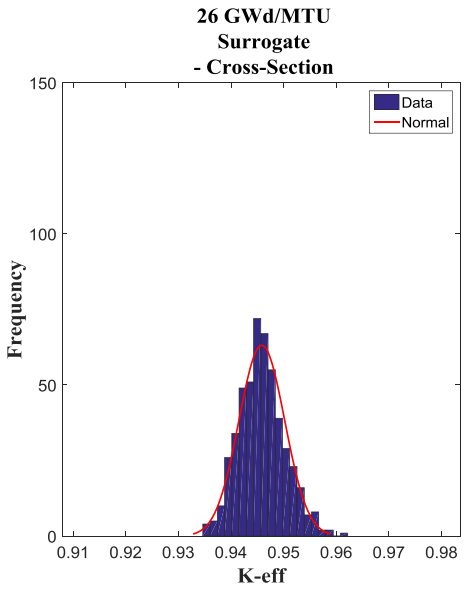
26 GWd/MTU
Surrogate
- Cross-Section
Data
Normal
Frequency
K-eff
0
50
100
150
0.91
0.92
0.93
0.94
0.95
0.96
0.97
0.98

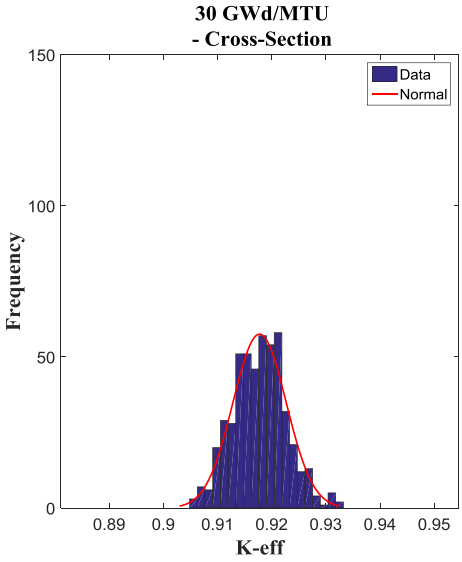
30 GWd/MTU
- Cross-Section
Data
Normal
Frequency
K-eff
0
50
100
150
0.89
0.9
0.91
0.92
0.93
0.94
0.95

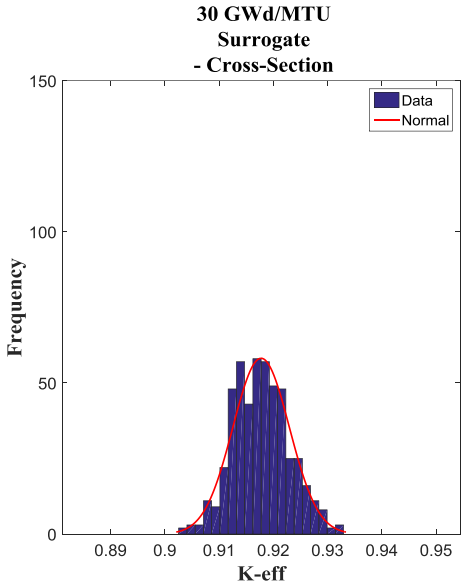
30 GWd/MTU
Surrogate
- Cross-Section
Data
Normal
Frequency
K-eff
0
50
100
150
0.89
0.9
0.91
0.92
0.93
0.94
0.95

Figure 99. Statistical sampling maximum pin power corresponding to samples of the nuclear data cross-sections. Left: obtained via running VERA-CS right: obtained via the surrogate model.

Nuclear Data Cross-Sections [*44groupcov*] → *Maximum Pin Power.*

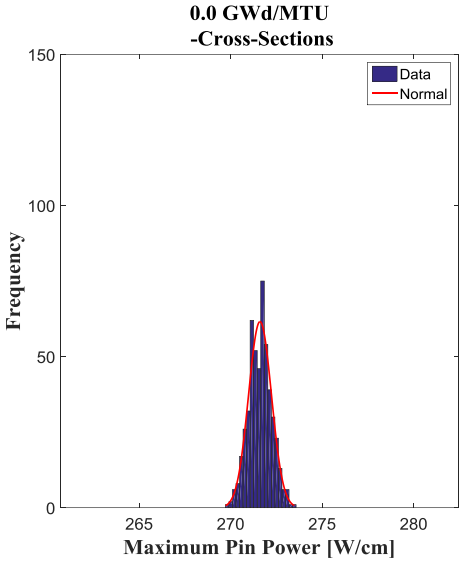
0.0 GWd/MTU
-Cross-Sections
Data
Normal
Frequency
Maximum Pin Power [W/cm]
0
50
100
150
265
270
275
280

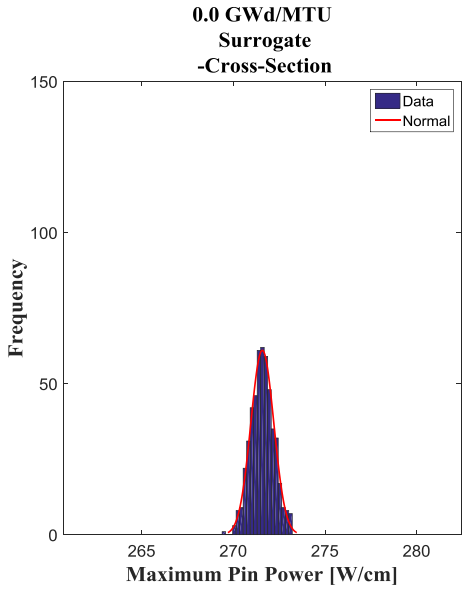
0.0 GWd/MTU
Surrogate
-Cross-Section
Data
Normal
Frequency
Maximum Pin Power [W/cm]
0
50
100
150
265
270
275
280

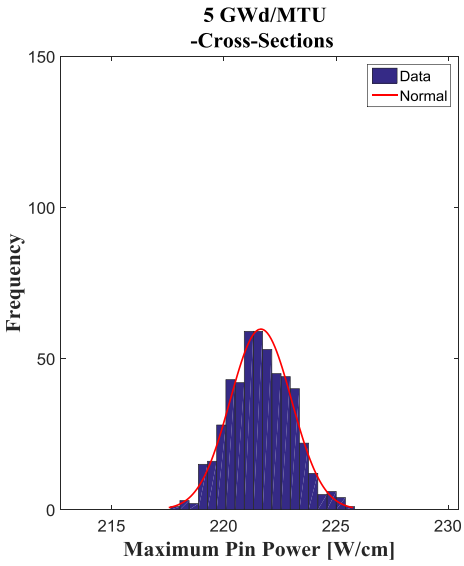
5 GWd/MTU
-Cross-Sections
Data
Normal
Frequency
Maximum Pin Power [W/cm]
0
50
100
150
215
220
225
230

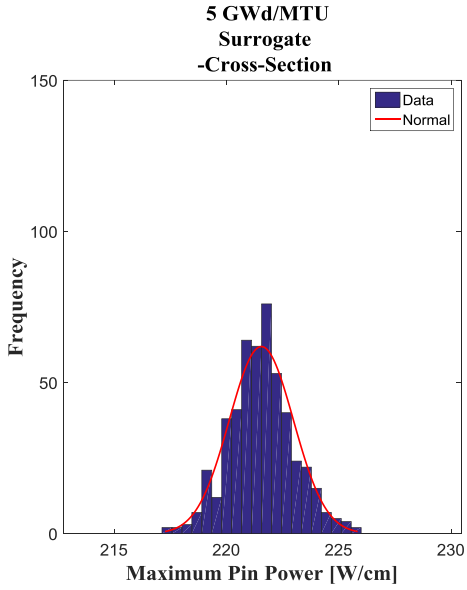
5 GWd/MTU
Surrogate
-Cross-Section
Data
Normal
Frequency
Maximum Pin Power [W/cm]
0
50
100
150
215
220
225
230

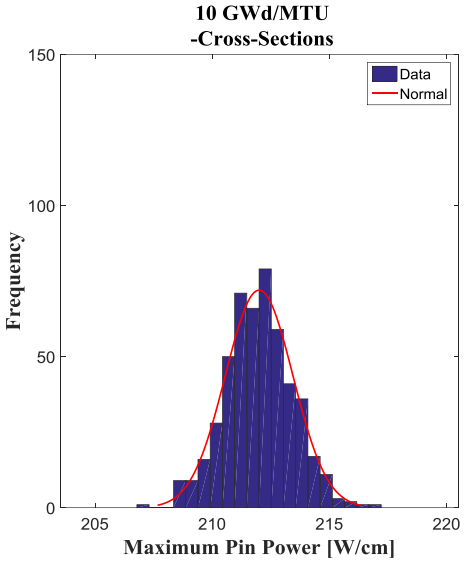
10 GWd/MTU
-Cross-Sections
Data
Normal
Frequency
Maximum Pin Power [W/cm]
0
50
100
150
205
210
215
220

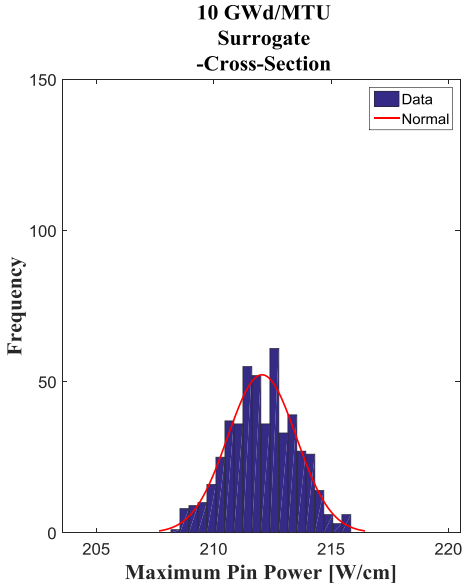
10 GWd/MTU
Surrogate
-Cross-Section
Data
Normal
Frequency
Maximum Pin Power [W/cm]
0
50
100
150
205
210
215
220

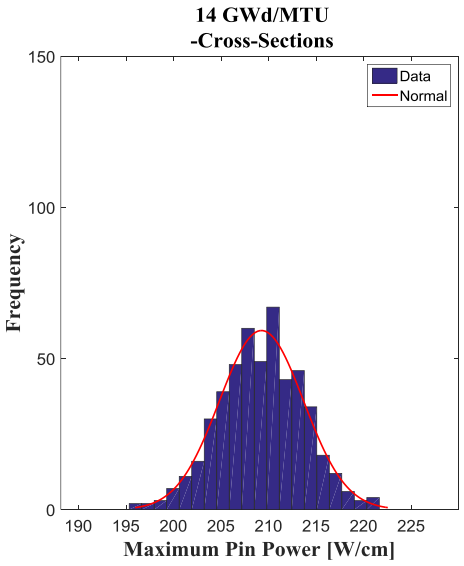
14 GWd/MTU
-Cross-Sections
Data
Normal
Frequency
Maximum Pin Power [W/cm]
0
50
100
150
190
195
200
205
210
215
220
225

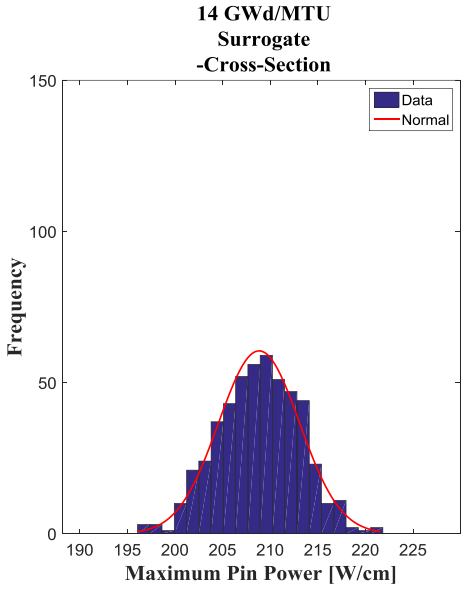
14 GWd/MTU
Surrogate
-Cross-Section
Data
Normal
Frequency
Maximum Pin Power [W/cm]
0
50
100
150
190
195
200
205
210
215
220
225

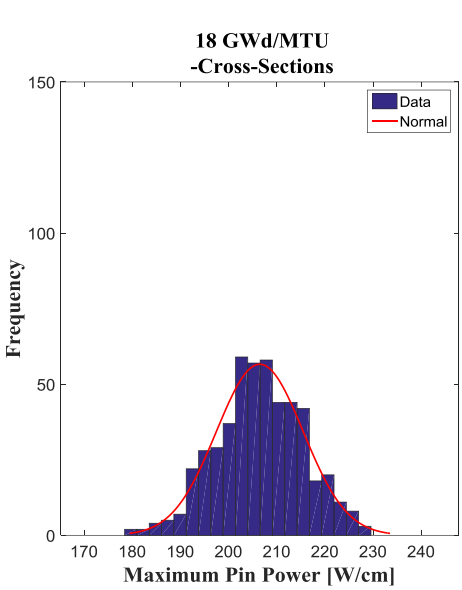
18 GWd/MTU
-Cross-Sections
Data
Normal
Frequency
Maximum Pin Power [W/cm]
0
50
100
150
170
180
190
200
210
220
230
240

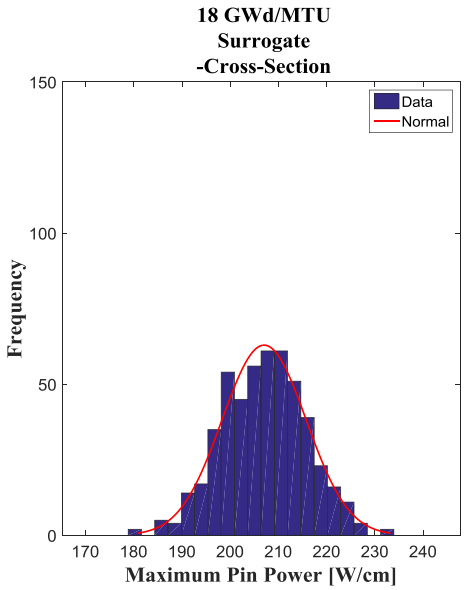
18 GWd/MTU
Surrogate
-Cross-Section
Data
Normal
Frequency
Maximum Pin Power [W/cm]
0
50
100
150
170
180
190
200
210
220
230
240

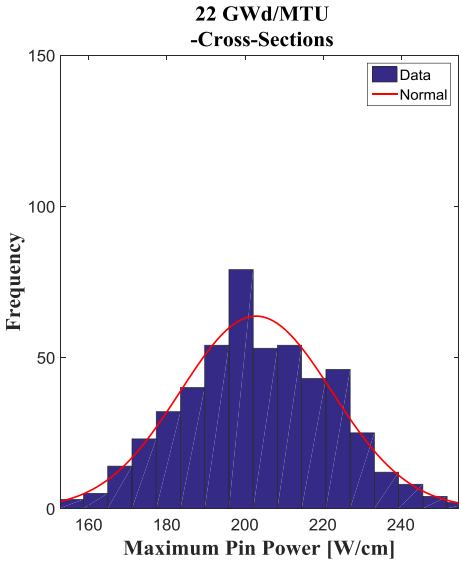
22 GWd/MTU
-Cross-Sections
Data
Normal
Frequency
Maximum Pin Power [W/cm]
0
50
100
150
160
180
200
220
240

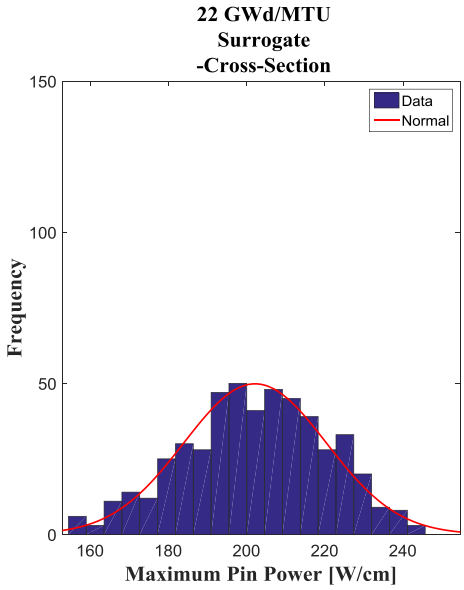
22 GWd/MTU
Surrogate
-Cross-Section
Data
Normal
Frequency
Maximum Pin Power [W/cm]
0
50
100
150
160
180
200
220
240

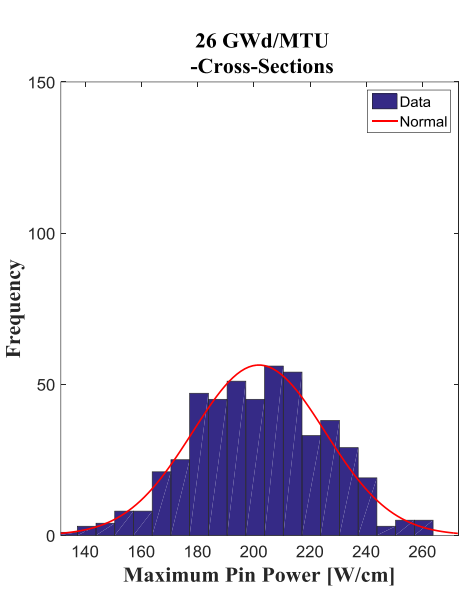
26 GWd/MTU
-Cross-Sections
Data
Normal
Frequency
Maximum Pin Power [W/cm]
0
50
100
150
140
160
180
200
220
240
260

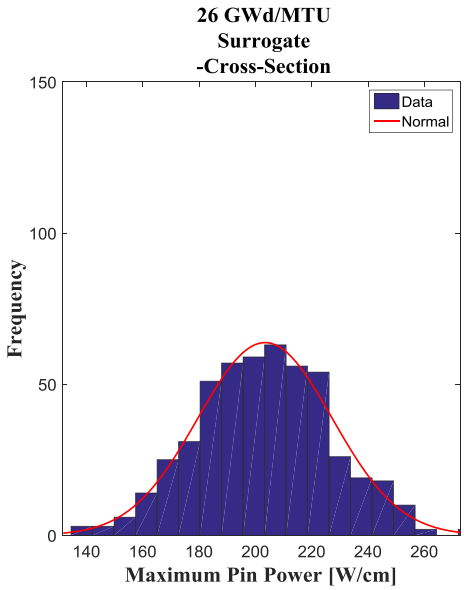
26 GWd/MTU
Surrogate
-Cross-Section
Data
Normal
Frequency
Maximum Pin Power [W/cm]
0
50
100
150
140
160
180
200
220
240
260

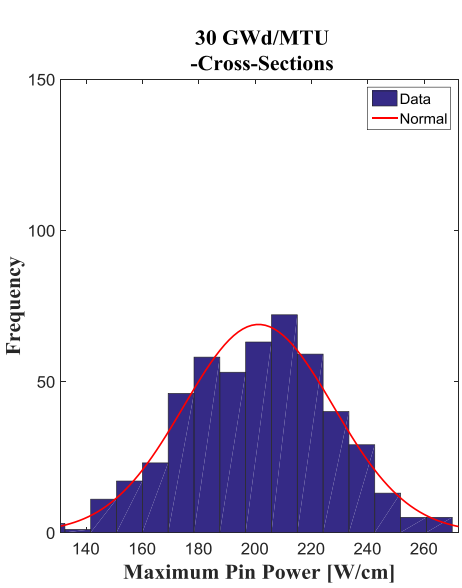
30 GWd/MTU
-Cross-Sections
Data
Normal
Frequency
Maximum Pin Power [W/cm]
0
50
100
150
140
160
180
200
220
240
260

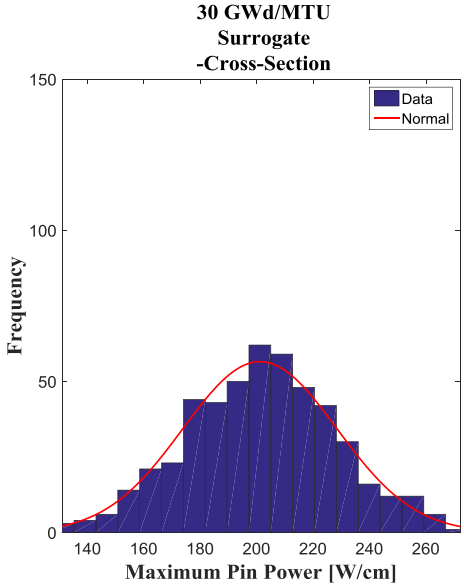
30 GWd/MTU
Surrogate
-Cross-Section
Data
Normal
Frequency
Maximum Pin Power [W/cm]
0
50
100
150
140
160
180
200
220
240
260

Figure 100. Statistical sampling maximum pin temperature corresponding to samples of the nuclear data cross-sections. Left: obtained via running VERA-CS right: obtained via the surrogate model.

Nuclear Data Cross-Sections [*44groupcov*] → *Maximum Pin Temperature.*

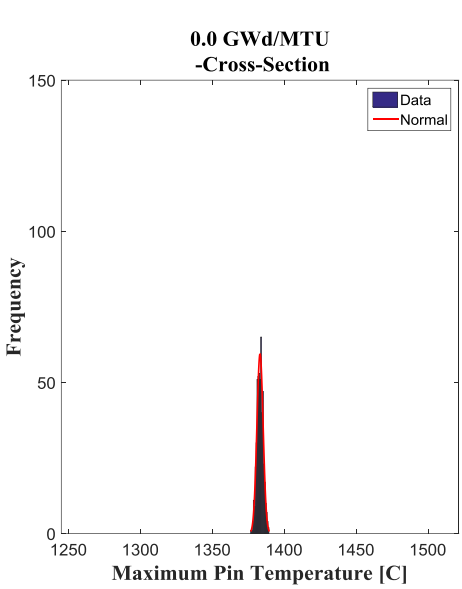
0.0 GWd/MTU
-Cross-Section
Data
Normal
Frequency
Maximum Pin Temperature [C]
0
50
100
150
1250
1300
1350
1400
1450
1500

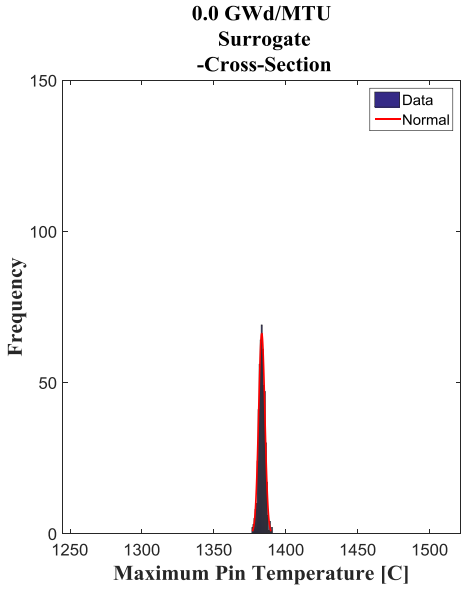
0.0 GWd/MTU
Surrogate
-Cross-Section
Data
Normal
Frequency
Maximum Pin Temperature [C]
0
50
100
150
1250
1300
1350
1400
1450
1500

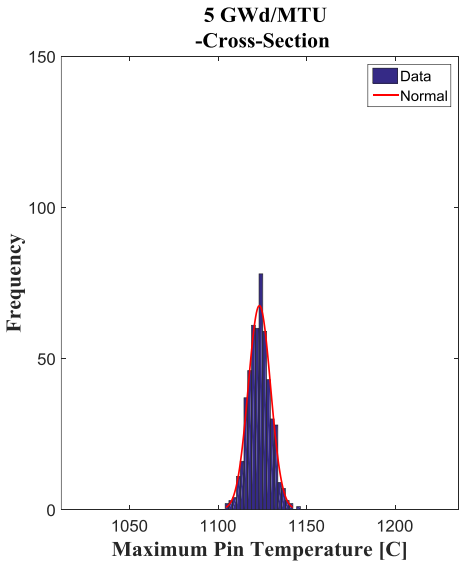
5 GWd/MTU
-Cross-Section
Data
Normal
Frequency
Maximum Pin Temperature [C]
0
50
100
150
1050
1100
1150
1200

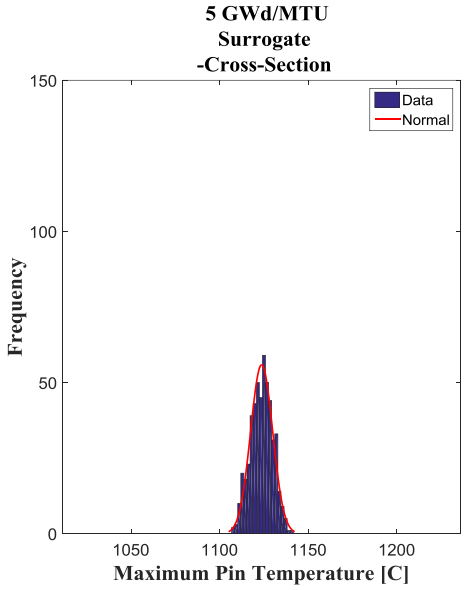
5 GWd/MTU
Surrogate
-Cross-Section
Data
Normal
Frequency
Maximum Pin Temperature [C]
0
50
100
150
1050
1100
1150
1200

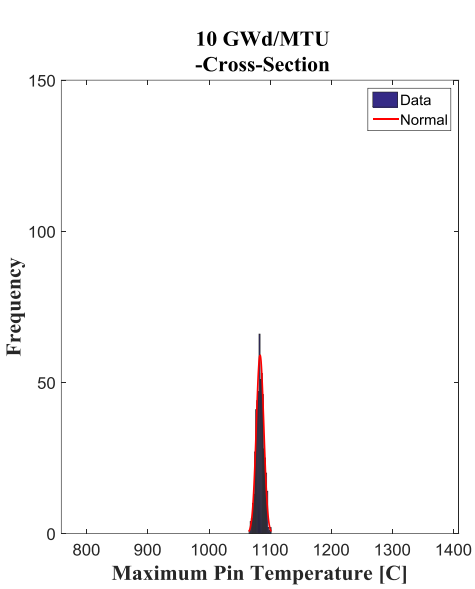
10 GWd/MTU
-Cross-Section
Data
Normal
Frequency
Maximum Pin Temperature [C]
0
50
100
150
800
900
1000
1100
1200
1300
1400

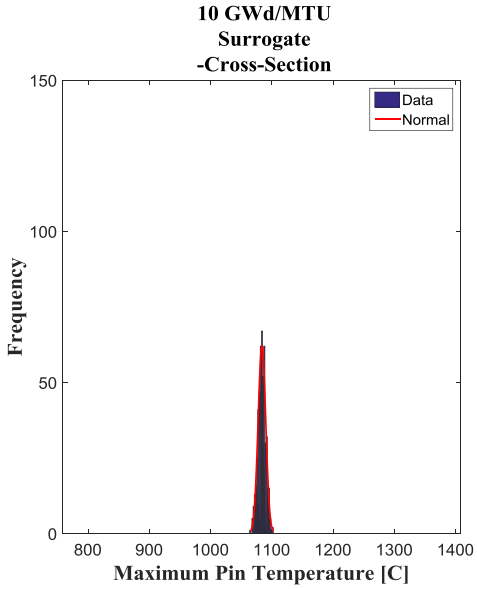
10 GWd/MTU
Surrogate
-Cross-Section
Data
Normal
Frequency
Maximum Pin Temperature [C]
0
50
100
150
800
900
1000
1100
1200
1300
1400

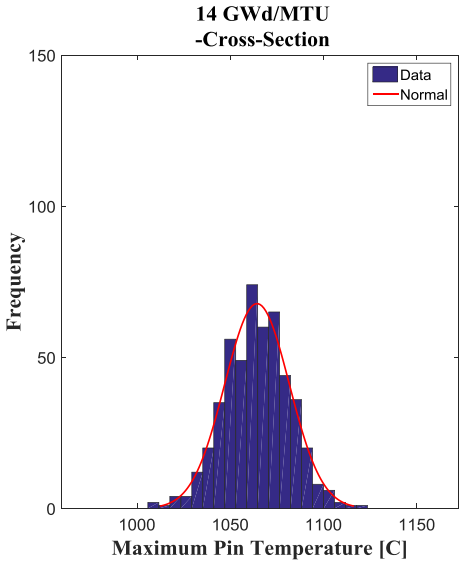
14 GWd/MTU
-Cross-Section
Data
Normal
Frequency
Maximum Pin Temperature [C]
0
50
100
150
1000
1050
1100
1150

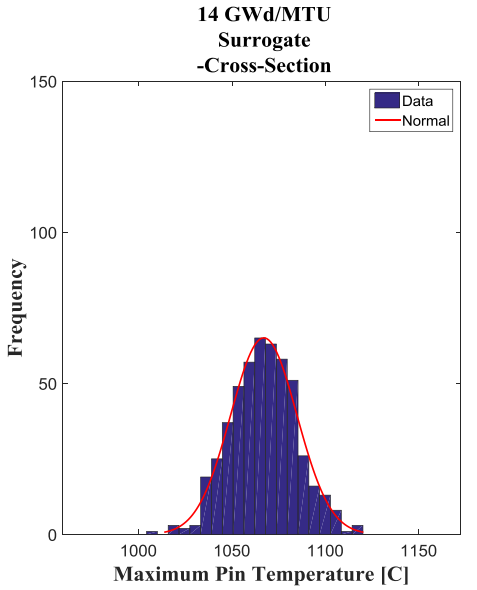
14 GWd/MTU
Surrogate
-Cross-Section
Data
Normal
Frequency
Maximum Pin Temperature [C]
0
50
100
150
1000
1050
1100
1150

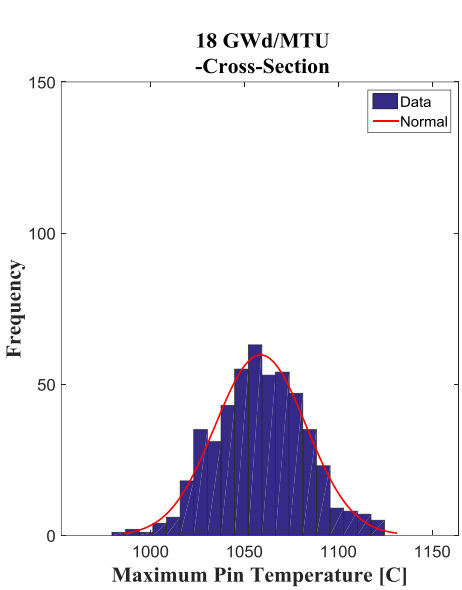
18 GWd/MTU
-Cross-Section
Data
Normal
Frequency
Maximum Pin Temperature [C]
0
50
100
150
1000
1050
1100
1150

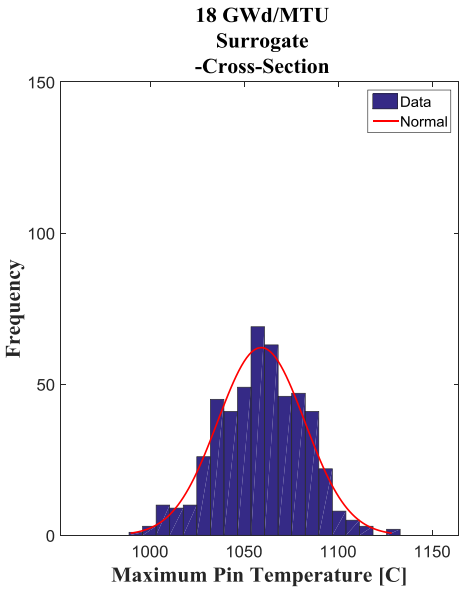
18 GWd/MTU
Surrogate
-Cross-Section
Data
Normal
Frequency
Maximum Pin Temperature [C]
0
50
100
150
1000
1050
1100
1150

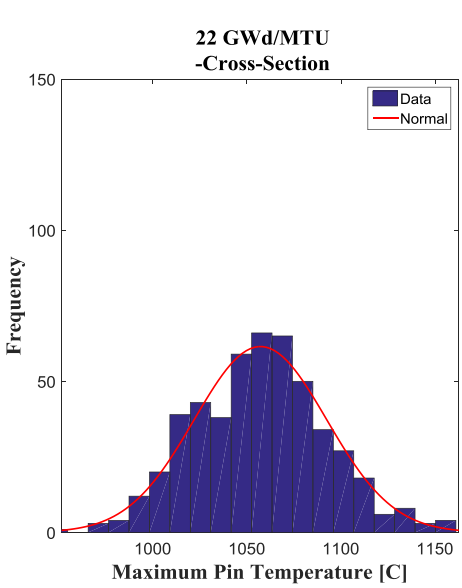
22 GWd/MTU
-Cross-Section
Data
Normal
Frequency
Maximum Pin Temperature [C]
0
50
100
150
1000
1050
1100
1150

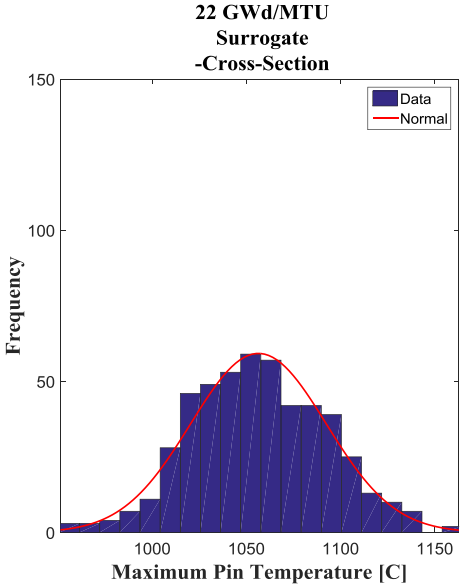
22 GWd/MTU
Surrogate
-Cross-Section
Data
Normal
Frequency
Maximum Pin Temperature [C]
0
50
100
150
1000
1050
1100
1150

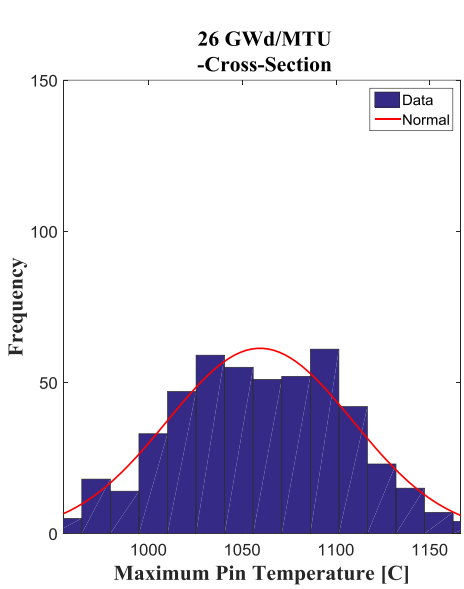
26 GWd/MTU
-Cross-Section
Data
Normal
Frequency
Maximum Pin Temperature [C]
0
50
100
150
1000
1050
1100
1150

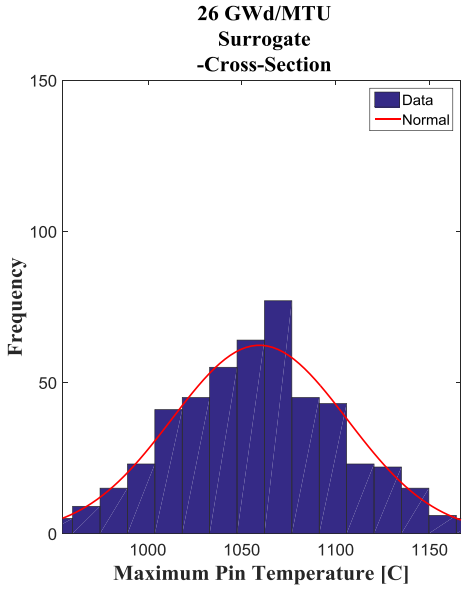
26 GWd/MTU
Surrogate
-Cross-Section
Data
Normal
Frequency
Maximum Pin Temperature [C]
0
50
100
150
1000
1050
1100
1150

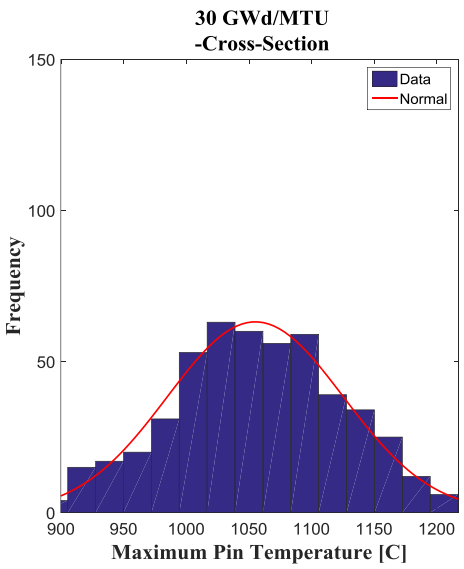
30 GWd/MTU
-Cross-Section
Data
Normal
Frequency
Maximum Pin Temperature [C]
0
50
100
150
900
950
1000
1050
1100
1150
1200

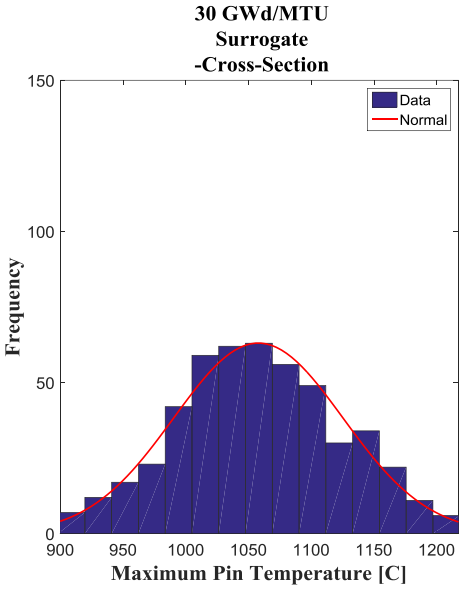
30 GWd/MTU
Surrogate
-Cross-Section
Data
Normal
Frequency
Maximum Pin Temperature [C]
0
50
100
150
900
950
1000
1050
1100
1150
1200

Figure 101. Statistical sampling k_{eff} corresponding to samples of the grid-loss. Left: obtained via running VERA-CS right: obtained via the surrogate model.

Grid-Loss $\rightarrow$ k_{eff}

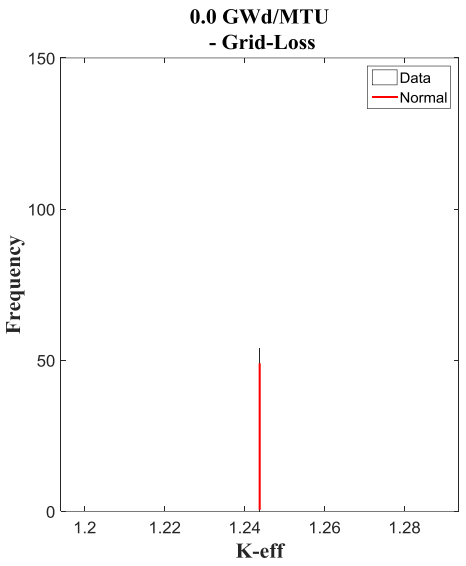
0.0 GWd/MTU
- Grid-Loss
Data
Normal
Frequency
K-eff
150
100
50
0
1.2
1.22
1.24
1.26
1.28

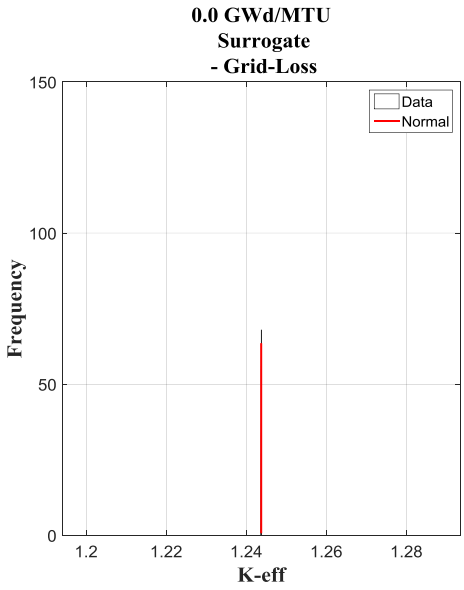
0.0 GWd/MTU
Surrogate
- Grid-Loss
Data
Normal
Frequency
K-eff
150
100
50
0
1.2
1.22
1.24
1.26
1.28

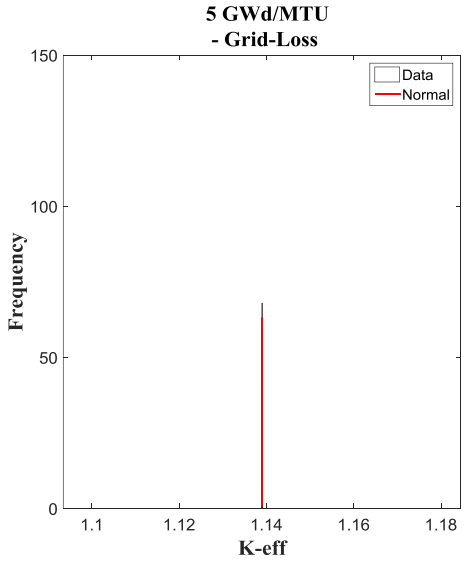
5 GWd/MTU
- Grid-Loss
Data
Normal
Frequency
K-eff
150
100
50
0
1.1
1.12
1.14
1.16
1.18

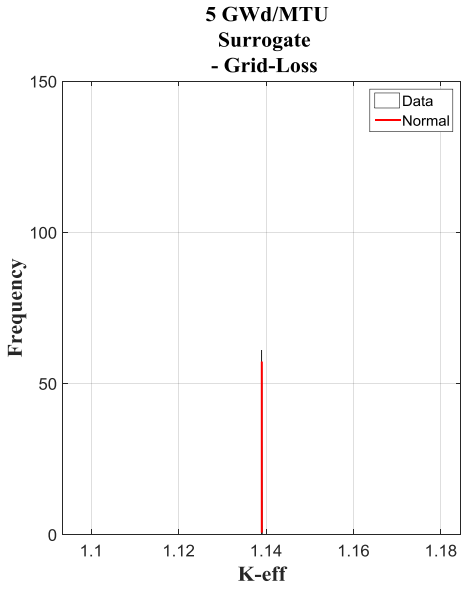
5 GWd/MTU
Surrogate
- Grid-Loss
Data
Normal
Frequency
K-eff
150
100
50
0
1.1
1.12
1.14
1.16
1.18

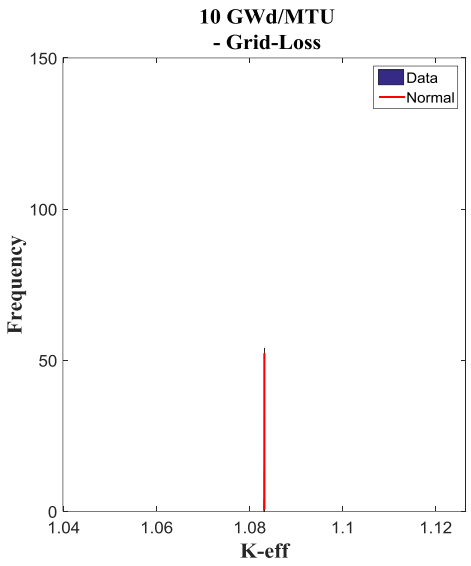
10 GWd/MTU
- Grid-Loss
Data
Normal
Frequency
K-eff
150
100
50
0
1.04
1.06
1.08
1.1
1.12

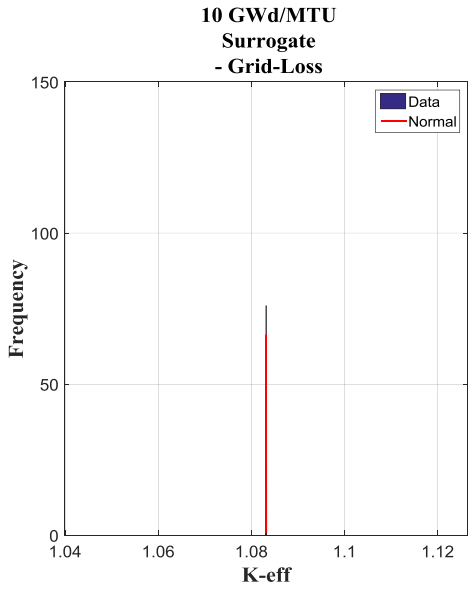
10 GWd/MTU
Surrogate
- Grid-Loss
Data
Normal
Frequency
K-eff
150
100
50
0
1.04
1.06
1.08
1.1
1.12

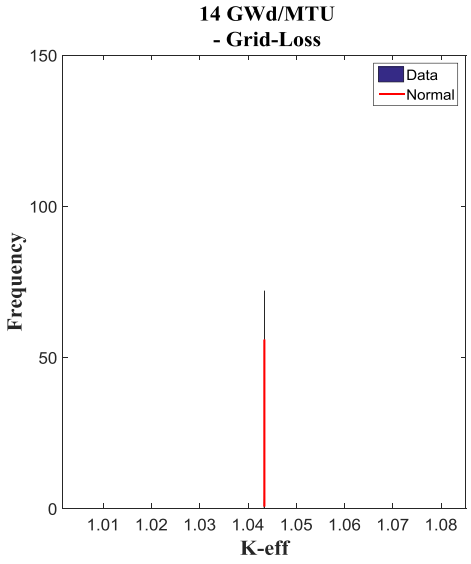
14 GWd/MTU
- Grid-Loss
Data
Normal
Frequency
K-eff
150
100
50
0
1.01
1.02
1.03
1.04
1.05
1.06
1.07
1.08


14 GWd/MTU
Surrogate
- Grid-Loss
Data
Normal
Frequency
K-eff
150
100
50
0
1.01
1.02
1.03
1.04
1.05
1.06
1.07
1.08

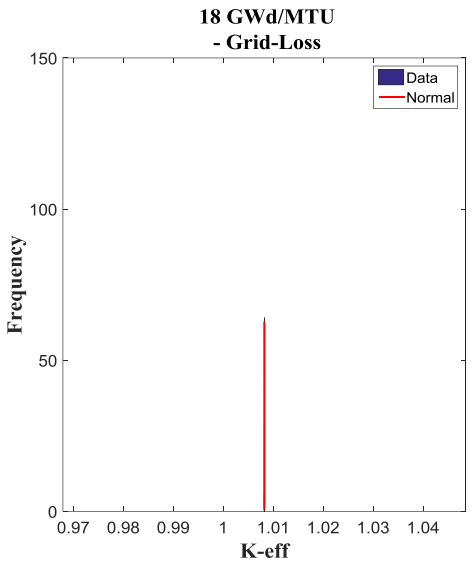
18 GWd/MTU
- Grid-Loss
Data
Normal
Frequency
K-eff
0
50
100
150
0.97
0.98
0.99
1
1.01
1.02
1.03
1.04

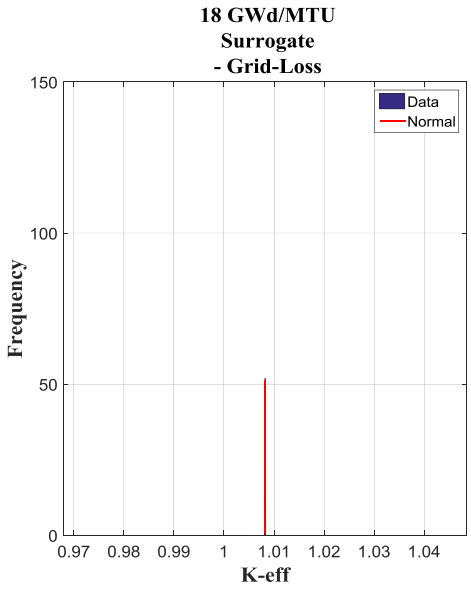
18 GWd/MTU
Surrogate
- Grid-Loss
Data
Normal
Frequency
K-eff
0
50
100
150
0.97
0.98
0.99
1
1.01
1.02
1.03
1.04

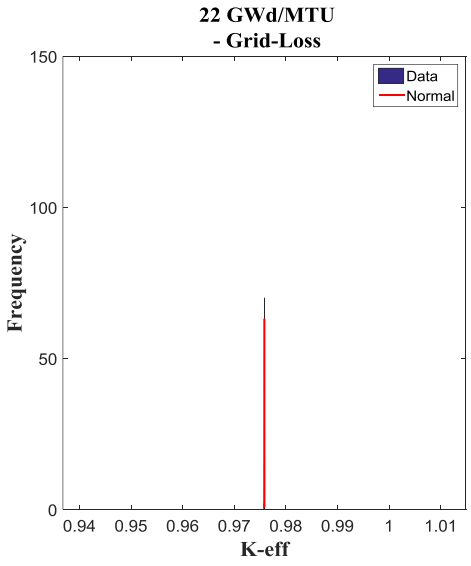
22 GWd/MTU
- Grid-Loss
Data
Normal
Frequency
K-eff
0
50
100
150
0.94
0.95
0.96
0.97
0.98
0.99
1
1.01

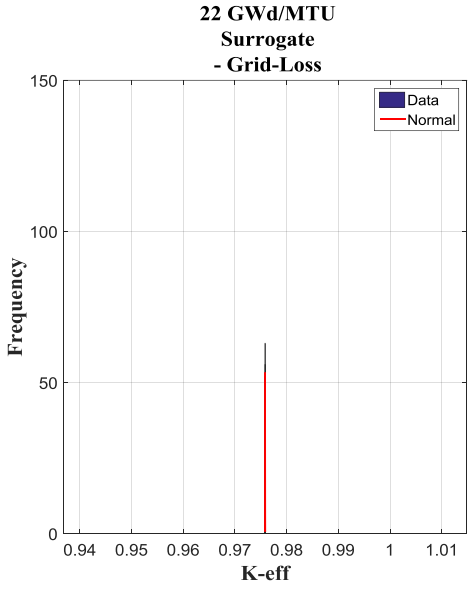
22 GWd/MTU
Surrogate
- Grid-Loss
Data
Normal
Frequency
K-eff
0
50
100
150
0.94
0.95
0.96
0.97
0.98
0.99
1
1.01

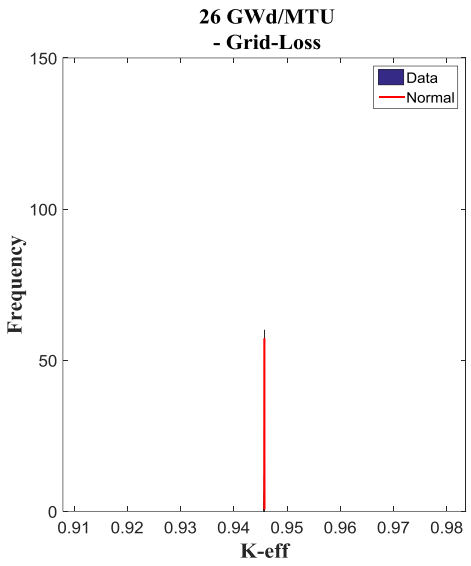
26 GWd/MTU
- Grid-Loss
Data
Normal
Frequency
K-eff
0
50
100
150
0.91
0.92
0.93
0.94
0.95
0.96
0.97
0.98

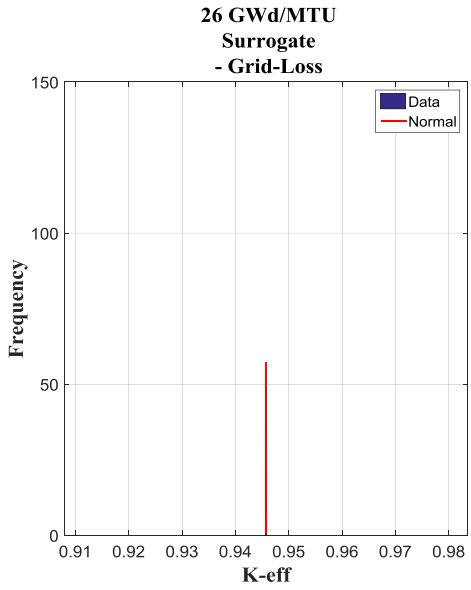
26 GWd/MTU
Surrogate
- Grid-Loss
Data
Normal
Frequency
K-eff
0
50
100
150
0.91
0.92
0.93
0.94
0.95
0.96
0.97
0.98

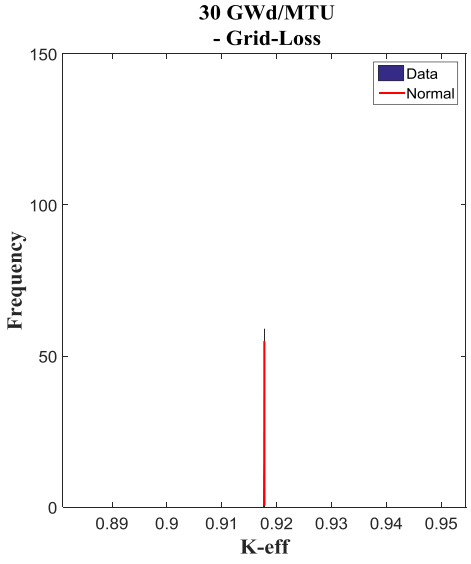
30 GWd/MTU
- Grid-Loss
Data
Normal
Frequency
K-eff
0
50
100
150
0.89
0.9
0.91
0.92
0.93
0.94
0.95

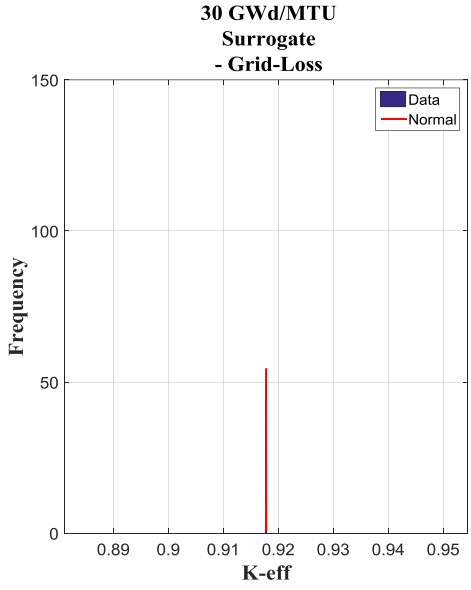
30 GWd/MTU
Surrogate
- Grid-Loss
Data
Normal
Frequency
K-eff
0
50
100
150
0.89
0.9
0.91
0.92
0.93
0.94
0.95

Figure 102. Statistical sampling maximum pin power corresponding to samples of the grid-loss. Left: obtained via running VERA-CS right: obtained via the surrogate model.

Grid-Loss → *Maximum Pin Power*

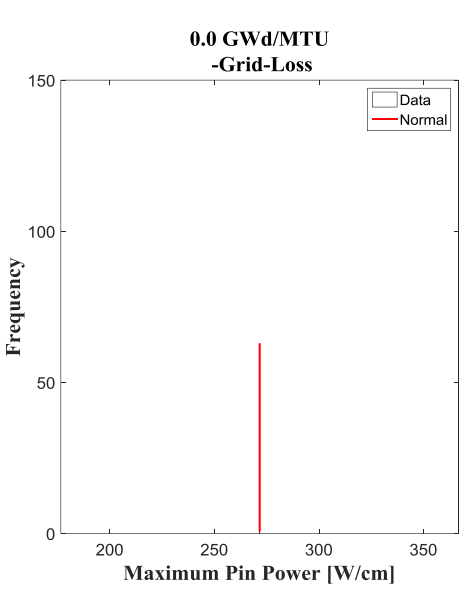
0.0 GWd/MTU
-Grid-Loss
Data
Normal
Frequency
Maximum Pin Power [W/cm]
0
50
100
150
200
250
300
350

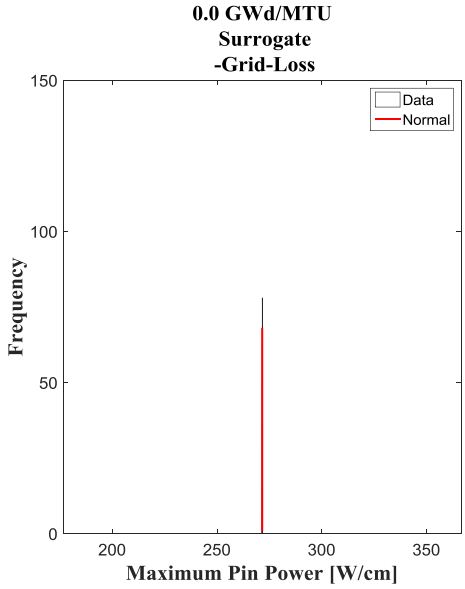
0.0 GWd/MTU
Surrogate
-Grid-Loss
Data
Normal
Frequency
Maximum Pin Power [W/cm]
0
50
100
150
200
250
300
350

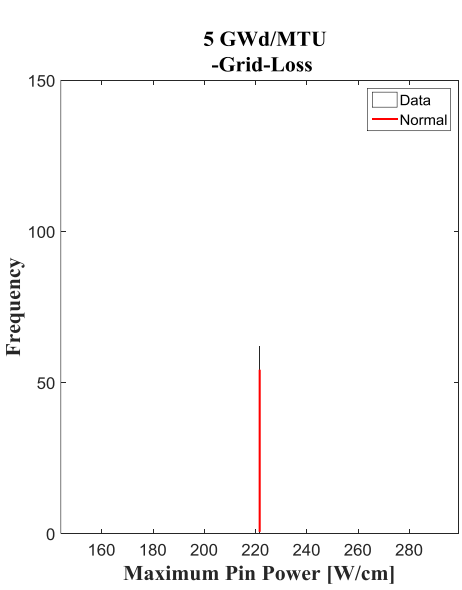
5 GWd/MTU
-Grid-Loss
Data
Normal
Frequency
Maximum Pin Power [W/cm]
0
50
100
150
160
180
200
220
240
260
280

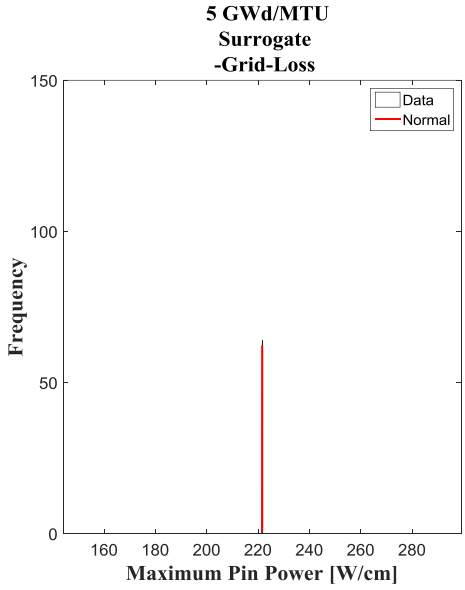
5 GWd/MTU
Surrogate
-Grid-Loss
Data
Normal
Frequency
Maximum Pin Power [W/cm]
0
50
100
150
160
180
200
220
240
260
280

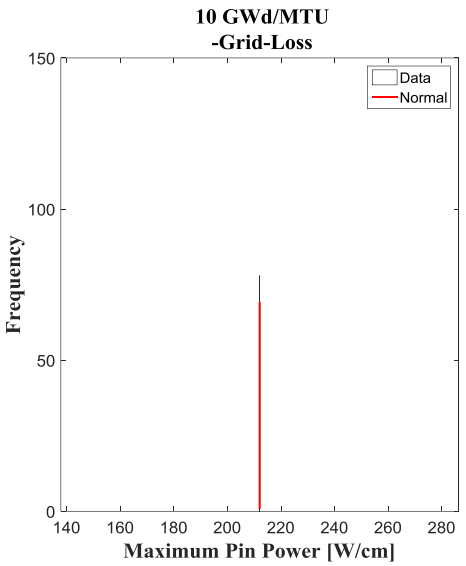
10 GWd/MTU
-Grid-Loss
Data
Normal
Frequency
Maximum Pin Power [W/cm]
0
50
100
150
140
160
180
200
220
240
260
280

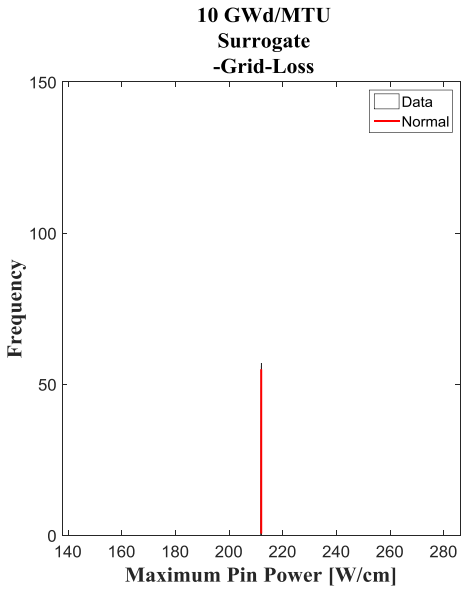
10 GWd/MTU
Surrogate
-Grid-Loss
Data
Normal
Frequency
Maximum Pin Power [W/cm]
0
50
100
150
140
160
180
200
220
240
260
280

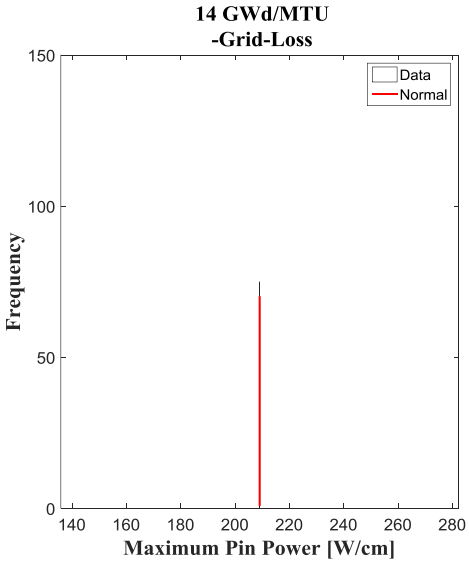
14 GWd/MTU
-Grid-Loss
Data
Normal
Frequency
Maximum Pin Power [W/cm]
0
50
100
150
140
160
180
200
220
240
260
280

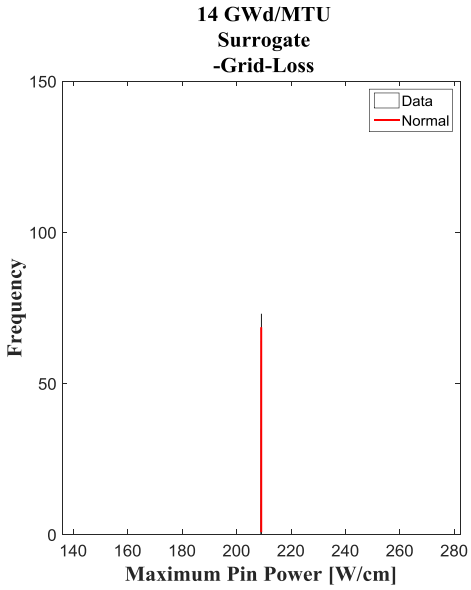
14 GWd/MTU
Surrogate
-Grid-Loss
Data
Normal
Frequency
Maximum Pin Power [W/cm]
0
50
100
150
140
160
180
200
220
240
260
280

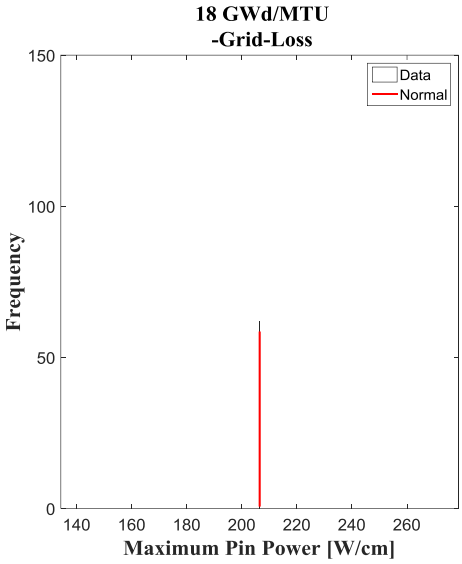
18 GWd/MTU
-Grid-Loss
Data
Normal
Frequency
Maximum Pin Power [W/cm]
0
50
100
150
140
160
180
200
220
240
260

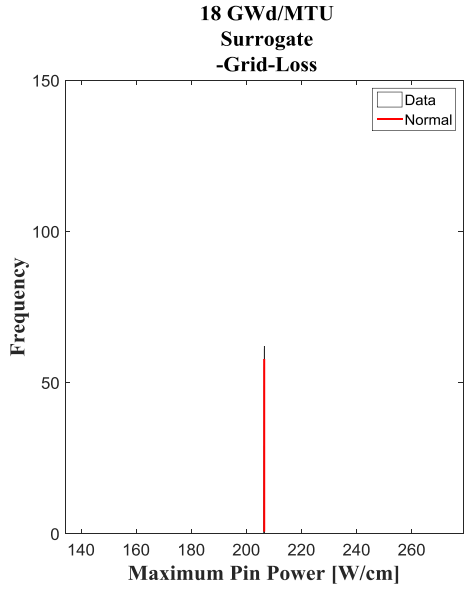
18 GWd/MTU
Surrogate
-Grid-Loss
Data
Normal
Frequency
Maximum Pin Power [W/cm]
0
50
100
150
140
160
180
200
220
240
260

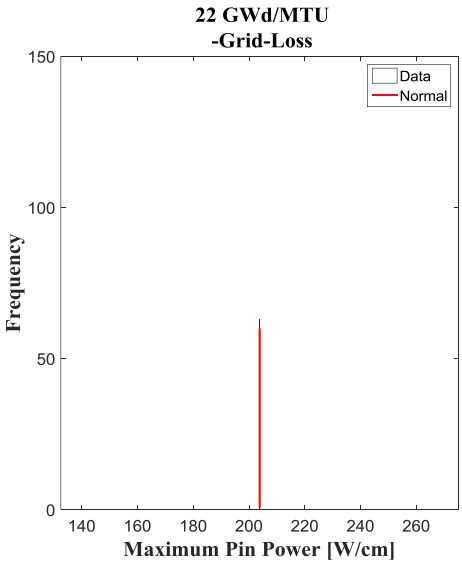
22 GWd/MTU
-Grid-Loss
Data
Normal
Frequency
Maximum Pin Power [W/cm]
0
50
100
150
140
160
180
200
220
240
260

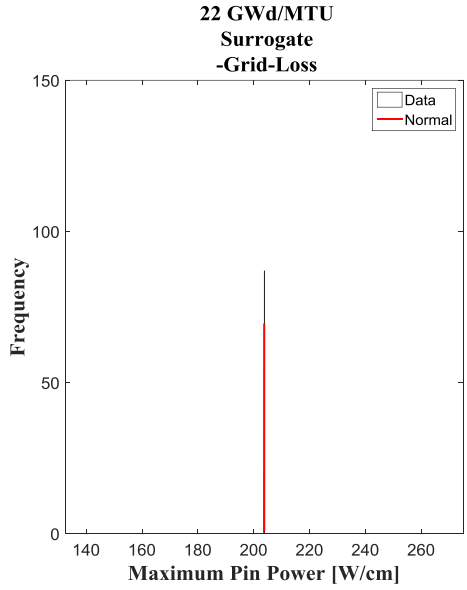
22 GWd/MTU
Surrogate
-Grid-Loss
Data
Normal
Frequency
Maximum Pin Power [W/cm]
0
50
100
150
140
160
180
200
220
240
260

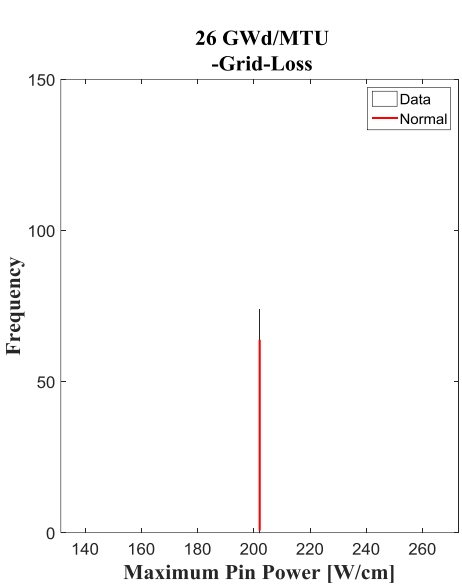
26 GWd/MTU
-Grid-Loss
Data
Normal
Frequency
Maximum Pin Power [W/cm]
0
50
100
150
140
160
180
200
220
240
260

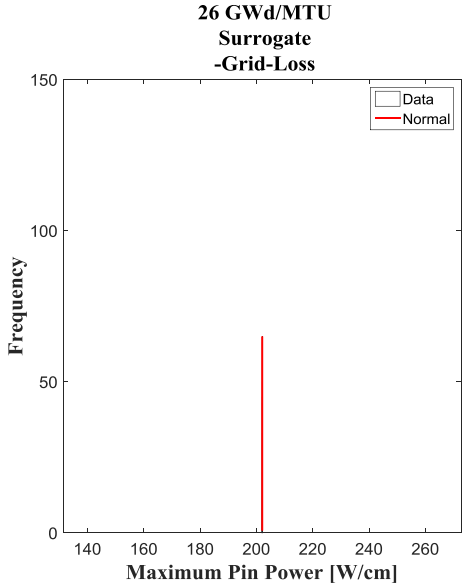
26 GWd/MTU
Surrogate
-Grid-Loss
Data
Normal
Frequency
Maximum Pin Power [W/cm]
0
50
100
150
140
160
180
200
220
240
260

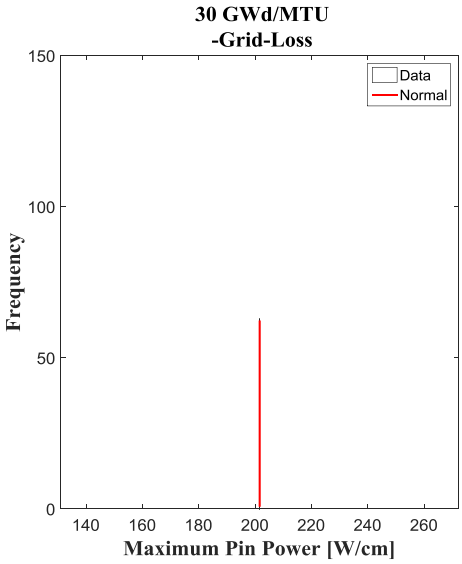
30 GWd/MTU
-Grid-Loss
Data
Normal
Frequency
Maximum Pin Power [W/cm]
0
50
100
150
140
160
180
200
220
240
260

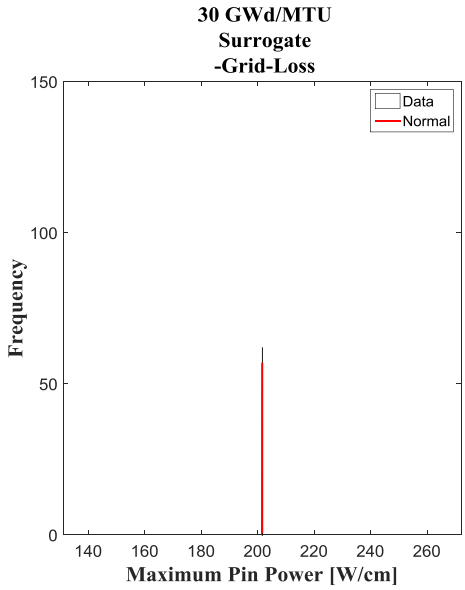
30 GWd/MTU
Surrogate
-Grid-Loss
Data
Normal
Frequency
Maximum Pin Power [W/cm]
0
50
100
150
140
160
180
200
220
240
260

Figure 103. Statistical sampling maximum pin temperature corresponding to samples of the grid-loss. Left: obtained via running VERA-CS right: obtained via the surrogate model.

Grid-Loss → Maximum Pin Temperature

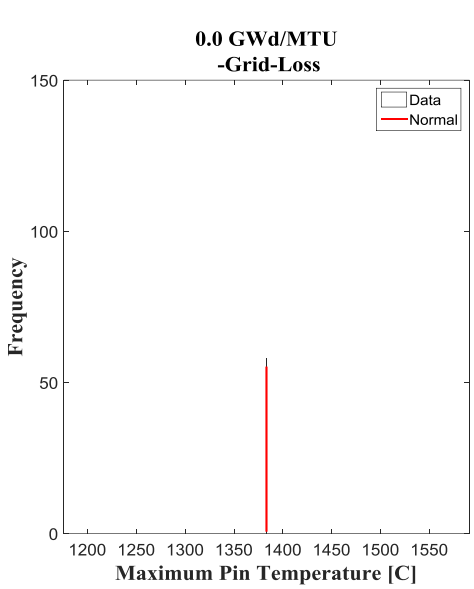
0.0 GWd/MTU
-Grid-Loss
Data
Normal
Frequency
Maximum Pin Temperature [C]

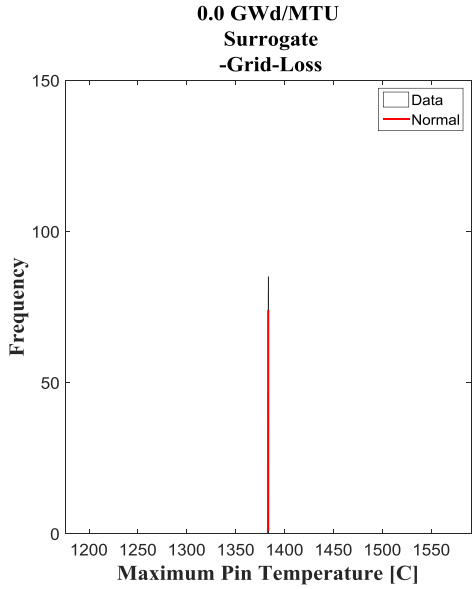
0.0 GWd/MTU
Surrogate
-Grid-Loss
Data
Normal
Frequency
Maximum Pin Temperature [C]

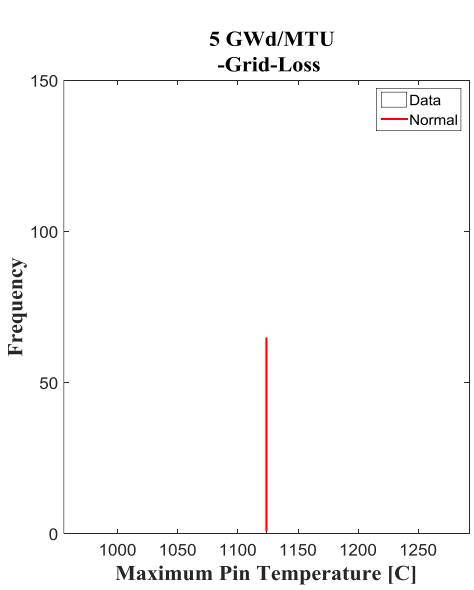
5 GWd/MTU
-Grid-Loss
Data
Normal
Frequency
Maximum Pin Temperature [C]

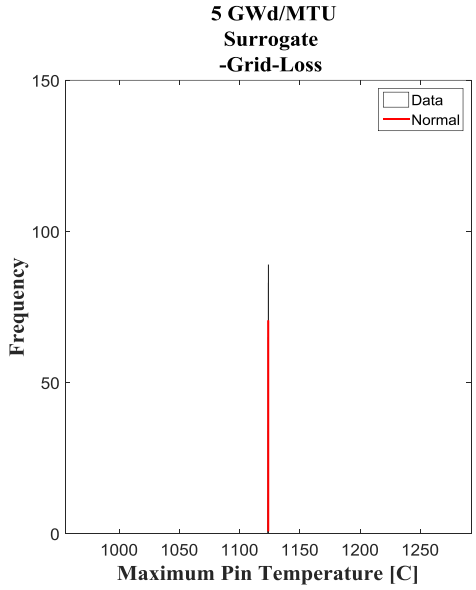
5 GWd/MTU
Surrogate
-Grid-Loss
Data
Normal
Frequency
Maximum Pin Temperature [C]

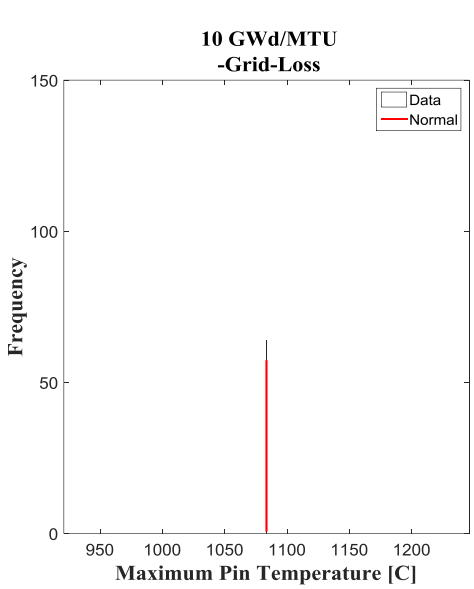
10 GWd/MTU
-Grid-Loss
Data
Normal
Frequency
Maximum Pin Temperature [C]
0
50
100
150
950
1000
1050
1100
1150
1200

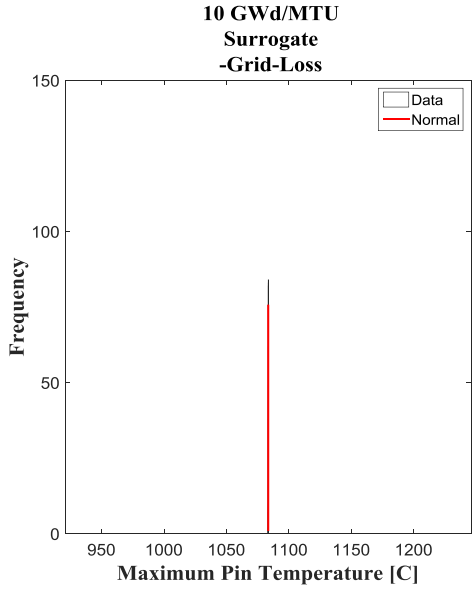
10 GWd/MTU
Surrogate
-Grid-Loss
Data
Normal
Frequency
Maximum Pin Temperature [C]
0
50
100
150
950
1000
1050
1100
1150
1200

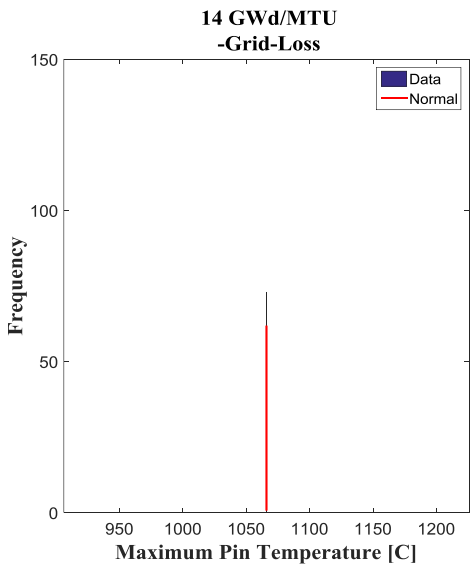
14 GWd/MTU
-Grid-Loss
Data
Normal
Frequency
Maximum Pin Temperature [C]
0
50
100
150
950
1000
1050
1100
1150
1200

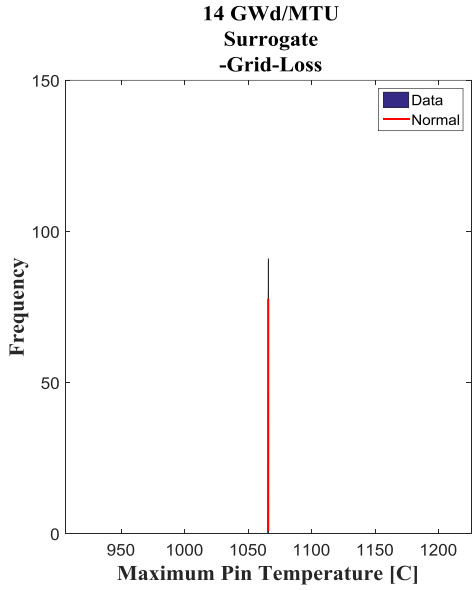
14 GWd/MTU
Surrogate
-Grid-Loss
Data
Normal
Frequency
Maximum Pin Temperature [C]
0
50
100
150
950
1000
1050
1100
1150
1200

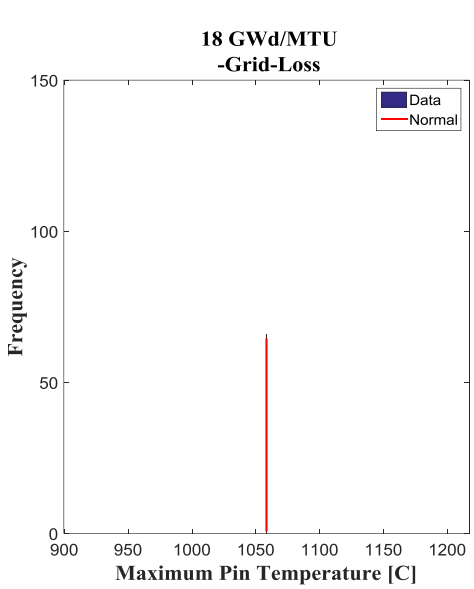
18 GWd/MTU
-Grid-Loss
Data
Normal
Frequency
Maximum Pin Temperature [C]
0
50
100
150
900
950
1000
1050
1100
1150
1200

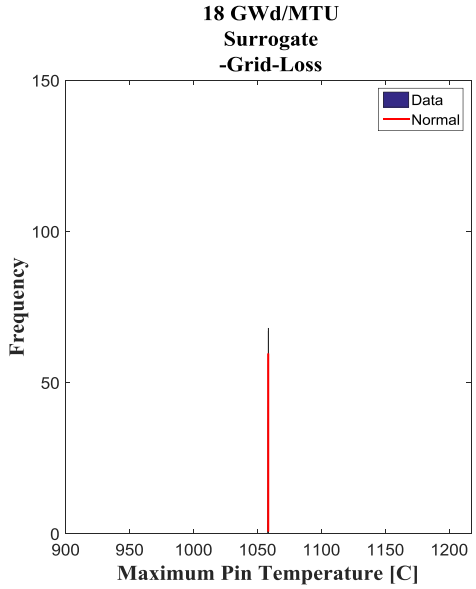
18 GWd/MTU
Surrogate
-Grid-Loss
Data
Normal
Frequency
Maximum Pin Temperature [C]
0
50
100
150
900
950
1000
1050
1100
1150
1200

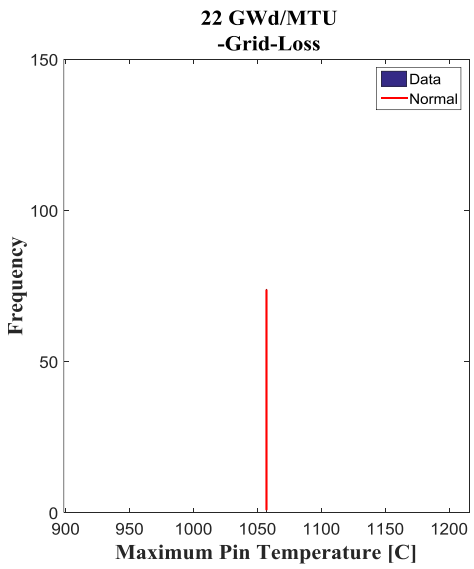
22 GWd/MTU
-Grid-Loss
Data
Normal
Frequency
Maximum Pin Temperature [C]
0
50
100
150
900
950
1000
1050
1100
1150
1200

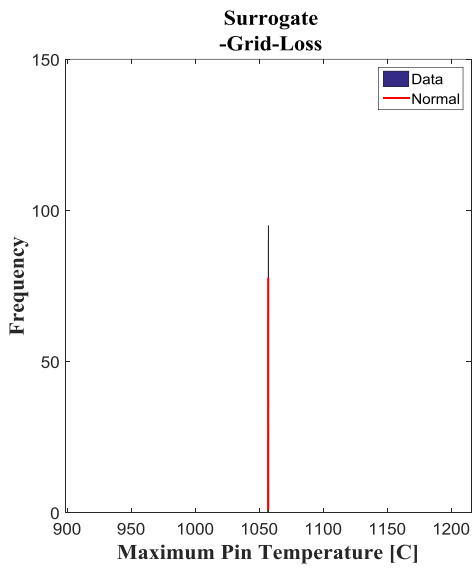
22 GWd/MTU
Surrogate
-Grid-Loss
Data
Normal
Frequency
Maximum Pin Temperature [C]
0
50
100
150
900
950
1000
1050
1100
1150
1200

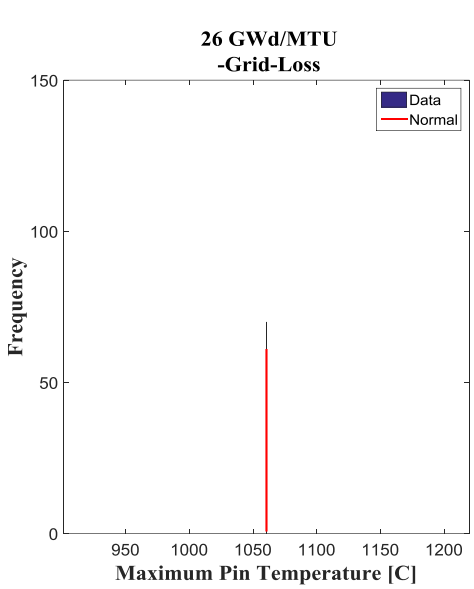
26 GWd/MTU
-Grid-Loss
Data
Normal
Frequency
Maximum Pin Temperature [C]
0
50
100
150
950
1000
1050
1100
1150
1200

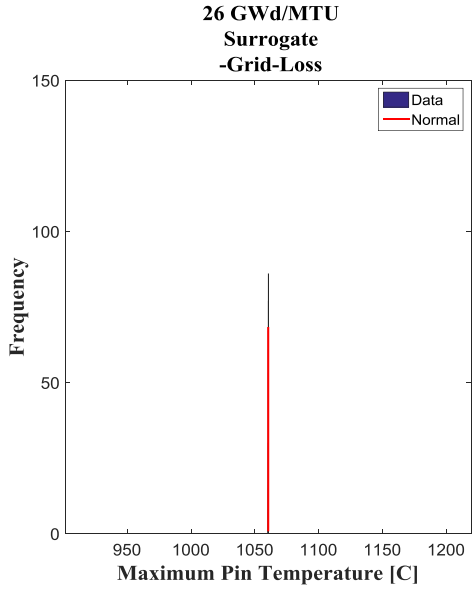
26 GWd/MTU
Surrogate
-Grid-Loss
Data
Normal
Frequency
Maximum Pin Temperature [C]
0
50
100
150
950
1000
1050
1100
1150
1200

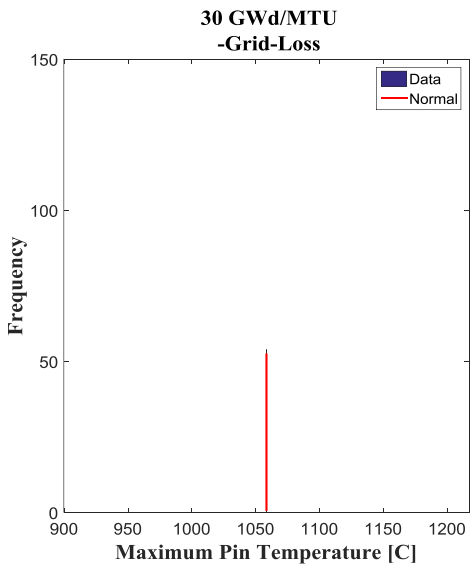
30 GWd/MTU
-Grid-Loss
Data
Normal
Frequency
Maximum Pin Temperature [C]
0
50
100
150
900
950
1000
1050
1100
1150
1200

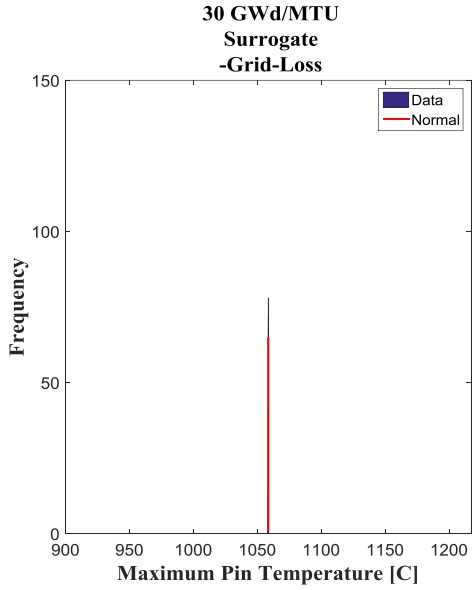
30 GWd/MTU
Surrogate
-Grid-Loss
Data
Normal
Frequency
Maximum Pin Temperature [C]
0
50
100
150
900
950
1000
1050
1100
1150
1200

Figure 104. Statistical sampling k_{eff} corresponding to joint samples. Left: obtained via running VERA-CS right: obtained via the surrogate model.

Joint - k_{eff}

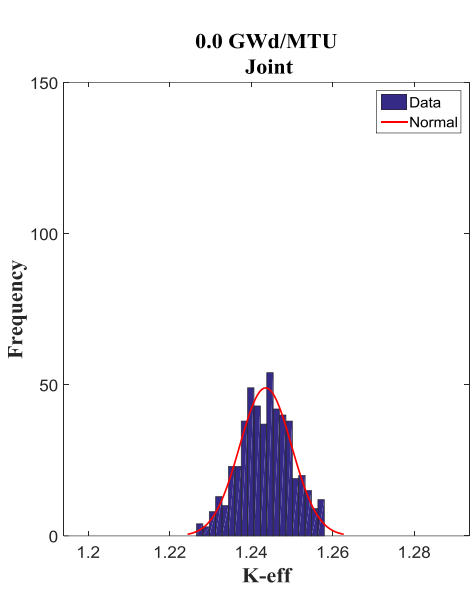
0.0 GWd/MTU
Joint
Data
Normal
Frequency
K-eff
0
50
100
150
1.2
1.22
1.24
1.26
1.28

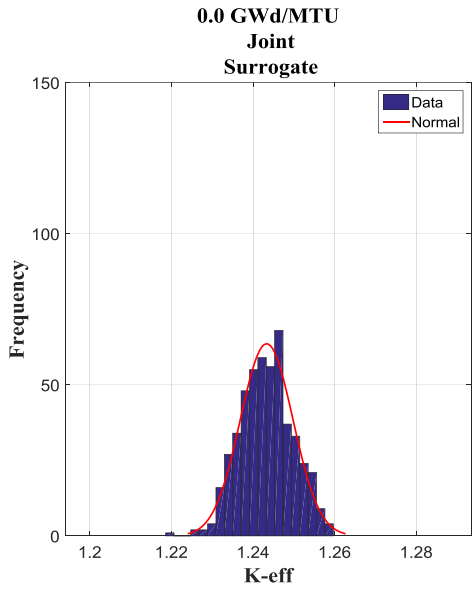
0.0 GWd/MTU
Joint
Surrogate
Data
Normal
Frequency
K-eff
0
50
100
150
1.2
1.22
1.24
1.26
1.28

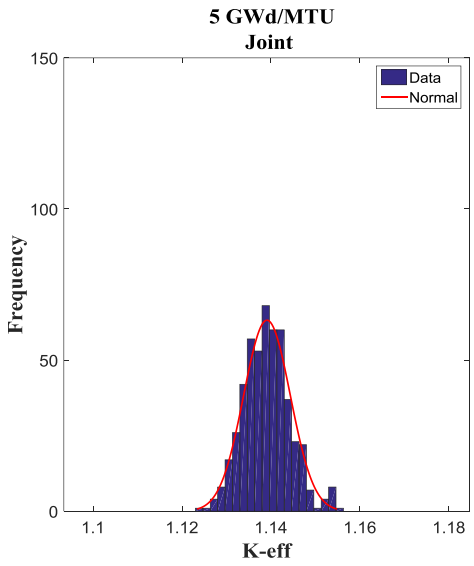
5 GWd/MTU
Joint
Data
Normal
Frequency
K-eff
0
50
100
150
1.1
1.12
1.14
1.16
1.18

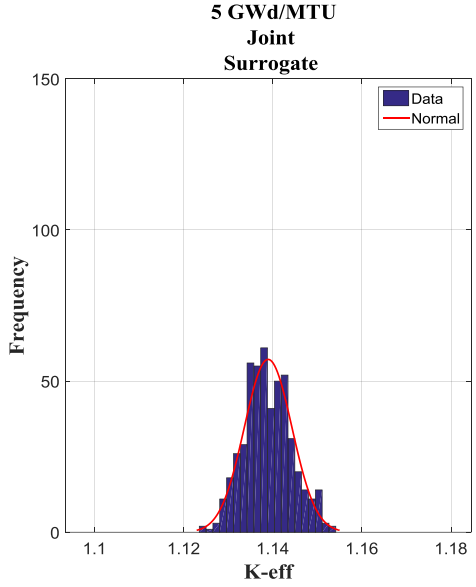
5 GWd/MTU
Joint
Surrogate
Data
Normal
Frequency
K-eff
0
50
100
150
1.1
1.12
1.14
1.16
1.18

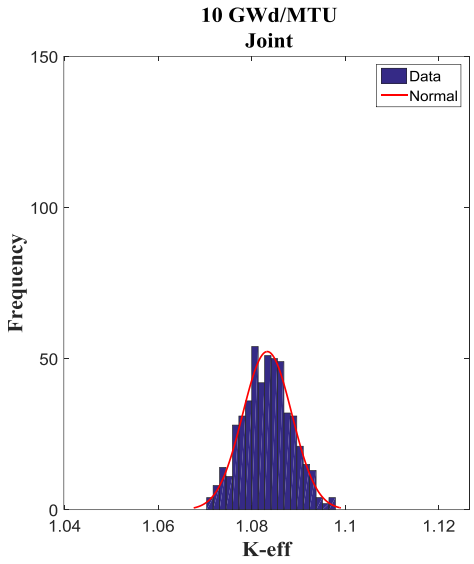
10 GWd/MTU
Joint
Data
Normal
Frequency
K-eff
0
50
100
150
1.04
1.06
1.08
1.1
1.12

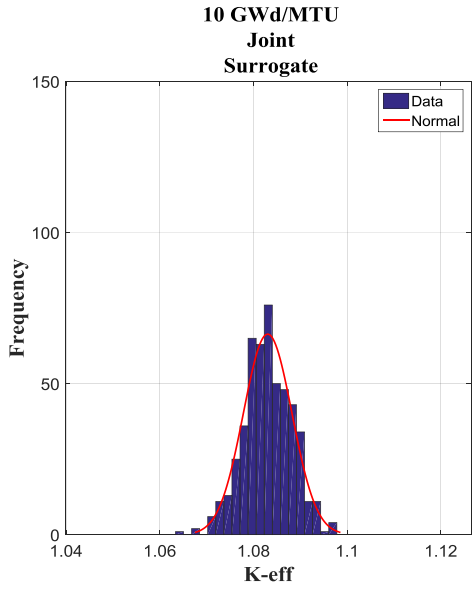
10 GWd/MTU
Joint
Surrogate
Data
Normal
Frequency
K-eff
0
50
100
150
1.04
1.06
1.08
1.1
1.12

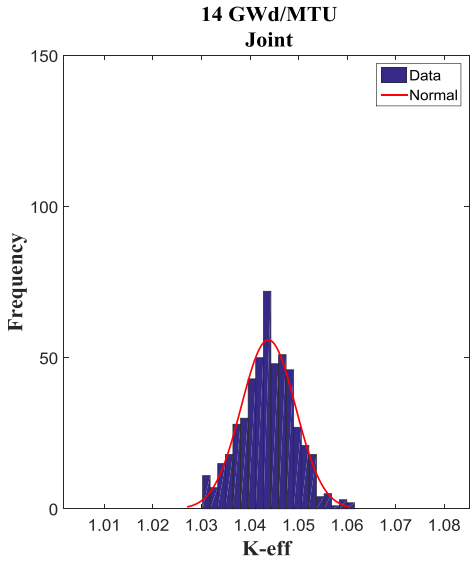
14 GWd/MTU
Joint
Data
Normal
Frequency
K-eff
0
50
100
150
1.01
1.02
1.03
1.04
1.05
1.06
1.07
1.08

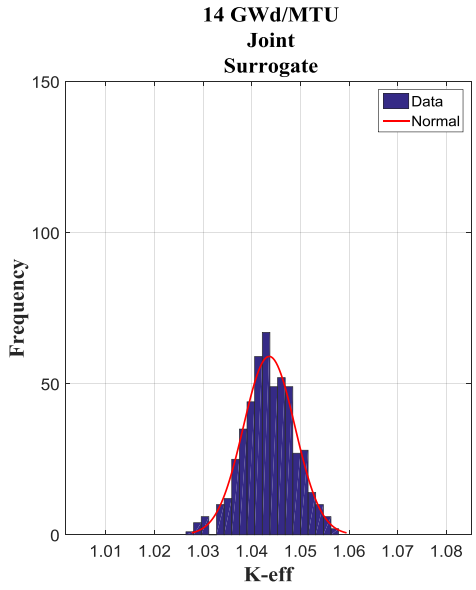
14 GWd/MTU
Joint
Surrogate
Data
Normal
Frequency
K-eff
0
50
100
150
1.01
1.02
1.03
1.04
1.05
1.06
1.07
1.08

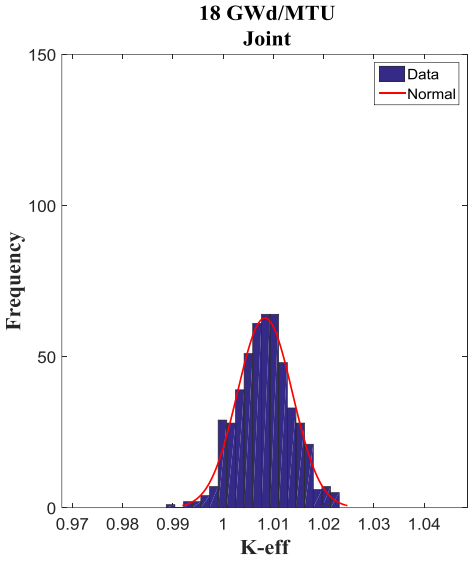
18 GWd/MTU
Joint
Data
Normal
Frequency
K-eff
150
100
50
0
0.97
0.98
0.99
1
1.01
1.02
1.03
1.04

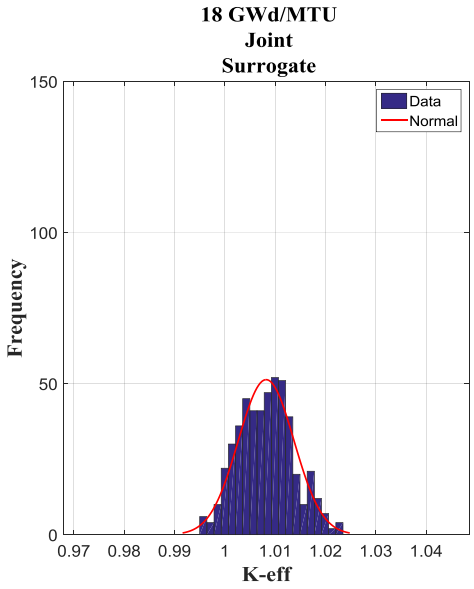
18 GWd/MTU
Joint
Surrogate
Data
Normal
Frequency
K-eff
150
100
50
0
0.97
0.98
0.99
1
1.01
1.02
1.03
1.04

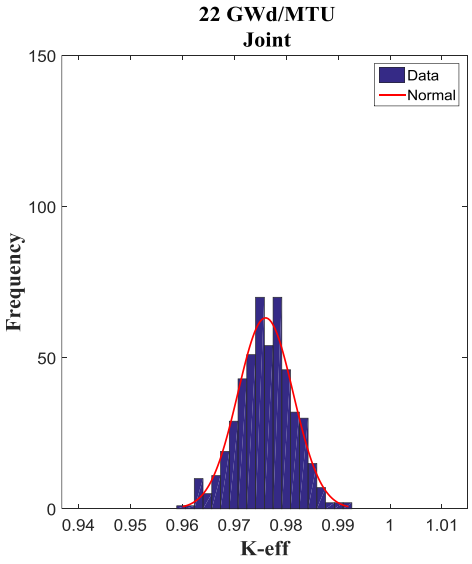
22 GWd/MTU
Joint
Data
Normal
Frequency
K-eff
150
100
50
0
0.94
0.95
0.96
0.97
0.98
0.99
1
1.01

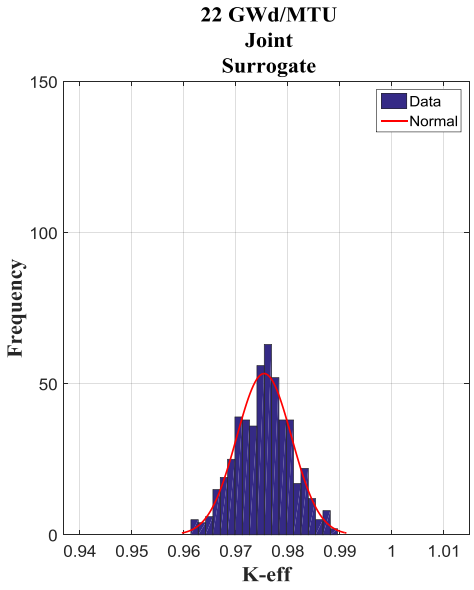
22 GWd/MTU
Joint
Surrogate
Data
Normal
Frequency
K-eff
150
100
50
0
0.94
0.95
0.96
0.97
0.98
0.99
1
1.01

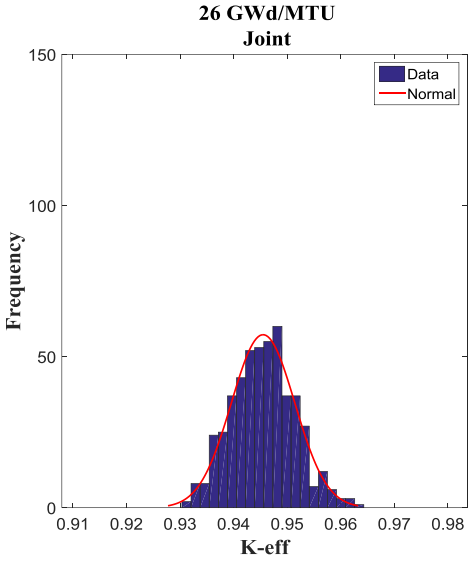
26 GWd/MTU
Joint
Data
Normal
Frequency
K-eff
150
100
50
0
0.91
0.92
0.93
0.94
0.95
0.96
0.97
0.98

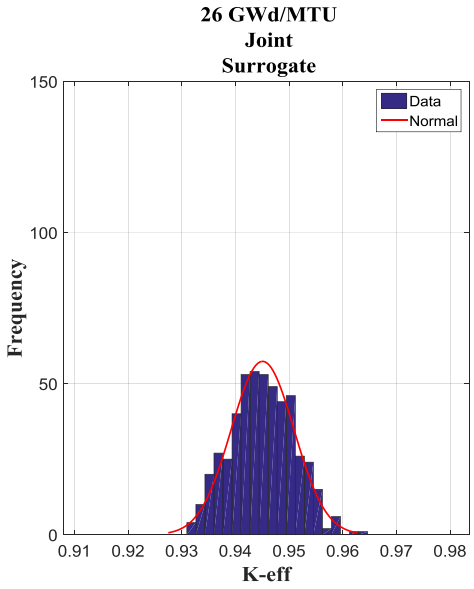
26 GWd/MTU
Joint
Surrogate
Data
Normal
Frequency
K-eff
150
100
50
0
0.91
0.92
0.93
0.94
0.95
0.96
0.97
0.98

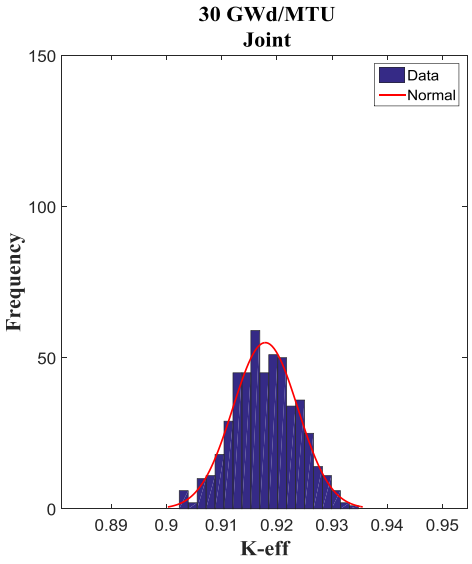
30 GWd/MTU
Joint
Data
Normal
Frequency
K-eff
150
100
50
0
0.89
0.9
0.91
0.92
0.93
0.94
0.95

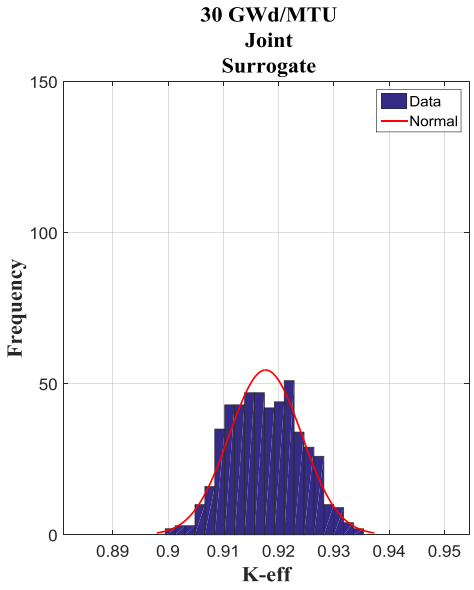
30 GWd/MTU
Joint
Surrogate
Data
Normal
Frequency
K-eff
150
100
50
0
0.89
0.9
0.91
0.92
0.93
0.94
0.95

Figure 105. Statistical sampling maximum pin power corresponding to joint samples. Left: obtained via running VERA-CS right: obtained via the surrogate model.

Joint – *Maximum Pin Power*

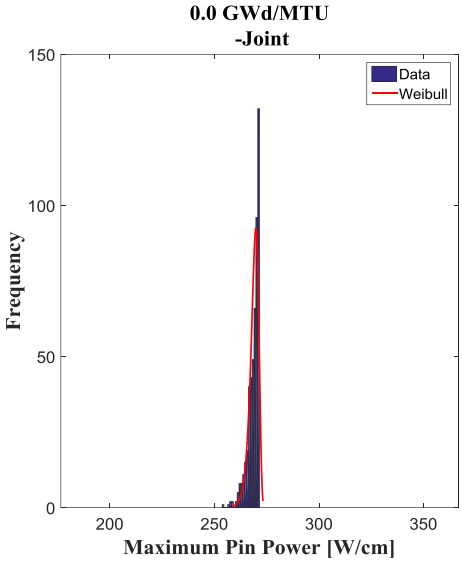
0.0 GWd/MTU
-Joint
Data
Weibull
Frequency
Maximum Pin Power [W/cm]
0
50
100
150
200
250
300
350

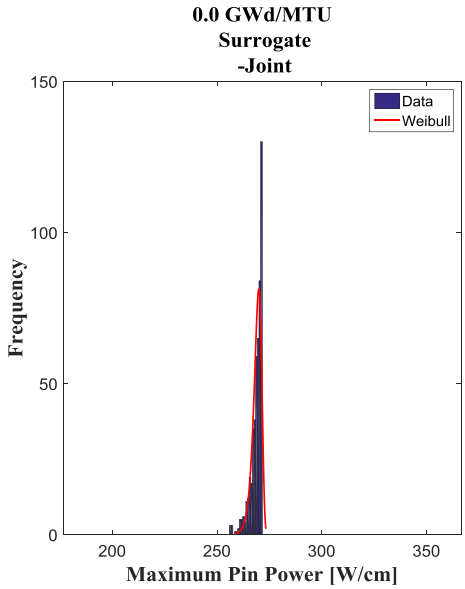
0.0 GWd/MTU
Surrogate
-Joint
Data
Weibull
Frequency
Maximum Pin Power [W/cm]
0
50
100
150
200
250
300
350

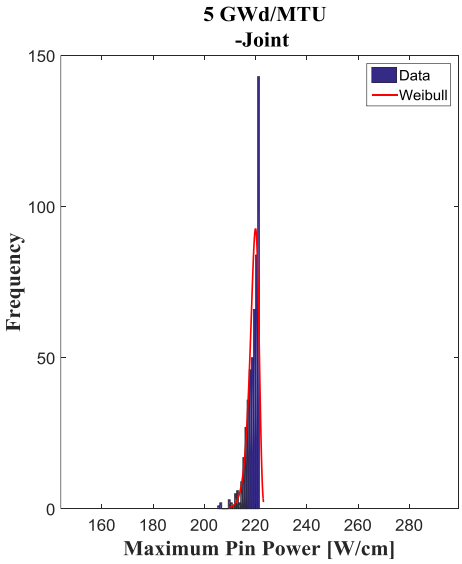
5 GWd/MTU
-Joint
Data
Weibull
Frequency
Maximum Pin Power [W/cm]
0
50
100
150
160
180
200
220
240
260
280

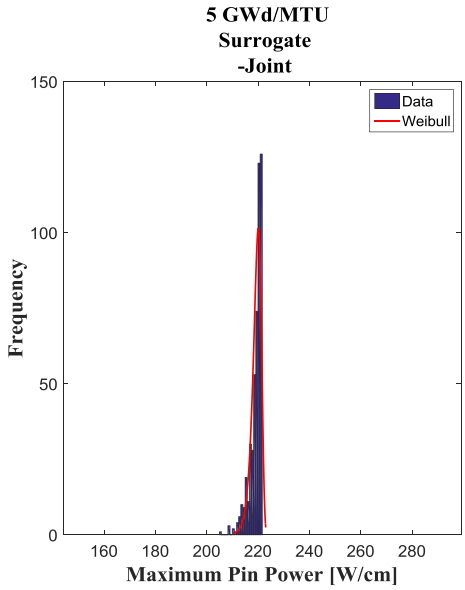
5 GWd/MTU
Surrogate
-Joint
Data
Weibull
Frequency
Maximum Pin Power [W/cm]
0
50
100
150
160
180
200
220
240
260
280

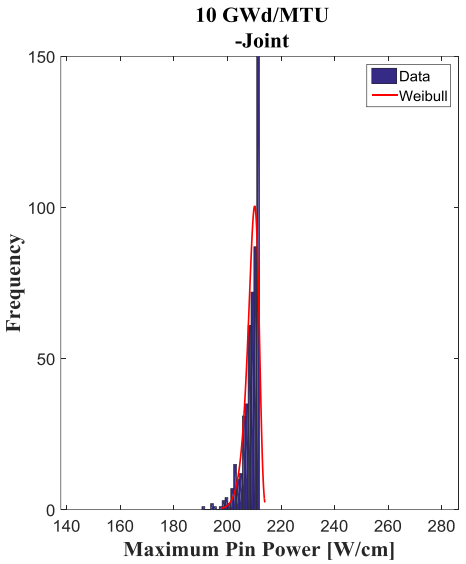
10 GWd/MTU
-Joint
Data
Weibull
Frequency
Maximum Pin Power [W/cm]
0
50
100
150
140
160
180
200
220
240
260
280

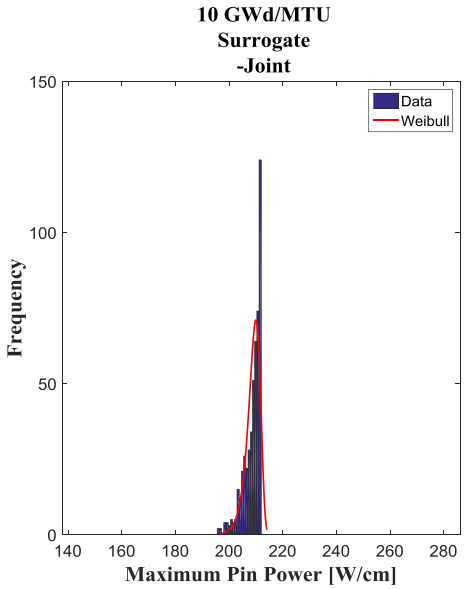
10 GWd/MTU
Surrogate
-Joint
Data
Weibull
Frequency
Maximum Pin Power [W/cm]
0
50
100
150
140
160
180
200
220
240
260
280

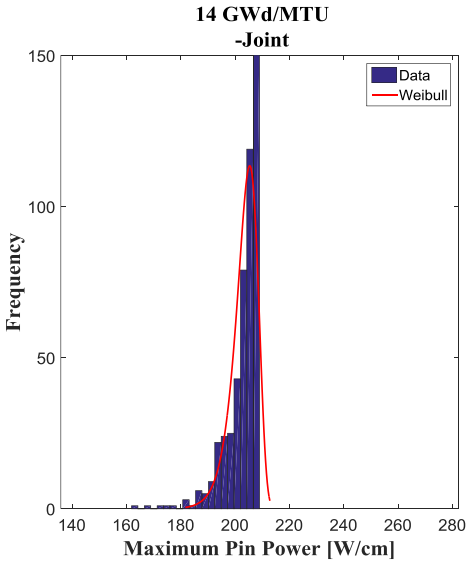
14 GWd/MTU
-Joint
Data
Weibull
Frequency
Maximum Pin Power [W/cm]
0
50
100
150
140
160
180
200
220
240
260
280

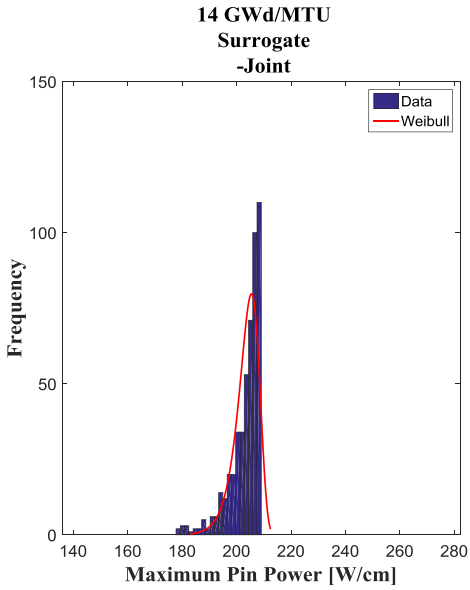
14 GWd/MTU
Surrogate
-Joint
Data
Weibull
Frequency
Maximum Pin Power [W/cm]
0
50
100
150
140
160
180
200
220
240
260
280

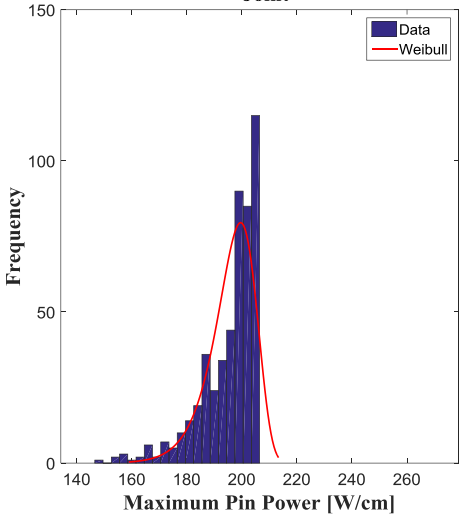
18 GWd/MTU
-Joint
Data
Weibull
Frequency
Maximum Pin Power [W/cm]
0
50
100
150
140
160
180
200
220
240
260

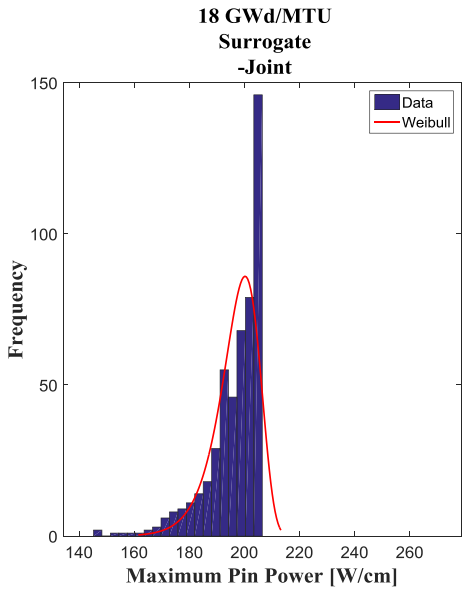
18 GWd/MTU
Surrogate
-Joint
Data
Weibull
Frequency
Maximum Pin Power [W/cm]
0
50
100
150
140
160
180
200
220
240
260

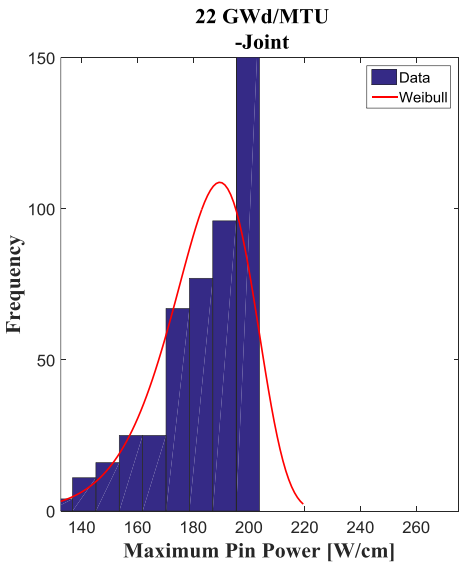
22 GWd/MTU
-Joint
Data
Weibull
Frequency
Maximum Pin Power [W/cm]
0
50
100
150
140
160
180
200
220
240
260

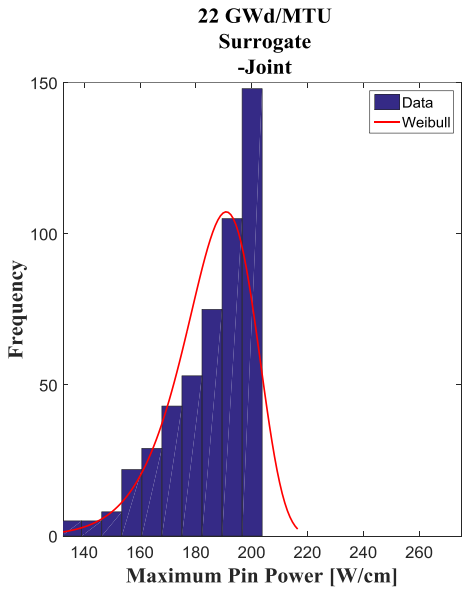
22 GWd/MTU
Surrogate
-Joint
Data
Weibull
Frequency
Maximum Pin Power [W/cm]
0
50
100
150
140
160
180
200
220
240
260

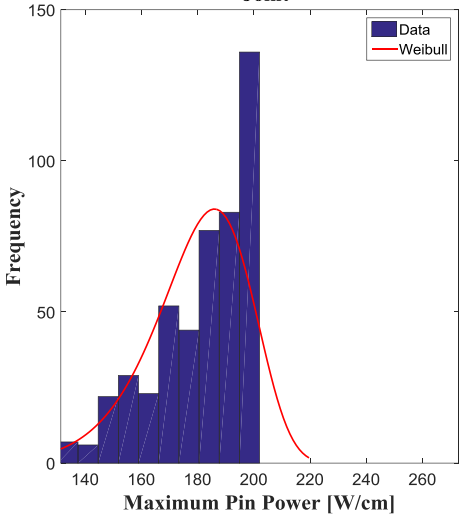
26 GWd/MTU
-Joint
Data
Weibull
Frequency
Maximum Pin Power [W/cm]
0
50
100
150
140
160
180
200
220
240
260

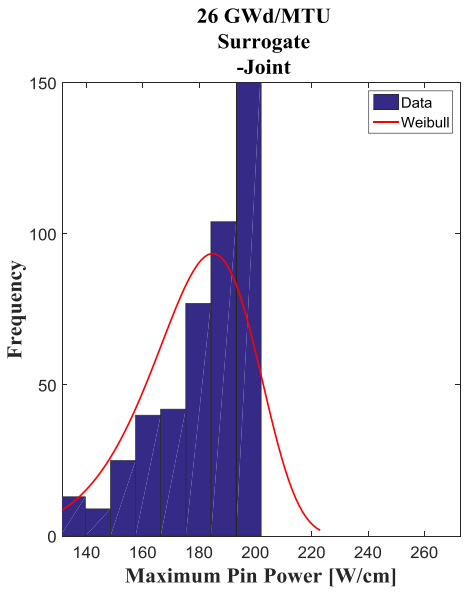
26 GWd/MTU
Surrogate
-Joint
Data
Weibull
Frequency
Maximum Pin Power [W/cm]
0
50
100
150
140
160
180
200
220
240
260

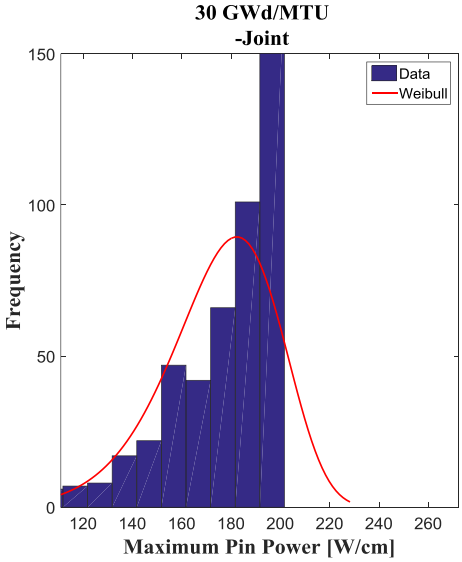
30 GWd/MTU
-Joint
Data
Weibull
Frequency
Maximum Pin Power [W/cm]
0
50
100
150
120
140
160
180
200
220
240
260

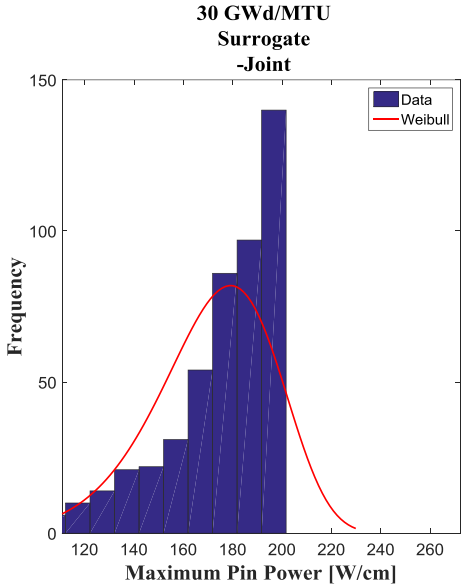
30 GWd/MTU
Surrogate
-Joint
Data
Weibull
Frequency
Maximum Pin Power [W/cm]
0
50
100
150
120
140
160
180
200
220
240
260

Figure 106. Statistical sampling maximum pin temperature corresponding to joint samples. Left: obtained via running VERA-CS right: obtained via the surrogate model.

Joint – Maximum Pin Temperature

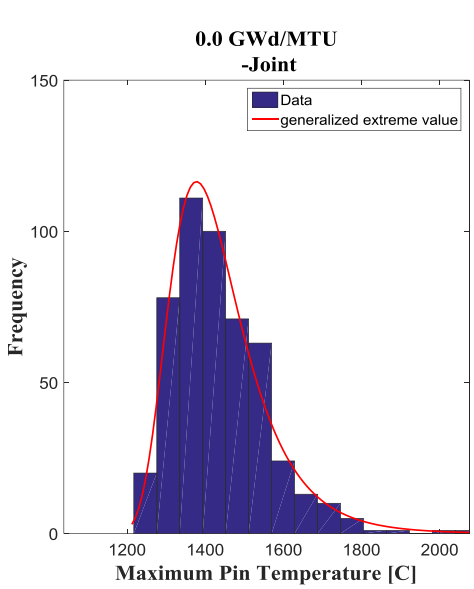
0.0 GWd/MTU
-Joint
Data
generalized extreme value
Frequency
Maximum Pin Temperature [C]
0
50
100
150
1200
1400
1600
1800
2000

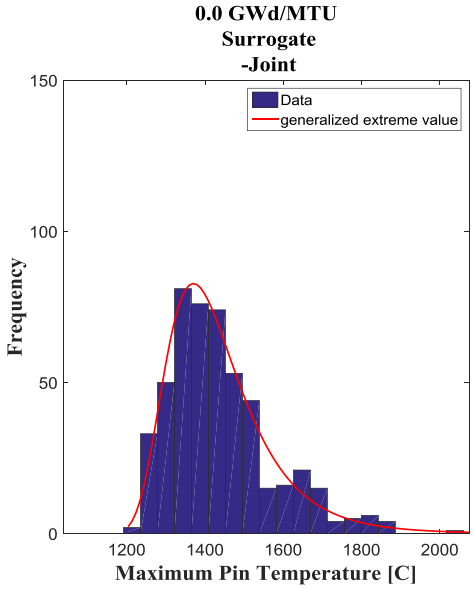
0.0 GWd/MTU
Surrogate
-Joint
Data
generalized extreme value
Frequency
Maximum Pin Temperature [C]
0
50
100
150
1200
1400
1600
1800
2000

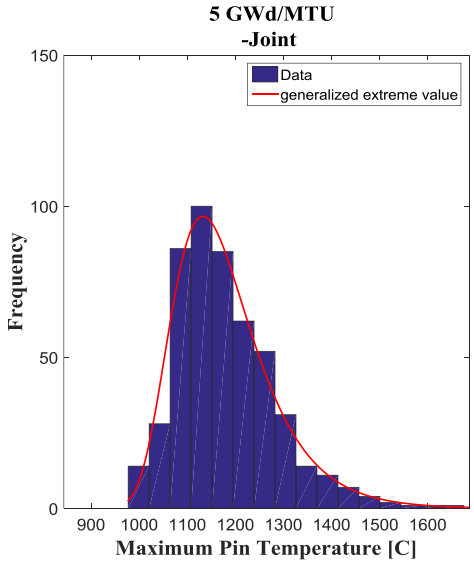
5 GWd/MTU
-Joint
Data
generalized extreme value
Frequency
Maximum Pin Temperature [C]
0
50
100
150
900
1000
1100
1200
1300
1400
1500
1600

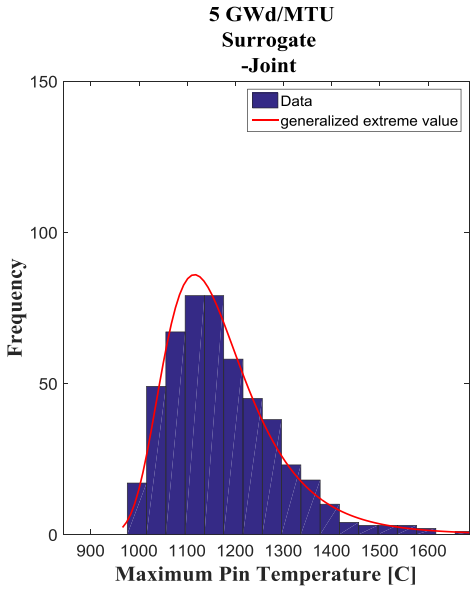
5 GWd/MTU
Surrogate
-Joint
Data
generalized extreme value
Frequency
Maximum Pin Temperature [C]
0
50
100
150
900
1000
1100
1200
1300
1400
1500
1600

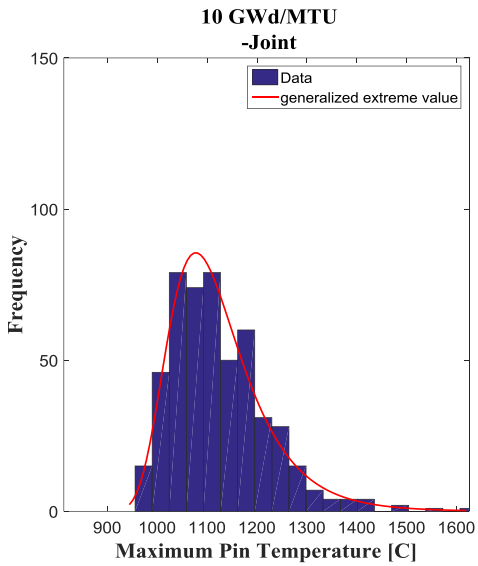
10 GWd/MTU
-Joint
Data
generalized extreme value
Frequency
Maximum Pin Temperature [C]

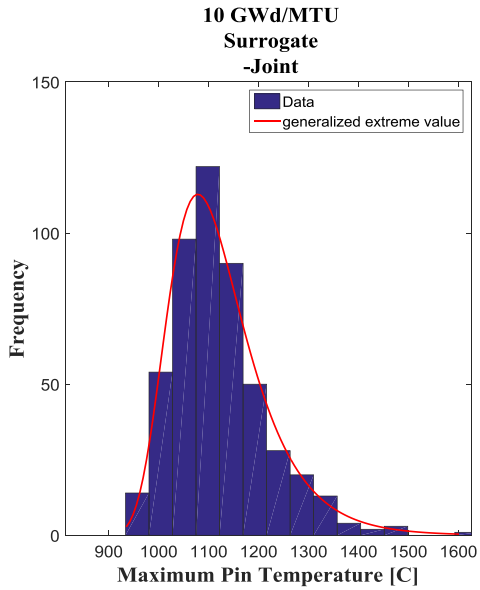
10 GWd/MTU
Surrogate
-Joint
Data
generalized extreme value
Frequency
Maximum Pin Temperature [C]

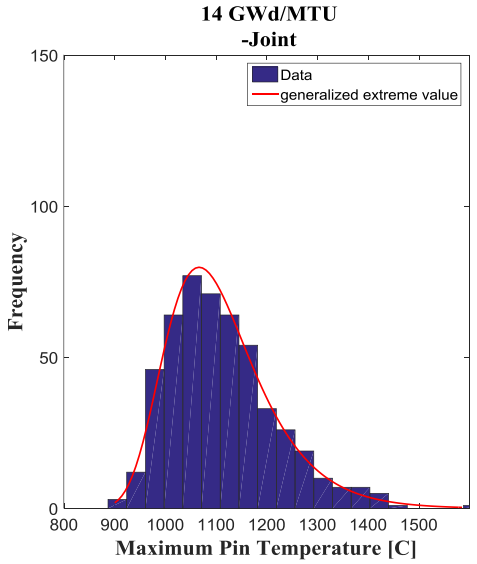
14 GWd/MTU
-Joint
Data
generalized extreme value
Frequency
Maximum Pin Temperature [C]

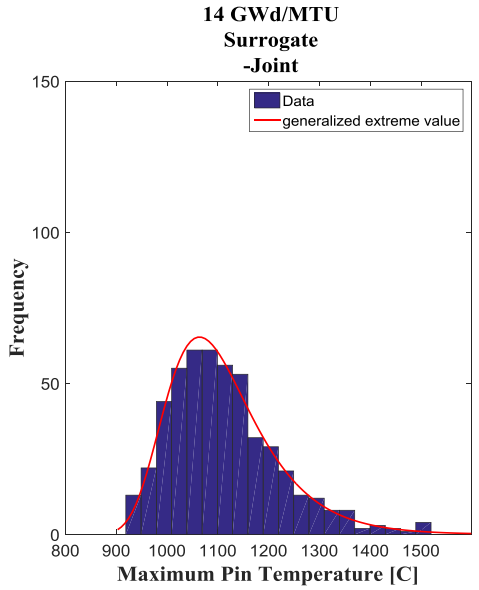
14 GWd/MTU
Surrogate
-Joint
Data
generalized extreme value
Frequency
Maximum Pin Temperature [C]

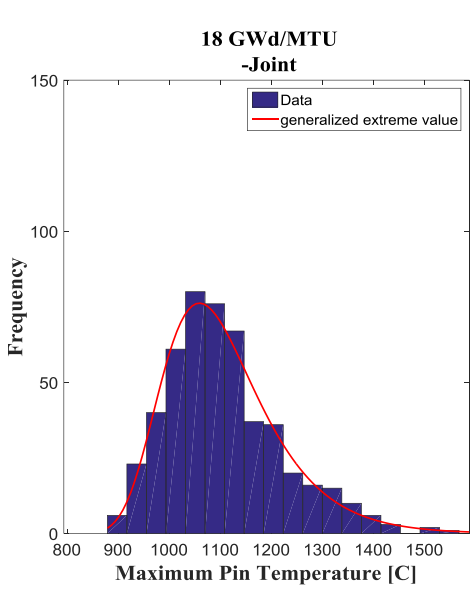
18 GWd/MTU
-Joint
Data
generalized extreme value
Frequency
Maximum Pin Temperature [C]

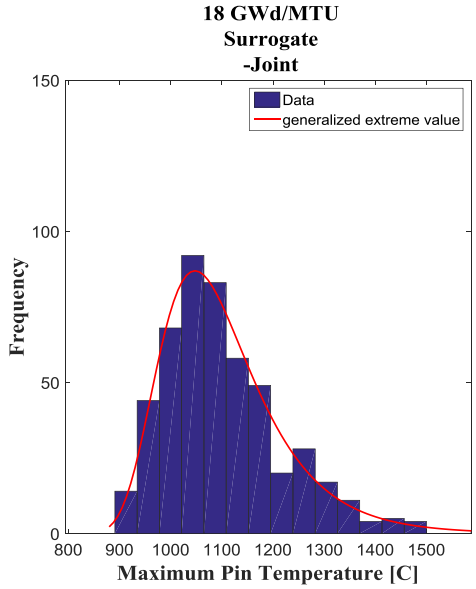
18 GWd/MTU
Surrogate
-Joint
Data
generalized extreme value
Frequency
Maximum Pin Temperature [C]

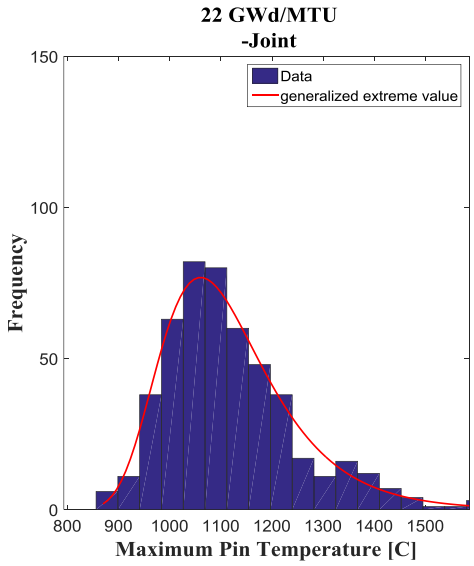
22 GWd/MTU
-Joint
Data
generalized extreme value
Frequency
Maximum Pin Temperature [C]

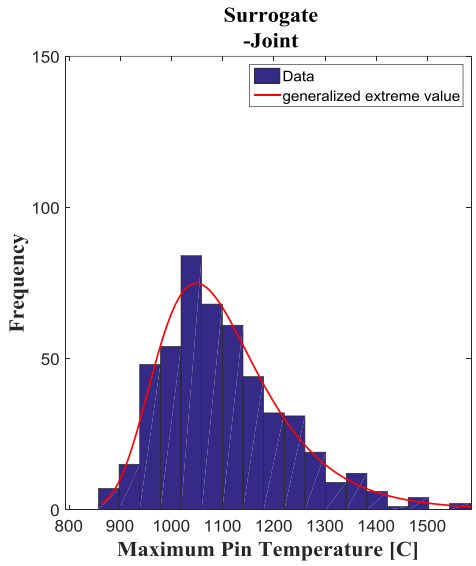
22 GWd/MTU
Surrogate
-Joint
Data
generalized extreme value
Frequency
Maximum Pin Temperature [C]

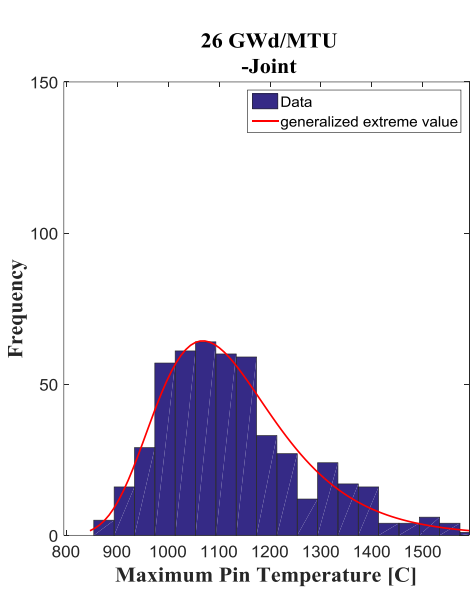
26 GWd/MTU
-Joint
Data
generalized extreme value
Frequency
Maximum Pin Temperature [C]
0
50
100
150
800
900
1000
1100
1200
1300
1400
1500

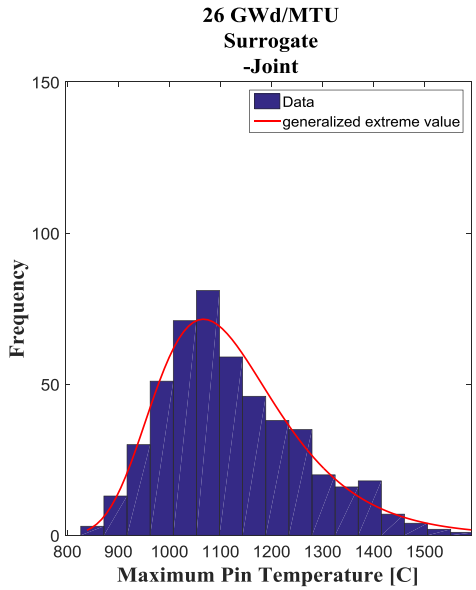
26 GWd/MTU
Surrogate
-Joint
Data
generalized extreme value
Frequency
Maximum Pin Temperature [C]
0
50
100
150
800
900
1000
1100
1200
1300
1400
1500

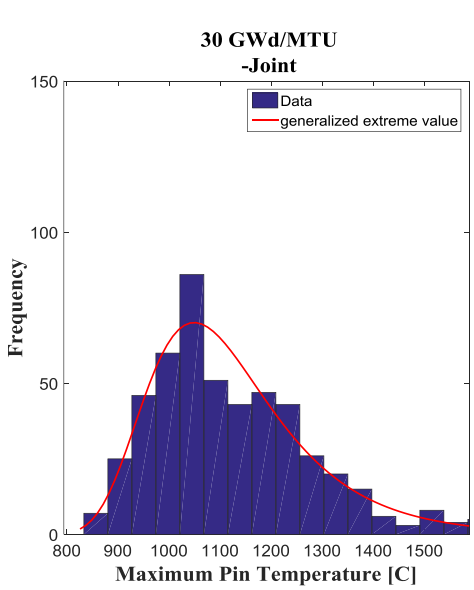
30 GWd/MTU
-Joint
Data
generalized extreme value
Frequency
Maximum Pin Temperature [C]
0
50
100
150
800
900
1000
1100
1200
1300
1400
1500

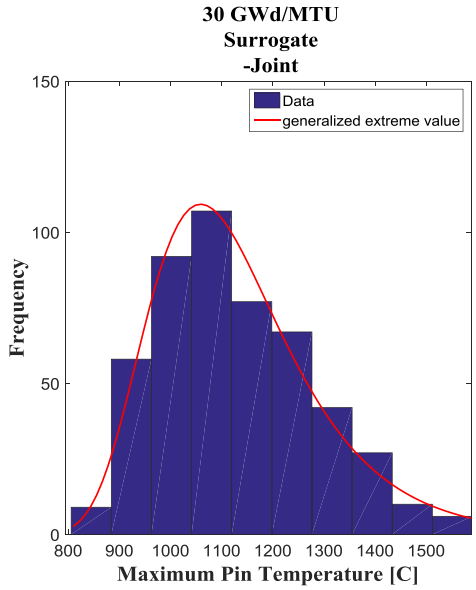
30 GWd/MTU
Surrogate
-Joint
Data
generalized extreme value
Frequency
Maximum Pin Temperature [C]
0
50
100
150
800
900
1000
1100
1200
1300
1400
1500

Appendix B

Frequency Distributions for the Multiplication Factor, Maximum Fuel Pin Power, Maximum Fuel Pin Temperature – CASL Progression Problem 9

Figure 107. Statistical sampling maximum pin power corresponding to samples of the Gap Conductivity, Grid-loss Coefficient, Cross- Sections and joint. Left: obtained via running VERA-CS right: obtained via the surrogate model.

Gap Conductivity [*hgap* W/m^2K], Grid-loss Coefficient, Cross- Sections and joint samples $\rightarrow k_{eff}$

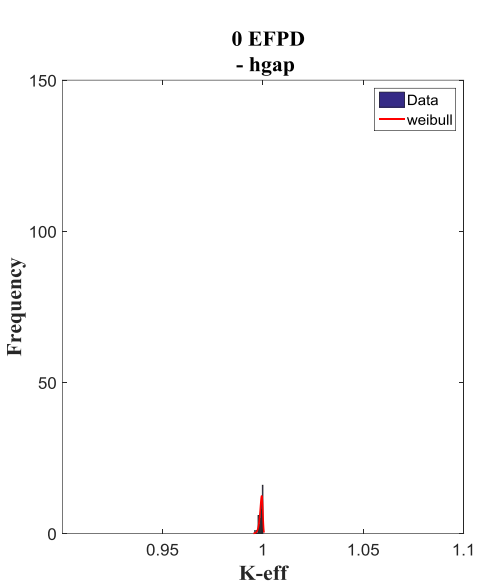
0 EFPD
- hgap
Data
weibull
Frequency
K-eff
0
50
100
150
0.95
1
1.05
1.1

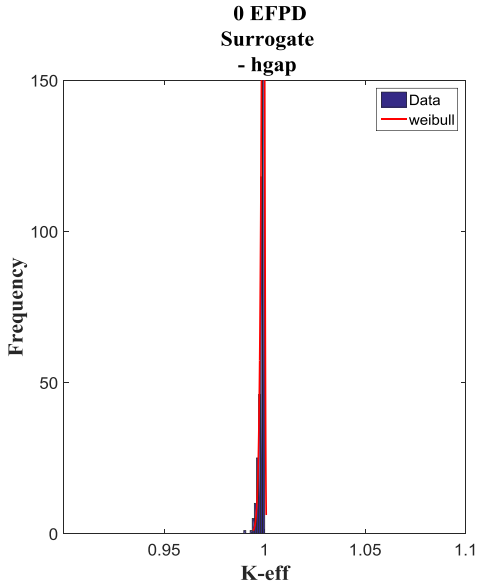
0 EFPD
Surrogate
- hgap
Data
weibull
Frequency
K-eff
0
50
100
150
0.95
1
1.05
1.1

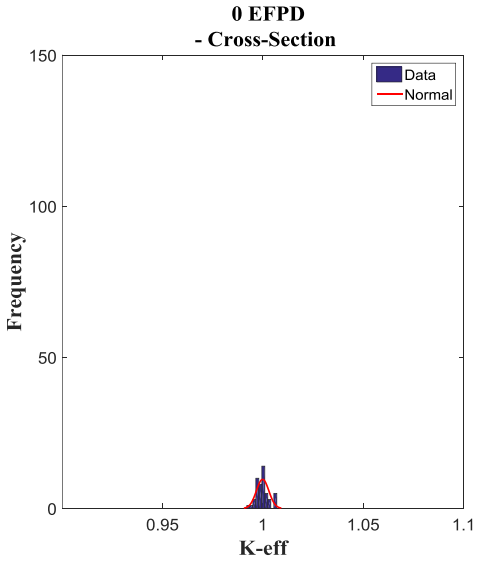
0 EFPD
- Cross-Section
Data
Normal
Frequency
K-eff
0
50
100
150
0.95
1
1.05
1.1

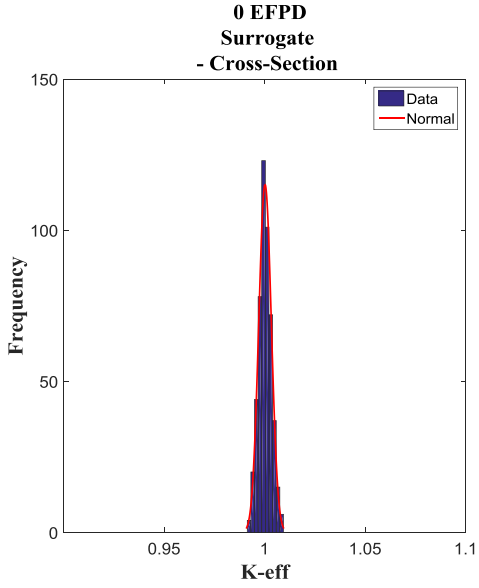
0 EFPD
Surrogate
- Cross-Section
Data
Normal
Frequency
K-eff
0
50
100
150
0.95
1
1.05
1.1

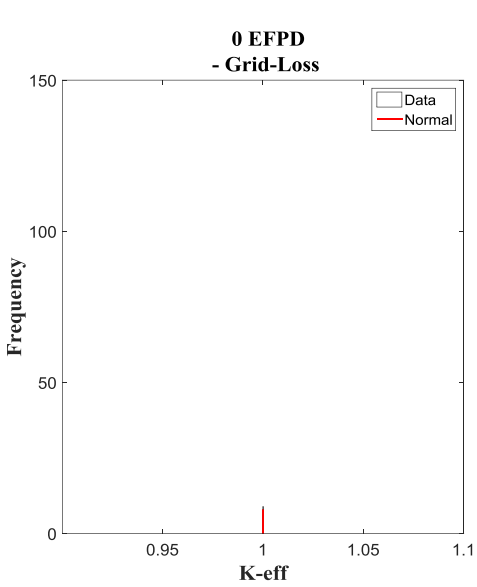
0 EFPD
- Grid-Loss
Data
Normal
Frequency
K-eff
0
50
100
150
0.95
1
1.05
1.1

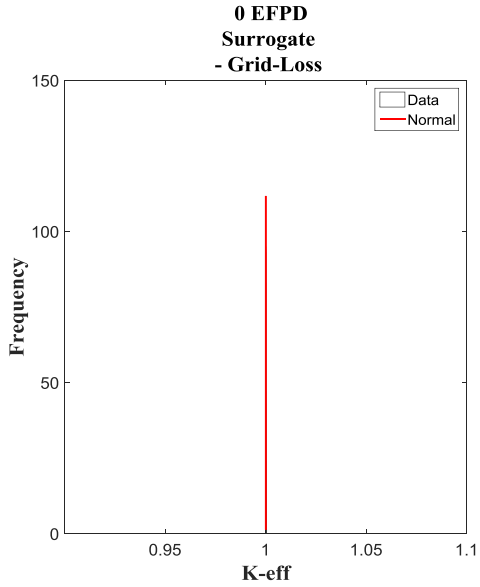
0 EFPD
Surrogate
- Grid-Loss
Data
Normal
Frequency
K-eff
0
50
100
150
0.95
1
1.05
1.1

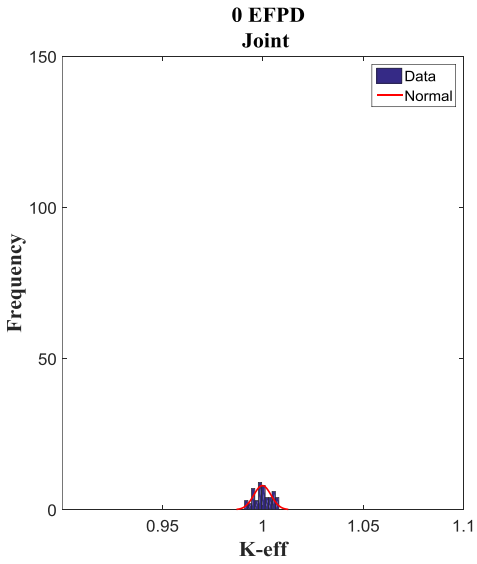
0 EFPD
Joint
Data
Normal
Frequency
K-eff
0
50
100
150
0.95
1
1.05
1.1

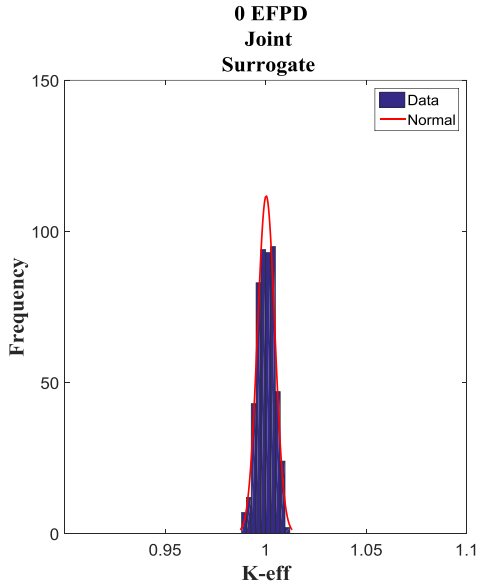
0 EFPD
Joint
Surrogate
Data
Normal
Frequency
K-eff
0
50
100
150
0.95
1
1.05
1.1

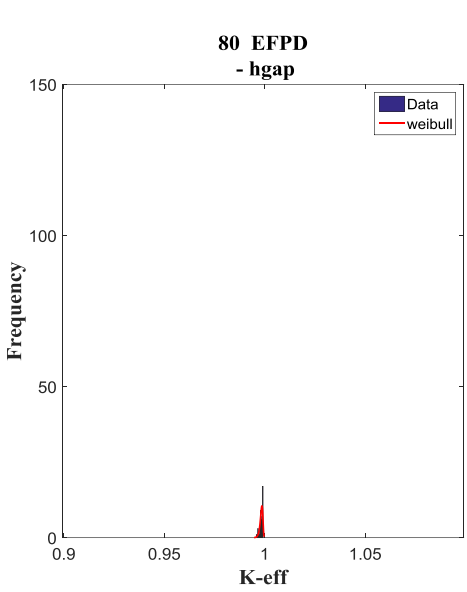
80 EFPD
- hgap
Data
weibull
Frequency
K-eff
0
50
100
150
0.9
0.95
1
1.05

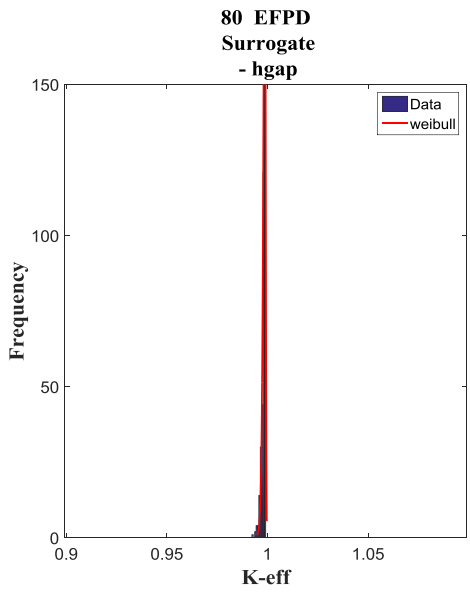
80 EFPD
Surrogate
- hgap
Data
weibull
Frequency
K-eff
0
50
100
150
0.9
0.95
1
1.05

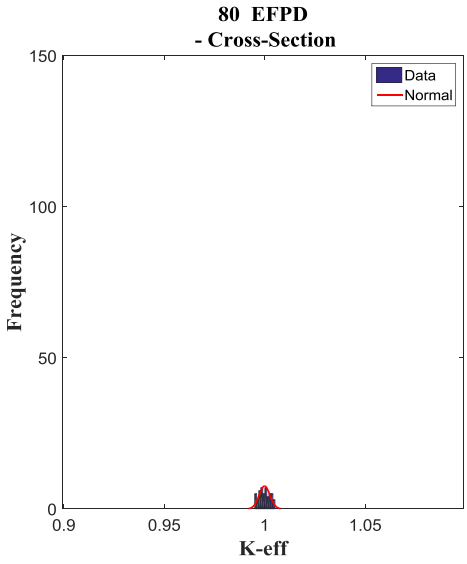
80 EFPD
- Cross-Section
Data
Normal
Frequency
K-eff
0
50
100
150
0.9
0.95
1
1.05

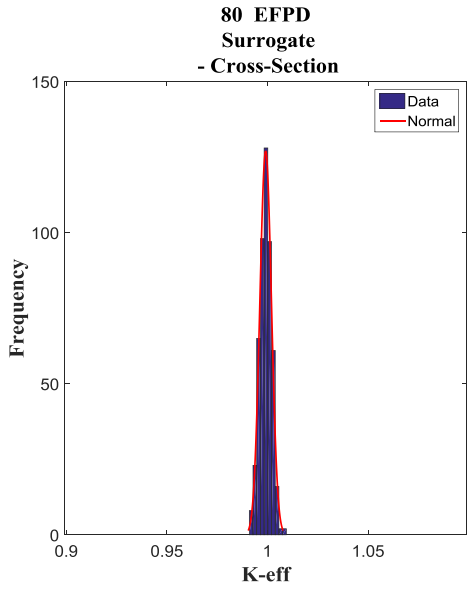
80 EFPD
Surrogate
- Cross-Section
Data
Normal
Frequency
K-eff
0
50
100
150
0.9
0.95
1
1.05

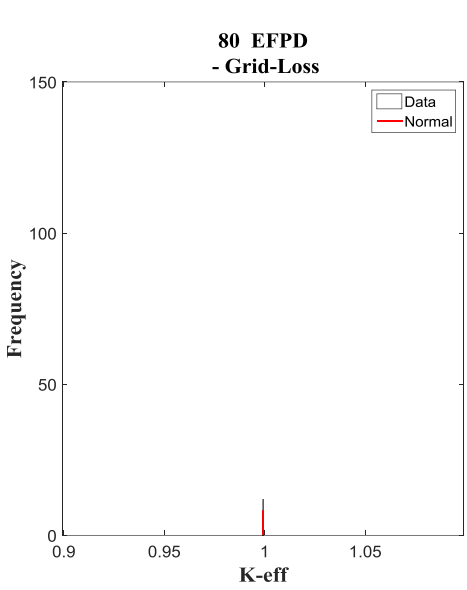
80 EFPD
- Grid-Loss
Data
Normal
Frequency
K-eff
0
50
100
150
0.9
0.95
1
1.05

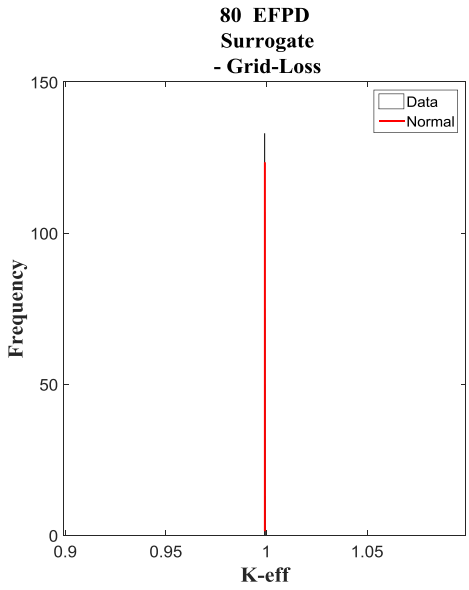
80 EFPD
Surrogate
- Grid-Loss
Data
Normal
Frequency
K-eff
0
50
100
150
0.9
0.95
1
1.05

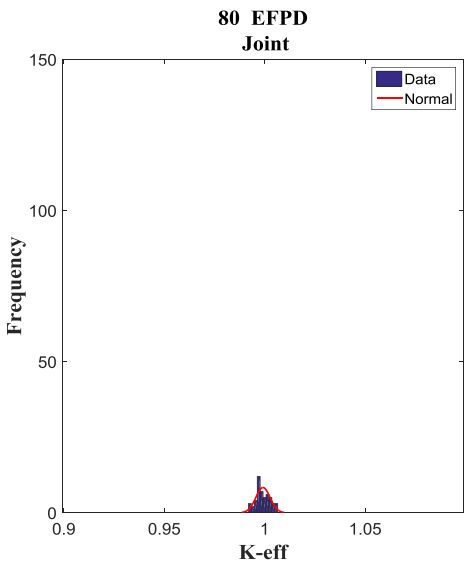
80 EFPD
Joint
Data
Normal
Frequency
K-eff
0
50
100
150
0.9
0.95
1
1.05

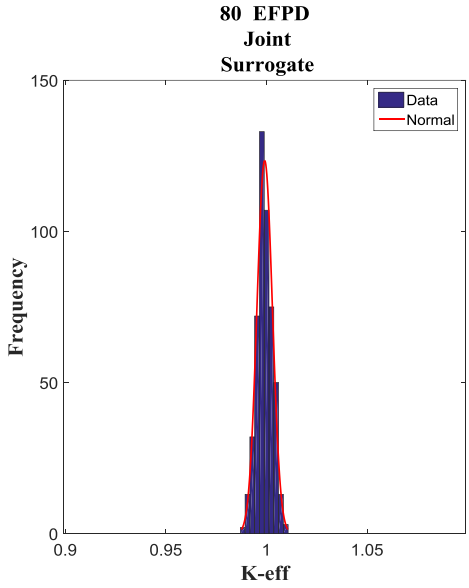
80 EFPD
Joint
Surrogate
Data
Normal
Frequency
K-eff
0
50
100
150
0.9
0.95
1
1.05

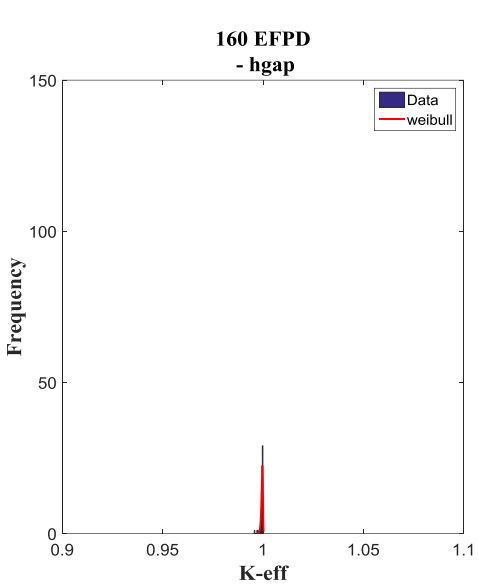
160 EFPD
- hgap
Data
weibull
Frequency
K-eff
0
50
100
150
0.9
0.95
1
1.05
1.1

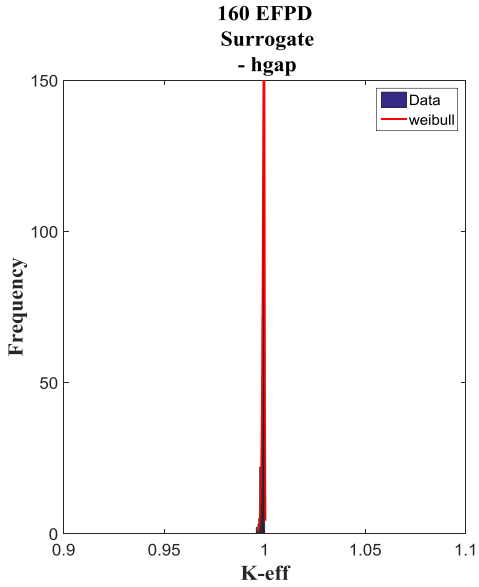
160 EFPD
Surrogate
- hgap
Data
weibull
Frequency
K-eff
0
50
100
150
0.9
0.95
1
1.05
1.1

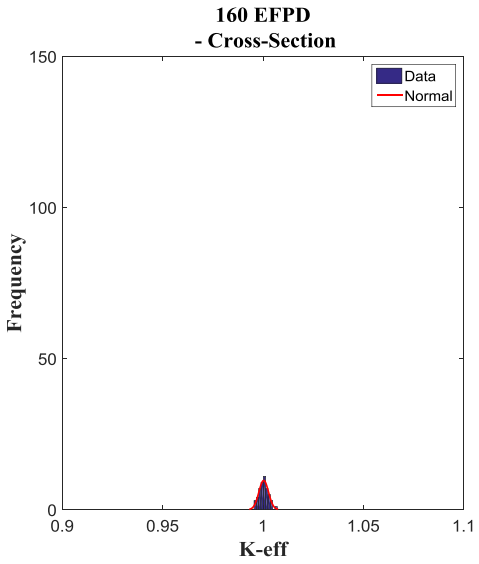
160 EFPD
- Cross-Section
Data
Normal
Frequency
K-eff
0
50
100
150
0.9
0.95
1
1.05
1.1

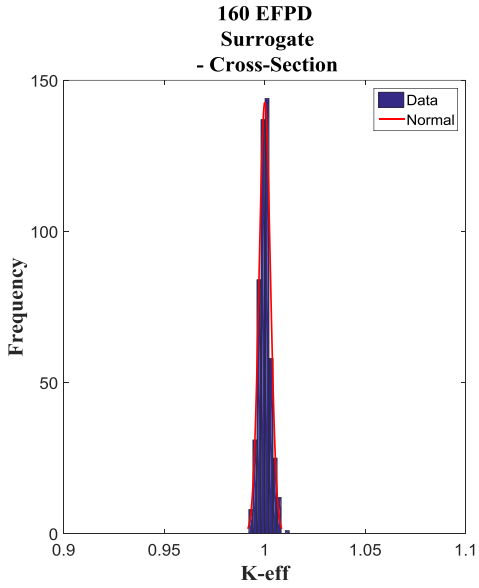
160 EFPD
Surrogate
- Cross-Section
Data
Normal
Frequency
K-eff
0
50
100
150
0.9
0.95
1
1.05
1.1

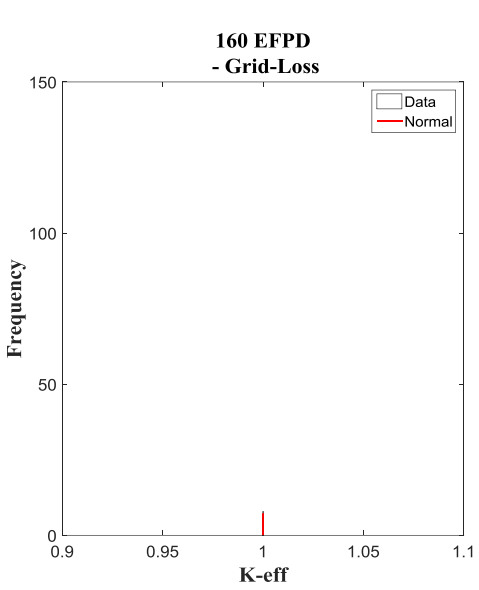
160 EFPD
- Grid-Loss
Data
Normal
Frequency
K-eff
0
50
100
150
0.9
0.95
1
1.05
1.1

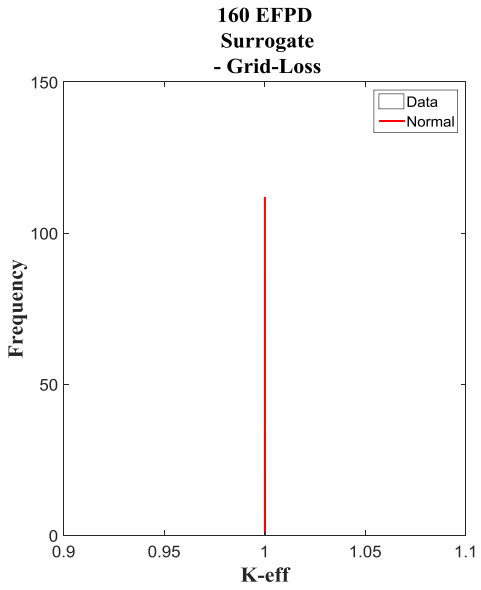
160 EFPD
Surrogate
- Grid-Loss
Data
Normal
Frequency
K-eff
0
50
100
150
0.9
0.95
1
1.05
1.1

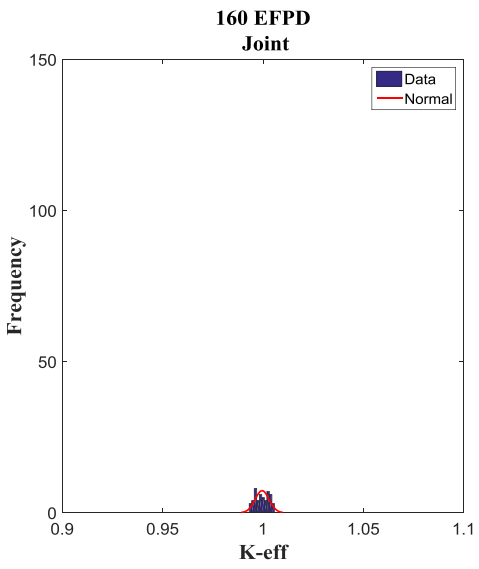
160 EFPD
Joint
Data
Normal
Frequency
K-eff
0
50
100
150
0.9
0.95
1
1.05
1.1

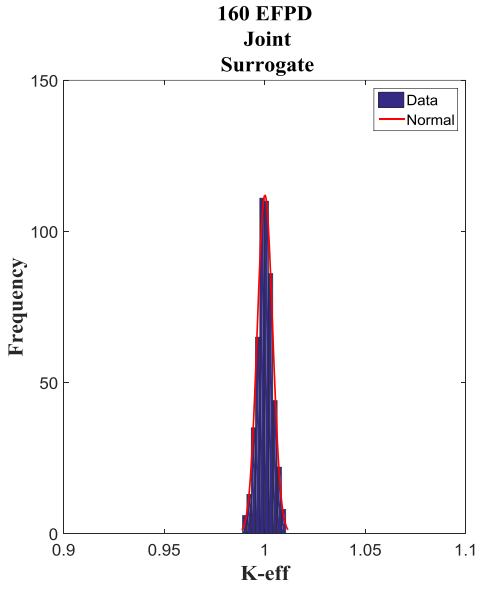
160 EFPD
Joint
Surrogate
Data
Normal
Frequency
K-eff
0
50
100
150
0.9
0.95
1
1.05
1.1

Figure 108. Statistical sampling maximum pin power corresponding to samples of the Gap Conductivity, Grid-loss Coefficient, Cross- Sections and joint. Left: obtained via running VERA-CS right: obtained via the surrogate model.

Gap Conductivity [*hgap* W/m^2K], Grid-loss Coefficient, Cross- Sections and joint samples → *Maximum Pin Power*

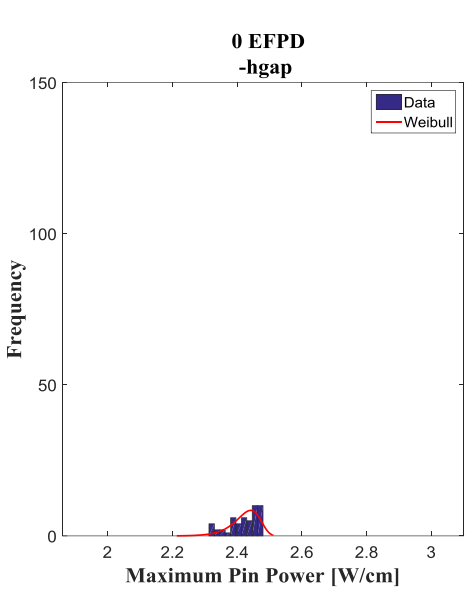
0 EFPD
-hgap
Data
Weibull
Frequency
Maximum Pin Power [W/cm]
0
50
100
150
2
2.2
2.4
2.6
2.8
3

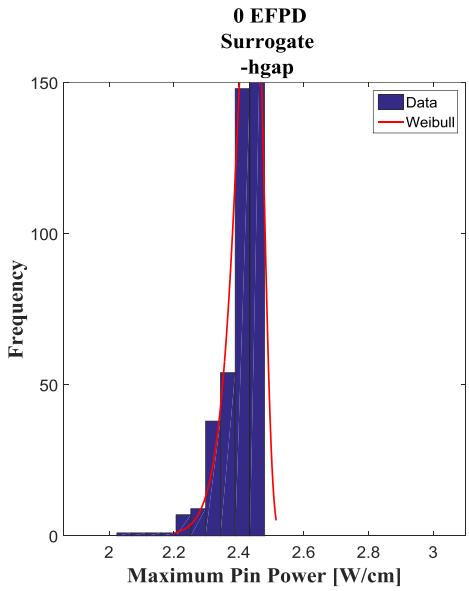
0 EFPD
Surrogate
-hgap
Data
Weibull
Frequency
Maximum Pin Power [W/cm]
0
50
100
150
2
2.2
2.4
2.6
2.8
3

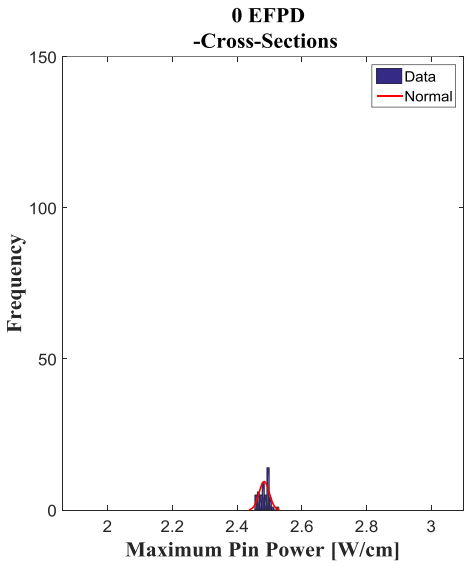
0 EFPD
-Cross-Sections
Data
Normal
Frequency
Maximum Pin Power [W/cm]
0
50
100
150
2
2.2
2.4
2.6
2.8
3

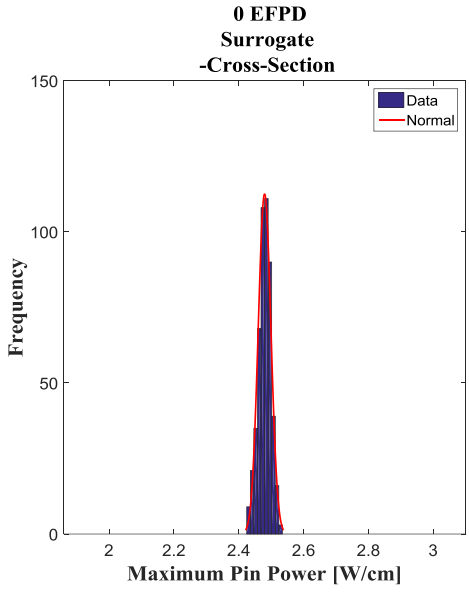
0 EFPD
Surrogate
-Cross-Section
Data
Normal
Frequency
Maximum Pin Power [W/cm]
0
50
100
150
2
2.2
2.4
2.6
2.8
3

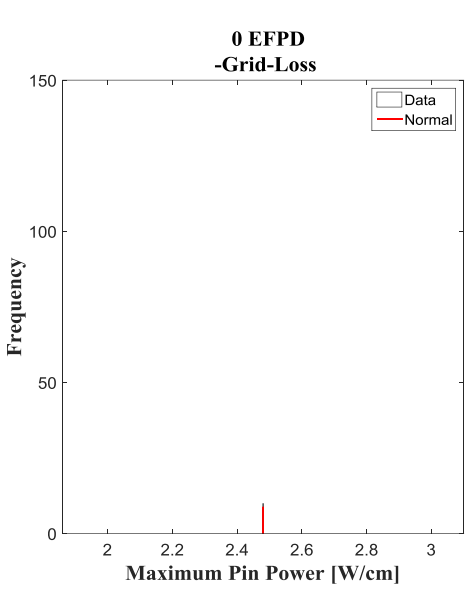
0 EFPD
-Grid-Loss
Data
Normal
Frequency
Maximum Pin Power [W/cm]

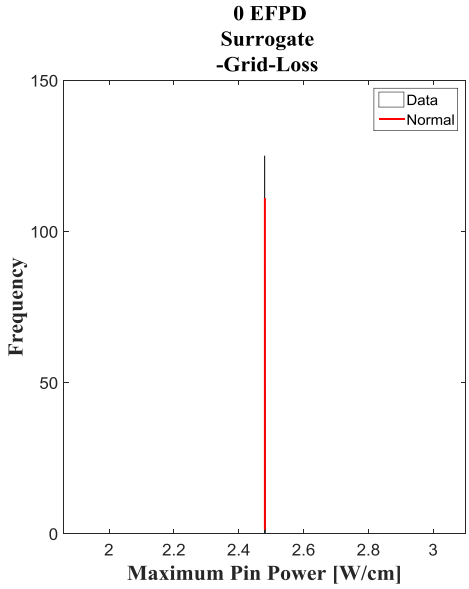
0 EFPD
Surrogate
-Grid-Loss
Data
Normal
Frequency
Maximum Pin Power [W/cm]

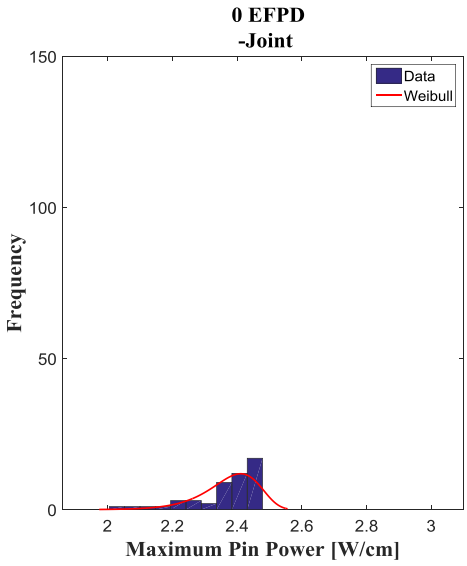
0 EFPD
-Joint
Data
Weibull
Frequency
Maximum Pin Power [W/cm]

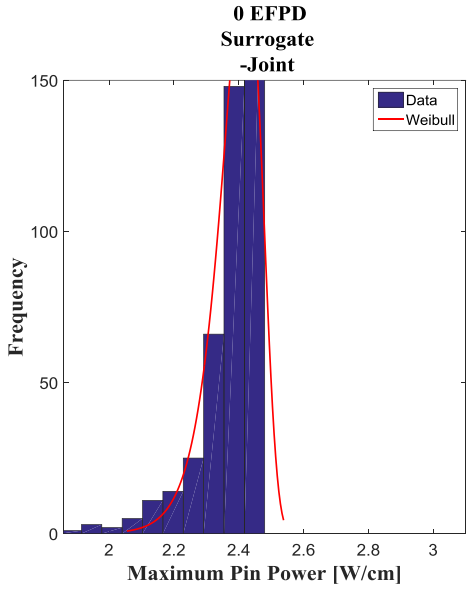
0 EFPD
Surrogate
-Joint
Data
Weibull
Frequency
Maximum Pin Power [W/cm]

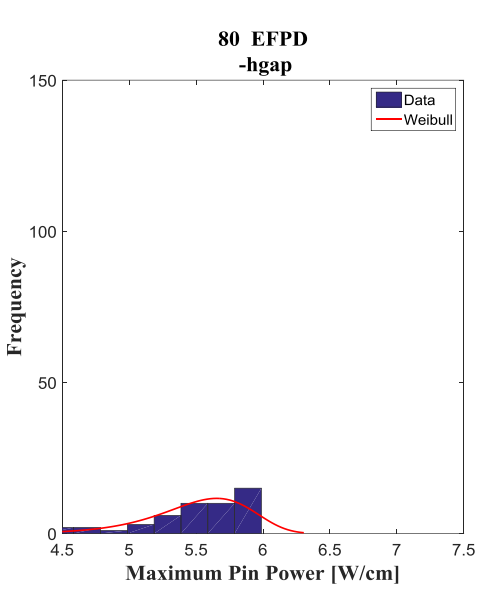
80 EFPD
-hgap
Data
Weibull
Frequency
Maximum Pin Power [W/cm]
0
50
100
150
4.5
5
5.5
6
6.5
7
7.5

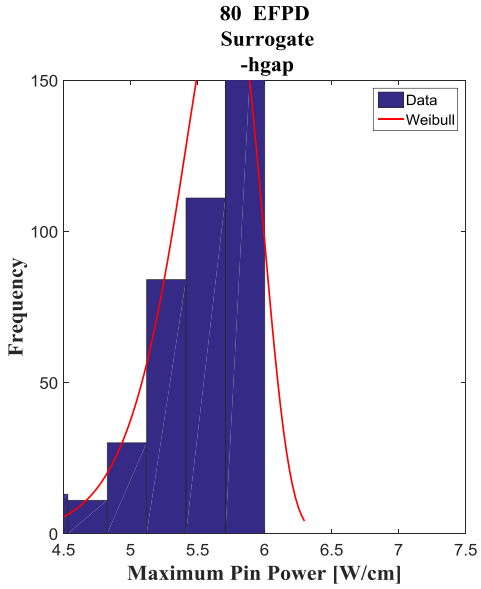
80 EFPD
Surrogate
-hgap
Data
Weibull
Frequency
Maximum Pin Power [W/cm]
0
50
100
150
4.5
5
5.5
6
6.5
7
7.5

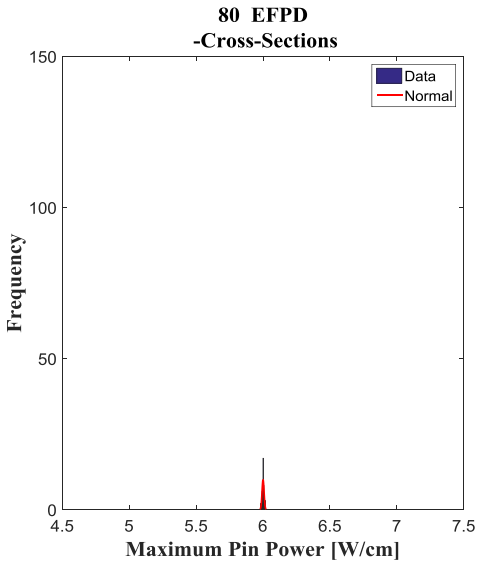
80 EFPD
-Cross-Sections
Data
Normal
Frequency
Maximum Pin Power [W/cm]
0
50
100
150
4.5
5
5.5
6
6.5
7
7.5

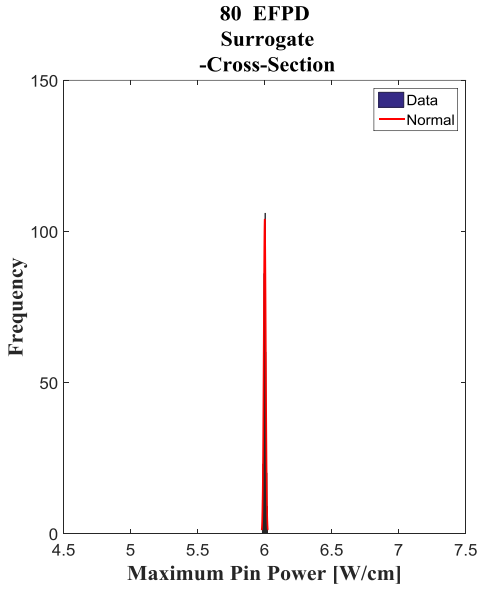
80 EFPD
Surrogate
-Cross-Section
Data
Normal
Frequency
Maximum Pin Power [W/cm]
0
50
100
150
4.5
5
5.5
6
6.5
7
7.5

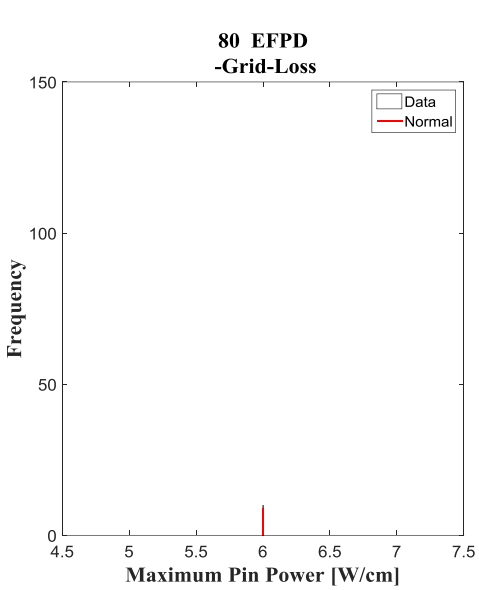
80 EFPD
-Grid-Loss
Data
Normal
Frequency
Maximum Pin Power [W/cm]
0
50
100
150
4.5
5
5.5
6
6.5
7
7.5

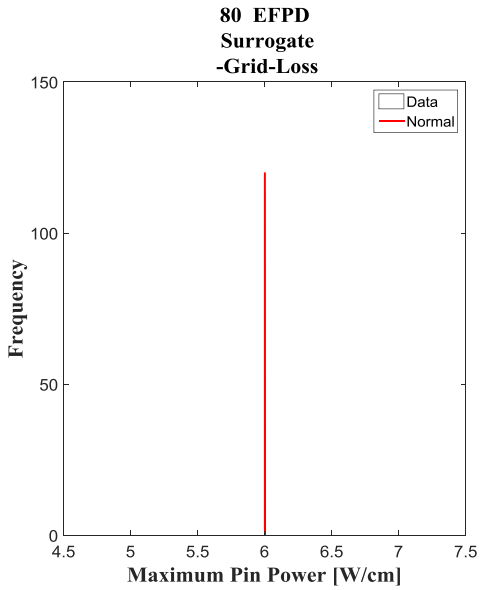
80 EFPD
Surrogate
-Grid-Loss
Data
Normal
Frequency
Maximum Pin Power [W/cm]
0
50
100
150
4.5
5
5.5
6
6.5
7
7.5

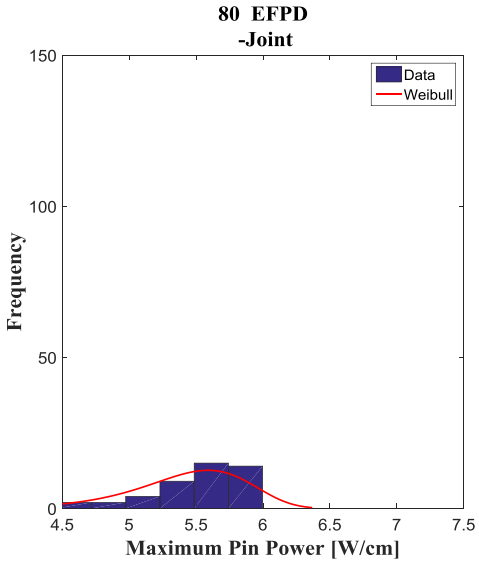
80 EFPD
-Joint
Data
Weibull
Frequency
Maximum Pin Power [W/cm]
0
50
100
150
4.5
5
5.5
6
6.5
7
7.5

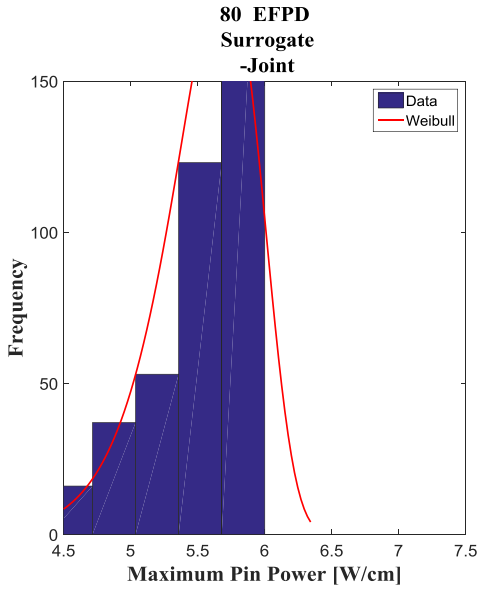
80 EFPD
Surrogate
-Joint
Data
Weibull
Frequency
Maximum Pin Power [W/cm]
0
50
100
150
4.5
5
5.5
6
6.5
7
7.5

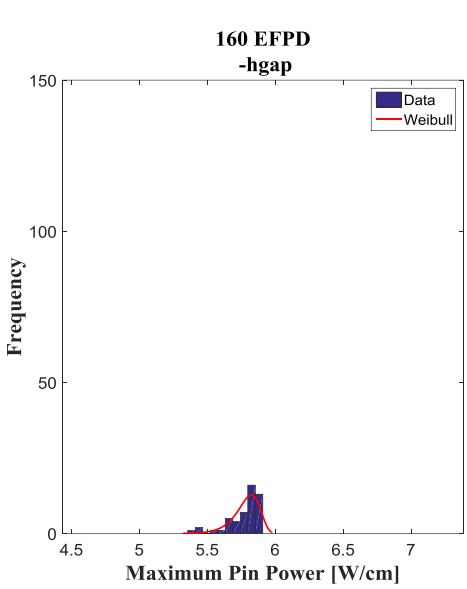
160 EFPD
-hgap
Data
Weibull
Frequency
Maximum Pin Power [W/cm]
0
50
100
150
4.5
5
5.5
6
6.5
7

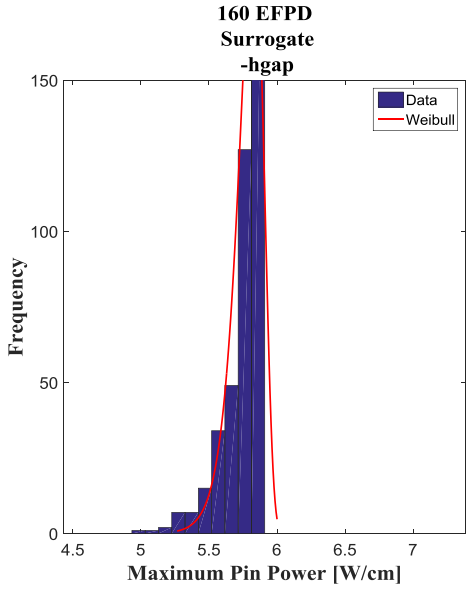
160 EFPD
Surrogate
-hgap
Data
Weibull
Frequency
Maximum Pin Power [W/cm]
0
50
100
150
4.5
5
5.5
6
6.5
7

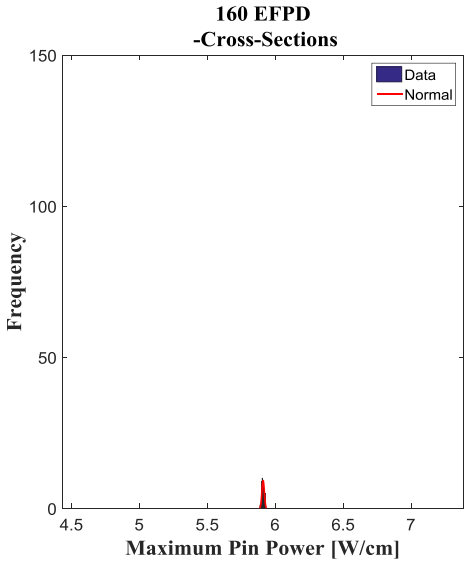
160 EFPD
-Cross-Sections
Data
Normal
Frequency
Maximum Pin Power [W/cm]
0
50
100
150
4.5
5
5.5
6
6.5
7

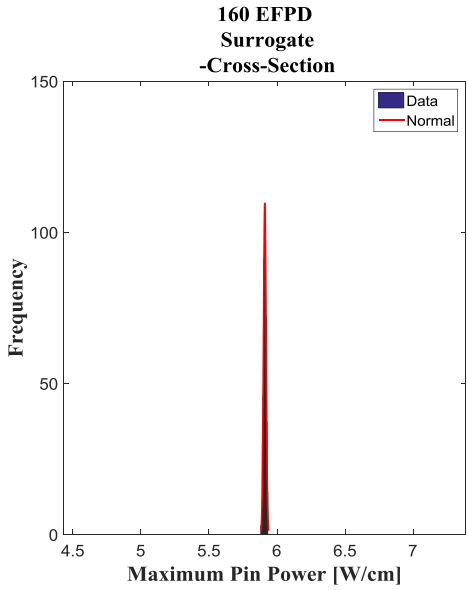
160 EFPD
Surrogate
-Cross-Section
Data
Normal
Frequency
Maximum Pin Power [W/cm]
0
50
100
150
4.5
5
5.5
6
6.5
7

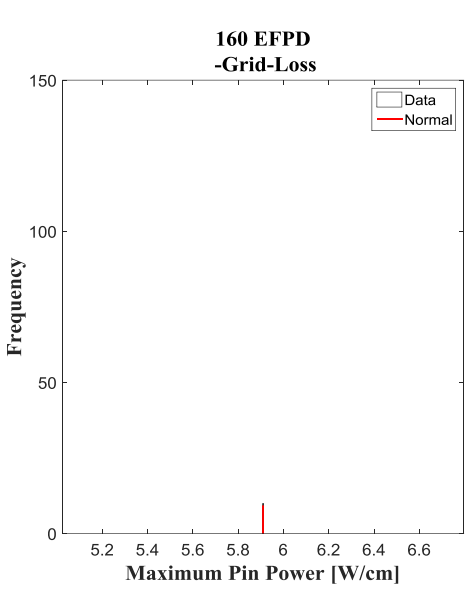
160 EFPD
-Grid-Loss
Data
Normal
Frequency
Maximum Pin Power [W/cm]
0
50
100
150
5.2
5.4
5.6
5.8
6
6.2
6.4
6.6

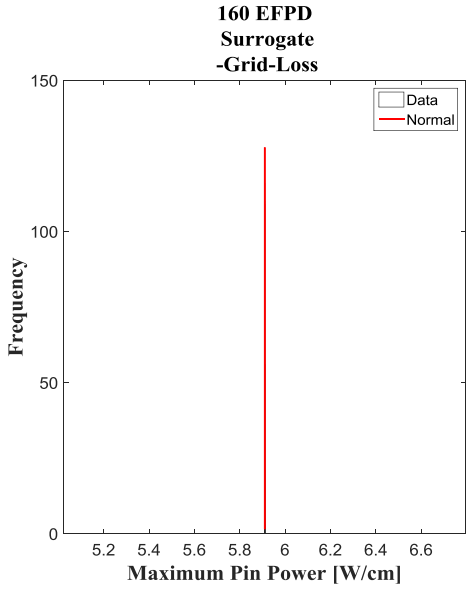
160 EFPD
Surrogate
-Grid-Loss
Data
Normal
Frequency
Maximum Pin Power [W/cm]
0
50
100
150
5.2
5.4
5.6
5.8
6
6.2
6.4
6.6

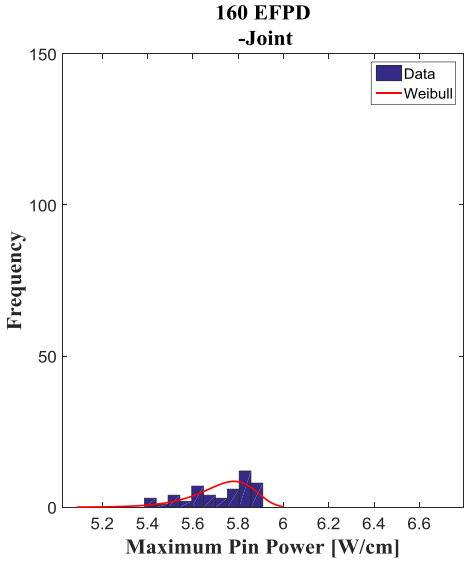
160 EFPD
-Joint
Data
Weibull
Frequency
Maximum Pin Power [W/cm]
0
50
100
150
5.2
5.4
5.6
5.8
6
6.2
6.4
6.6

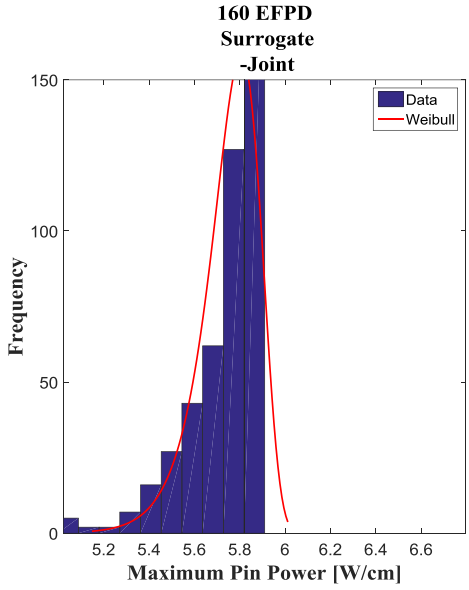
160 EFPD
Surrogate
-Joint
Data
Weibull
Frequency
Maximum Pin Power [W/cm]
0
50
100
150
5.2
5.4
5.6
5.8
6
6.2
6.4
6.6

Figure 109. Statistical sampling maximum pin temperature corresponding to samples of the Gap Conductivity, Grid-loss Coefficient, Cross- Sections and joint. Left: obtained via running VERA-CS right: obtained via the surrogate model.

Gap Conductivity [*hgap* W/m^2K], Grid-loss Coefficient, Cross- Sections and joint samples → *Maximum Pin Temperature*

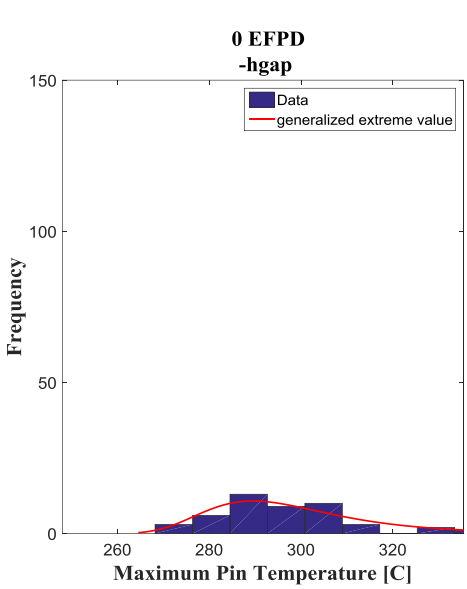
0 EFPD
-hgap
Data
generalized extreme value
Frequency
Maximum Pin Temperature [C]

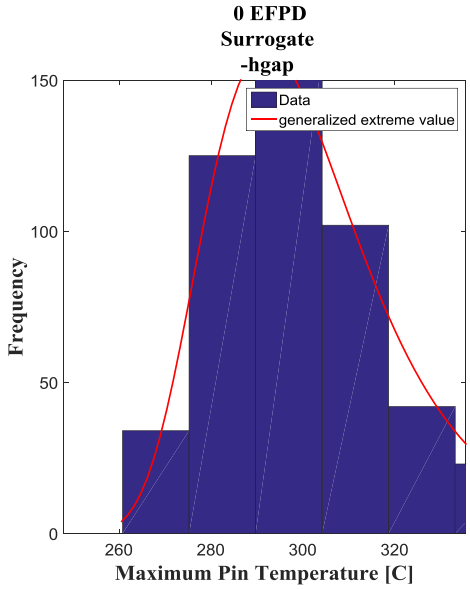
0 EFPD
Surrogate
-hgap
Data
generalized extreme value
Frequency
Maximum Pin Temperature [C]

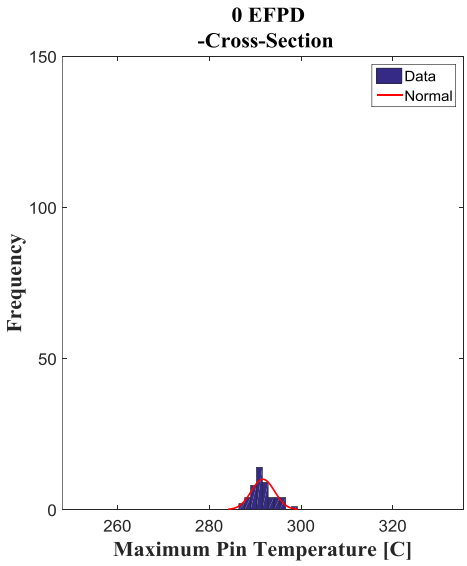
0 EFPD
-Cross-Section
Data
Normal
Frequency
Maximum Pin Temperature [C]

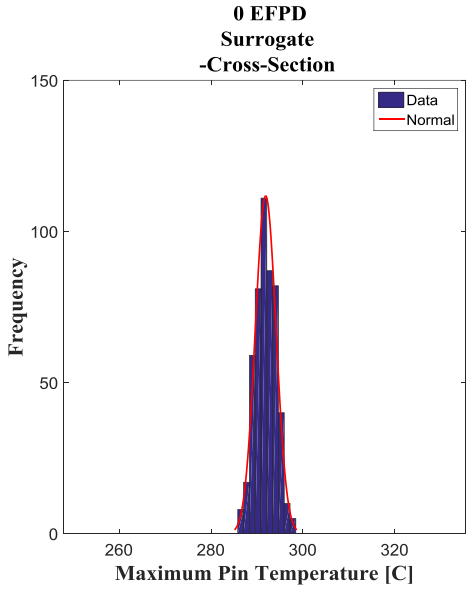
0 EFPD
Surrogate
-Cross-Section
Data
Normal
Frequency
Maximum Pin Temperature [C]

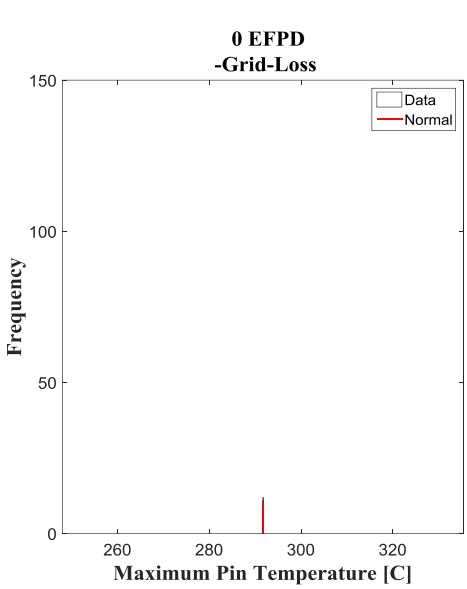
0 EFPD
-Grid-Loss
Data
Normal
Frequency
Maximum Pin Temperature [C]
0
50
100
150
260
280
300
320

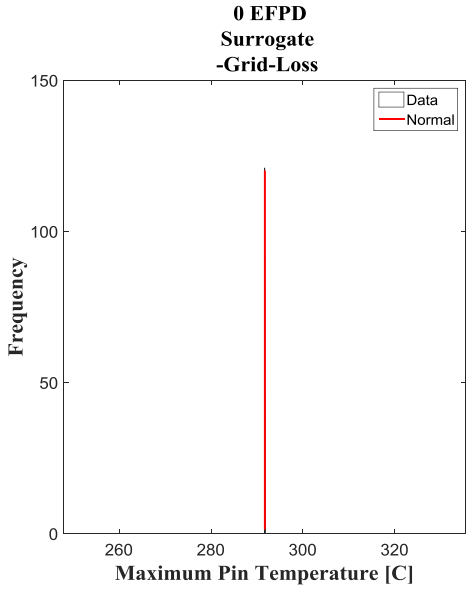
0 EFPD
Surrogate
-Grid-Loss
Data
Normal
Frequency
Maximum Pin Temperature [C]
0
50
100
150
260
280
300
320

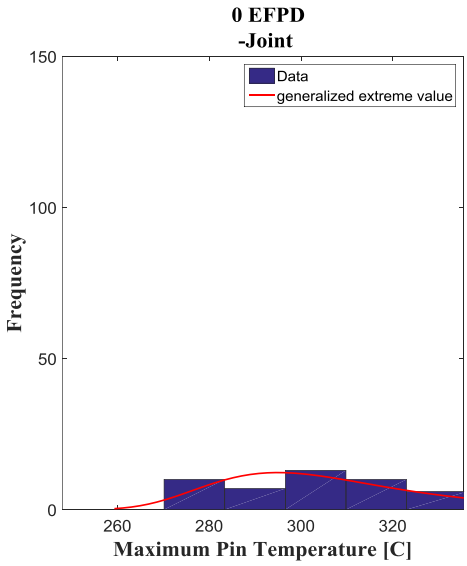
0 EFPD
-Joint
Data
generalized extreme value
Frequency
Maximum Pin Temperature [C]
0
50
100
150
260
280
300
320

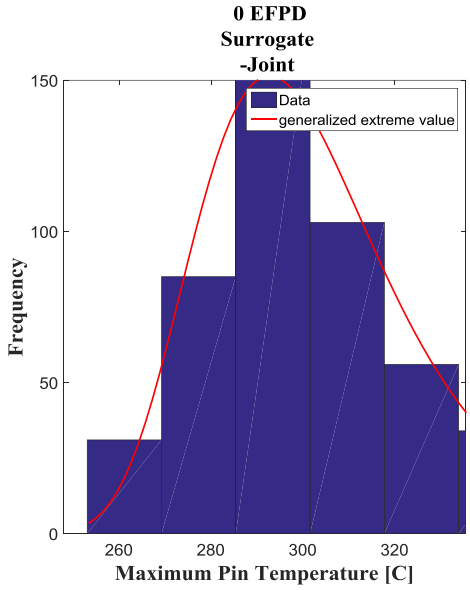
0 EFPD
Surrogate
-Joint
Data
generalized extreme value
Frequency
Maximum Pin Temperature [C]
0
50
100
150
260
280
300
320

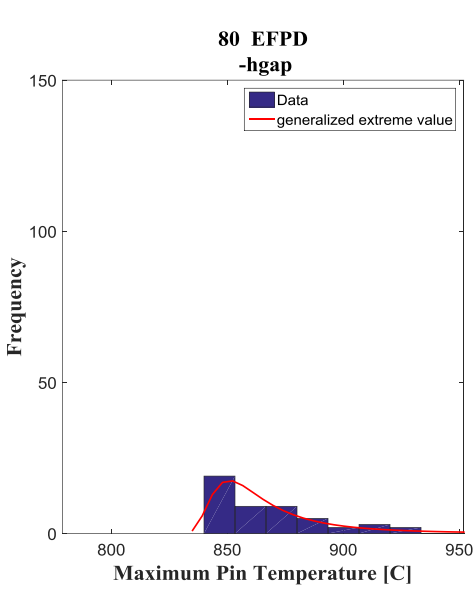
80 EFPD
-hgap
Data
generalized extreme value
Frequency
Maximum Pin Temperature [C]
0
50
100
150
800
850
900
950

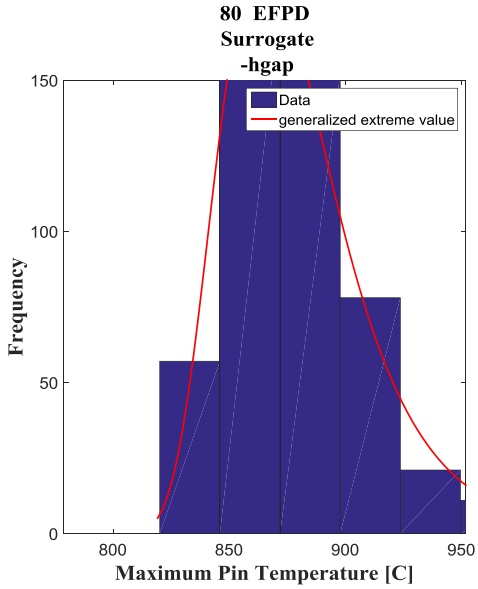
80 EFPD
Surrogate
-hgap
Data
generalized extreme value
Frequency
Maximum Pin Temperature [C]
0
50
100
150
800
850
900
950

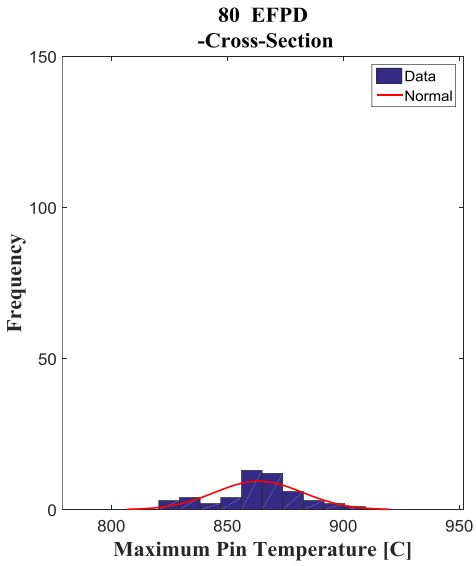
80 EFPD
-Cross-Section
Data
Normal
Frequency
Maximum Pin Temperature [C]
0
50
100
150
800
850
900
950

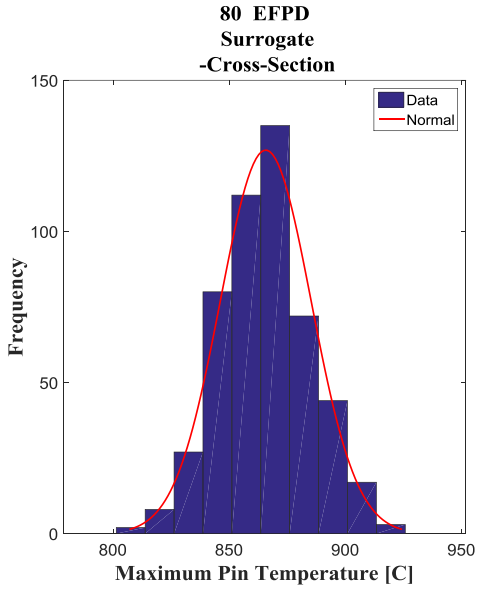
80 EFPD
Surrogate
-Cross-Section
Data
Normal
Frequency
Maximum Pin Temperature [C]
0
50
100
150
800
850
900
950

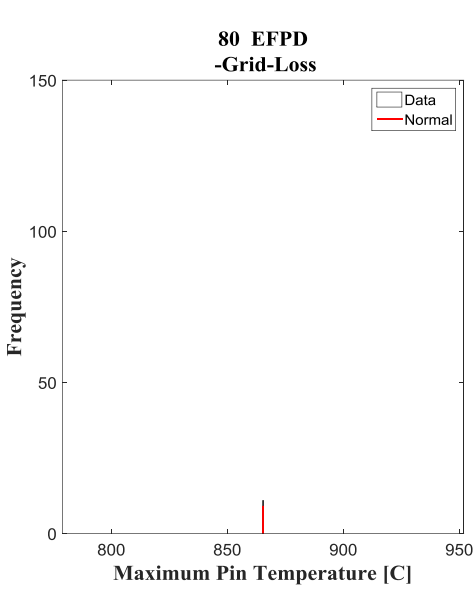
80 EFPD
-Grid-Loss
Data
Normal
Frequency
Maximum Pin Temperature [C]
0
50
100
150
800
850
900
950

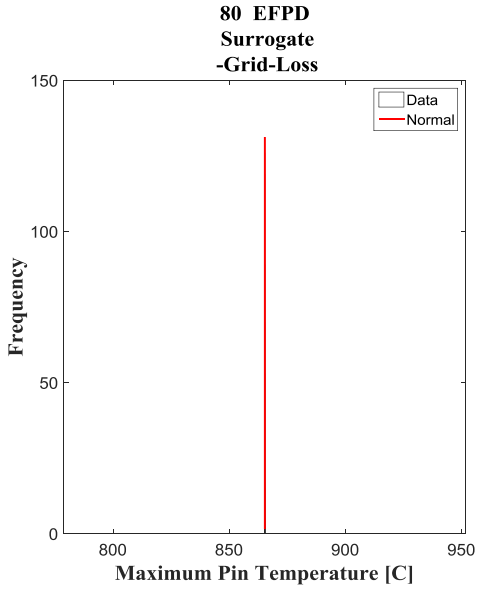
80 EFPD
Surrogate
-Grid-Loss
Data
Normal
Frequency
Maximum Pin Temperature [C]
0
50
100
150
800
850
900
950

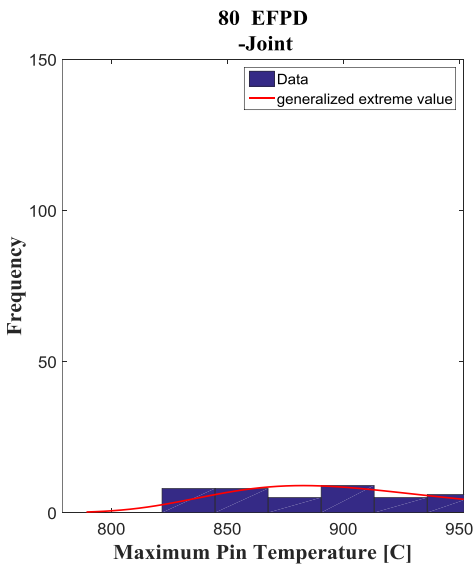
80 EFPD
-Joint
Data
generalized extreme value
Frequency
Maximum Pin Temperature [C]
0
50
100
150
800
850
900
950

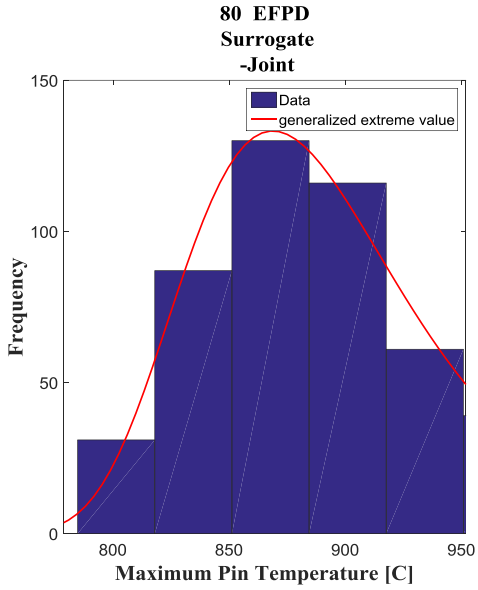
80 EFPD
Surrogate
-Joint
Data
generalized extreme value
Frequency
Maximum Pin Temperature [C]
0
50
100
150
800
850
900
950

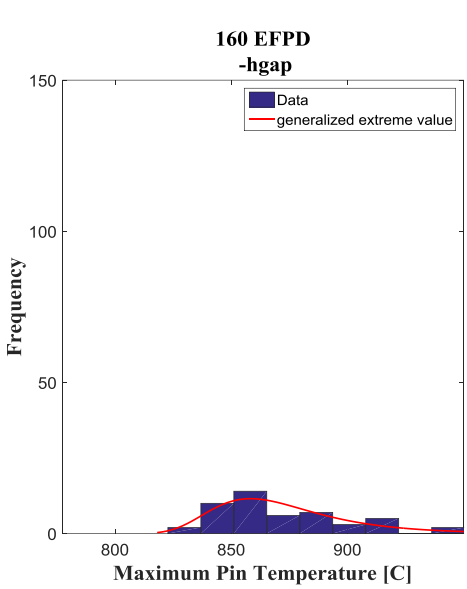
160 EFPD
-hgap
Data
generalized extreme value
Frequency
Maximum Pin Temperature [C]
0
50
100
150
800
850
900

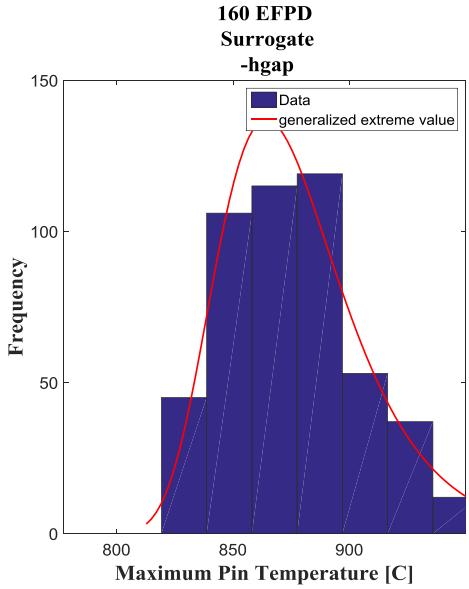
160 EFPD
Surrogate
-hgap
Data
generalized extreme value
Frequency
Maximum Pin Temperature [C]
0
50
100
150
800
850
900

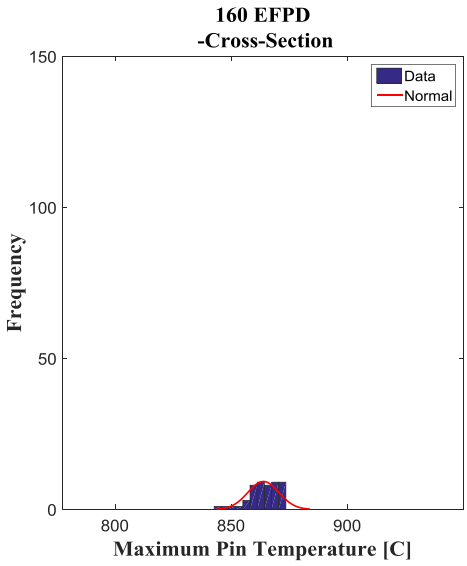
160 EFPD
-Cross-Section
Data
Normal
Frequency
Maximum Pin Temperature [C]
0
50
100
150
800
850
900

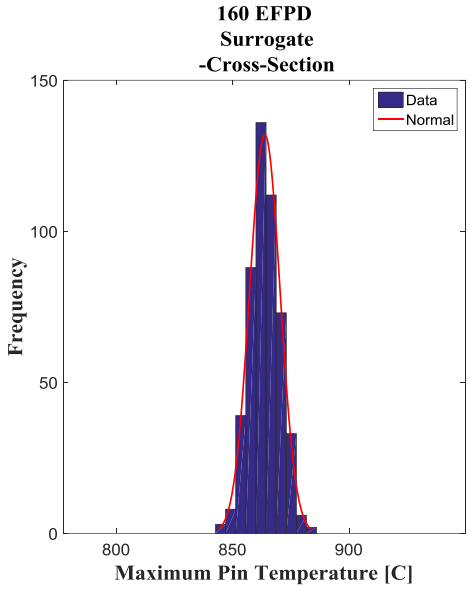
160 EFPD
Surrogate
-Cross-Section
Data
Normal
Frequency
Maximum Pin Temperature [C]
0
50
100
150
800
850
900

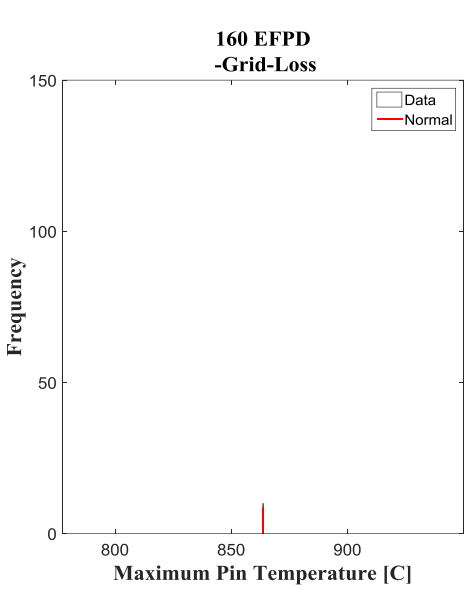
160 EFPD
-Grid-Loss
Data
Normal
Frequency
Maximum Pin Temperature [C]
0
50
100
150
800
850
900

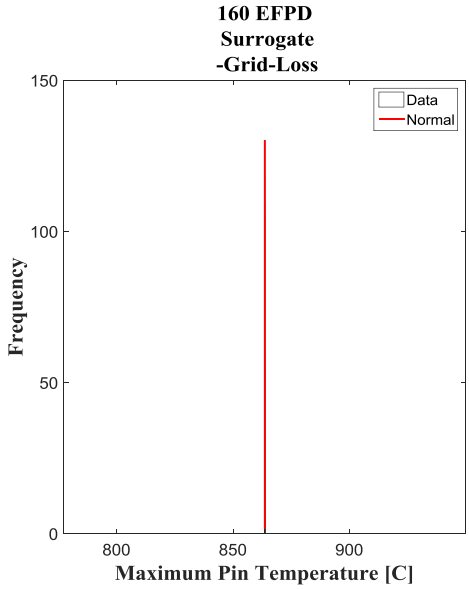
160 EFPD
Surrogate
-Grid-Loss
Data
Normal
Frequency
Maximum Pin Temperature [C]
0
50
100
150
800
850
900

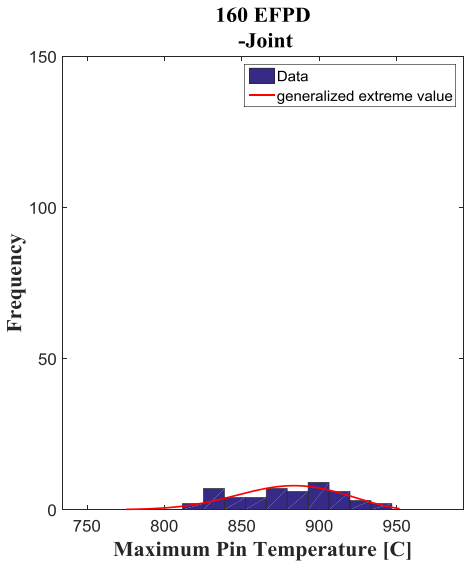
160 EFPD
-Joint
Data
generalized extreme value
Frequency
Maximum Pin Temperature [C]
0
50
100
150
750
800
850
900
950

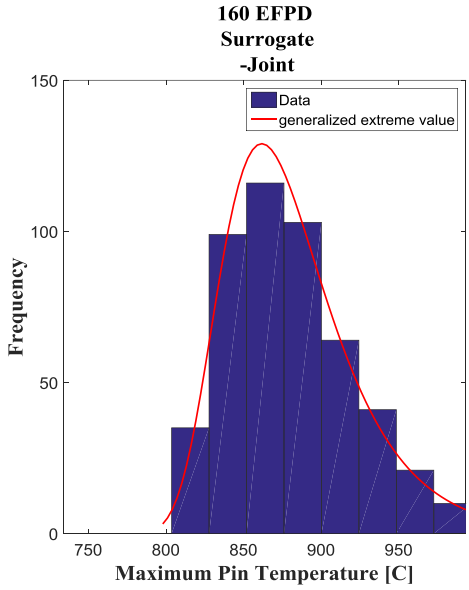
160 EFPD
Surrogate
-Joint
Data
generalized extreme value
Frequency
Maximum Pin Temperature [C]
0
50
100
150
750
800
850
900
950